Transactions of the ASME®

Technical Editor
ARTHUR J. WENNERSTROM
Senior Associate Technical Editor
G. K. SEROVY
Associate Technical Editors
Advanced Energy Systems
M. J. MORAN
Environmental Control
H. E. HESKETH
Fuels and Combustion Technologies
R. E. BARRETT
Gas Turbine
T. H. OKIISHI
Internal Combustion Engine
J. A. CATON
Nuclear Engineering
S. M. CHO
Power
R. W. PORTER

BOARD ON COMMUNICATIONS
Chairman and Vice-President
R. NICKELL

Members-at-Large
J. LLOYD
R. REDER
F. SCHMIDT
M. FRANKE
M. KUTZ
T. MIN
F. LANDIS
R. ROCKE
W. WINER
R. GENTILE
R. MATES

President, E. L. DAMAN
Executive Director,
D. L. BELDEN
Treasurer, ROBERT A. BENNETT

PUBLISHING STAFF
Mng. Dir., Publ., JOS. SANSONE
Managing Editor,
CORNELIA MONAHAN
Sr. Production Editor,
VALERIE WINTERS
Editorial Prod. Asst.,
MARISOL ANDINO

Transactions of the ASME, Journal of Turbomachinery (ISSN 0889-504X) is published quarterly (Jan., Apr., July, Oct.) for $100 per year by The American Society of Mechanical Engineers, 345 East 47th Street, New York, NY 10017. Second-class postage paid at New York, NY and additional mailing offices. POSTMASTER: Send address change to The Journal of Turbomachinery, c/o The AMERICAN SOCIETY OF MECHANICAL ENGINEERS, 22 Law Drive, Box 2300, Fairfield, NJ 07007-2300."

CHANGES OF ADDRESS must be received at Society headquarters seven weeks before they are to be effective. Please send old label and new address.

PRICES: To members, $29.00, annually; to nonmembers, $100.00. Add $15.00 for postage to countries outside the United States and Canada.

INDEXED by Applied Mechanics Reviews and Engineering Information, Inc.

Journal of Turbomachinery

Published Quarterly by The American Society of Mechanical Engineers

VOLUME 110 • NUMBER 4 • OCTOBER 1988

TECHNICAL PAPERS

ANNOUNCEMENTS

Design of High-Performance Fans Using Advanced Aerodynamics Codes

G. Karadimas
Chief of Aerodynamic Department,
SNECMA Villaroche,
Moissy Cramayel, France

In the recent past, the performance of transonic fans has been significantly improved. In addition, through the extensive use of advanced aerodynamic computation codes, the development time required has been considerably reduced. Methods used range from the definition of airfoils in quasi-three-dimensional flow with boundary layer optimization to the analysis of three-dimensional inviscid flow for stage operation at the design point and in off-design conditions. Such a set of methods was used to design the fan blade of the CFM56-5 engine to a very high performance level. This paper will discuss the optimization of rotor and stator airfoils, the assessment of off-design performance, and the operational stability of this fan. A detailed comparison of full-size component test data with computation results shows the validity of these methods and also identifies those areas where research is still required.

1 Introduction

Until recently, fans and axial compressors were designed and analyzed through a set of methods introduced in the 1950s, such as the quasi-three-dimensional flow approach of Wu (1951) and Johnson et al. (1965). The airfoil sections used were in geometric configurations such as those of the NACA 65 series, or the Multiple Circular Arc (MCA) airfoils. Viscous effects were exclusively introduced through empirical correlations, and were developed from the analysis of test data.

Using the possibilities offered by advanced computers, we have developed a new fan and axial compressor design methodology over the last 10–12 years. This methodology is based on (1) three-dimensional flow calculations through the blade/vane rows; (2) definition of airfoil sections by means of inverse or semi-inverse analytical methods; and (3) introduction of viscous effects through the computation of boundary layers and secondary flows. Operational stability aspects (surge, aeroelasticity) are also included.

We have already used this set of methods to produce very high-performance research axial compressors, and also to validate the selected methods, assumptions, and approaches.

After describing the procedure used with the new methods, this paper reviews the definition of the CFM56-5A fan, full-scale component tests, the test data analysis, and comparison with theoretical calculations.

2 Calculation Procedure

The calculation procedure is illustrated in Fig. 1. The starting point is an inverse throughflow calculation using our streamline curvature method.

In this calculation phase, the blockage factors simulating the secondary flows, the blade/vane stage blockage and losses, and the variation of work in the blade are estimated. The midspan shroud is also accounted for by a blockage factor. This calculation is used to optimize the flowpath, and, for a

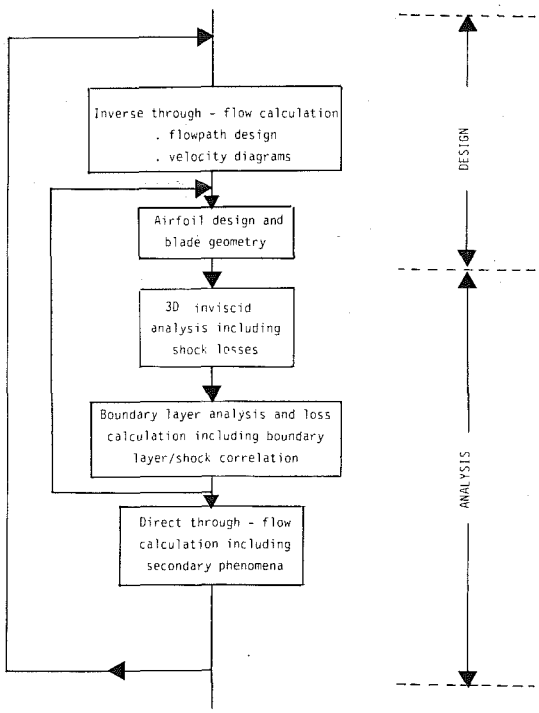

Fig. 1 Fan calculation procedure

Contributed by the International Gas Turbine Institute and presented at the 33rd International Gas Turbine and Aeroengine Congress and Exhibition, Amsterdam, The Netherlands, June 5–9, 1988. Manuscript received by the International Gas Turbine Institute October 1987. Paper No. 88-GT-141.

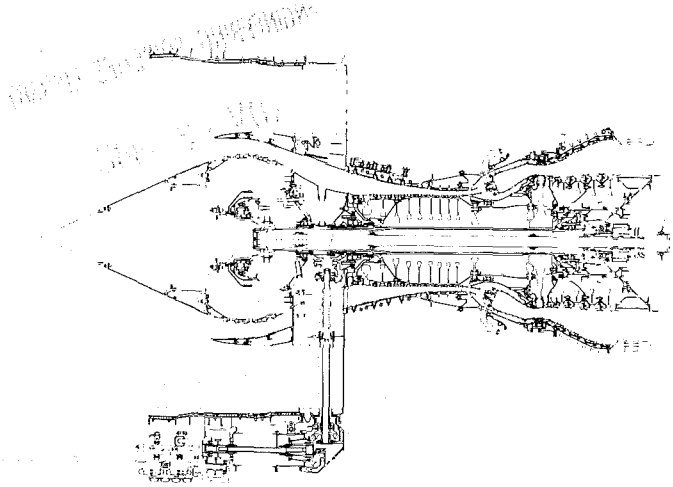

Fig. 2 CFM56-5A cross section

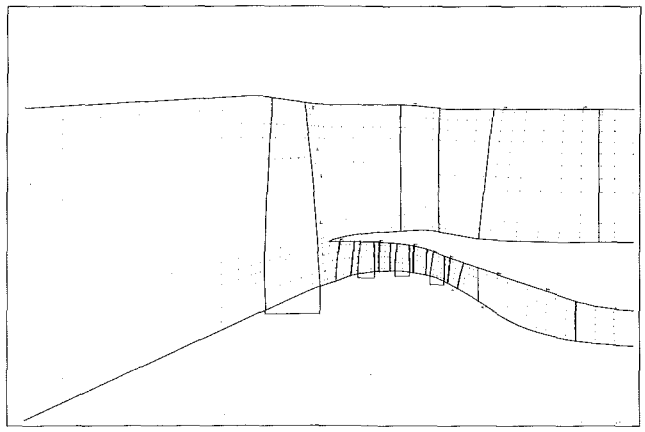

Fig. 3 Fan and booster flowpath

given radial total pressure distribution, yields the velocity diagrams needed to design the blade and vane profiles.

Subsonic or slightly transonic airfoil sections are defined using an inverse method, while supersonic sections are generated by means of a semi-inverse method. Airfoil section definition will be discussed in the next section. When the blade is defined, the design phase is complete.

The subsequent analysis phase covers a complete speed line defined by five to six points, instead of a single operating point.

The analysis phase starts with an inviscid three-dimensional calculation and yields a better computation of the flow around the blade than the conventional approach involving throughflow and blade-to-blade calculations. This three-dimensional calculation includes shock losses only; the other losses are estimated subsequently. The next step involves the boundary layer calculation of the airfoils. This is based on the flow distribution provided by the three-dimensional calculation along the streamlines. The method used is valid for a flow which is free from strong shocks. It however accepts slight flow separations and is found to provide a satisfactory evaluation of profile losses. Centrifugal and Coriolis corrections are not yet included. Shock/boundary layer interaction and strong shock separation losses are calculated by means of correlations.

At this stage of the analysis, the airfoil sections are examined in terms of boundary layer stability and losses are recalculated. An iterative process is used until satisfactory airfoil sections are obtained.

To achieve a satisfactory prediction of compressor performance, secondary losses must also be considered. A direct throughflow calculation coupled with a calculation of secondary flows provides the spanwise variations of pressure, temperature and efficiency in a final phase. These parameters are compared with goals and iterations are made until the profiles are optimized.

An aerodynamic stability phase (surge) and an aeroelastic phase can be added to this procedure.

3 Overall Characteristics and Performance Goals

The CFM56-5A (Fig. 2) is the third member of the CFM56 engine family, coming after the CFM56-2 and CFM56-3 versions. To maintain a thrust growth potential while limiting the costs and development time, a number of choices were settled that affect the CFM-5A fan characteristics. These are:

1 Same fan and low-pressure-turbine outer diameters as CFM56-2.

2 Four-stage LP turbine, like the CFM56-2 and CFM56-3, which leads to a practically unchanged nominal LP shaft rotation speed (5000 rpm, compared with 5175 rpm).

These choices lead to a high fan tip speed $Ue = 453$ m/s (1486 ft/sec), and a specific flow rate of $D/A = 203$ kg/s/m^2 (41.6 lb/sec/ft^2). The goal adiabatic efficiency of the bypass flow was selected to be consistent with the state of the art at the time of the project design (early 1984).

The main characteristics of the fan are summarized in the following table:

Outer diameter:	ϕ_e	1732 mm	68.2 in.
Tip speed:	U_e	453 m/s	1486 ft/sec
Total mass flow:	D	420 kg/s	926 lb/sec
Hub-to-tip ratio:	ν	0.35	
Specific flow rate:	D/A	203 kg/s/m^2	41.6 lb/sec/ft^2
Bypass pressure ratio:	λ	1.63	

4 Throughflow Calculation

The inverse throughflow calculation is done on both the core and bypass flows, with an optimization of the flow splitter. Figure 3 shows the flowpath with calculation stations. We selected 21 stream tubes for the fan rotor, 7 for the core flow and 16 for the bypass flow. This paper covers the fan blade and bypass O.G.V. only and not the core flow booster stages.

Nomenclature

A = annulus area
D = corrected mass flow
i = incidence
M = Mach number
P = stagnation pressure
p = static pressure
R = radius
U = blade speed
w = loss coefficient, percent

$$= \left(\frac{P_1' - P_2'}{P_1' - P_1}\right) \times 100$$

η = adiabatic efficiency
θ_c = throttle coefficient, percent

$$= \left(\frac{p_2}{p_{2dn}} - 1\right) \times 100$$

ξ = span, percent

$$= \left(\frac{R - R_h}{R_t - R_h}\right) \times 100$$

ϕ = diameter

Subscripts

1 = at inlet
2 = at outlet
dn = at design
h = at hub
t = at tip

Superscripts

$'$ = relative to a blade row

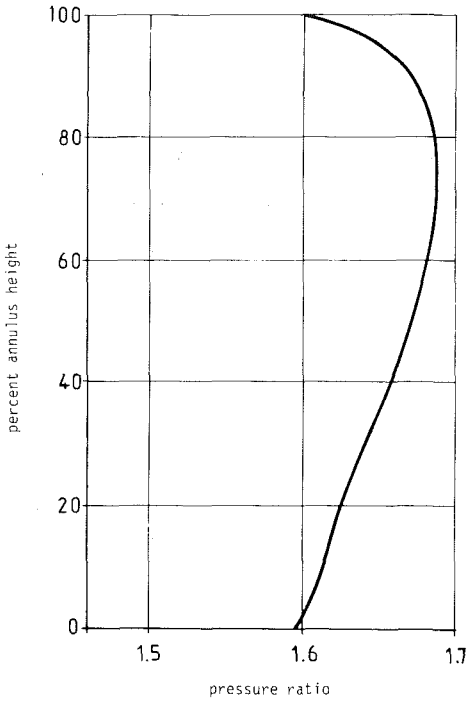

Fig. 4 Spanwise total pressure distribution

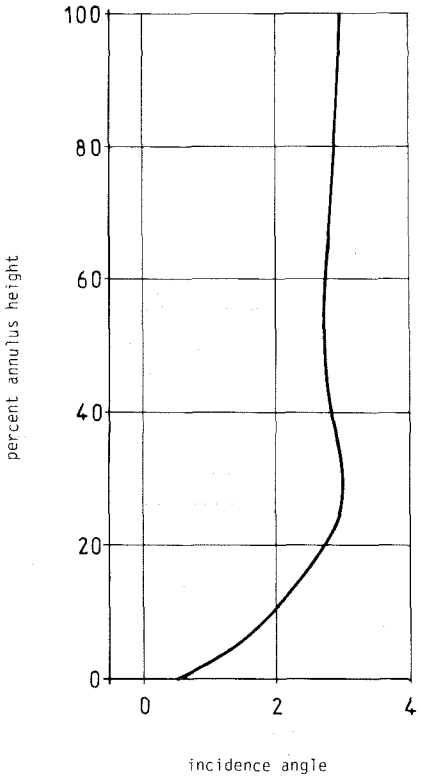

Fig. 5 Spanwise fan blade incidence angle

The spanwise distributions of total pressure and adiabatic efficiency were based on our experience acquired from experimental fans. The lower tip section pressure ratio (Fig. 4) reduces the relative flow angle deflection and limits the secondary flow effects. At this calculation step the secondary flows at hub and tip and the blade midspan shroud were accounted for through local blockage factors.

The bypass flowpath configuration has been designed to achieve the best compromise between the variation in Mach number on the hub wall, OGV inlet Mach number at the hub, and diffusion through the OGV and downstream up to the fan frame struts.

5 Rotor Design

The fan blade design is based on selected incidence angles and deviation angles. Adequate throat margins are selected by assuming losses upstream of the throat. The selected incidence angles (Fig. 5) take account of the unique incidence concept, and also of our experience acquired with other experimental fans.

Initially deviation angles are estimated, but these were modified as calculations proceeded, and the final choice was based on the three-dimensional calculation.

Increased leading edge thickness to improve the foreign object ingestion performance of the fan blade was a major constraint in the definition of airfoil sections.

5.1 Airfoil Sections. Twelve basic airfoil sections were used to define the fan blade. The lower two sections were calculated by means of the Karadimas (1972) inverse method. In this method the pressure and suction surface diffusion was controlled using inviscid and boundary layer analyses. The other ten sections were defined by means of our semi-inverse method applicable to supersonic inlet flow airfoils.

The airfoil sections were generated using a number of selected aerodynamic parameters. These are:

1 incidence angle
2 deviation angle
3 throat margin and location, and other geometric parameters such as maximum thickness, leading edge dihedral, and chord length (or airfoil section area).

The three-dimensional inviscid calculation, which includes shock losses and correlations for shock wave/boundary layer interaction, was used to analyze the supersonic sections. The main optimization parameters were:

1 shock wave position and intensity
2 starting margin
3 total losses

5.2 Midspan Shroud. The midspan shroud has elliptical cross sections located at a meridional surface. Its radial location is the result of a compromise between aerodynamic and mechanical requirements.

The three-dimensional calculation shows that a shroud leading edge aligned to the real flow angle could be better matched. This real flow angle varies significantly from a meridional line in the intrablade region.

5.3 Rotor Blade Definition. The rotor blade is generated by stacking the sections on their center of gravity while taking account of adjustments for blade deformation. At this stage, particular attention is paid to smooth shape, an important factor for blade manufacturing and inspection. If needed, some sections are redesigned, while monitoring the aerodynamic optimization through the three-dimensional calculation. When the blade shape has been defined, the throat margin and the internal contraction ratio are accurately checked.

6 Three-Dimensional Analysis

The calculation method used was developed in cooperation with ONERA (Viviand and Veuillot, 1978; Brochet, 1980). This calculation solves the Euler equations by means of a pseudo-unsteady method. This method was adapted by us and is currently used on IBM 3090 or CRAY1 computer.

To calculate the CFM56-5A fan flow, we used a 10,000-point mesh (Fig. 6). Results of this analysis are shown

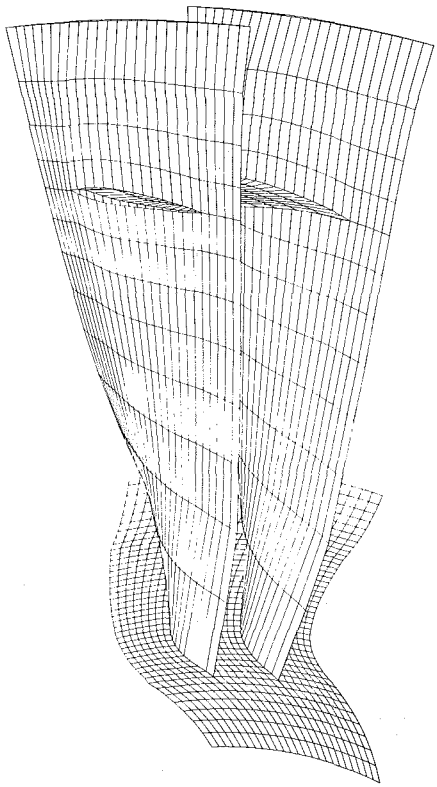

Fig. 6 Fan blade mesh

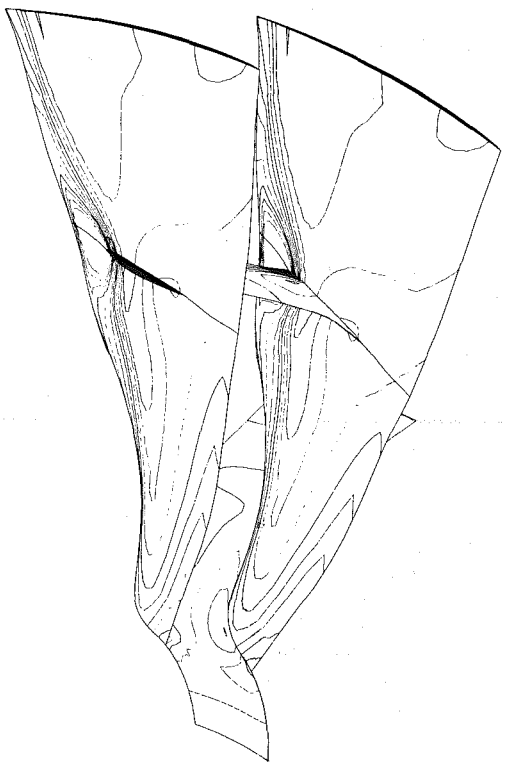

Fig. 7 Fan blade flow analysis

in Fig. 7, on the pressure and suction sides of the airfoil and on the platform and shroud.

This calculation was repeated for several throttling values for each speed line and for different speed lines. Figures 8 and

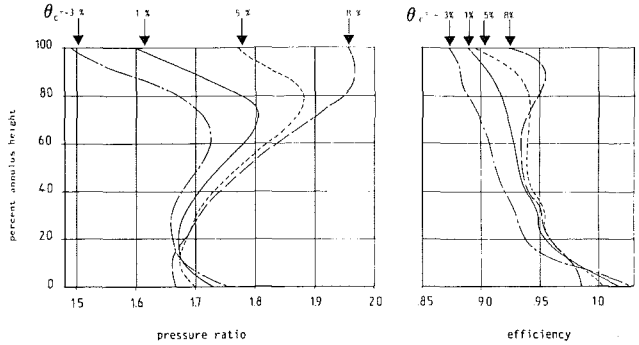

Fig. 8 Spanwise pressure ratio and efficiency distribution for design speed

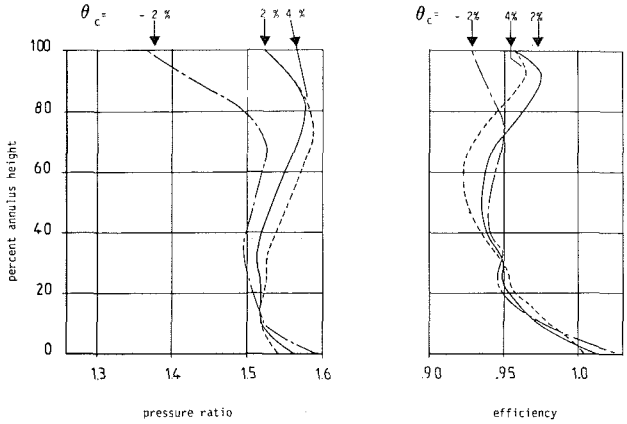

Fig. 9 Spanwise pressure ratio and efficiency distribution for 90 percent design speed

9 show the spanwise variation of pressure ratio and efficiency for design and 90 percent design speeds. Near the hub, as the flow is shock-free, the efficiency, calculated from the Euler three-dimensional equations, used to be close to 100 percent. In this calculation some numerical problems with the entropy variation near the subsonic hub exist and sometimes the computed efficiency exceeds 100 percent slightly.

7 Performance Evaluation

As stated above, the three-dimensional inviscid calculation takes account of shock losses only. The following procedure was used to calculate the other losses, while using the results of the three-dimensional calculation:

- Losses due to leading edge bow shock, locally detached, were calculated through an ONERA method proposed by Le Meur (1983).
- Viscous losses were calculated through the Papailiou (1974) boundary layer method. When the shock wave/boundary layer interaction is strong, the result is corrected by means of an empirical correlation.
- Losses due to the midspan shroud were evaluated using the Roberts (1978) proposal.

Figure 10 shows schematically the spanwise evolution of rotor losses for one throttling value of the nominal speedline.

8 Stator Design

8.1 Airfoil Definition. As the stator incoming flow Mach number is subsonic, all airfoil sections were generated by means of the Karadimas (1972) inverse method. The direct Luu–Monfort (1983) method coupled with a Papailiou (1974)

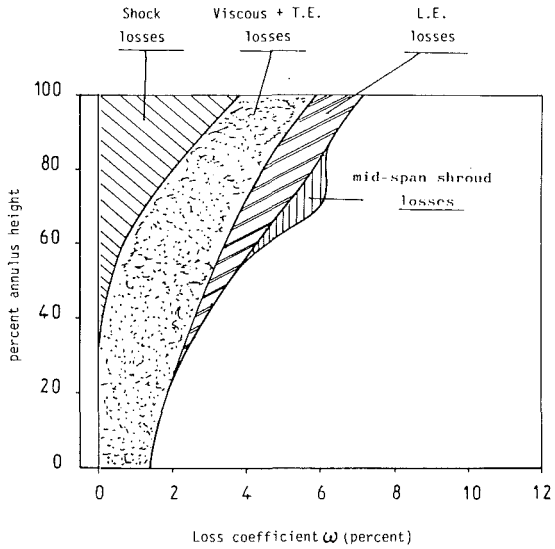

Fig. 10 Spanwise evolution of rotor losses

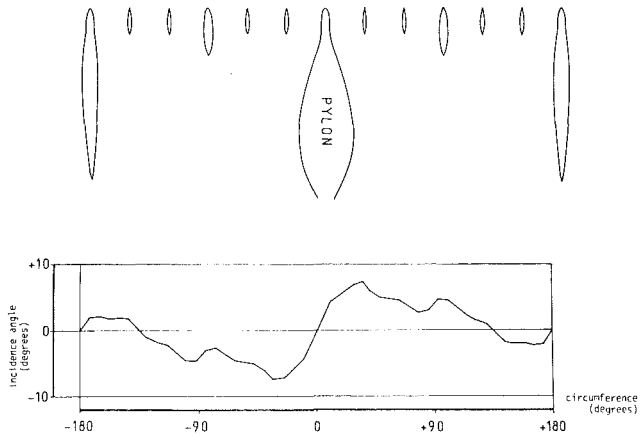

Fig. 11 Upstream influence of pylon and fan frame struts

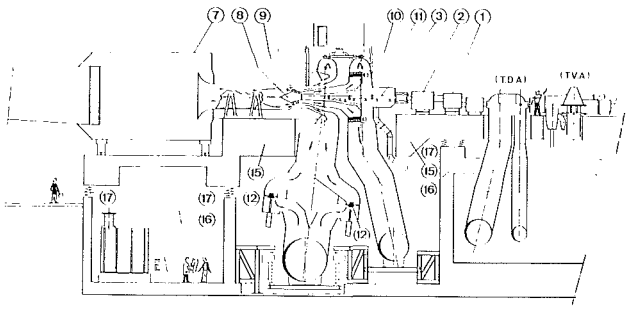

Fig. 12 Saclay compressor rig cross section

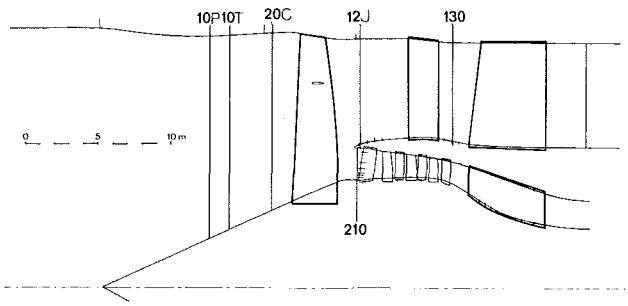

Fig. 13 Measurement stations

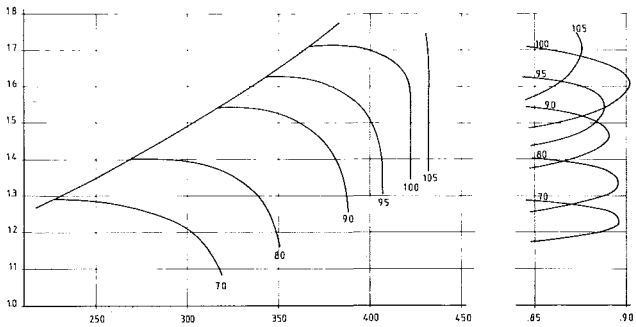

Fig. 14 Measured fan map

boundary layer calculation was used to analyze these sections. Airfoil sections were calculated while seeking an operation free from boundary layer separation over a wide range of incidence angles (-4 to $+6$ deg). This was necessary to account for the high circumferential variation of the angle due to interaction with the pylon and the downstream struts. This will be described below.

8.2 Interaction With Downstream Pylon and Struts. The pylon, with its large dimensions, and the fan frame struts produce a disturbed upstream flow field including large circumferential variations of the OGV inlet angle. Knowledge of the characteristics of this flow field is essential to obtain an adequate optimization of the stator. Figure 11 shows the calculated result at the inner flowpath of the bypass duct. For this calculation the Henry (1975) singularity method was used.

9 Test Bed and Instrumentation

The full-size fan and booster were tested in the CEPr compressor rig at Saclay near Paris. This compressor rig (Fig. 12) has a maximum power rating of 40,000 kW, and incorporates a high-performance data acquisition system of more than 2000 channels.

The measurement stations are shown in Fig. 13. The instrumentation covers two types of test:

1 Tests made to plot the characteristic map at several speed lines, with several data points for each speed line

2 Tests to achieve a detailed measurement of the flow for several significant data points, in particular downstream of the OGV

In the first type of test, eight radial rakes comprising eight combined pressure and temperature sensors were used at the OGV outlet plane.

In the second type of test, eight segments of about 6 deg, which corresponds to the OGV pitch, are traversed by ten-sensor arc rakes distributed around the periphery. This set can also account for the effect to the struts. However, for accessibility reasons, no rake was installed in the vicinity of the pylon.

The flow rate was calibrated from total pressure traverse located at the front of the fan and from boundary layer rakes at the same station. The accuracy of this system is ± 0.8 percent.

10 Test Data Analysis and Discussion

Since the radial rakes did not adequately cover the OGV wake, we have defined the exact performance of the fan by

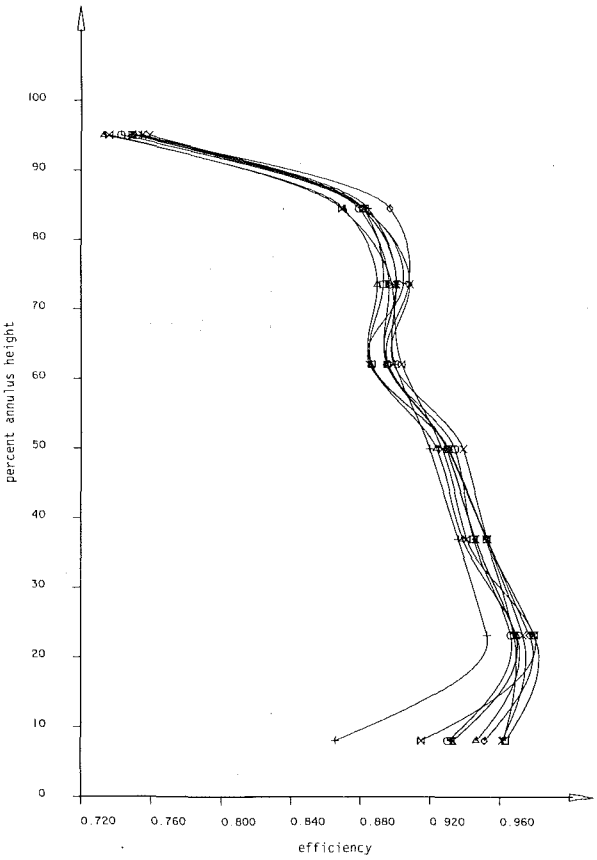

Fig. 15 Spanwise efficiency distribution

eight arc rakes in ten operating points and correlated the data between the eight radial rakes and the eight arc rakes. Figure 14 shows the map obtained.

At the design point (cruise), the test mass flow and pressure ratio met the performance goal. However the test efficiency exceeds the goal by 2.8 points, along with substantial surge margin. At a part speed rating of 90 percent the maximum efficiency dropped by about 1 percent, but increased slightly again at lower ratings.

Integrating of all pressure and temperature wakes gives the overall (fan plus OGV) spanwise efficiency variation plotted in Fig. 15. The low disturbance due to the midspan shroud can be noticed, with a corresponding loss of 0.5 percent against 0.8 percent used for the calculation.

Finally we undertook to compare the test results to our calculations for the bypass flow section of the fan rotor blade.

As already stated, the starting point of theoretical calculations is a three-dimensional calculation including the shock losses. The pressure and suction side boundary layers are calculated from the Mach number distributions provided by this three-dimensional calculation. Then, we add the leading edge, midspan shroud and trailing edge losses.

The losses defined as above are introduced in a throughflow calculation coupled with the Brochet and Falchetti (1987) calculation of endwall losses. Comparison with test data for a running point close to the design point is shown in Figs. 16 and 17.

This comparison shows a fair assessment of the pressure gradient, except near the hub where the flow is disturbed by the upstream effect of the pylon. The efficiency variation is also fairly well predicted. The effect of midspan shroud is less marked in the test data, but this is related to the fact that the analysis is made from measurements downstream of the OGV instead of immediately behind the rotor.

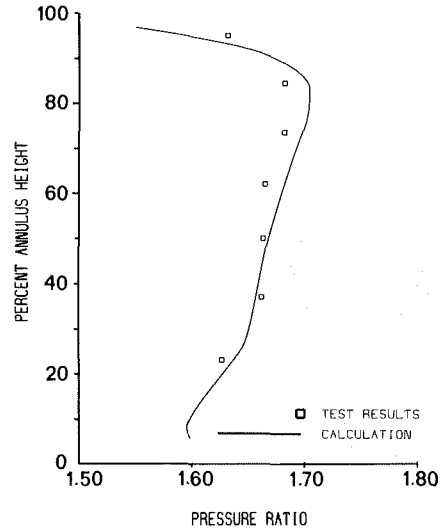

Fig. 16 Fan blade pressure ratio: test versus calculation

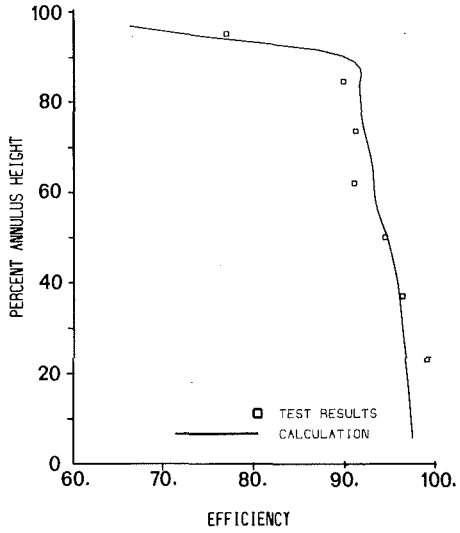

Fig. 17 Fan blade efficiency: test versus calculation

11 Conclusions

- We have been able to design very high-performance fans using advanced aerodynamic computation codes such as inviscid three-dimensional calculation, boundary layer calculation, and secondary flow calculation.
- The flow description, computed by the above system, is better than what is obtained from a quasi-three-dimensional approach involving throughflow radial equilibrium and blade-to-blade calculations.
- The CFM56-5A fan designed by this methodology yielded outstanding performance levels as early as the first test, considering the inlet Mach number level.
- Introduction of midspan shroud and airflow splitter, boundary layer coupling, and combined rotor/stator calculations are the next steps, already being implemented, which will allow three-dimensional calculations to provide an even better solution of the flow, in particular in the off-design conditions.

Acknowledgments

The author would like to express his gratitude to SNECMA for permission to present this paper.

References

Brochet, J., 1980, "Calcul Numérique d'Écoulements Internes tridimensionnels Transsoniques," La Recherche Aérospatiale, No. 1980-5, pp. 301–315, English translation ESA TT 673.

Brochet, J., and Falchetti, F., 1987, "Secondary Flow Computation in Multistage Axial Flow Compressors," 8th ISABE, Cincinnati, OH, USA.

Henry, C., 1975, "Solution numérique pour une méthode de singularités du problème de l'écoulement compressible sur des surfaces de courant axisymétriques," Thèse de Docteur Ingénieur, Université de Lyon, France.

Johnson, X. X., et al., 1965, "Aerodynamic Design of Axial-Flow Compressors, Revised," NASA SP-36.

Karadimas, G., 1972, "Increasing the Aerodynamic Loading of Axial Flow Turbines," ASME Paper No. 72-GT-78.

Le Meur, A., 1983, "Computation of Blade Cascade Aerodynamic Losses Due to Detached Shock Waves," 6th ISABE, Paris, France.

Luu, T. S., and Monfort, G., 1983, "Blade-to-Blade Transonic Flow Calculation in Axial Turbomachines," 6th ISABE, Paris, France.

Papailiou, K. D., 1974, Optimisation des dispositifs décélérateurs à forte charge fondée sur une théorie intégrale de la couche limite," Thèse du Doctorat es Sciences, Université de Lyon, France.

Roberts, W. B., 1978, "A Design Point Correlation for Losses Due to Part-Span Dampers on Transonic Rotor," ASME Paper No. 78-GT-153.

Viviand, H., and Veuillot, J. P., 1978, "Méthodes Pseudo-Instationnaires pour les Calculs d'Écoulements Transsoniques," ONERA publication No. 1978-4; English translation ESA.TT.561.

Wu, C. H., 1951, "A General Through-Flow Theory of Fluid Flow With Subsonic or Supersonic Velocity in Turbomachines of Arbitrary Hub and Casing Shapes," NACA TH 2302.

Design Point Variation of Three-Dimensional Loss and Deviation for Axial Compressor Middle Stages

W. B. Roberts
Flow Application Research,
Fremont, CA 94539

G. K. Serovy
Iowa State University,
Mechanical Engineering Department,
Ames, IA 50011

D. M. Sandercock
NASA-Lewis Research Center
Cleveland, OH 44135

Three-dimensional spanwise pressure loss and flow angle deviation variations have been deduced from NASA, university, and industrial sources from middle-stage research compressors operating near design point. These variations are taken as the difference above or below that predicted by blade element theory at any spanwise location. It was observed that the magnitude of the three-dimensional loss and deviation in the endwall regions is affected by hub and casing boundary layer thickness, camber, solidity, and blade channel aspect ratio for stators and rotor hubs. Rotor tip variations were found to depend on casing boundary layer thickness and tip clearance. Simple design point loss models derived from these data can aid in the design of axial compressor middle stages.

Introduction

The flow field associated with multistage axial compressors is extremely complicated. It is viscous, compressible, unsteady, three-dimensional, and rotational. Presently, there is no closed-form computational solution that predicts this flow field accurately without empirical input.

An important part of the general prediction problem is the determination of the design point flow field. Here, simple loss models can be useful. They allow the evolution of the compressor configuration to proceed through the design phase and into analysis where the computer solutions are the most powerful. A careful study of loss and flow angle deviation data from middle-statge, subsonic research compressors from NASA, university and industrial sources (Adkins et al., 1982; Johnsen et al., 1985, Smith, 1970; Wisler et al., 1987) has revealed that *at or near* the design point, the flow field past any blade row in a multistage axial compressor can be subdivided into a core flow that behaves in a nearly inviscid manner[1] and a region of higher loss near the endwalls. In the core flow region, losses are caused by relatively small blade wakes that are spread by turbulent diffusion and spanwise wake flow. Here there is little interaction between the wake and the main flow.

In the vicinity of the endwalls, strong vortical motions, induced by the interaction of blade and endwall boundary layers and pressure fields, cause localized regions of high loss and turbulent mixing. A simple flow model of this phenomenon showing the main endwall flows is given in Fig. 1. The resulting loss variation can be seen in the schematic of Fig. 2 where the three-dimensional or secondary losses are superimposed on the primary or profile losses.

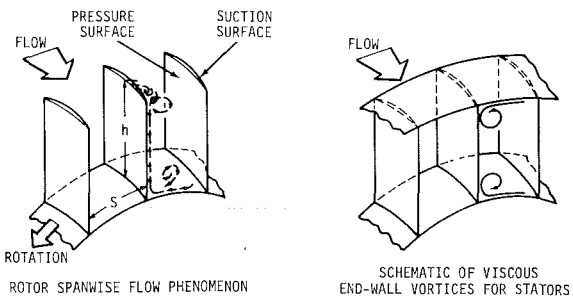

Fig. 1 Endwall vortex flow model

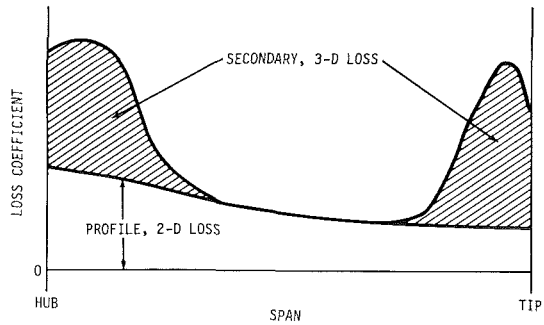

Fig. 2 Schematic of the secondary three-dimensional loss variation superimposed on the profile or two-dimensional loss variation

[1] Although the core flow might not be actually inviscid, in that it can have relatively high turbulence and dissipation, it behaves approximately like a potential flow.

Contributed by the International Gas Turbine Institute and presented at the 33rd International Gas Turbine and Aeroengine Congress and Exhibition, Amsterdam, The Netherlands, June 5–9, 1988. Manuscript received by the International Gas Turbine Institute September 15, 1987. Paper No. 88-GT-57.

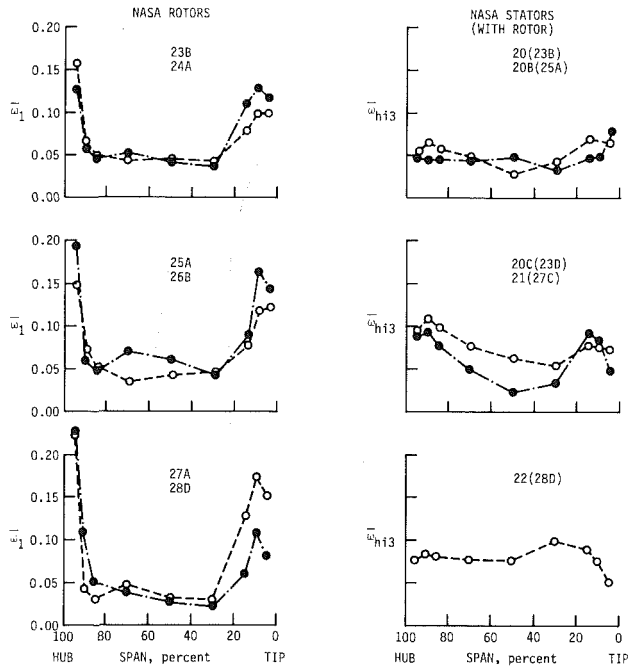

Fig. 3 Spanwise variation of loss coefficient for NASA rotors and stators (Britsch et al., 1979—rotor and stators listed above go with the open circle, solid below)

At or near the design point, where the core flow is fully attached to the blading, the profile losses can be readily estimated using two-dimensional computer codes (LeFoll, 1965; McFarland, 1984; McNally, 1970; Van den Braembussche, 1973) or empirical correlations (Horlock, 1958; Howell, 1963 Johnsen et al., 1965). However, an estimate of the additional loss due to three-dimensional or secondary effects has been much more difficult to develop since middle-stage data sets with sufficient flow detail in the endwall region have been very limited. The objective of the present work is to use the available data to derive simple empirical models for the spanwise variation of three-dimentional viscous loss coefficient for middle-stage axial compressor blading.

Data Base

The initial data used in this study were from twelve (12) NASA subsonic multistage configurations covering a wide range of design parameters (Britsch et al., 1979; Roberts et al., 1978). All NASA data considered were from operation near the design point and at the design tip speed of 244 m/s. Additional useful data were found in the open literature from General Electric Company (Adkins et al., 1982; Wisler, 1977, 1980), National Research Institute for Machine Design in Czechoslovakia (SVÚSS) (Cyrus, 1986), United Technologies Research Center (Dring et al., 1982), and Kyushu University (Inoue et al., 1986). All of the data used from these sources were taken at or near design point operation.

Three-Dimensional Loss Model: Total Pressure Loss Data

An example of the spanwise variation of loss coefficient for several NASA rotors and stators is shown in Fig. 3. The NASA data had the boundary layer defined only at the rotor and stator tips. The Kyushu loss data (Fig. 11) were taken only at the rotor tip region, and these loss coefficients were divided by the constant 1.52 to account for compressibility and radius change in the definition of dynamic pressure. The GE rotor data (Wisler, 1977, 1980), both single- and multistage, were taken with a rotating and translating pressure probe at the respective rotor exit. Finally, the hub and tip rotor and stator geometries for the SVÚSS data (Cyrus, 1986) were extrapolated from mean radius values using the free vortex radial equilibrium equations (Johnsen et al., 1965) to deduce flow angles and, therefore, required variation of blade solidity, stagger, and camber.

In a previous paper (Roberts et al., 1986), the present authors proposed an approximate method of reducing rotor and stator performance data that separate three-dimensional from blade element effects (i.e., two-dimensional or core flow effects). The method entails taking the total performance parameter to be studied (i.e., deviation or loss) and subtracting the part due to two-dimensional effects. For this paper, the spanwise distribution of blade element loss was

Nomenclature

AR_c = channel aspect ratio = h/s_m
c = mean blade chord, cm
D = diffusion factor
h = mean span or mean blade height, cm
LP_{2D} = two-dimensional loss parameter, equation (2)
P = total pressure, N/cm^2
p = static pressure, N/cm^2
r = radius, cm
S = distance along the span from either endwall measured at the blade outlet along the radial direction, cm
$\bar{S}_{3D}$ = extent of three-dimensional loss region in fraction of span
$(\bar{S}_{3D})_{max}$ = location of maximum three-dimensional loss in fraction of span
s = blade spacing, cm
TC = rotor blade tip clearance, mm
β_1 = inlet flow angle, relative to meridional direction, deg
β_2 = outlet flow angle, relative to meridional direction, deg
δ = flow deviation angle, deg
δ_1^* = inlet displacement thickness, mm
$\bar{\Delta}$ = difference in deviation = $(\delta-\delta_{2D})-(\delta-\delta_{2D})_{50}$, deg
σ = solidity = c/s
ϕ = blade camber angle, deg
$\bar{\omega}$ = loss coefficient = $(P_1-P_2)/(P_1-p_1)$

Subscripts

1 = inlet
2 = outlet
5 = 5 percent of span from tip; measured at the blade outlet
50 = 50 percent of span (midspan), measured at the blade outlet
2D = equivalent two-dimensional conditions
3D = three-dimensional conditions
avg = average
h = hub
hi3 = average of the high three values measured in a circumferential survey of multiple blade-to-blade space
m = midspan value
max = maximum
ov = overall
rt = rotor tip
s = stator
t = tip
w = wall (endwall)

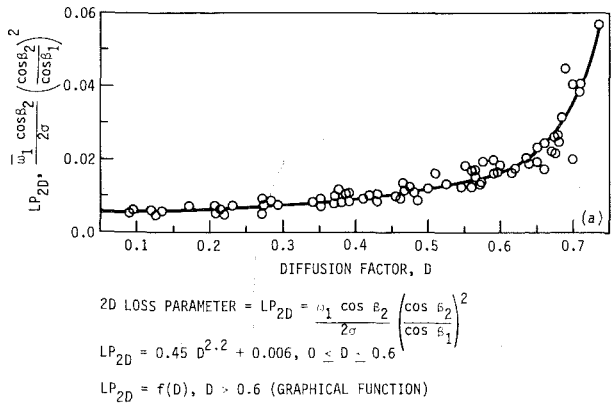

Fig. 4 Variation of loss parameter with diffusion factor at reference minimum-loss incidence angle computed from low-speed cascade data of NACA 65: (A_{10}) ten blades (Johnsen et al., 1965)

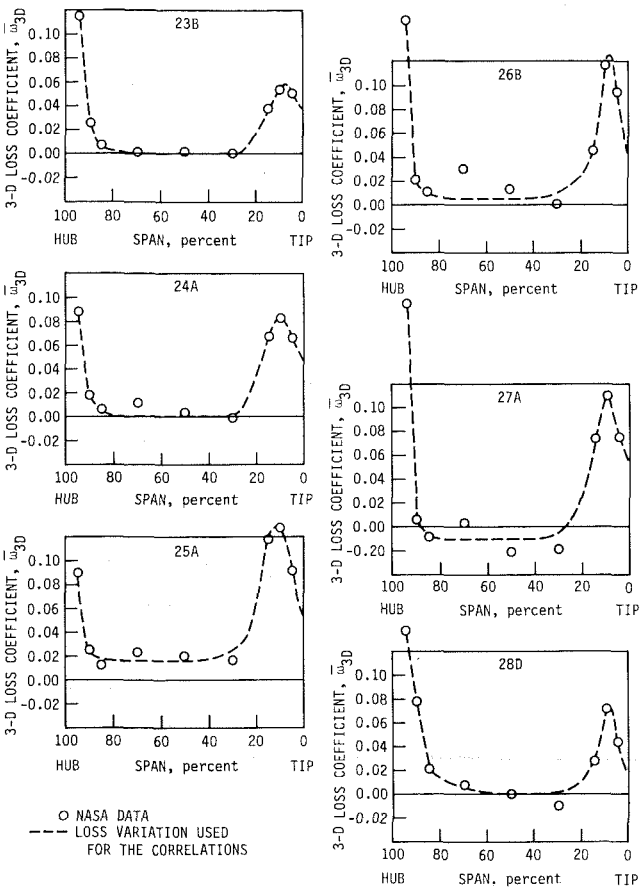

Fig. 5 Three-dimensional variation of loss coefficient for NASA rotors (Britsch et al., 1979)

estimated from the variation of Diffusion Factor,[2] D, along the blade height combined with relations derived from Fig. 4:

$$LP_{2D} \simeq 0.045D^{2.2} + 0.006, \qquad 0 \le D \le 0.6$$
$$LP_{2D} \simeq f(D), \qquad D > 0.6, \text{ see Fig. 4} \tag{1}$$

Using equation (1), an estimate of the two-dimensional loss parameter LP_{2D} can be made, and from this the loss coefficient can be calculated with equation (2):

[2]The values of the diffusion factor used were calculated from blade element data that accounted for the effects of streamline shift and axial velocity changes (see method of Seyler et al., 1967).

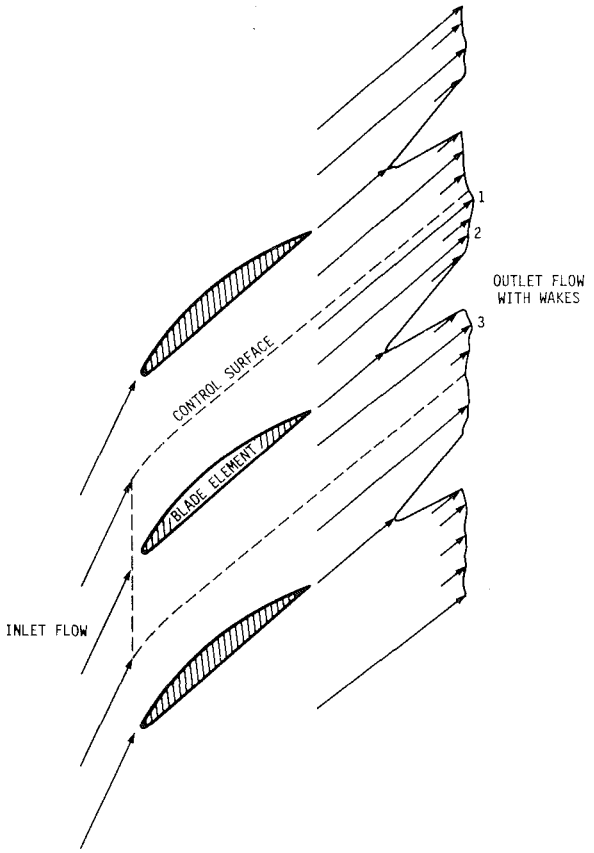

Fig. 6 Schematic of blade element flow showing the location of the high three (hi3) pressure readings in the wake of one blade

$$\bar{\omega}_{2D} = \frac{2\sigma LP_{2D}}{\cos\beta_2}\left(\frac{\cos\beta_1}{\cos\beta_2}\right)^2 \tag{2}$$

After this, the two-dimensional loss coefficient variation is subtracted from the total loss coefficient distribution across the blade span. The remainder is taken as the loss due to three-dimensional effects. An example of this three-dimensional variation of loss coefficient for rotors is given in Fig. 5.

The stator three-dimensional loss coefficient variation was estimated by a different method from the rotors. Rotor wakes and pressure velocity gradients that pass through the stator mask the true stator-generated losses and make them appear higher. To have a better approximation of the stator-generated losses, circumferential traverses at the stator exit have been used to calculate a wake loss coefficient. The stator inlet total pressure P_1 is assumed to be the same as an average of the three (3) highest total pressure measurements in the downstream circumferential traverse (Fig. 6).[3] Therefore, the stator wake loss coefficient on any streamline becomes

$$\bar{\omega}_{hi3} = \frac{P_{hi3} - P_{2,\,avg}}{(P-p)_1} \tag{3}$$

where the stator inlet dynamic pressure $(P-p)_1$ is the average of four (4) circumferential locations at a fixed radius (Britsch et al., 1979). To verify that equation (3) is the best estimate of stator loss, a simple comparison was made.

The stage performance data (Britsch et al., 1979) were used to find the overall stator loss coefficient using the NASA equations for blade element efficiency (Johnsen et al., 1965, p. 253). It is possible to isolate overall stator blade row loss coefficient by comparing overall rotor and stage efficiencies, calculating the relative stator pressure ratio that accounts for

[3]Variations from much of the non-NASA data are not shown since they could be directly estimated from the literature.

Table 1 Comparison of overall loss coefficients for NASA stator blade rows

STATOR (w/Rotor)	Total Pressure Loss Coefficient, $\bar{\omega}$: Calc. from Difference in Rotor to Overall Stage Performance, $\bar{\omega}_{ov}$	Calc. from Stator Wake, $\bar{\omega}_{hi3}$	Calc. from in- and outlet Probe Data, $\bar{\omega}_1$
20 (23B)	.071	.051	.112
20 (24A)	.070	.060	.100
20B (25A)	.120	.047	.098
20C (23D)	.084	.073	.125
20C (24B)	.060	.080	.129
21 (27C)	.049	.057	.103
22 (28D)	.096	.080	.160

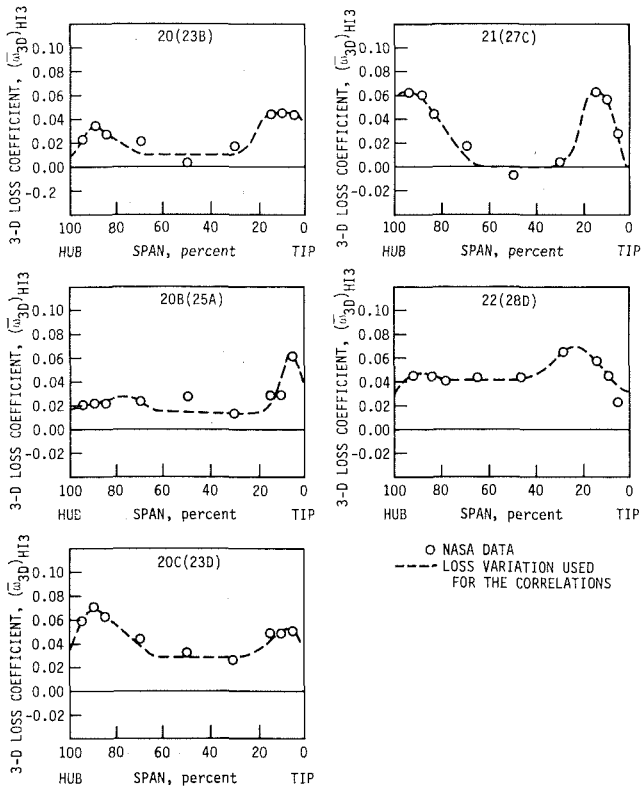

Fig. 7 Three-dimensional variation of loss coefficient for NASA stators (Britsch et al., 1979)

the efficiency difference, and then solving the appropriate equation for loss coefficient. This overall stator loss coefficient $\bar{\omega}_{ov}$ was then compared to those computed by the mass-averaged hi3 technique, $\bar{\omega}_{hi3}$, and the usual loss coefficient found by mass-averaging the inlet and outlet radial pressure variation, $\bar{\omega}_1$. The results are shown in Table 1.

It can be seen that the hi3 loss coefficient $\bar{\omega}_{hi3}$ is in much better agreement with the loss coefficient derived from total blade row data. This is because it better isolates the loss due to the stator instead of also measuring the effects of rotor wakes and pressure gradients passing from the rotor through the stator. Therefore, the spanwise distribution of hi3 loss coefficient was used as the best available approximation to the loss variation for stators.[4] This was combined with the calculated two-dimensional loss distribution, equations (1) and (2), to estimate three-dimensional loss variation. An example of three-dimensional loss coefficient distributions for stators is shown in Fig. 7.

The plots of Figs. 5 and 7 show an estimated variation of three-dimensional loss over a rotor of stator blade span operating at or near design point. As such, the three-dimensional loss values in the midspan regions should be at or near zero. This is not always the case, especially for the stator data. The reason for this discrepancy could be due to the simplicity of the two-dimensional loss model, measurement errors, or in the case of the stators, interference from rotor wakes and associated flow phenomenon. Some combination of all these effects probably applies. However, for both rotors and stators, a rather consistent spanwise distribution of the three-dimensional loss coefficient, showing peaks near the endwalls, is apparent. So, the following method was used to isolate the three-dimensional flow effects. It was assumed that, for each rotor and stator, a two-dimensional core flow exists at the midspan (50 percent) streamline so that $\bar{\omega}_{3D} \equiv 0$ and $\bar{\omega}_1 \equiv \bar{\omega}_{2D}$. Using this assumption, the dotted-line variations were drawn on the loss variations of Figs. 5 and 7. Then the three-dimensional loss coefficient distribution is estimated with respect to the dotted-line midspan value as if that value was zero. The criteria for "fairing in" the dotted-line variations was that (1) the distribution be continuous with only two loss maxima at the hub and tip, and (2) be within ± 0.01 of all

[4] Stator data from GE and SVÚSS were presented in the equivalent of the hi3 form. There were no stator data from Kyushu University.

Table 2 Three-dimensional loss coefficients and geometry for rotor tip regions

ROTOR	$(\bar{\omega}_{3D})_{max,rt}$	$(\bar{s}_{3D})_{max,rt}$	$\bar{\delta}_t^*$	$\overline{TC}$
NASA 23B	.058	.080	.0150	.0071
23D	.074	.100	.0150	.0077
24A	.087	.100	.0120	.0108
24B	.106	.100	.0160	.0108
25A	.102	.100	.0160	.0083
26B	.120	.100	.0156	.0100
27A	.120	.100	.0146	.0100
27C	.117	.100	.0185	.0095
27D	.110	.100	-	.0110
28B	.135	.080	-	.0093
28D	.075	.100	.0120	.0089
GE-A, 3rd Stage*	.0721	.050	.009	.0136
GE-A, Single-Stage	.0883	.050	.011	.0136
SVÚSS	.018	.050	.010	.0850
Kyushu** 0.5	.088	.03	.011	.0056
1.0	.096	.04	.015	.0112
2.0	.128	.06	.013	.0224
3.0	.152	.08	.016	.0335
5.0	.208	.10	.017	.0559

*GE-A, 3rd Stage - measurements made on the 3rd stage of a 4-stage compressor.

**Kyushu Univ. loss coefficients have been modified to NASA standard.

Table 3 Three-dimensional loss coefficients and geometry for stators and rotor hub regions

STATORS (w/Rotor)	$(\bar{\omega}_{3D})_{max}$	$(\bar{s}_{3D})_{max}$	$\bar{\delta}_t^*$	ϕ(deg)	AR_c	σ
NASA 20(23B)	.035	.10	.0100	55.40	1.90	1.60
Tip 20(24A)	.060	.10	.0135	55.40	1.90	1.60
20B(25A)	.050	.08	.0110	55.40	1.42	1.20
20C(23D)	.020	.10	.0090	55.40	2.34	2.00
20C(24B)	.040	.10	.0160	55.40	2.34	2.00
21(27C)	.060	.12	.0135	68.50	2.48	1.80
22(28D)	.027	.20	.0050	82.50	1.63	1.80
GE-A, 3rd Stage tip*	.025	.10	.0090	50.37	1.73	1.40
GE-A, 3rd Stage hub	~0	-	.0010	45.20	1.73	1.52
GE-A, Single-Stage tip	.035	.05	.0125	50.37	1.73	1.40
GE-A, Single-Stage hub	.010	.05	.0013	45.20	1.73	1.52
SVÚSS - Tip	.090	.10	.0225	40.20	1.80	0.73
SVÚSS Hub	.060	.16	.0220	45.30	1.80	1.10
ROTOR HUBS						
GE-A, 3rd Stage	.045	.10	.0100	40.10	1.40	1.27
GE-A, Single Stage	.100	.05	.0300	40.10	1.40	1.27
SVÚSS**	.120	.05	.0150	63.00	1.90	1.10

*GE-A, 3rd Stage - measurements made on the 3rd stage of a 4-stage compressor.

**SVÚSS geometrical parameters were calculated using free-vortex swirl distribution (see Ref. 16).

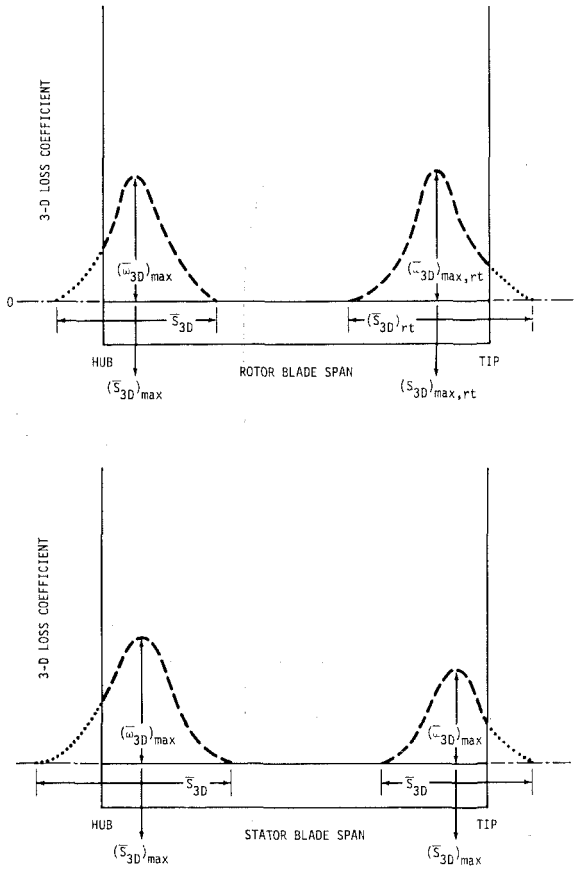

Fig. 8 Schematic of three-dimensional loss variation

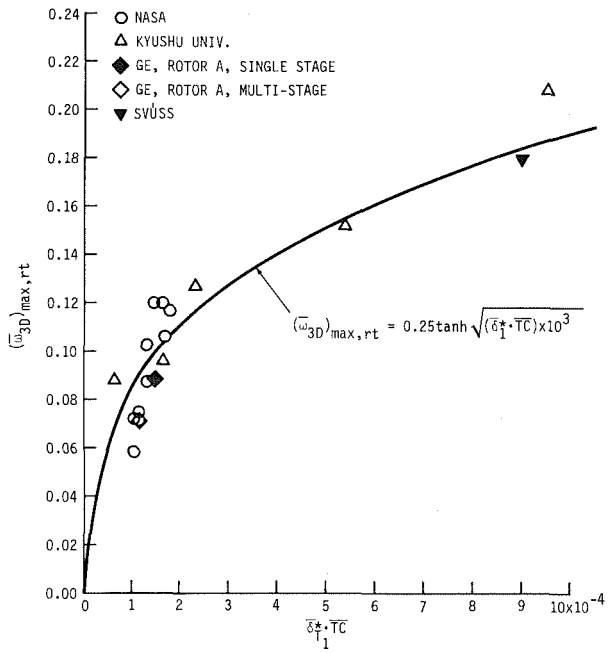

Fig. 9 Correlation of model with tip region maximum three-dimensional loss coefficient for rotors

data if (1) is not violated. Appropriate parameters of loss coefficient and location observed from these plots were used to construct simple design point loss models. These parameters are given in Table 2 for rotor tip flows and in Table 3 for stators and rotor hubs.

Loss Models

The physical parameters that this and a previous study (Roberts et al., 1986) have indicated to affect rotor and stator spanwise distribution of loss are blade camber ϕ, blade channel aspect ratio AR_c, solidity σ, rotor tip clearance TC, and endwall boundary layer thickness at the blade row inlet, represented by the inlet boundary layer displacement thickness, δ_1^*. All of the above parameters, except displacement thickness, are generally available in the axial compressor performance literature. However, the previous work by the present authors (Roberts et al., 1986) has indicated that endwall displacement thickness is a very important performance parameter. Therefore, almost all the data in the literature are unusable. After a literature search, only three (3) additional usable sources were found to supplement the NASA data (Britsch et al., 1979): those mentioned in the previous section (Cyrus, 1986; Inoue et al., 1986; Wisler, 1977, 1980). Other data that quoted displacement thickness variation used loss coefficients that were incompatible with, or that could not be converted to, the NASA loss coefficient.

Rotor Tip Loss Model

The data listed in Table 2 were used in various combinations to model the rotor three-dimensional loss distributions (see Fig. 5). Those distributions indicate that three-dimensional losses are concentrated near the hub and tip as two maxima: three-dimensional losses build from or near zero at midspan to a maximum value at ~10 percent of span from the hub or tip endwall in an approximately "normal" type curve and then decrease "normally" toward the endwall. A schematic of this variation is shown in Fig. 8. To model this type of variation, three parameters must be estimated: (1) the maximum value of three-dimensional loss coefficient in the hub and tip region, (2) the location of the maximum loss, and (3) the extent of the three-dimensional loss region.

Maximum Tip Region Loss. The first parameter above is perhaps the most important, since it appears to have the widest range of values. Using Table 2, eight (8) models were used in the attempt to correlate the rotor tip region three-dimensional maximum loss coefficient $(\bar{\omega}_{3D})_{max,rt}$.

It appeared that the combination of parameters that best estimate the change in tip region maximum three-dimensional loss is the same as that used to model rotor tip flow angle underturning in the present authors' previous work (Roberts et al., 1986):

$$(\bar{\omega}_{3D})_{max,rt} = f(\delta_1^* \cdot \overline{TC})$$

This correlation is shown in Fig. 9.

The plot of this model can be fitted with a hyperbolic curve of the form

$$(\bar{\omega}_{3D})_{max,rt} \simeq A \tanh (\delta_1^* \cdot \overline{TC})^n$$

where A and n are constants. This is a physically realistic variation because the value of $(\bar{\omega}_{3D})_{max,rt}$ does not continue to increase as the product $(\delta_1^* \cdot TC)$ increases. As TC approaches infinity, e.g., for an unshrouded fan or blade row, the maximum three-dimensional loss or drag value reaches a fixed finite value. Furthermore, the value of δ_1^* is bounded by the annulus height. Therefore, the value of $(\bar{\omega}_{3D})_{max,rt}$ should reach a maximum fixed value as $(\delta_1^* \cdot TC)$ increases without bound. Figure 9 shows the correlation with a fitted curve of the form shown above

$$(\bar{\omega}_{3D})_{max,rt} = 0.25 \tanh \sqrt{(\delta_1^* \cdot TC) \times 10^3} \quad (4)$$

According to this relationship, the highest value possible for $(\bar{\omega}_{3D})_{max,rt} = 0.25$. This is a reasonable value for rotors with typical blade clearance and blockage operating near design point.

Equation (4) is a specific relationship derived from limited

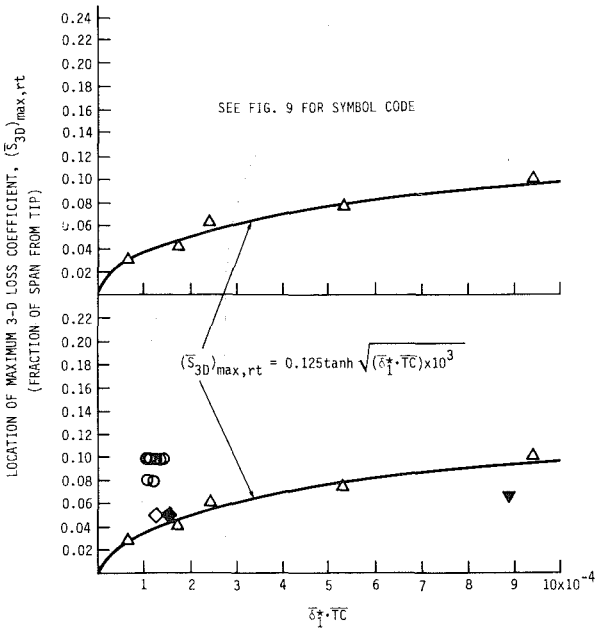

Fig. 10 Correlation of model with location of maximum three-dimensional loss coefficient for the rotor tip region

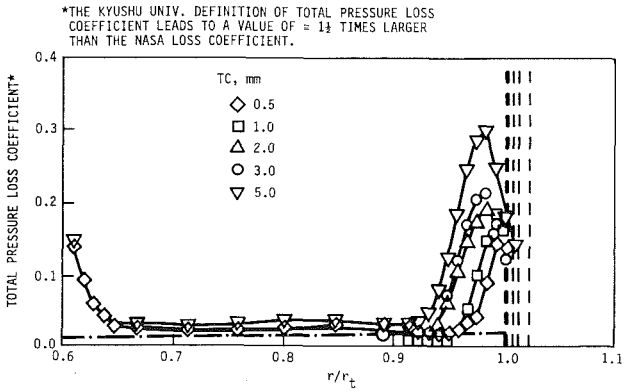

Fig. 11 Variation of loss coefficient for Kyushu University rotor (Inoue et al., 1986)

data. However, the model could well be applicable to similar subsonic compressor stages since it is based on data for a reasonably wide range of the important variables.

Location of Maximum Loss. Table 2 lists the maximum three-dimensional loss location for all rotors used in this study. A perusal of this table indicates that the location of maximum loss, $(\bar{S}_{3D})_{max,rt}$, occurs between the endwall and 10 percent of span from the casing. The values show a variation between 3 and 10 percent of span.

Four (4) combinations of parameters from Table 2 were correlated with the location of maximum loss using various models. The most successful of these is shown in Fig. 10, where all but the NASA data appear to correlate well. However, if the Kyushu University data are taken out of any of the model variations and plotted separately, it is clear that they are the reason for the apparent correlation.

The Kyushu data correlate well with all the models. This is probably due to the systematic variation of rotor tip clearance in the Kyushu testing. No other data used herein had a systematic variation of tip clearance in the tests. Furthermore, the loss variation in the tip region of the Kyushu rotor was very well defined by data taken every 2 percent of span right to the endwall (see Fig. 11). Thus, the Kyushu distributions were better defined than any of the other data. Perhaps with better definition, the other data would correlate also.

For simplicity, the data plot of Fig. 10 was chosen to correlate with maximum loss location. A hyperbolic tangential curve has been fitted that is similar to that used for equation (4):

$$(\bar{S}_{3D})_{max,rt} \simeq 0.125 \tanh \sqrt{(\bar{\delta}_1^* \cdot TC) \times 10^3} \qquad (5)$$

where equation (5) gives the fraction of span from the tip endwall with 0.125 as the maximum value.

The variation is physically realistic for the same reason that it was for the maximum loss variation of Fig. 9.

Considering the lack of data to corroborate equation (5), this relation must be used with caution. However, in the absence of a comprehensive data base, it can give an indication of the location of rotor tip maximum three-dimensional loss coefficient.

Extent of Rotor Tib Loss Region. From a review of all data, it can be observed that the maximum loss coefficient is located toward the endwall in the three-dimensional loss region and the extent of the three-dimensional loss region from the casing is somewhat more than twice the distance of the maximum loss location

$$(\bar{S}_{3D})_{rt} \simeq 2.5(\bar{S}_{3D})_{max,rt} \qquad (6)$$

The loss coefficient variation in the tip region is shown schematically in Fig. 8 where the loss is normally distributed around the location of maximum loss. This accounts for the nonzero loss at the endwalls, as seen in most loss variations.

Rotor Hub and Stator Loss Model

The available data with sufficient detail to model the three-dimensional loss variation are listed in Table 3. This includes NASA stator tip data, and GE and SVUSS rotor hub data and stator hub and tip data. Three-dimensional loss variations were all similar to those shown in Fig. 7. From these distributions, it can be seen that the same type of model applies to rotor hubs and stators as to rotor tip regions. So Fig. 8 applies to rotor hubs and stators as well, and the same modeling concept was used for the rotor tip region.

Maximum Three-dimensional Loss Coefficient. All stators were shrouded at both hub and tip, so clearances have no part of this correlation. From the data listed on Table 3, three (3) models were used to attempt to correlate maximum three dimensional loss coefficient in the endwall region for stators and rotor hubs.

A combination of parameters that have previously modeled the three-dimensional deviation (Roberts et al., 1986), $\phi(\delta_1^*)^2/AR_c\sqrt{\sigma}$,[5] make the best correlation with the three-dimensional loss coefficient for rotor hubs and stators, $(\bar{\omega}_{3D})_{max}$. For the same reasons as for the rotor tip region, the maximum three-dimensional loss coefficient cannot grow without bound. As the correlating parameter tends toward infinity, the maximum three-dimensional loss coefficient will tend toward a greatest finite value. Figure 12 shows the correlation and the hyperbolic tangential fitted curve

$$(\bar{\omega}_{3D})_{max} \simeq 0.20 \tanh 15\left(\frac{\phi \cdot \bar{\delta}_1^{*2}}{AR_c\sqrt{\sigma}}\right) \qquad (7)$$

where equation (7) applies to rotor hubs, and stator hub and tip regions with maximum three-dimensional loss coefficient less than or equal to 20 percent.

Location of Maximum Loss. Table 3 indicates that there is no discernible correlation for location of maximum loss. The

[5] The values of ϕ, δ_1^*, and σ are those from the appropriate endwall (hub or tip), while AR_C is evaluated by the midspan location.

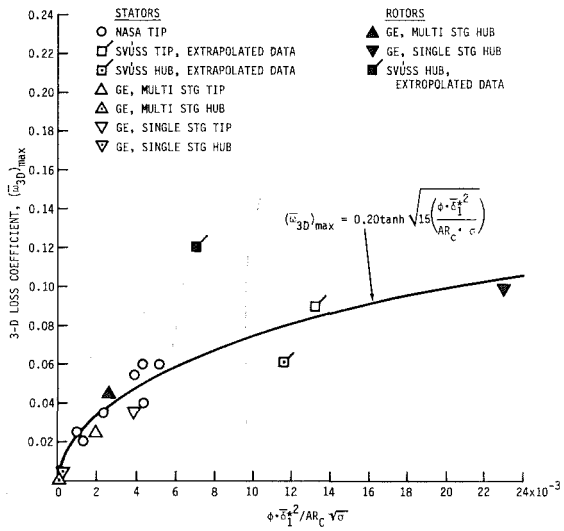

Fig. 12 Correlation of model with maximum three-dimensional loss coefficient for stators and rotors hubs

data indicate that most maxima occur at or near 10 percent of span from the endwall. Therefore, in the absence of more detailed data, the location of maximum loss will be set at a constant value

$$(\bar{S}_{3D})_{max} \simeq 0.1 \tag{8}$$

where equation (8) is the fraction of span from hub or tip endwall for rotor hubs and stators.

Extent of Three-Dimensional Loss Region. As for the rotor tip region, the loss region is approximately two and a half times the distance to the location of maximum loss (see Fig. 7)

$$\bar{S}_{3D} \simeq 2.5(\bar{S}_{3D})_{max} \tag{9}$$

The loss variation is the same as shown in Fig. 8.

Results

Figures 13 and 14 show the rotor and stator three-dimensional loss models compared with the data for a typical rotor and stator. In Fig. 13(*a*), the two-dimensional loss distribution from equation (2) is shown with the three-dimensional loss distribution, from equations (4) to (9), superimposed. The qualitative agreement is reasonable. However, when the loss distribution is adjusted so that the midspan values are the same, as seen in Figs. 13(*b*) and 14, the qualitative and quantitative agreement is fair to good, which is as it should be, since all available data were used in the correlations.

Three-Dimensional Deviation Models

Previous work reported by the present authors (Roberts et al., 1986) modeled the three-dimensional effects on flow deviation angle for axial compressor middle stages. That paper demonstrates that it is possible to predict design point deviation within the range of data used for correlation. After the publication of the paper, the authors were informed of unpublished tests, outside the range of the Roberts et al. (1986) data, where the model greatly over-estimated three-dimensional deviation (Citavý communication, 1986). This can be attributed to the linear variation of deviation proposed in that paper instead of the more physically realistic hyperbolic variation proposed here (see Figs. 9, 10, and 12).

Although there is always a risk in applying empirical models beyond the range of data, it is best to have as realistic a prediction as possible. Therefore, the three-dimensional deviation variations given in Roberts et al. (1986) have been changed to reflect the more realistic, bounded hyperbolic variations proposed herein. Equations (1), (3), and (4) of Roberts et al.

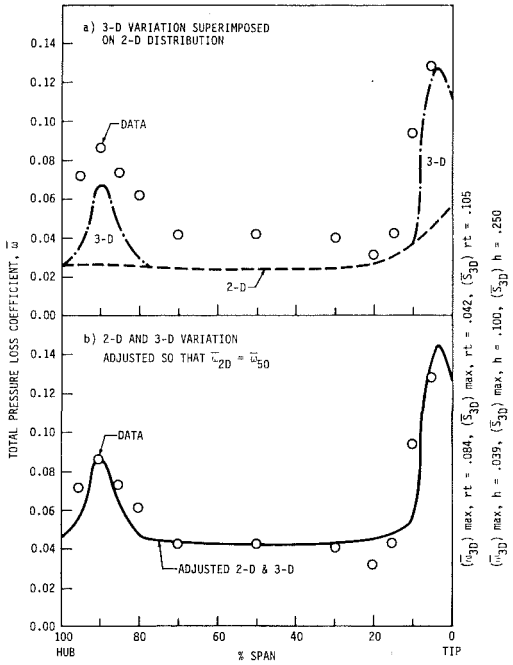

Fig. 13 Comparison of rotor three-dimensional loss models to data from the third-stage rotor of the GE four-stage research compressor (Wisler, 1977, 1980)

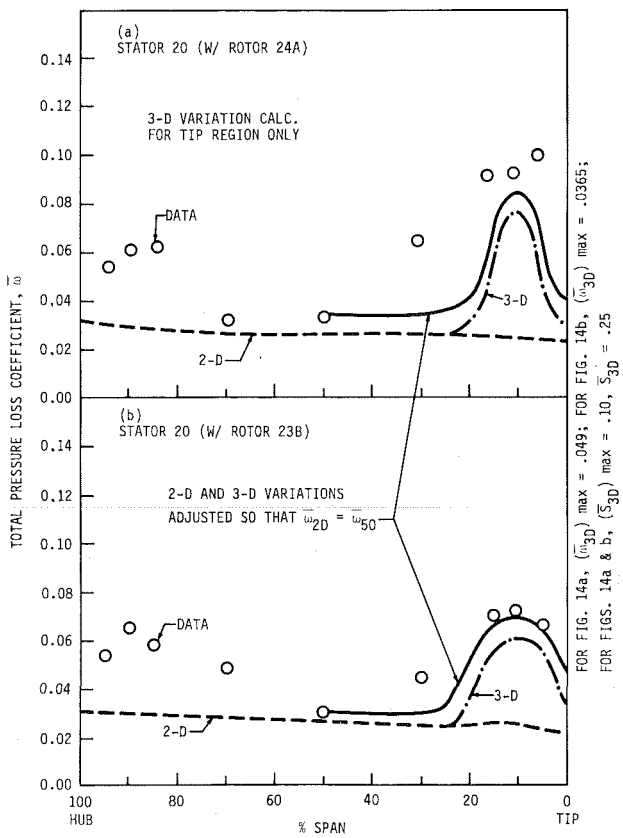

Fig. 14 Comparison of stator three-dimensional loss model to data from NASA stator 20 operating with two rotors (Britsch et al., 1979)

(1986) have been changed below to give the best hyperbolic, tangential fit to the data:

$$\bar{\Delta}_{\max} = 15 \tanh \left(\tfrac{1}{2} \frac{\phi\, \bar{\delta}_1^{*2}}{AR_c\sigma} \times 10^3 \right) \quad \text{(1—Rob., '86)}$$

$$\bar{\Delta}_{\max} - \bar{\Delta}_w = 20 \tanh \left(\frac{\tfrac{1}{2}\phi \bar{\delta}_1^{*2}}{AR_c\sigma} \times 10^3 \right) \text{(2—Rob., '86)}$$

$$\bar{\Delta}_5 = 30 \tanh \left(\bar{\delta}_1^{*} \cdot \overline{TC} \cdot 10^3 \right) \quad \text{(4—Rob., '86)}$$

where the equations are numbered to indicate their origin in Roberts et al. (1986).

A comparison between the values predicted by the equations above and those of the deviation paper showed no significant differences in data match (see Figs. 11 and 12 of Roberts et al., 1986).

Summary and Discussion

Using equations (4)–(9), it is possible to estimate the design point variations of three-dimensional spanwise loss coefficient for middle-stage rotors and stators. These equations are derived from a data base that consists of seven (7) NASA single-stage rotor/stator combinations, plus single-stage data from Kyushu University (rotor only), single- and multistage data from General Electric (the multistage data are from a four-stage rig), and rotor/stator single-stage data from the National Research Institute for Machine Design in Czechoslovakia (SVÚSS).

A model for the spanwise variation of three-dimensional loss coefficient is given in Fig. 8. The three-dimensional loss grows from zero or near zero in the midspan core region to a maximum near the hub and tip endwalls in a normal type distribution. The losses then decrease to the endwall along a normal curve. However, they usually do not decrease to a value of zero at the endwall, but retain approximately one-half of the peak value. The maximum value of the three-dimensional loss coefficient, the location of the maximum, and the extent of the three-dimensional loss region can be estimated using the equations mentioned above. These losses then can be added to the spanwise distribution of blade element profile losses computed during the design process.

The revised equations for flow angle deviation (equation (1), (3), and (4), Roberts et al., 1986) can be used in place of those in the original paper to estimate the hub-to-tip variation of three-dimensional deviation angle for rotor and stator blade rows. These revised equations better reflect the flow physics at high values of the correlating parameters, i.e., there are finite bounds to deviation angle for any combination of blade geometry and flow blockage.

Considering the importance of endwall displacement thickness (i.e., blockage) to the estimation of spanwise loss effects, it is essential to be able to approximate its variation through a multistage compressor. Such a variation might be obtained from a data base of similar compressors or a calculating procedure for blockage (Stratford, 1967).

Conclusion

Simple design-point models have been proposed for the spanwise variation of secondary flow losses and deviation of blade rows from subsonic, axial compressor middle stages. The models were developed from observations of an experimental data base consisting of fifteen (15) axial flow stages. The model allows axial compressor designers to estimate quickly the total loss and deviation across the blade span when the three-dimensional distribution is superimposed on the two-dimensional variation calculated for each blade element.

These correlations were derived from a limited data base and extrapolated estimates should be used with caution.

Acknowledgments

The work reported herein was supported by the U.S. Army and NASA, under Grant NAG 3-521. The authors thank Gilbert Weden of AVSCOM, Propulsion Directorate, and Lewis Research Center for this support.

References

Adkins, G. G., Jr., and Smith, L. H., Jr., 1982, "Spanwise Mixing in Axial-Flow Turbomachines," ASME *Journal of Engineering for Power*, Vol. 104, No. 1, pp. 97–110.

Britsch, W. R., Osborn, W. M., and Laessig, M. R., 1979, "Effects of Diffusion Factor, Aspect Ratio, and Solidity on Overall Performance of 14 Compressor Middle Stages," NASA Technical Paper 1523.

Citavý, J., 1986, Private communication with Head of Fluid Mech. Dept., SVÚSS, Prague, Czechoslovakia.

Cyrus, V., 1986, "Experimental Study of Three-Dimensional Flow in an Axial Compressor Stage," ASME Paper 86-GT-118.

Dring, R. P., Joslyn, D. H., and Hardin L. W., 1982, "An Investigation of Axial Compressor Rotor Aerodynamics," ASME *Journal of Engineering for Power*, Vol. 104, No. 1, pp. 84–96.

Horlock, J. H., 1958, *Axial Flow Compressors—Fluid Mechanics and Thermodynamics*, Butterworths, London.

Howell, W. T., 1963, "Approximate Three-Dimensional Flow Theory for Axial Turbomachines," *Aeronaut.Q.*, Vol. 14, p. 125.

Inoue, M., Kuroumaru, M., and Fukuhara, M., 1986, "Behavior of Tip Leakage Flow Behind an Axial Compressor Rotor," ASME *Journal of Engineering for Gas Turbines and Power*, Vol. 108, pp. 7–14.

Johnsen, I. A., and Bullock, R. O., eds., 1965, *Aerodynamic Design of Axial-Flow Compressors*, NASA SP-36.

LeFoll, J., 1965, "A Theory of the Representation of Boundary Layers on a Plane," *Proceedings of the Seminar on Advanced Problems in Turbomachinery*, von Karman Institute.

McFarland, E. R., 1984, "A Rapid Blade-to-Blade Solution for Use in Turbomachinery Design," ASME *Journal of Engineering for Gas Turbines and Power*, Vol. 106, pp. 376–382.

McNally, W. D., 1970, "Fortran Program for Calculating Compressible Laminar and Turbulent Boundary Layers in Arbitrary Pressure Gradients," NASA TND-5681.

Roberts, W. B., Johnson, K. L., and Sandercock, D. M., 1978, "Boundary Layer Development Through the Tip Regions of Core Compressor Stages," Final Scientific Report, NASA Grant NAS-3133.

Roberts, W. B., Serovy, G. K., and Sandercock, D. M., 1986, "Modeling the 3-D Flow Effects on Deviation Angle for Axial Compressor Middle Stages," ASME *Journal of Engineering for Gas Turbines and Power*, Vol. 108, pp. 131–137.

Seyler, D., and Smith, L. H., Jr., 1967, "Single Stage Experimental Evaluation of High Mach Number Compressor Rotor Blading," NASA CR-54581, pp. 26–28.

Smith, L. J., Jr., 1970, "Casing Boudnary Layers in Multistage Axial-Flow Compressors," in: *Flow Research on Blading*, L. S. Dzung, ed., Elsevier, Amsterdam, p. 275.

Stratford, B. S., 1967, "The Use of Boundary Layer Technique to Calculate Blockage From the Annulus Boundary Layers in a Compressor," ASME Paper No. 67-WA/GT-7.

Van den Braembussche, R. A., 1973, "Calculation of Compressible Subsonic Flow in Cascades With Varying Blade Height," ASME Paper No. 73-GT-59.

Wisler, D. C., 1977, "Core Compressor Exit Stage Study," Vol. I, Blading Design, NASA CR-135391, and 1980, Vol. II, Data and Performance Report for the Baseline Configuration, NASA CR-159498.

Wisler, D. C., Bauer, R. C., and Okiishi, T. H., 1987, "Secondary Flow Turbulent Diffusion and Mixing in Axial-Flow Compressors," ASME JOURNAL OF TURBOMACHINERY, Vol. 109, pp. 455–482.

Effect of the Inlet Velocity Profile in the Three-Dimensional Flow in a Rear Axial Compressor Stage

V. Cyrus
Research Engineer,
The National Research Institute for Machine Design (SVÚSS),
250 97 Prague 9-Běchovice, Czechoslovakia

A detailed investigation of the three-dimensional flow was carried out in a low-speed rear axial compressor stage with an aspect ratio of 1. Experimental data were obtained for both an inlet velocity profile with thin endwall boundary layer thickness and a distorted inlet velocity profile with a high turbulence intensity level. The distortion was produced by a specially designed screen. The flow mechanism in the rotor and stator blade rows is analyzed for these two velocity profiles at the design flow coefficient.

Introduction

It is impossible to design new types of high-efficiency and pressure ratio axial compressors without knowledge of flow phenomena in the blading. For this reason a great deal of effort has been devoted, in the last decade, to research on three-dimensional flow fields, mainly in low-speed isolated rotor blade rows (Dring et al., 1982; Hunter and Cumpsty, 1982) and compressor stages (Lakshminarayana, 1980; Joslyn and Dring, 1984; Dong et al., 1987; Cyrus, 1986). The majority of experimental studies, however, focus on the aerodynamics of front and middle stages. The problems of rear-stage flows have been dealt with only in a small number of research papers.

The rear stages of a multistage compressor have large operating ranges. Consequently, they are designed with lower aerodynamic loading than the front and middle stages. The aspect ratio of the blade rows is low (usually $AR < 1.5$). Therefore the three-dimensional annulus boundary layers represent a major portion of the flow field in a rear stage. The exit stages of a multistage machine work under conditions of high turbulence intensity $Tu = 5$–8 percent, as follows, e.g., from Schlichting and Das (1970), and Grant (1979).

Wisler (1984) at General Electric undertook an investigation of new rear stages for high-efficiency aircraft engine compressor. The stages were examined on a four-stage, low-speed rig having airfoil aspect ratio $AR = 1.3$. The thickness of the endwall boundary layers was small, however. The effect of the shape of the inlet velocity profile on the performance of a stage or the isolated rotor blade row was studied by Ikui et al. (1977) and Wagner et al. (1985). In either case the turbulence intensity was not artificially raised. From these works it follows that many of the complex flow phenomena in the exit compressor stages of multistage machines are not yet fully understood. In particular, there is a need for more detailed investigation of the effect of endwall boundary layer size and turbulence intensity on stage performance. The designers need an improved model of flow in rear stages to attain higher compressor pressure rise and efficiency.

At the SVÚSS Institute, detailed measurements were recently made in an industrial-class axial compressor rear stage. Its aero-dynamic loading was lower than that of typical aircraft engine compressors. The inlet flow field of the rear stage was modified with a specially devised screen and lengthened inlet annulus to produce, simultaneously, a deformation of the velocity profile and growth of the turbulence intensity. This paper presents results comparing the three-dimensional flows in a rotor and a stator blade row for both an idealized inlet velocity profile with small endwall boundary layers and for a distorted inlet velocity profile with increased turbulence intensity.

Test Rig and Measurement Technique

The low-speed test compressor consists of inlet guide vanes, rotor, stator, and outlet guide vanes (Figs. 1 and 2). The outer and inner diameters of the stage are constant. The hub–tip ratio is 0.871 and the external diameter is 800 mm. The profiles of the rotor and stator airfoils are NACA 65 series with circular arc camber lines.

Some parameters of the stage blading design are presented in Table 1. The blade geometry is defined at midspan. The tip clearance of the rotor blade row is 1.4 percent span. At the casing and hub of stator vane row there is no clearance. The design value of the flow coefficient is 0.74. The Reynolds number, $\mathrm{Re}_1 = w_{r1m} \cdot c_R/\nu$, is $\mathrm{Re}_1 \doteq 300{,}000$ for design flow rate. Measurements were performed at a shaft speed of 2200 rpm.

Experimental investigations were made using a stationary five-hole conical probe, with head diameter of 2.2 mm, in measuring planes 1, 2, and 3 (Fig. 2). The probe was adjusted to the flow direction. The total temperature was measured in planes 1 and 2 by thermocouples. A rotating five-hole conical probe having a head diameter of 2.5 mm was placed in the plane behind the rotor blade row. During operation, the rotating probe was moved peripherally to the rotor blades by

Contributed by the International Gas Turbine Institute and presented at the 33rd International Gas Turbine and Aeroengine Congress and Exhibition, Amsterdam, The Netherlands, June 5–9, 1988. Manuscript received by the International Gas Turbine Institute September 15, 1987. Paper No. 88-GT-46.

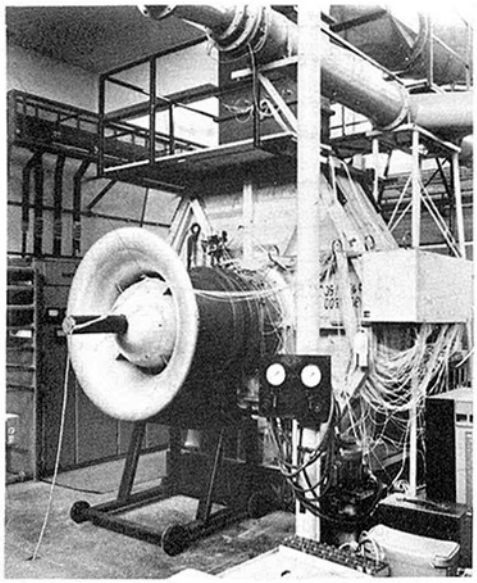

Fig. 1 Test rig

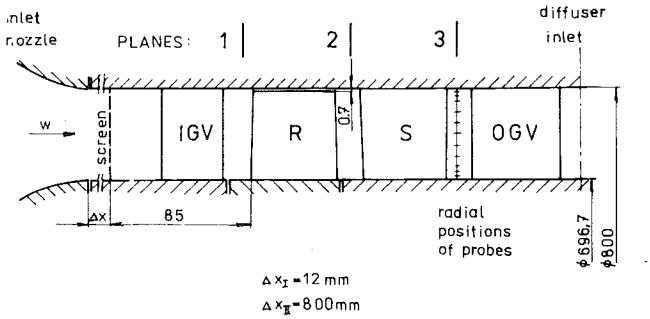

Fig. 2 Flow path and measuring planes

Table 1 Stage geometry at midspan

	Rotor row	Stator row
Blade number	53	62
Blade chord, mm	51.9	48.5
Blade chamber, deg	26.3	27.7
Stagger angle, deg	28.0	28.0
Solidity	1.18	1.28
Aspect ratio	1.0	1.07

means of a specially devised traversing mechanism (Cyrus, 1985). The probe can be turned by 15 deg around its axis to follow approximately the flow direction established using data from the stationary probes. The flow parameters were determined using an indirect method, where the probe was not turned into the flow direction during traversing. At the rotor inlet, measurements were also taken of the total pressure of the relative flow using the rotating total pressure probe shown in Fig. 8. The measurements were carried out within two blade pitches at 35 to 40 circumferential points and on 11 and 12 radial locations (Fig. 2). For close proximity to the endwall the rotating total pressure probe was not used. The rotating system pressures were converted to the stationary system by a pressure transfer device (Cyrus, 1985).

The flow parameters obtained from the pressure probe and thermocouple data were averaged over a blade pitch. The average value of axial velocity was determined by means of the continuity equation. The mean values of the peripheral and radial velocity components, total pressure, and total temperature were obtained by mass averaging. The static temperature and pressure were then calculated using fundamental relationships of fluid dynamics. The average values of flow angle was established on the basis of averaged axial and peripheral velocity components.

The absolute uncertainty of the pressure measurement was ± 0.4 percent of the dynamic pressure Q_u based on wheel speed U_M. The flow angles measured by the stationary and rotating probe were recorded with accuracies of ± 0.7 deg and ± 1 deg, respectively. The measurement uncertainty for temperature was estimated at ± 0.3 K.

Modeling of the Stage Inlet Flow Field

In our research program we tried to investigate the three-dimensional flow in the rear compressor stage blading both for idealized inlet velocity profile with small endwall boundary layers and for a distorted inlet velocity profile with increased turbulence intensity. We desired to increase the annular

Nomenclature

AR = aspect ratio $= h/c$
A = flow area
b = atmospheric pressure, wake width
c = blade chord
C_p = relative total pressure coefficient $= (\bar{P}_{r1} - P_{r2})/Q_u$
C_{PT} = total pressure coefficient $= (P_3 - \bar{P}_1)/Q_u$
h = blade height
i = incidence angle
P = total pressure
Q = dynamic head
Q_u = dynamic head based on mean radius wheel speed $= 1/2\ \rho_1 U_M^2$
Q_n = flow rate determined from nozzle data
r = radius
s = blade pitch
Tu = turbulence intensity
U = wheel speed
w = velocity
x = axial coordinate
y = peripherial coordinate
z = coordinate normal to endwall
δ = endwall boundary layer thickness, deviation
η = adiabatic efficiency
ν = kinematic viscosity
ρ = fluid density
ϕ = flow coefficient $= Q_n/(A \cdot U_M)$
φ = circumferential angle
ψ = pressure coefficient $= (\bar{P}_3 - \bar{P}_1)/Q_u$
ω = loss coefficient: for rotor $\omega_R = (\bar{P}^x_{r2} - \bar{P}_{r2})/Q_{r1}$; for stator $\omega_S = (\bar{P}_2 - \bar{P}_3)/Q_2$

Subscripts

a = axial
D = design
IGV = inlet guide vanes
h = at hub
m = at midspan
M = at mean radius: $r_M = \sqrt{\dfrac{(r_t^2 + r_h^2)}{2}}$
R = rotor
r = relative to rotor blade row
ref = reference
S = stator
t = at casing
1, 2, 3 = planes of axial compressor stage (Fig. 2)
I, II = velocity profiles

Superscripts

$(\bar{\ })$ = pitchwise-averaged value
$(\bar{\bar{\ }})$ = average over the entire measuring plane
$(\ )^x$ = ideal

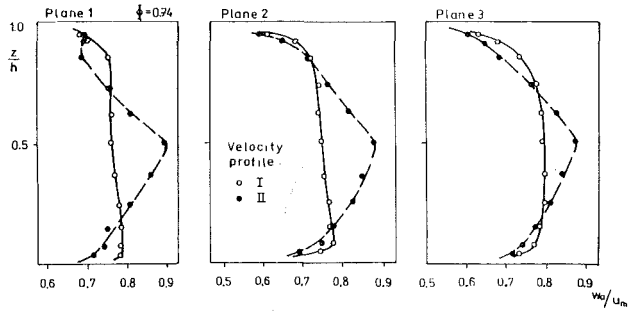

Fig. 3 Spanwise distributions of axial and velocity

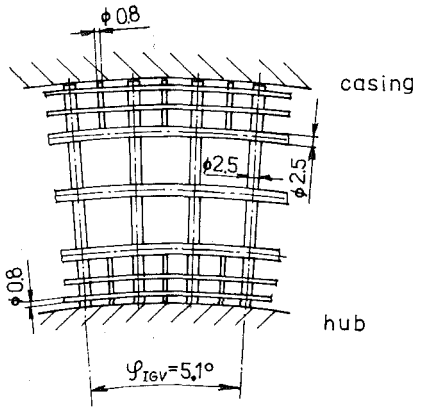

Fig. 4 Screen

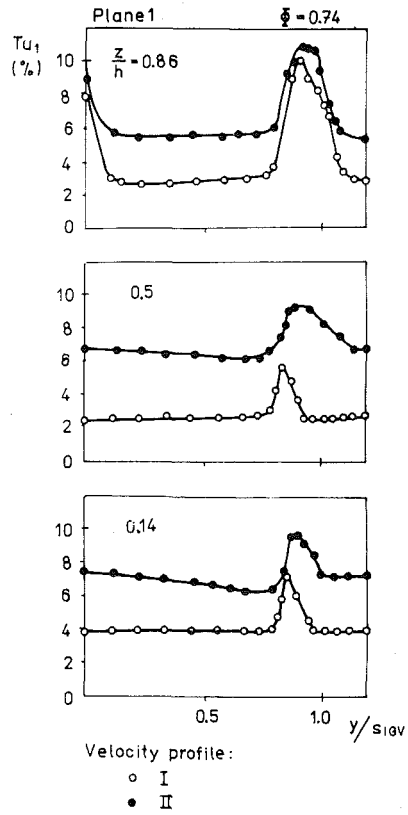

Fig. 5 Pitchwise distributions of turbulence intensity

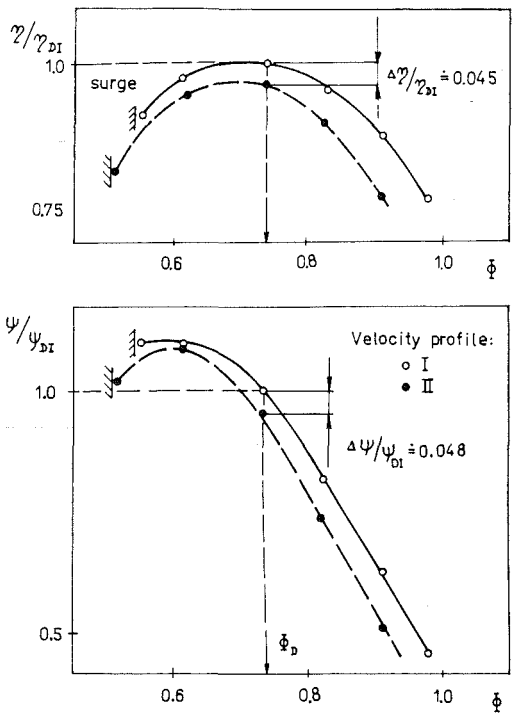

Fig. 6 Stage performance for two inlet conditions

boundary layer thickness to one-half the vane height. Such a distorted inlet velocity profile of the middle and exit stages has been previously supposed by Howel (1945). In current rear stages of multi-stage compressors such large velocity distortion does not always occur. However, we intended to create such an inlet velocity profile to represent the upper limit of possible distortion, which may be important in assessing the aerodynamic performance of a rear stage.

When the inlet nozzle was located immediately ahead of the blading ($\Delta x = 12$ mm: Fig. 2) the spanwise distribution of axial velocity was measured in plane 1 as indicated in Fig. 3. This distribution is denoted by Roman numeral I. The thickness of the boundary layer on the hub and casing reached approximately the values of $\delta_{1h} \doteq 0.07\ h$ and $\delta_{1t} \doteq 0.15\ h$, respectively.

The distortion increase in the inlet velocity profile was created by a lengthened inlet annulus ($\Delta x = 800$ mm: Fig. 2) and a specially designed screen (Fig. 4). This resulted in the required turbulence intensity increase relative to the case where the inlet velocity field had not been modified (profile I—Fig. 3). This can be seen in Fig. 5, which shows turbulence intensities at three spanwise points located in plane 1 and within the spacing of the inlet guide vanes. At midspan, outside the wake of the inlet guide vanes, the value T_{u1} was 6–7 percent. This agrees with the values of turbulence intensity obtained in multistage compressors (Schlichting and Das, 1970; Grant, 1979). The screen was designed on the basis of experimental data obtained in the low-speed wind tunnel. In subsequent paragraphs the distorted velocity profile will be denoted with Roman numeral II.

Discussion of Results

Figure 6 shows the dependence of relative pressure coefficient ψ/ψ_{DI} and efficiency of the blading (rotor, stator, outlet guide vanes) η/η_{DI} on flow coefficient for two shapes of the stage's inlet velocity profile. In order to be able to measure the performance characteristics of the blading, an axial fan had to be serially attached to the investigated stage when the flow field was modified by the screen and lengthened inlet annulus. Modification of the inlet flow to simulate the working conditions of a rear stage brought about a deterioration of its performance, as seen in Fig. 6. At the design value of the coefficient ϕ, the efficiency and pressure coefficient dropped by $\Delta\eta/\eta_{DI} = 4.5$ percent and $\Delta\psi/\psi_{DI} = 4.8$ percent, respectively, compared to the unmodified inlet velocity profile. There was also a shift between the characteristics. With velocity profile II the surge point moved toward lower flow rates ($\Delta\phi/\phi_D = 4.7$

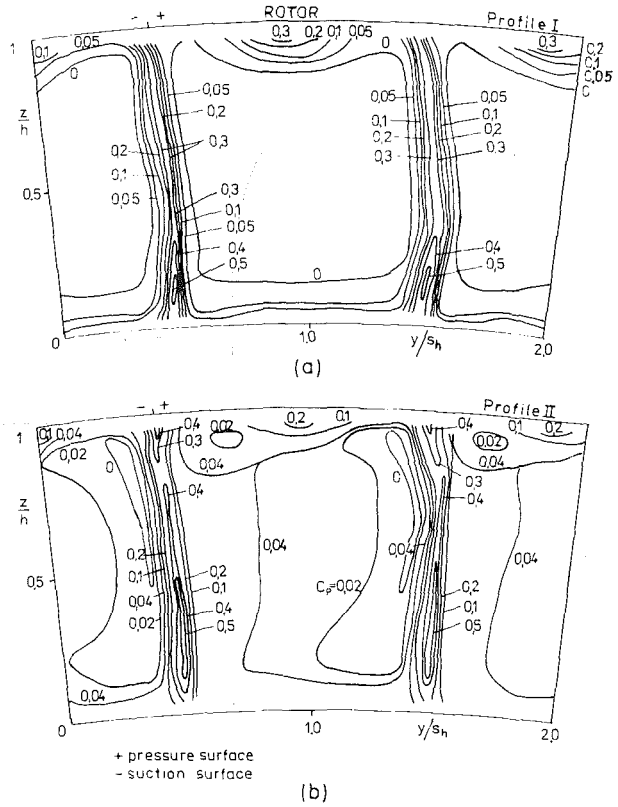

Fig. 7 Rotor exit relative total pressure contours

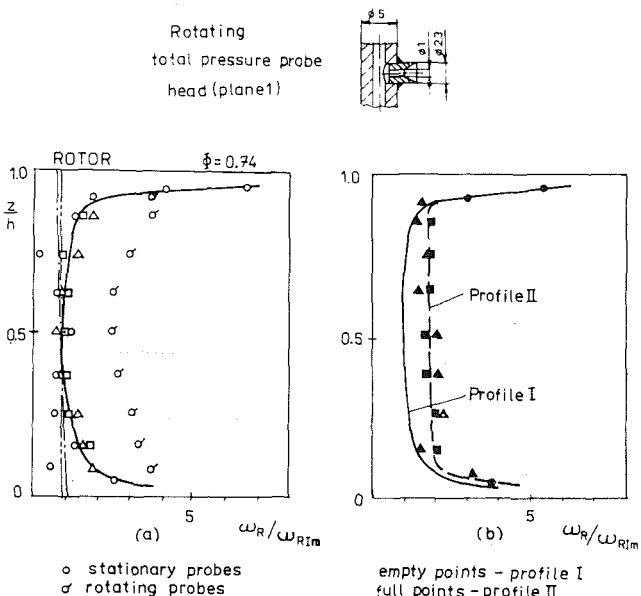

Fig. 8 Spanwise rotor loss coefficient distribution

percent). Overall, our results agree with (Ikui et al., 1977) where the inlet velocity profile was only deformed, without artificial enhancement of turbulence intensity, by a lengthened inlet annulus. The decline of performance and pressure coefficient values caused by the modification of the inlet velocity profile in our blading was not as large as in that found by Ikui et al. (1977).

The subsequent discussion will endeavor to show the cause of the decline of the rear stage performance at the design flow rate value of $\phi = 0.74$. An analysis of both rotor and stator flow conditions will be presented.

Rotor Blade Row. Figure 7 shows the distribution of relative total pressure coefficient C_P in the plane behind the rotor row for two shapes of inlet velocity profile at $\phi = 0.74$. In the case of velocity profile I, about 30 percent blade height near the hub and 15 percent near the casing was affected by secondary flow (Fig. 7*a*). In the corner between the suction side of the blade and the hub wall there is an observable area of low-energy fluid. This fluid was transported from the region of the inlet boundary layer on the hub to the corner, as a consequence of the pressure gradient between the suction and pressure sides of the adjacent blades. In the corner there is a separated zone causing high losses. The low energy fluid area in the corner is smaller than that in the rotor rows of Dring et al. (1982) and Cyrus, (1986) since the aerodynamic loading of the our rotor is lower. A low-energy fluid area appeared near the casing as a result of tip clearance flow and relative movement of the endwall against the blade tip. Figure 7(*a*) shows a major loss-free area in the middle part of the blade passage.

With the distortion of the inlet velocity profile and the increase of turbulence intensity (profile II) the area of loss-free flow in the blade row practically disappeared (Fig. 7*b*). The area of high coefficients ($C_p = 0.4$–0.5) occurs in the wake along the whole blade span and is not confined to the vicinity of the corner as in the case of velocity profile I. Probably it is created by transport of low-energy fluid to the midspan region. There may also be some influence of flow separation at the trailing edge of the airfoil, which will be dealt with in subsequent section on the stator row. The area of low-energy fluid at the casing shrank after modification of the inlet velocity profile, as did the maximum value of coefficient $C_p = 0.2$ compared to profile I. This may be explained through a decline of the velocity gradient at the casing, which plays a major role in the secondary loss mechanism caused by the relative movement of the end wall against the blade tip.

Figure 8 shows the distribution of rotor loss coefficient ω_R along the blade span. The streamlines of the axisymmetric flow lie approximately on the cylindrical surfaces. It holds, therefore, that $\bar{P}^x_{r2} = \bar{P}_{r1}$. In the case of a unmodified inlet velocity profile, the coefficient ω_R was evaluated in several different ways (Fig. 8*a*), as in Cyrus (1986). First, the loss coefficient was determined from the stationary probe data (points indicated by empty circles). In calculating further ω_R values we used the relative total pressure in the plane behind the rotor row, $\bar{P}_{r2}$, derived from data provided by the rotating conical probe.

$\bar{P}_{r1}$ was defined from data provided by the total pressure rotating probe (Fig. 8). The relative total pressure $\bar{P}_{r1}$ was corrected (empty triangles) or uncorrected (flagged circles) according to the method developed at SVÚSS (Čamek, 1983), which considers the effect of flow pulsations on the pressure-probe data. The SVÚSS method is briefly described in the appendix. The pressure $\bar{P}_{r1}$ was also determined from the pitchwise relative total pressure distribution $P_{r2}(r, \varphi)$ as the arithmetic mean of the three largest values of $P_{r2}(r, \varphi)$ at midspan. The value $\bar{P}_{r1}$ obtained from the stationary conical probe data in plane 1 was not employed in calculation of ω_R because of a minor peripheral flow irregularity. This was caused by the outlet casing when the diffuser was situated immediately behind the blading (Figs. 1 and 2). As in (Cyrus, 1986), the coefficient ω_R attained the value for an equivalent plane cascade. The "full" line goes through the test points (Fig. 8*a*). However, while developing the curve the values of ω_R obtained from the uncorrected data for the total pressure rotating probe in plane 1 were not taken into account.

Figure 8(*b*) shows the distribution of the loss coefficient ω_R along the rotor blade span after modification of the inlet

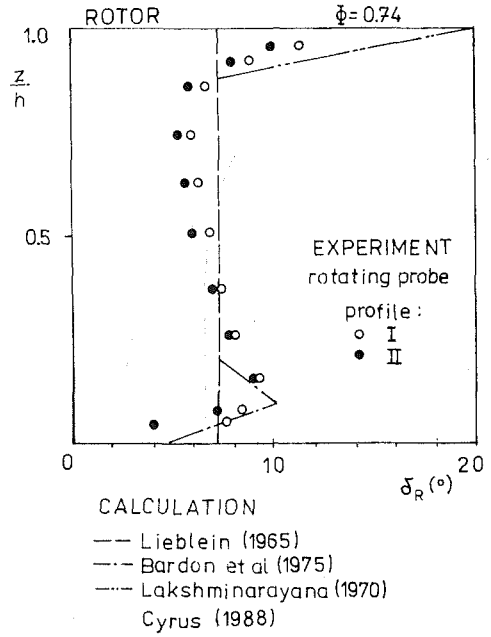

Fig. 9 Spanwise rotor deviation angle distribution

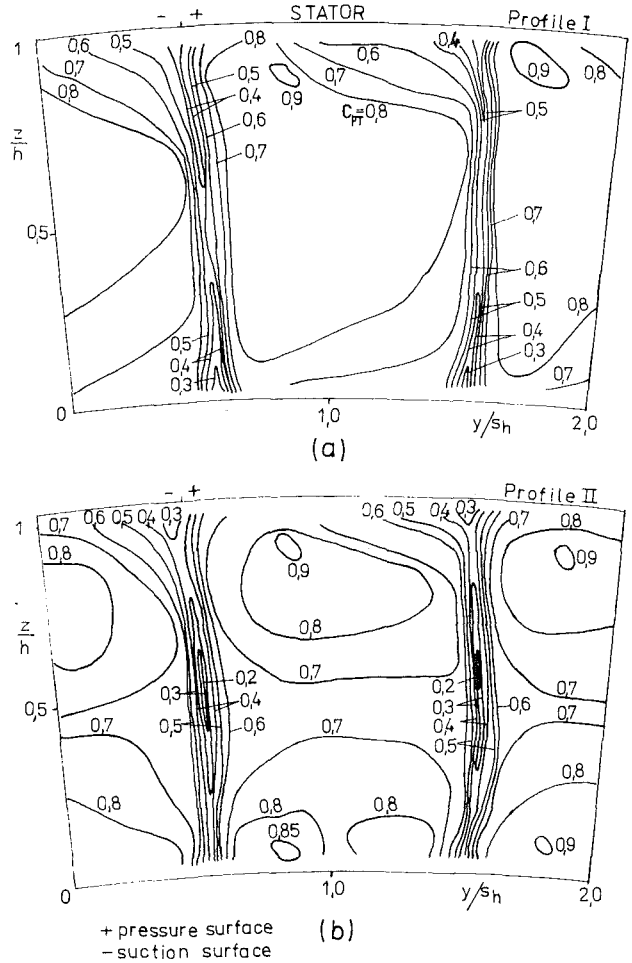

Fig. 10 Stator exit total pressure contours

velocity profile (profile II). The full line indicates ω_R for profile I derived in Fig. 8(a). For clarity it includes values of ω_R obtained from the rotating probes only. These are plotted with a dashed line. As shown, the loss coefficient ω_R at midspan is about double the value obtained with the unmodified velocity profile. This is in agreement with the results of Ikui et al. (1977) and Dring et al. (1982), obtained without artificially increased inlet turbulence intensity. Thus, it appears that the increased turbulence intensity level has minimal effect on the rotor loss coefficient value in the midspan region. Near the endwalls the coefficient ω_R remains unaffected by the shape of the velocity profile. The same results are given by Ikui et al. (1977). However, in the UTRC isolated rotor (Wagner et al., 1985), the losses near the endwalls were lower for the velocity profile with thick annulus boundary layers than for the idealized velocity profile with thin annulus boundary layers.

Figure 9 shows the distribution of the deviation angle along the blade span. It will be seen that the deviation angle is not significantly affected by the shape of the inlet velocity profile. In the midspan region the deviation angle was lower by 0.8–1.0 deg in the case of profile II, in contrast to profile I. The distortion of the inlet velocity profile brought about a reduction of the incidence angle by 4 deg at midspan.

Figure 9 also shows the computed distribution of plane cascade deviation angle according to Lieblein (1965) for the idealized velocity profile (profile I). The curve includes added corrections for the secondary flow effects ascertained at the hub and casing by using the method of Bardon et al. (1975) and Lakshminarayana (1970), respectively, and modified by Cyrus (1988). A reasonable agreement between computation and measurement is evident, even though the inviscid models of the secondary passage vortex (Bardon et al., 1975) and the tip clearance flow (Lakshminarayana, 1970) do not give a reliable description of the endwall flow.

Stator Blade Row. Figures 10 shows the contours of total pressure coefficients C_{PT} in the plane behind the rotor row for the two shapes of the inlet velocity profile under investigation.

In contrast to the rotor blade row, another definition of the pressure coefficient was used. This is due to the irregular distribution of total pressure in the peripheral direction in plane 2. The wakes of the inlet guide vanes are not yet dissipated because of the small distance between the blade rows. According to the original definition, the coefficients C_P for the midspan came out as negative values.

In the case of inlet velocity profile I, about 30 percent of the span near the hub and 25 percent near the casing is affected by secondary flow. At both endwalls there are observable corner stall regions with low total pressure fluid. When the inlet velocity profile was distorted and the turbulence intensity increased, major areas with low coefficient (C_{PT} = 0.2–0.3), i.e., high flow energy losses, appear in the wake of the midspan like in the rotor row. This is probably due to transport of the low-energy fluid. Similarly, the regions found in the midspan outside the wakes have a lower fluid energy than those occurring near the endwalls.

Figure 11 shows the results of flow visualization on the suction surface of the stator blades. The blade surface was covered by white polyethylene tape using a visualization mixture of oil and fine carbon particles. The flow traces on the suction part of the blade show the corner areas that arise near the midchord of the stator blade. In the case of the velocity profile I, in the corners are observable flow separation areas with backward flow (black spots). When the inlet velocity profile is distorted, the trailing edge backward flow domain covers practically the whole blade span. This may contribute to the growth of total pressure losses over the middle part of the blade. No further differences can be found between visualization patterns for the cases with inlet velocity profiles I and II.

The radial distribution of the loss coefficient for the stator blade row is plotted in Fig. 12 for both flow cases under investigation. Again, the modification of the inlet flow field produced a growth of the loss coefficient in the midspan

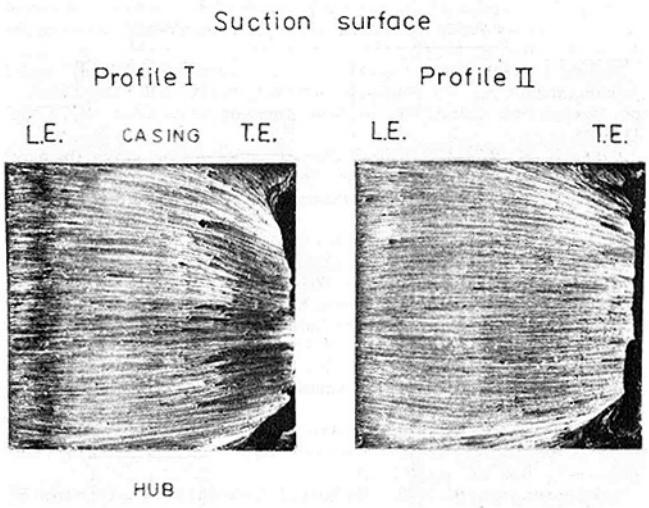

Fig. 11 Stator visualization patterns

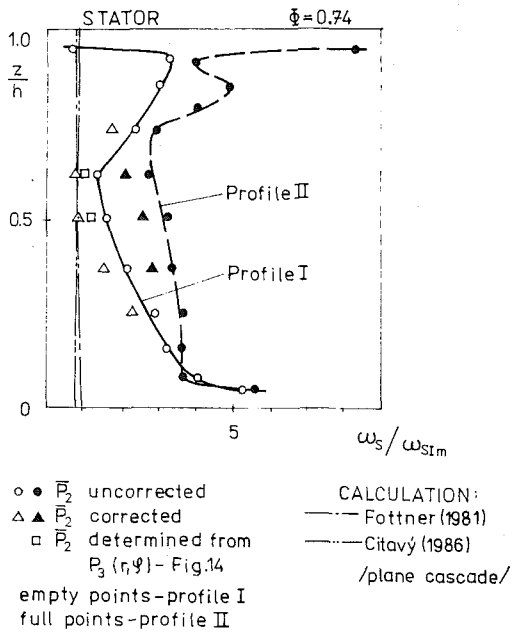

Fig. 12 Spanwise stator loss coefficient distribution

region, as in the rotor row. Moreover, there was an increase of flow energy losses near the casing. This can be accounted for by increased aerodynamic loading in this part of the stator blade, as follows from the incidence angle distribution along the span (Fig. 13). In the midspan are plotted values of the coefficient ω_s obtained from the stationary probe data. The values of total pressure from the conical pressure probe in plane 2 were corrected in accordance with the SVÚSS method (Appendix).

With velocity profile I, the midspan total pressure $\bar{P}_2$ used for assessment of coefficient ω_s was determined as the average value for the distribution of pressure P_3 (r, φ). The pitchwise pressure distribution was interpolated in the wakes (dotted line—Fig. 14). Figure 12 indicates that, in the case of an idealized unmodified inlet velocity profile in the mid-span, the loss coefficient approaches the value for an equivalent plane cascade when the flow pulsation effect on the probe reading has been corrected for. The same result was obtained for the case of the rotor row.

Figure 15 shows the distribution of deviation angle along the span for the two shapes of the inlet velocity profile. The differences between the two curves are not significant. In the midspan the deviation angle is smaller by 2 deg for profile II

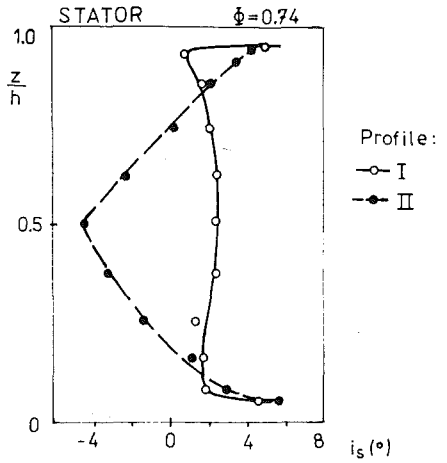

Fig. 13 Stator incidence angle along span

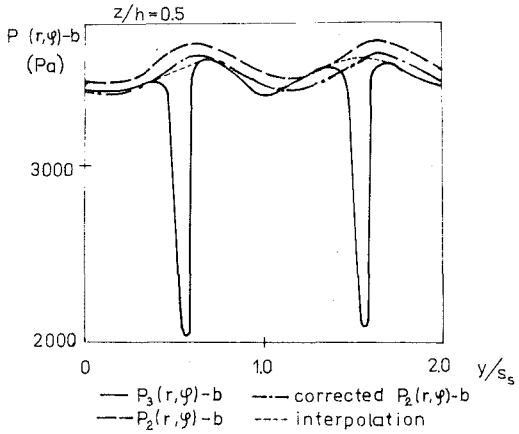

Fig. 14 Distribution of total pressure along stator pitch

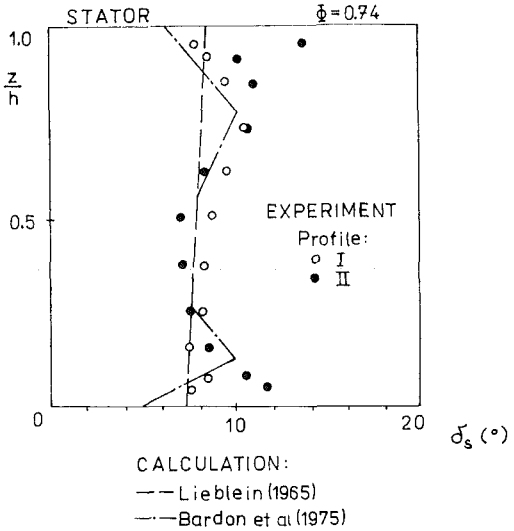

Fig. 15 Spanwise stator deviation angle distribution

than the deviation angle for profile I. This is apparently due, as in the rotor row, to the change of aerodynamic loading of the blade (Fig. 13).

As in the rotor row, the deviation angle was calculated as the sum of the value obtained for a plane cascade (Lieblein, 1965) and the corrections for the secondary flow effect for velocity profile I. Since there is no tip clearance at the hub and casing, the method of Bardon et al. (1975) was used to determine the correction. The agreement between computation and

measurement was good except for the hub region. This is probably due to the fact that the inviscid model of the secondary passage vortex does not describe the endwall flow with sufficient accuracy.

Figure 3 describes the development of the axial velocity profile within the stage blading. Obviously, at the design value of the flow coefficient, there was no considerable change of the axial velocity distribution along the span for both investigated cases of the inlet flow field. This is in constrast with the experimental results of Ikui et al. (1977) where about the same distribution of axial velocity was found in the outlet plane for different shapes of velocity profiles in the inlet plane. This can be accounted for by smaller distortion of the inlet velocity profile of Ikui et al. (1977) than in our case. There may also be some influence of the increased inlet flow turbulence intensity and different geometrical parameters of the compared stages.

Conclusion

The paper presents results of an experimental investigation of three-dimensional flow in the rear stage of an industrial-class axial compressor. The working conditions of a multistage compressor stage have been modeled with the aid of a specially designed screen and lengthened inlet annulus. These flow path elements produced an increase in axial velocity profile distortion and inlet turbulence intensity. Some original results have thereby been obtained concerning simultaneous effects of velocity profile distortion and increased turbulence intensity on the three-dimensional flow in the rear stage of this type of axial compressor.

Modeling of the "realistic" inlet flow field for a rear stage, in contrast to an unmodified, relatively uniform inlet flow field, resulted in:

- deterioration of the aerodynamic performance of the stage. The reduction of efficiency and pressure ratio at the design state was $\Delta\eta/\eta_{DI}=4.5$ percent and $\Delta\psi/\psi_{DI}=4.8$ percent, respectively.
- (at the design value of coefficient $\phi=0.74$):

(a) growth of the loss coefficient in the midspan region of the rotor and stator blade row, and (b) no significant effect on the distribution of deviation angle along the span in both blade rows.

Acknowledgments

This work was carried out for CKD-Works in Prague under monitoring of Dr. Svoboda and Mr. Feierefeil. The author is grateful to the National Research Institute for Machine Design (SVÚSS) and CKD-Works for permission to publish the results.

References

Bardon, M. F., Moffat, W. C., and Randall, J. L., 1975, "Secondary Flow Effects on Gas Exit Angles in Rectilinear Cascades," ASME *Journal of Engineering for Power*, Vol. 97, pp. 93–99.

Čamek, J., 1983, "Calibration of Pressure Probes in Unstationary Flow Field" [in Czech.], *Strojírenství*, Vol. 33, pp. 3–9.

Citavý, J., 1987, "Performance Prediction of Straight Compressor Cascades Having an Arbitrary Profile Shape," ASME JOURNAL OF TURBOMACHINERY, Vol. 109, pp. 114–122.

Cyrus, V., 1986, "Experimental Study of Three-Dimensional Flow in an Axial Compressor Stage," ASME Paper No. 86-GT-118.

Cyrus, V., 1985, "Experimental Investigation of Losses and Secondary Flow in Axial Compressor Stage," *Forschung im Ingenieurwesen*, Vol. 51, No. 2, pp. 33–40.

Cyrus, V., 1988, "Secondary Flow in Axial Compressors and Its Effect on Aerodynamic Characteristics," SVÚSS Monographs and Memoranda, No. 38, Prague.

Dong, Y., Gallimore, S. J., and Hodson, H. P., 1987, "Three-Dimensional Flows and Loss Reduction in Axial Compressors," ASME JOURNAL OF TURBOMACHINERY, Vol. 109, pp. 354–361.

Dring, R. P., Joslyn, H. D., and Hardin, L. W., 1982, "An Investigation of Axial Compressor Rotor Aerodynamics," ASME *Journal of Engineering for Power*, Vol. 104, pp. 84–96.

Fottner, L., 1981, "Survey on Diffusion Factors and Profile Losses," Agard Advisory Report, No. 175, Propulsion and Energetics Panel Working Group 12 on Through-flow Calculations in Axial Turbomachines, Chap. II.2.1, pp. 116–126.

Grant, H. P., 1979, "Turbulence Characterisitics of Compressor Discharge Flows," NASA Conference Pub., No. 79-24994, pp. 5–31.

Howell, A. R., 1945, "Fluid Dynamics of Axial Compressors," *Proc. IMechE*, Vol. 153, p. 441.

Hunter, I. H., and Cumpsty, N. A., 1982, "Casing Wall Boundary Layer Development Through an Isolated Compressor Rotor," ASME *Journal of Engineering for Power*, Vol. 104, pp. 805–817.

Ikui, T., Inoue, E., and Kuroumaru, M., 1977, "Development of Velocity Profile Through a Stage of Axial Flow Turbomachinery," *Proceedings of Joint Gas Turbine Congress*, Tokyo, pp. 311–318.

Joslyn, H. D., and Dring, R. P., 1985, "Axial Compressor Stator Aerodynamics," ASME *Journal of Engineering for Gas Turbines and Power*, Vol. 107, pp. 485–493.

Lakshminarayana, B., 1980, "An Axial Flow Research Compressor Facility Designed for Flow Measurement in Rotor Passages," ASME *Journal of Fluids Engineering*, Vol. 102, pp. 402–411.

Lakshminarayana, B., 1970, "Methods of Predicting the Tip Clearance Effects in Axial Flow Turbomachinery," ASME *Journal of Basic Engineering*, Vol. 92, pp. 467–482.

Lieblein, S., 1965, "Experimental Flow in Two-Dimensional Cascades," NASA SP36, pp. 183–226.

Schlichting, H., and Das, A., 1970, "On the Influence of Turbulence Level on Aerodynamic Losses of Axial Turbomachines," in: *Flow Research on Blading*, X. X. Dzung, ed., Elsevier, Amsterdam.

Wagner, J. H., Dring, R. P., and Joslyn, H. D., 1985, "Inlet Boundary Layer Effects in an Axial Compressor Rotor: Part I—Blade-to-Blade Effects," ASME *Journal of Engineering for Gas Turbines and Power*, Vol. 107, pp. 374–380.

Wisler, D. C., 1985, "Loss Reduction in Axial-Flow Compressors Through Low-Speed Model Testing," ASME *Journal of Engineering for Gas Turbines and Power*, Vol. 107, pp. 354–363.

APPENDIX

Dynamic Calibration of Pressure Probes

The SVÚSS method (Čamek, 1983) is based on the calibration of pressure probes in well-defined pulsating flow. This is generated by an air turbine wheel situated in the exit plane of the nozzle. The pressure amplitudes depend on the distance behind the turbine blades. The required frequency of the flow pulsations is given by the number of blades. The wake dimensionless width (b/s) is changed along the radius of the turbine wheel. The results of the calibration were expressed in the form of the coefficient (Cyrus, 1985)

$$X_P=\frac{P_m-P}{Q_m} \tag{1}$$

where P_m means the measured average value of total pressure by a probe in a pulsating flow behind turbine wheel; P is the true average value of total pressure of the pulsating flow determined by application of the method. In the method (Čamek, 1983) it is supposed that the same distribution of the loss coefficient exists along the turbine blade pitch as in the case of the stationary cascade. Q_m is the average value of the dynamic head of the pulsating flow measured by probe.

The typical values of calibration coefficient X_p (Cyrus, 1985) for the five-hole conical or total pressure probe (Fig. 8) obtained for values of $b/s=0.27$, flow unsteadiness frequency $f=1500$ Hz, and Mach number $M=0.35$ are $X_P=0.017$ and 0.034, respectively. The true (corrected) average value of total pressure P measured by the pressure probe located in a turbomachine is calculated according to relation (1) with the use of the coefficient X_P. Then, the subscript m denotes the measured values of flow parameters obtained on the basis of the usual probe calibration in steady flow.

Performance of a Compressor Cascade Configuration With Supersonic Entrance Flow—A Review and Comparison of Experiments in Three Installations

G. K. Serovy
Anson Marston Distinguished Professor.

T. H. Okiishi
Professor.

Department of Mechanical Engineering
and Engineering Research Institute,
Iowa State University,
Ames, IA 50011

A cascade geometry derived from a research program on high-throughflow, transonic, axial-flow compressors was tested with similar supersonic entrance flow conditions in three linear cascade test facilities. The airfoil section used was representative of advanced rotor-blade, tip-region profiles designed to operate at inlet relative Mach numbers of 1.4 to 1.8. Objectives in the experiments were to study the reproducibility of test conditions and measured performance in facilities that are considered to be "state-of-the-art," and to generate data sets that could be used as test cases or "benchmark" results to validate computational methods for turbomachine application. It was recognized from the beginning of the project that the aerodynamic regime involved represents a very difficult combination of problems in both experimentation and computation. This difficulty was certainly encountered; the experimental problems are fully discussed in this paper and the companion papers originating in two of the test groups. An excellent series of data sets has been obtained, and our confidence in the results is supported by the exchange of information and personnel that occurred during all phases of the experiments. The results presented here and in the forthcoming AGARD Propulsion and Energetics Panel "test case" compendium should serve as a standard for evaluating current and future computational efforts.

Origins and Organization of the Test Program

A series of meetings and working group activities organized during the past 15 years by the Propulsion and Energetics Panel (PEP) of AGARD[1] produced reports that focused attention on the importance of "benchmark" experimental data sets in validating computational methods for turbomachine and other internal flows (NATO/AGARD Propulsion and Energetics Panel, 1976; NATO/AGARD Propulsion and Energetics Panel Working Group 12, 1981; NATO/AGARD Propulsion and Energetics Panel, 1985; NATO/AGARD Propulsion and Energetics Panel, 1987). On the basis of conclusions of AGARD/PEP Working Group 12 (NATO/AGARD) Propulsion and Energetics Panel, 1976; NATO/AGARD Propulsion and Energetics Panel, 1981), the AGARD Panel voted in 1984 to set up PEP Working Group 18 on Test Cases for Computation of Internal Flows in Aero Engine Components. Before the formal establishment of Working Group 18, individuals associated with the earlier PEP work held discussions during 1981 on the selection of experimental data sets. It was recognized that one significant, complex, and controversial type of "benchmark" data would come from tests of axial-flow compressor cascade configurations designed for supersonic entrance region flow conditions in the range from $M_1 = 1.4$ to 1.8. In meetings involving leaders of three highly regarded turbomachine research agencies, Jean Fabri (Direction de l'Energètique, ONERA), Gert Winterfeld (Institute für Antriebstechnik, DFVLR), and Arthur Wennerstrom (Air Force Wright Aeronautical Laboratories, USAF), with the senior author of this paper, it was decided that the basis for a test case already existed in USAF research supporting development of high-throughflow, transonic, axial-flow compressor stages.

The USAF Aero Propulsion Laboratory work summarized by Wennerstrom (1984) produced a single-stage, axial-flow compressor having very good aerodynamic performance. Research supporting the USAF high-throughflow program included experiments at Detroit Diesel Allison (DDA) on a linear cascade developed from a rotor-tip-region blade section (Wennerstrom, 1984). The DDA results (Fleeter et al., 1975), reported in some detail, were recent enough so that records were complete and the memories of DDA researchers clear.

[1] Acronyms are defined, along with symbols and notation, in the Nomenclature.

Contributed by the International Gas Turbine Institute and presented at the 33rd International Gas Turbine and Aeroengine Congress and Exhibition, Amsterdam, The Netherlands, June 5–9, 1988. Manuscript received by the International Gas Turbine Institute July 20, 1987. Paper No. 88-GT-211.

Because supersonic, linear cascade wind tunnels have been developed and continually improved over a long period at ONERA and DFVLR, and because both facilities are operated by experienced research teams, it was agreed that experiments on cascade blading similar to the USAF/DDA configuration would permit studies of reproducibility of test conditions as well as comparison of measurement and data reduction procedures, and that the collected results would contain test case data sets likely to be accepted by the turbomachinery research and development community.

New cascade blade sets were fabricated during 1983 by both DFVLR and ONERA. Experimental runs were initiated at DFVLR and at ONERA during the last half of 1983. Internal reporting on the ONERA and DFVLR experiments and on the experimental facilities used began in 1984 and continues to date. Selected results are being evaluated and will be presented in a forthcoming AGARD/PEP publication with a wide range of other "test case" data.

High-Throughflow Research Compressor Project

As part of the generalized research program directed toward development of high-throughflow, multistage, axial compressors, a single-stage transonic compressor configuration was designed and tested (Wennerstrom, 1984). The design-point rotor-tip speed for the stage was 457 m/s (1500 ft/sec). The stage was designed with a steady, axisymmetric, streamline-curvature throughflow computer code. For an axisymmetric stream surface intersecting the leading edge of the rotor at a radius about six percent of the blade span from the tip (SL19), the design-point, leading-edge relative Mach number was 1.61. The SL19 trailing edge Mach number at the design point was predicted as 0.88, and the static pressure ratio across the rotor was computed as 2.16. The corresponding AVDR was 1.16. For these conditions a cascade geometry made up of arbitrary airfoils was designed to produce the required leading and trailing edge SL19 flow parameters on the basis of estimates of turning and loss distribution between the leading and trailing edge. The rotor design was "optimized" by iteration between the throughflow and cascade computations for the various stream surfaces and by stacking of these cascade sections on a hub-to-tip line.

The experimental aerodynamic performance of the USAF stage was eventually found to be excellent. However, as is common in development programs, early linear cascade tests were scheduled in support of the design method and as a preliminary means for evaluating blade-section performance. This element of the program was carried out by the Research Department of the Detroit Diesel Allison Division (now Allison Gas Turbine Division) of the General Motors Corporation (DDA).

Cascade Airfoil Section Development and Fabrication

As the first step in the DDA cascade investigation, a modified, linear cascade airfoil section and cascade geometry were developed in cooperation with the USAF research group (Fleeter et al., 1975). This cascade configuration geometry is defined by Table 1 and the airfoil geometry is shown in Fig. 1. Figure 1 also shows some of the sign conventions and terminology used. Detailed blade coordinates prescribed for manufacturing are given in Appendix A. Subsequently, these USAF/DDA coordinates were used to scale airfoil manufacturing coordinates by ONERA and DFVLR. The Table 1 geometry and the USAF/DDA airfoil coordinates define what all groups concerned now call the "SL19" cascade.

The DDA/USAF blades were manufactured in a milling, grinding, and polishing process to obtain the airfoil profile. DFVLR airfoils were shaped by a grinding process in the spanwise direction with wheels contoured to the suction and

Nomenclature

AVDR = axial-velocity-density ratio = $\rho_2 V_{x,2}/\rho_1 V_{x,1}$
c = chord length
h = blade span
LE = leading edge
M = Mach number
P = pressure
Re = Reynolds number based on entrance region velocity and chord
s = tangential distance between corresponding points on adjacent airfoils
TE = trailing edge
t = blade thickness
V = fluid velocity
x = distance measured along chord line from leading edge
XP = pressure surface coordinate (Fig. 1)
YP = pressure surface coordinate (Fig. 1)
XS = suction surface coordinate (Fig. 1)
YS = suction surface coordinate (Fig. 1)
α = flow angle in spanwise direction measured from cascade plane
β = flow angle measured from axial direction in cascade plane
$D\beta$ = flow angle measured from reference direction in cascade plane (Fig. 7*b*)
γ = stagger angle, angle between chord line and axial direction
η = coordinate measured in tangential direction
ρ = fluid density
σ = cascade solidity = c/s
$\bar{\omega}$ = total pressure loss coefficient (Figs. 7 and 8)

Superscripts

$\bar{}$ = average

Subscripts

max = maximum
N = nozzle exit
x = axial component
0 = total condition
1 = cascade entrance
2 = cascade exit

Acronyms

DDA = Detroit Diesel Allison Division of General Motors Corporation (now Allison Gas Turbine Division)
DFVLR = Deutsche Forschungs- und Versuchsanstalt für Luft- und Raumfahrt
ONERA = Office National d'Études et de Recherches Aérospatiales
USAF = United States Air Force
AGARD/PEP = Advisory Group for Aerospace Research and Development, Propulsion and Energetics Panel
RAE = Royal Aircraft Establishment

pressure surface coordinates. ONERA cascade blades were manufactured by an electrical erosion process. Local inspections were conducted for all three sets; in addition, during the program, sample blades from the three sets were sent to the NASA Lewis Research Center for coordinate checks performed on a single inspection system (Pratt & Whitney Blade Profiler). Detailed results are not reported here, but local deviations on the order of 0.05 to 0.10 mm (0.002 to 0.004 in.) from NASA blade tolerances were measured for some chordwise stations on some blades in all three blade sets, with the vast majority of deviations in the leading and trailing edge regions. These deviations were not considered to reduce the validity of the experiments.

Comparison of the Three Experiments

Blading and Test Sections. In addition to the DDA cascade configuration geometry, Table 1 also shows corresponding values for the ONERA and DFVLR cascade tests. The test sections of the three tunnels for the test series are shown schematically in Figs. 2, 3, and 4. Each test section has been developed over an extended period within its parent organization.

The DDA test-section entrance flow is generated by a fixed nozzle, as is also the case for the ONERA section. The nominal test-section inlet Mach numbers were 1.5 in both cases. The DFVLR test section uses an adjustable-wall nozzle for rapid change of the tunnel nominal inlet Mach number. All three test sections operate so that the primary adjustment of the cascade entrance region (leading-edge) M is produced by wave patterns initiated by the first (leading) blade or wedge (DDA only), as discussed by Lichtfuss and Starken (1974).

Wall boundary layers at the cascade entrance were subject to control by cascade endwall suction systems, and in the DDA tunnel the side-wall boundary layer flow was removed through a porous bleed strip. The flow immediately downstream of all three cascade blade arrays was influenced to control periodicity by adjustable tailboard systems. The DDA and DFVLR tailboards were perforated and slotted, respectively.

The DDA cascade was operated with transparent, solid, side-wall surfaces in the interblade passages. Both ONERA and DFVLR used suction ports in the transparent interblade walls to remove side-wall region flow. Back pressure (downstream/upstream static pressure ratio) was adjusted by combinations of tailboard or throttle adjustment or both.

Table 1 Comparison of design test cascade geometries

Variable	Experiment		
	DDA	ONERA	DFVLR
Number of blades	6	7	5
Aerodynamic chord, c, mm	69.42	83.41	85.0
Blade-to-blade-spacing, s, mm	45.39	54.28	55.58*
Span, h, mm	76.66	100.0	152.4
Stagger angle, γ, deg	56.934	56.934	56.934
Solidity = c/s = σ	1.5294	1.5367	1.5294
t_{max}/c	0.0255	0.0255	0.0255
Mean-line tangent angle†			
LE deg	52.032	52.032	52.032
TE deg	54.923	54.923	54.923
Camber angle, ϕ	-2.891	-2.891	-2.891
Metal angle, leading edge tangent			
suction surface, deg	53.797	53.797	53.797
pressure surface, deg	50.947	50.947	50.947
LE radius/chord	0.00128	0.00128	0.00128
TE radius/chord	0.00128	0.00128	0.00128

*Assuming constant solidity of 1.5294.
†Blade angles are measured from the axial direction (perpendicular to cascade leading-edge plane).

Facilities. The three supersonic cascade wind tunnel facilities were somewhat different in physical arrangement. The ONERA facility was a closed-loop system with the system pressure variable to allow test-section inlet total pressures from about 0.2 to 1.0 bar (20 to 100 kPa), with 80 kPa used in the SL19 tests. A heat exchanger between the system compressor and the test section was used to maintain section inlet total temperature at about 310 K. Fixed nozzle blocks are available for supersonic cascade test-section inlet M levels of 1.3, 1.5, and 1.7.

The DFVLR cascade tunnel also operated as a closed-loop system. Test section inlet total pressures from about 0.9 to 2.5 bar could be maintained, and for the SL19 experiments, a nominal cascade inlet total temperature of about 310 K was measured with inlet total pressure from about 100 to 130 kPa.

The DDA supersonic cascade tunnel was an open system with a compressed air supply and an ejector system to provide downstream suction. Typical test section inlet total conditions maintained during the USAF/DDA tests were about 127 kPa and 315 K.

In all three facilities, test section air was filtered and dried. Previous tunnel calibrations verified the necessary degree of uniformity and steadiness of nozzle Mach numbers.

Instrumentation and Measurement Systems. For all experimental data sets, the test section was instrumented to measure flow periodicity in the leading- and trailing-edge-plane regions, trailing-edge region blade-to-blade distributions of total and static pressure and flow angle, and suction- and pressure-surface static pressure distributions. Table 2 summarizes the individual arrangements for the three sets.

The three downstream survey probes were all calibrated over a range of Mach numbers that included all test levels.

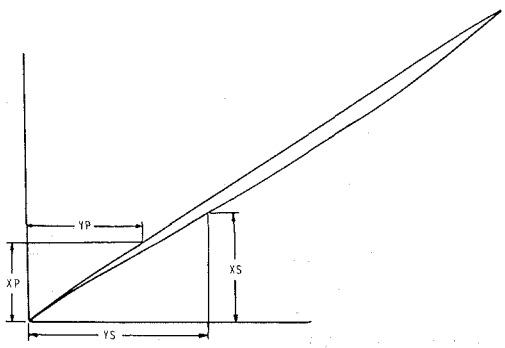

Fig. 1(*a*) Airfoil section as defined for DDA/USAF tests of SL19 cascade [6]

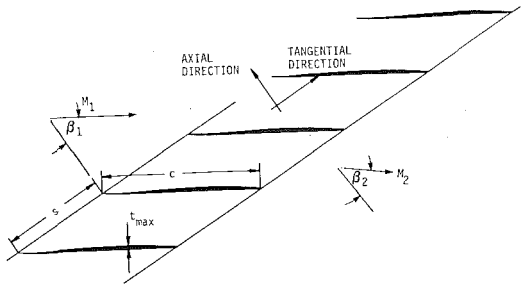

Fig. 1(*b*) Cascade nomenclature and sign conventions

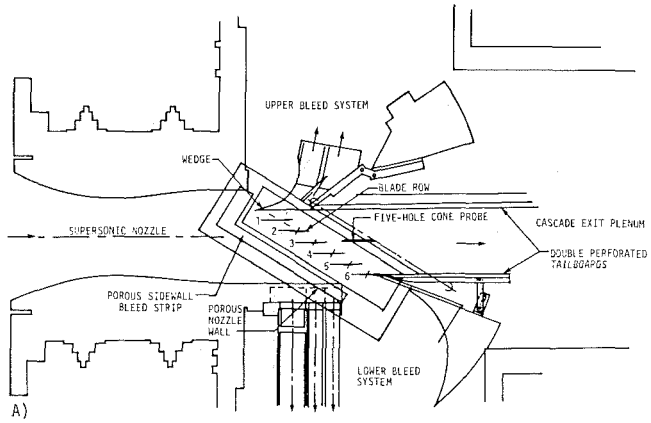

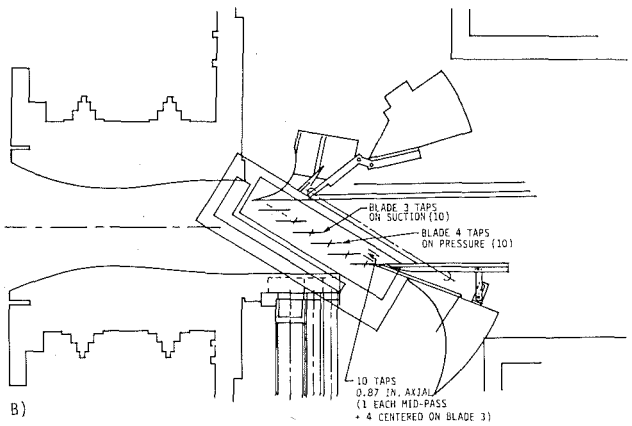

Fig. 2 Schematic drawing of DDA cascade test section

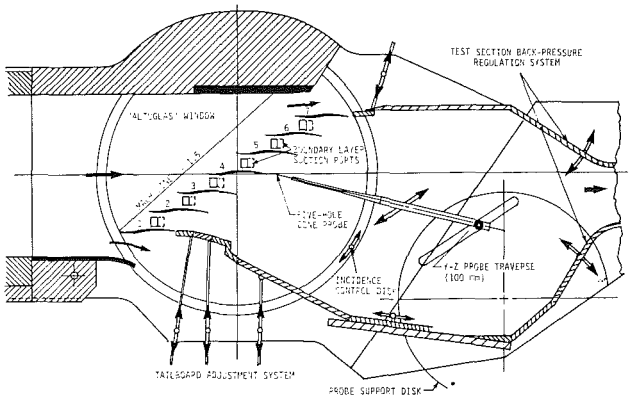

Fig. 3 Schematic drawing of ONERA cascade test section

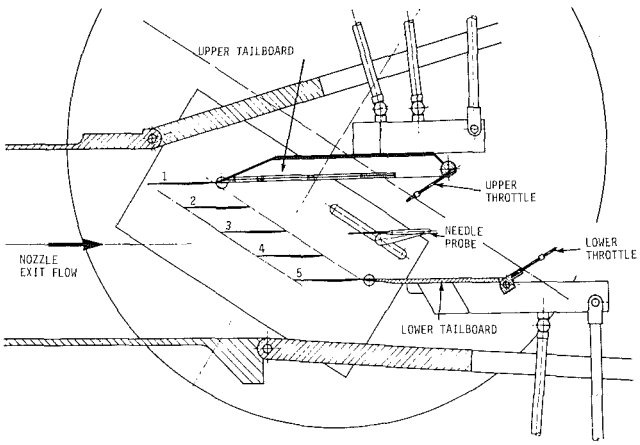

Fig. 4 Schematic drawing of DFVLR cascade test section

Aerodynamic Boundary Conditions and Test Procedures

In the experiments carried out by DDA, ONERA, and DFVLR, all runs were made with the cascade operating in the "started" mode (Lichtfuss and Starken, 1974; Chauvin et al., 1970). In this mode, the dependent variables β_2, $\bar{\omega}$, and M_2 are functions of the independent variables M_1, Re, the turbulence characteristics of the entering flow, AVDR $= \rho_2 V_{x,2}/\rho_1 V_{x,1}$, and P_2/P_1. For given values of M_1 and Re, the cascade operates at a "unique" incidence (Lichtfuss and Starken, 1974; Chauvin et al., 1970). In the current experiments, the Reynolds numbers in the three facilities were different (but high, i.e., $\gg 5 \times 10^5$) and turbulence intensity was only measured by DFVLR (<1 percent).

The tests were generally carried out in sets at a nearly constant inlet Mach number level. Data were taken at increasing back pressure level, while the side-wall suction and thus AVDR were controlled so as to reach the highest possible back pressure before the spill point (unstarting) occurred. It should be remembered that the side-wall boundary layer removal systems and the slots in the interblade passages were not the same in the three cases. For example, DDA had no blade passage suction, and DFVLR used two side-wall port geometries during the course of the program (see Fig. 5). These differences assure that the variation of AVDR, and consequently the stream tube thickness through the cascade, will not be the same in the three facilities for a given AVDR across the row.

At a given data point setting, the data taken generally included wall and blade surface static pressures and downstream tangential (blade-to-blade direction) probe surveys at the midspan of the blades. Additional data were taken in a limited number of cases, as indicated in Table 2 for optical flow field measurements. Some checks of spanwise variations in performance were made by ONERA and DFVLR, and some low Re data were taken by ONERA. DDA tests were made at three inlet M levels, about 1.54, 1.62, and 1.68; ONERA limited testing to M_1 of about 1.62 to 1.66; DFVLR carried out a greater number of tests over a range of M_1 from about 1.3 up to 1.71.

Data Reduction and Presentation. The data recorded were processed within the three test groups by use of tested data reduction codes and plotting systems. While it is not possible to guarantee consistency among the three systems, the approach taken by each is consistent, and possible areas of disagreement will be described here for cascade entrance conditions and overall performance evaluation.

At the cascade entrance (leading edge region), DDA, ONERA, and DFVLR all had different methods for calculating the M_1 and β_1 values reported. These are discussed by Fourmaux et al. (1988) and Tweedt et al. (1988). In the case of DFVLR experiments, a few measurements of M_1 and β_1 were made with a laser velocimeter ("L2F") system. Example leading-edge region variations are shown in Fig. 6, along with the DFVLR-reported β_1 and M_1 levels. The substantial blade-to-blade variation is noteworthy.

At the downstream survey station, all values computed for average station 2 conditions were calculated on both mass-flow-weighted and "mixed-out" bases (Schimming and Starken, 1975). The three groups of experiments all used "mixing-out" methods to compute loss coefficients and other flow parameters on the basis of a computed uniform downstream condition that assumes conservation of mass flow and tangential and axial momentum components, with a constant streamtube thickness during mixing.

Table 2 Comparison of measurement methods

DDA	ONERA	DFVLR
Downstream survey measurements		
Conical 5-hole probe at station 17.3 mm axially downstream from trailing-edge plane for Mach number, total pressure and flow direction.	Conical 5-hole pressure probe (Galliard, 1983) to measure flow 20 mm axially downstream from trailing-edge plane including total pressure, static pressure and both yaw and pitch angles	Total pressure crossed-wedge angle probe with separate spanwise displaced needle head for static pressure all at 26.2 mm axially downstream from trailing-edge plane
(calibrated M = 0.35 –1.80)	37 equally-spaced points in survey (24 points used in average for loss)	40 equally spaced points in survey
21 equally spaced points in survey		
Airfoil surface static pressure taps		
20 taps, 10 on suction (blade 3) surface, 10 on pressure (blade 4) surface	17 static pressure taps on pressure surface of blade 5	Same tap locations as DDA
	15 static pressure taps on suction surface of blade 4	
Side-wall static pressure taps		
1 tap on each side of the tunnel located upstream of the wedge wave system	12-14 upstream taps aligned in the streamwise direction near each mid-passage between blades 2 through 6	7 taps in top and bottom nozzle extension plates
1 tap ahead of each blade	1 downstream tap near each mid-passage between blades 2 through 6	7 upstream taps and 7 downstream taps distributed tangentially over the 4 blade passages
10 taps downstream of the cascade exit plane; 1 tap at each mid-passage location, and 4 others centered around blade 3		12 upstream taps distributed in the streamwise direction for one blade passage.
Optical measurements		
Schlieren flow visualization was used for all runs	Schlieren flow visualization was not used	Schlieren flow visualization was used for all runs
Laser anemometry was used for some flow field measurements	Laser anemometry was not used	Laser anemometry (L2F) was used in cascade leading-edge region plane to measure Mach number and yaw angle variation along cascade front

Example Results From Experiments

In this paper several examples of data and data comparison are offered (1) to show the type of data presentation formats used by DFVLR and ONERA, (2) to illustrate representative variations in key parameters in a given test run, and (3) to compare test results from the three organizations. Figure 7(*a*) shows the trend in blade surface Mach number for an example test point as computed by DFVLR for an isentropic flow to local stations that is based on upstream total pressure and local surface static pressure. Downstream values shown on Fig. 7(*a*) are calculated for "mixed-out" conditions. Figure 7(*b*) shows tangential variations of flow angle and pressure and a total pressure loss coefficient based on downstream survey station measurements made with the DFVLR combination survey probe. As demonstrated by the variation of $D\beta_2$ shown, it was not possible to achieve exact periodicity of the cascade exit flow in all tests.

Figures 8(*a*) and 8(*b*) show a similar typical data display for one ONERA test point. The downstream survey information includes Mach number, total pressure recovery ratio, and the local values of both yaw and pitch angle as measured with the ONERA five-hole conical probe. The near-zero pitch angle values indicate little spanwise flow at the midspan survey station.

Results from all three of the test programs are shown for comparison in Figs. 9 through 12. Figure 9 shows unique cascade inlet flow angle as a function of inlet Mach number. The solid lines represent predicted values as reported by Tweedt et al. (1988). The methods used by ONERA and DDA for determining experimental values of inlet angle lead to a single value of β_1 at each M_1. In Figs. 10, 11, and 12 the solid lines represent correlations of the data developed by DFVLR (Tweedt et al., 1988), and the symbols indicate "mixed-out" experimental values from ONERA and DDA. ONERA loss coefficient values were calculated from reported total pressure ratios (Fourmaux, 1984) and $P_1/P_{0,1}$ values corresponding to $M_1 = 1.66$ and a specific heat ratio of 1.40.

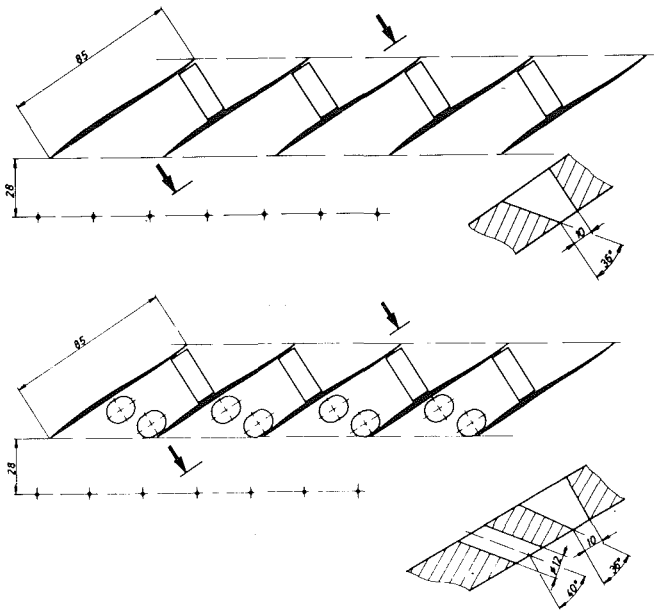

Fig. 5 Two side-wall suction port configurations used in the DFVLR test series

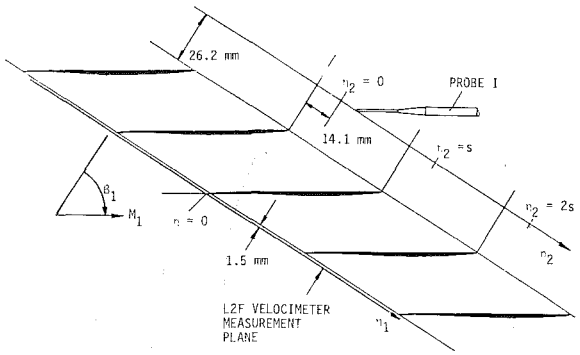

Fig. 6(*a*) DFVLR laser velocimeter measurement nomenclature

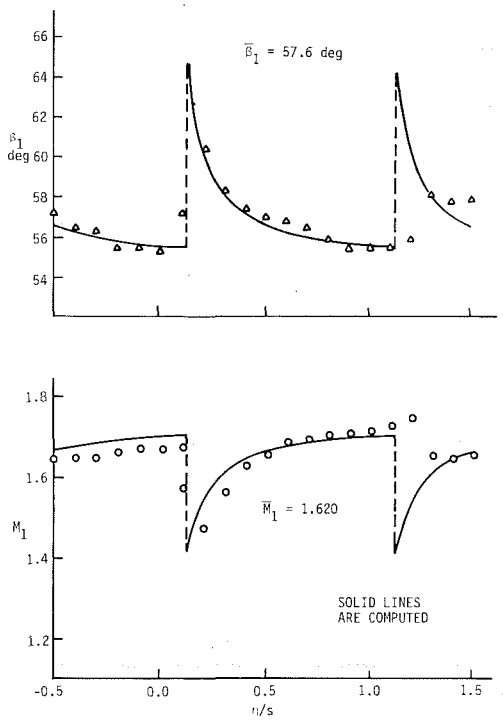

Fig. 6(*b*) Typical DFVLR laser velocimeter measurements in cascade leading edge region

Evaluation of Results

In three different test sections with cascade aspect ratio varying from 1.10 to 1.79, and with differing systems for AVDR control, difficulty might be expected in generating comparable data. This expectation was confirmed throughout the ONERA and DFVLR test programs. Nevertheless, there were few obvious inconsistencies in the newer data sets, and both new sets of results tended to confirm the validity of the earlier DDA results as reported by Fleeter et al. (1975).

Comparison of DDA and ONERA test results with the DFVLR correlations (Figs. 10–12) lead to several conclusions. The value of inlet Mach number M_1 associated with the ONERA tests was enough larger than for the DFVLR and DDA tests being considered to be noticeable when data were compared. For example, the maximum static pressure ratio achievable with $M_1 = 1.66$ (ONERA) was larger than that possible with $M_1 = 1.61$ (DFVLR) or 1.616 (DDA). This is the trend suggested by Tweedt et al. (1988). Also, the loss coefficient values corresponding to $M_1 = 1.66$ were generally higher than those associated with the lower M_1 values, another trend suggested by Tweedt et al. (1988).

Inspection of Figs. 10 through 12 indicates that the DDA

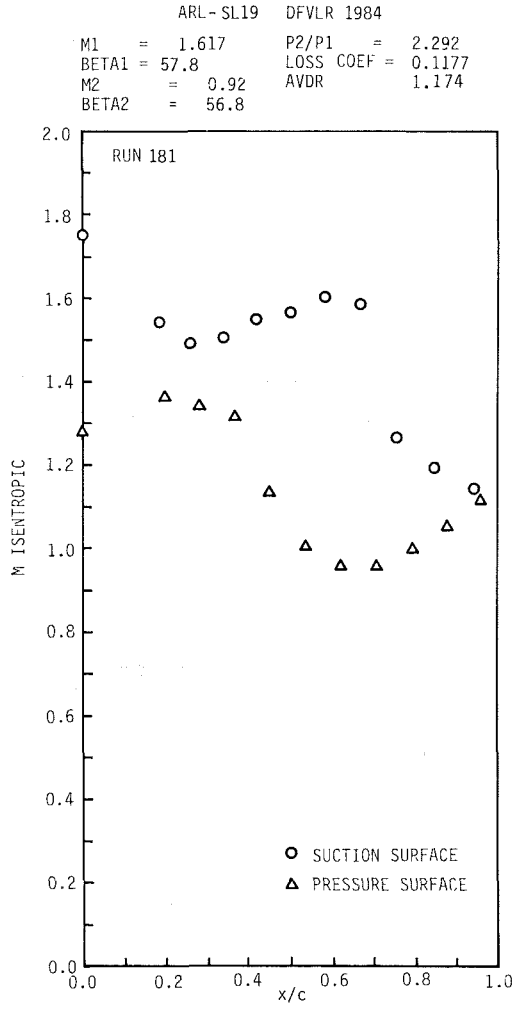

Fig. 7(*a*) Estimated surface M values based on static pressure tap data (DFVLR)

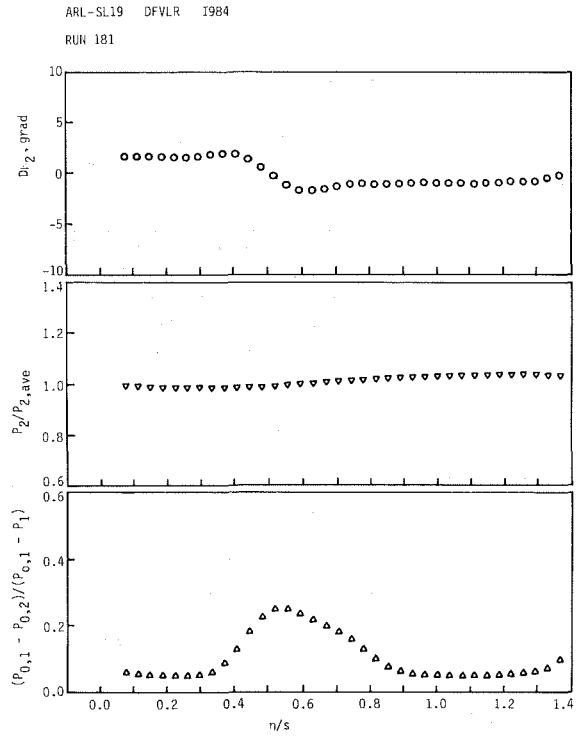

Fig. 7(*b*) Variation in tangential direction of downstream survey station measured quantities for typical DFVLR run

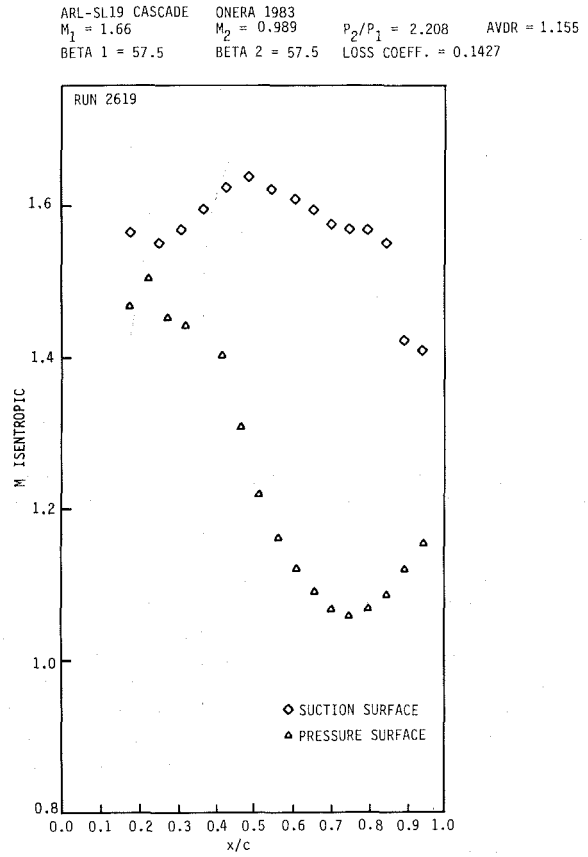

Fig. 8(a) Estimated surface M values based on static pressure tap data (ONERA)

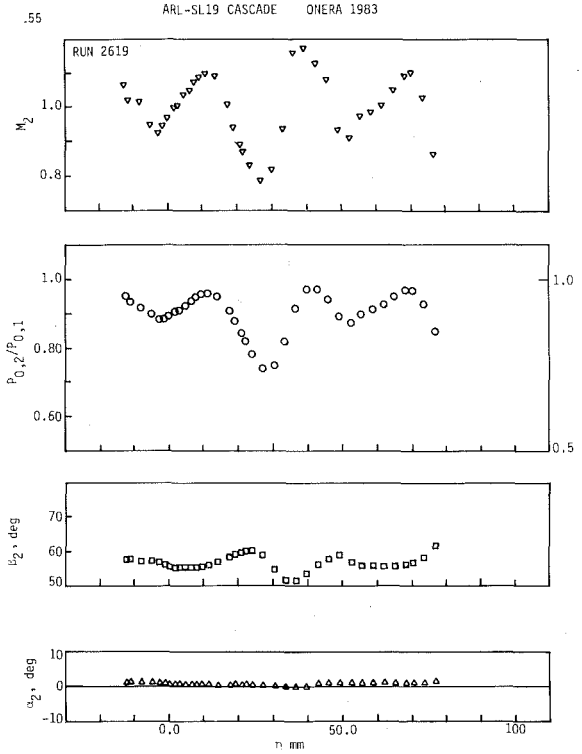

Fig. 8(b) Variation in tangential direction of downstream survey station measured quantities for typical ONERA run

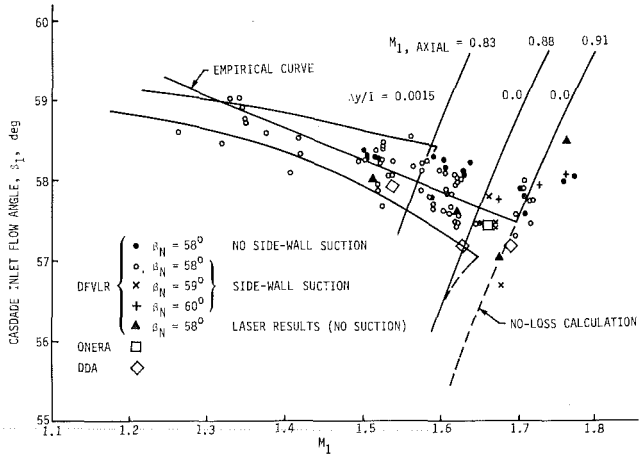

Fig. 9 Unique cascade inlet flow angle as estimated by DFVLR and measured by DFVLR, ONERA and DDA

data are in excellent agreement with the correlations of Tweedt et al. (1988). The ONERA data are generally consistent wtih the DFVLR correlations in their trends. All of the data suggest a nearly linear decrease of exit Mach number M_2 with increase in static pressure ratio P_2/P_1, with a small influence of axial velocity density ratio AVDR (see Fig. 10). The comparisons of Fig. 11 confirm the DFVLR observations (1) that the exit flow angle β_2 decreases with increase in axial velocity density ratio AVDR when the static pressure ratio P_2/P_1 is held constant; and (2) that the exit flow angle β_2 reaches a maximum value, in the vicinity of the sonic exit flow condition, when axial velocity density ratio AVDR is held constant and the static pressure ratio P_2/P_1 is varied.

Figure 12 shows that the DDA and ONERA data support the DFVLR proposal that loss coefficient $\bar{\omega}$ decreases with increase in axial velocity density ratio AVDR when the static pressure ratio P_2/P_1 is greater than about 1.8.

The differences between systems for control of AVDR and the results obtained prompt some questions about future test section development. The reported AVDR values are overall values and depend strongly on the downstream flow angle measured and used in computing axial velocity. Consideration should be given to the design of improved side-wall suction control systems.

Utilization of the Data in Testing Computation Methods. Genuinely useful computational approaches to the cascade flow problem in compressor cases must predict fluid turning and total pressure loss. Inviscid solution methods have limited value unless used in parallel with boundary layer codes in inviscid-viscous interation schemes (Calvert, 1983). The data generated in the combined DDA/DFVLR/ONERA SL19 cascade experiments will be of value in developing and testing inviscid-viscous methods because of the extensive ranges of Mach number and static pressure ratio covered.

Many of the Navier–Stokes solution codes developed to date for cascade flows are two-dimensional. That is, they do not allow stream-tube thickness variation through the blade passage. This restriction severely limits the usefulness of the codes in relation to current compressor design systems and trends. However, as AVDR accounting is introduced, the SL19 cascade data will again be quite useful.

Conclusions

1 This experimental program, combining the efforts of four turbomachinery research groups and using three supersonic cascade test facilities, produced data sets for a broad

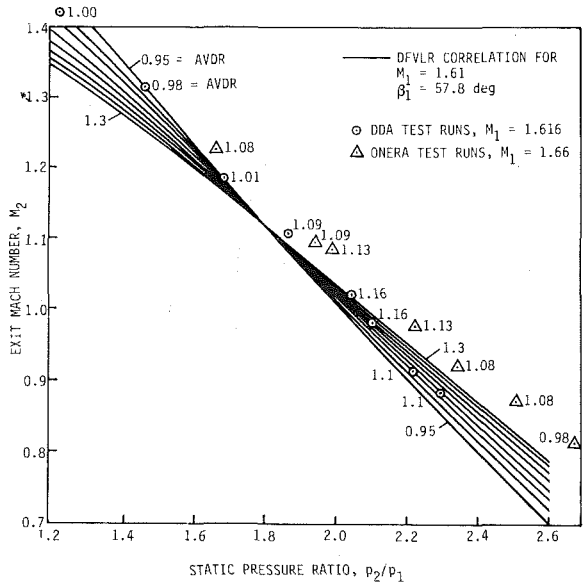

Fig. 10 Cascade exit region Mach number for ARL SL19 cascade experiments

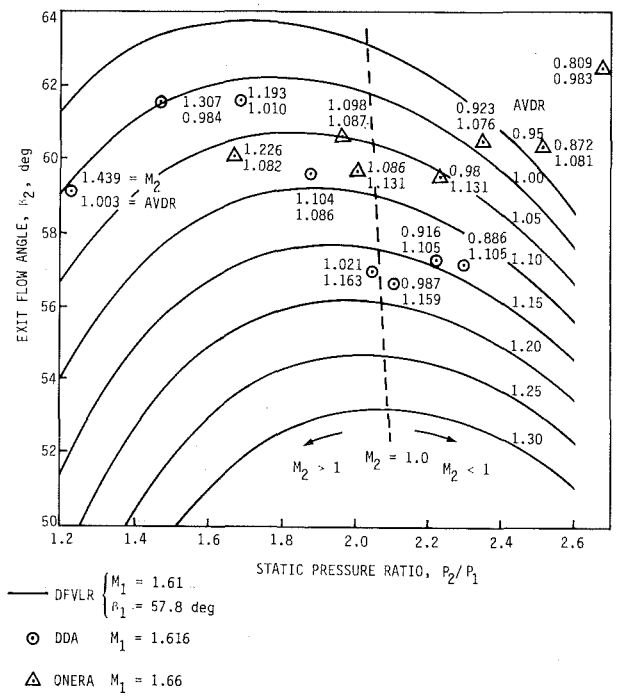

Fig. 11 Exit flow angle dependence on static pressure ratio and AVDR based on correlation of DFVLR data at M_1 = 1.61, β_1 = 57.8 deg and data for ONERA at M_1 = 1.66, DDA at M_1 = 1.616

range of operating points for the SL19 cascade configuration. The data are consistent and sufficiently documented for computation test case use.

2 Definition of leading edge region flow (unique incidence and Mach number just upstream of the cascade) deserves continued attention in terms of both experiments and analyses. These are important variables in compressor design systems.

3 Accurate determination of downsteam flow angles and velocities should be emphasized because of the reported performance sensitivity to these measured variables. Tangential surveys should be made at several downstream locations for a few cascade operating points.

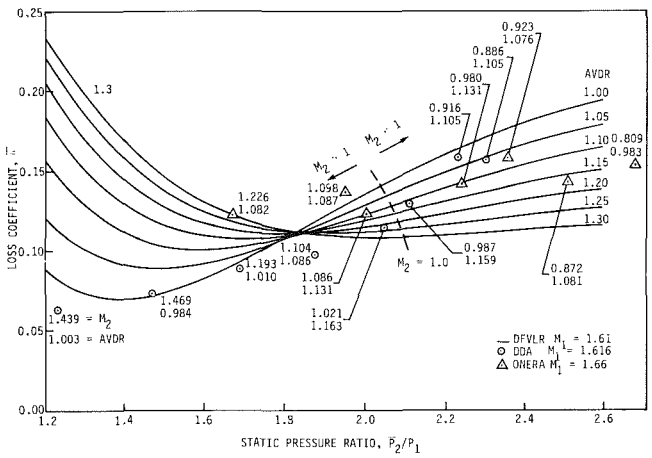

Fig. 12 Loss coefficient for ONERA and DDA experimental points compared with DFVLR correlation based on M1 = 1.61, β1 = 57.8 deg

4 The influence of AVDR distribution through the blade passage should be investigated experimentally.

5 Continued reliance on and development of the linear cascade as one of the key experimental facilities in turbomachinery research is justified. Programs such as the SL19 effort and the recent turbine cascade cooperative project (Kiock et al., 1986) should continue, with the objective of reducing misunderstandings in the reporting and use of test data.

Acknowledgments

The research effort summarized here was unquestionably greater than any of us expected in 1981. Throughout, there was excellent cooperation and exchange of ideas within and among all of the participating organizations and individuals. The initial ideas leading to the "AGARD/PEP test case" effort must be credited to John Dunham of the RAE. Art Wennerstrom suggested the SL19 cascade as a basis for a joint project. Jean Fabri and Gert Winterfeld supported the SL19 idea and worked hard to get the necessary approvals and financial backing within ONERA and DFVLR. The experiments were organized and carried out as shown below:

ONERA
Direction de l'Energetique
Georges Meauzé
Antoine Fourmaux

DFVLR
Institut für Antriebstechnik
Hans Starken
Heinz Schreiber
Dan Tweedt (collaborator from ISU)

Direction de l'Aerodynamique
J. Hoorelbeke
G. Losfeld
P. L. Mesthé
R. Gaillard

Ron York and Bob Holtman of Allison Gas Turbines, who were involved in the original DDA investigation of the ARL SL19 cascade, commented generously on the DDA results, and filled in gaps in the information available to ONERA and DFVLR.

The ISU work was partly supported by the USAF Air Force Office of Scientific Research through Contract F 49620-83-K-0023.

We are grateful for the help received from ISU Engineering Research Institute Office of Editorial Services personnel. Their expertise in preparing the manuscripts and illustrations is valued.

Table A1 SL19 design blade coordinates (in inches)

STATION	XS	YS	XP	YP
1	0.0	0.0	0.0	0.0
2	-0.000858	0.005087	0.004661	0.000780
3	0.017358	0.029973	0.024148	0.024799
4	0.035559	0.055383	0.043650	0.049341
5	0.053745	0.081301	0.063167	0.074391
6	0.071917	0.107713	0.082700	0.099966
7	0.090073	0.134618	0.102247	0.126048
8	0.108214	0.162017	0.121809	0.152610
9	0.126355	0.189879	0.141371	0.179649
10	0.144481	0.218190	0.160948	0.207168
11	0.162608	0.246950	0.180524	0.235120
12	0.180719	0.276113	0.200116	0.263491
13	0.198815	0.305681	0.219708	0.292266
14	0.216927	0.335607	0.239300	0.321414
15	0.235038	0.365877	0.258907	0.350907
16	0.253134	0.396462	0.278499	0.380713
17	0.271246	0.427330	0.298091	0.410789
18	0.289357	0.458423	0.317668	0.441119
19	0.307483	0.489740	0.337260	0.471644
20	0.325624	0.521222	0.356822	0.502333
21	0.343766	0.552823	0.376384	0.533156
22	0.361922	0.584529	0.395931	0.564085
23	0.380093	0.616295	0.415448	0.595058
24	0.398279	0.648091	0.434965	0.626076
25	0.416480	0.679901	0.454467	0.657094
26	0.434696	0.711682	0.473955	0.688097
27	0.452927	0.743433	0.493427	0.719085
28	0.471173	0.775139	0.512869	0.750013
29	0.489449	0.806755	0.532297	0.780867
30	0.507739	0.838297	0.551709	0.811661
31	0.526045	0.869734	0.571107	0.842365
32	0.544381	0.901081	0.590474	0.872979
33	0.562731	0.932308	0.609827	0.903503
34	0.581097	0.963431	0.629164	0.933938
35	0.599478	0.994449	0.648472	0.964298
36	0.617888	1.025346	0.667780	0.994554
37	0.636313	1.056154	0.687058	1.024748
38	0.654754	1.086859	0.706306	1.054853
39	0.673224	1.117458	0.725539	1.084885
40	0.691709	1.147967	0.744757	1.114856
41	0.710224	1.178388	0.763945	1.144737
42	0.728754	1.208702	0.783118	1.174559
43	0.747299	1.238913	0.802261	1.204306
44	0.765874	1.269033	0.821390	1.233977
45	0.784479	1.299049	0.840488	1.263560
46	0.803099	1.328961	0.859571	1.293082
47	0.821749	1.358768	0.878625	1.322515
48	0.840428	1.388470	0.897649	1.351873
49	0.859123	1.418067	0.916657	1.381142
50	0.877847	1.447530	0.935636	1.410320
51	0.896602	1.476888	0.954585	1.439408
52	0.915386	1.506110	0.973504	1.468392
53	0.934185	1.535199	0.992393	1.497272
54	0.953014	1.564167	1.011266	1.526061
55	0.971873	1.593002	1.030110	1.554746
56	0.990763	1.621702	1.048924	1.583326
57	1.009665	1.650253	1.067723	1.611816
58	1.028615	1.678683	1.086478	1.640203
59	1.047608	1.706965	1.105187	1.668514
60	1.066647	1.735096	1.123853	1.696751
61	1.085731	1.763079	1.142457	1.724911
62	1.104889	1.790911	1.161017	1.753013
63	1.124106	1.818593	1.179487	1.781055
64	1.143399	1.846128	1.197913	1.809068
65	1.162767	1.873526	1.216233	1.837049
66	1.182209	1.900761	1.234494	1.865016
67	1.201756	1.927876	1.252650	1.892968
68	1.221394	1.954824	1.270717	1.920935
69	1.241135	1.981655	1.288679	1.948903
70	1.260981	2.008322	1.306520	1.976885
71	1.280947	2.034868	1.324258	2.004911
72	1.301032	2.061264	1.341876	2.032969
73	1.321238	2.087526	1.359374	2.061070
74	1.341592	2.113639	1.376722	2.089216
75	1.362082	2.139617	1.393937	2.117588
76	1.382705	2.165445	1.411016	2.145719
77	1.403493	2.191140	1.427931	2.174074
78	1.424431	2.216669	1.444696	2.202506
79	1.445534	2.242048	1.461297	2.231026
80	1.466801	2.267280	1.477718	2.259636
81	1.488247	2.292359	1.493976	2.288336
82	1.491111	2.290347	1.491111	2.290347

APPENDIX

The coordinates listed in Table A1 are the design values for the DDA/USAF SL19 cascade as reported by Fleeter et al. (1975). The numerical values are in inches and refer to Fig. 1.

References

Calvert, W. J., 1983, "Application of an Inviscid-Viscous Interaction Method to Transonic Compressor Cascades," in: *Viscous Effects in Turbomachines*, AGARD-CP-351, Paper No. 2.

Chauvin, J., Sieverding, C., and Griepentrog, H., 1970, "Flow in Cascades With a Transonic Regime," in: *Flow Research on Blading*, Elsevier, Amsterdam, pp. 151–196.

Fleeter, S., Holtman, R. L., McClure, R. B., and Sinnet, G. T., 1975, "Experimental Investigation of a Supersonic Compressor Cascade," USAF Air Force Systems Command ARL 75-0208.

Fourmaux, A., 1984, "Resultats d'Essais à S5 CH d'Une Grille d'Aubes ARL (Aerospace Research Laboratory)," ONERA Technical Report No. 5/3568 EN, 13 Mars 1984 (also available as NASA TM-77510).

Fourmaux, A., Gaillard, R., Losfeld, G., and Meauzé, G., 1988, "Test Results on the ARL 19 Supersonic Blade Cascade," ASME JOURNAL OF TURBOMACHINERY, Vol. 110, this issue.

Gaillard, R., 1983, "Calibration and Utilization of ONERA 'Five-Hole' Probes," in: *Proceedings of Seventh Symposium on Measuring Techniques for Transonic and Supersonic Flow in Cascades and Turbomachines*, RWTH, Aachen.

Kiock, R., Lehthaus, F., Baines, N. C., and Sieverding, C. H., 1986, "The Transonic Flow Through a Plane Turbine Cascade as Measured in Four European Wind Tunnels," ASME *Journal of Engineering for Gas Turbines and Power*, Vol. 108, pp. 277–284.

Lichtfuss, H. J., and Starken, H., 1974, "Supersonic Cascade Flow," in: *Progress in Aerospace Science*, Pergamon Press, Oxford, Vol. 15, pp. 27–149.

NATO/AGARD Propulsion and Energetics Panel, 1976, "Through-Flow Calculations in Axial Turbomachinery," AGARD-CP-195.

NATO/AGARD Propulsion and Energetics Panel Working Group 12, 1981, "Through-Flow Calculations in Axial Turbomachines," AGARD-AR-175.

NATO/AGARD Propulsion and Energetics Panel, 1985, "3-D Computation Techniques Applied to Internal Flows in Propulsion Systems," AGARD-LS-140.

NATO/AGARD Propulsion and Energetics Panel, 1987, "Transonic and Supersonic Phenomena in Turbomachines," AGARD-CP-401.

Schimming, P., and Starken, H., 1975, "Data Reduction of Two-Dimensional Cascade Measurements," in: *Modern Methods of Testing Rotating Components of Turbomachines* (*Instrumentation*), AGARD-AG-207.

Tweedt, D. L., Schreiber, H. A., and Starken, H., 1988, "Experimental Investigation of the Performance of a Supersonic Compressor Cascade ARL-SL19 at DFVLR Cologne," ASME JOURNAL OF TURBOMACHINERY, Vol. 110, this issue.

Wennerstrom, A. J., 1984, "Experimental Study of a High-Throughflow Transonic Axial Compressor Stage," ASME *Journal of Engineering for Gas Turbines and Power*, Vol. 106, pp. 552–560.

A. Fourmaux

R. Gaillard

G. Losfeld

G. Meauzé

Office National d'Etudes et de Recherches Aérospatiales, BP 72-92322 Châtillon Cedex, France

Test Results on the ARL 19 Supersonic Blade Cascade

This paper presents the ONERA contribution in a joint experimental program on the aerodynamics of supersonic airfoil cascades. The first part deals with the specific ONERA way of running cascade tests: description of the test facility, the test model, the instrumentation, and data reduction. Then, after a brief theoretical analysis of the ARL 19 cascade, some experimental results are presented and discussed.

1 Introduction

A cooperative program of research involving at the beginning ISU,[1] DFVLR,[2] and ONERA has been in progress for several years. This program includes parallel experimental investigations at DFVLR and ONERA, earlier experiments at the Detroit Diesel Allison (DDA) Division (now Allison Gas Turbine Operations) of General Motors Corporation, and analysis by ISU personnel (Fleeter et al., 1975).

The center of this program is the ARL 19 cascade, which was designed, fabricated, and tested by DDA. The DDA objective has been to obtain cascadetype aerodynamic performance data, and the objective of the cooperative program has been to obtain other data from tests made in various wind tunnels.

The aim of this paper is to present the ONERA contribution in the joint program. Therefore, a significant part of the paper is dedicated to the specific ONERA way of running supersonic cascaded tests. Some experimental results are shown as typical examples.

In the same ASME session, the DFVLR contribution is presented by Tweedt et al. (1988), and Serovy and Okiishi (1988).

2 Test Facility

2.1 Wind Tunnel—General Features. The ONERA S5Ch facility is a versatile closed-loop transonic and supersonic wind tunnel (Fig. 1). A 1400 kW electrical power unit drives a 12-stage axial compressor. The main features of this facility are as follows:

- maximum pressure ratio 5.6
- total pressure 0.2 bar $\leq P_{to} \leq$ 1.0 bar
- total temperature $\simeq$ 310 K

A series of adjustable nozzle blocks is available for setting test section Mach number from 0.4 to 3.0.

The usual hygrometric rate is less than 1 g of water per kg of air, and can be reduced to 0.1 g/kg by an air drying system.

Actually there are two bypassed test sections. Then using one or the other test section makes it possible to study various flow configurations.

2.2 Cascade Test Section and Test Model. When the S5Ch facility is utilized in cascade experiments, a special cascade test section is installed in the main loop (Fig. 2). This test section reduces the flow passage dimension to a cascade airfoil length (span) of 100 mm.

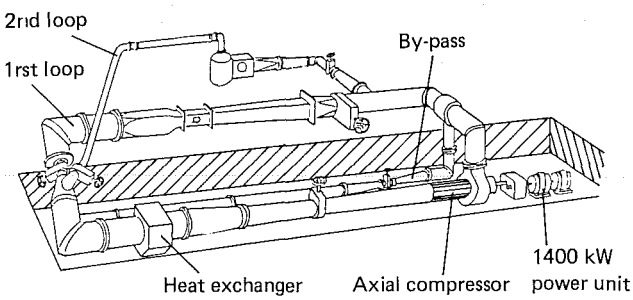

Fig. 1 S5Ch wind tunnel

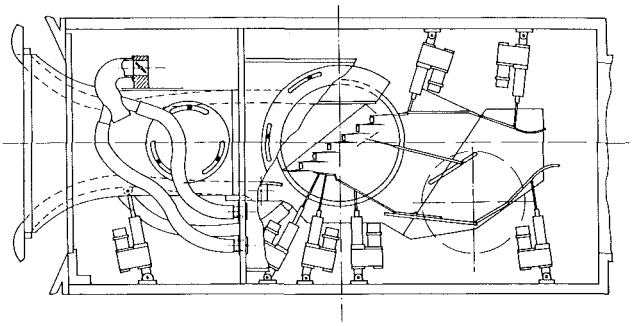

Fig. 2 Cascade test section

[1]ISU: Iowa State University.

[2]DFVLR: Deutsche Forchungs- und Versuchsanstalt für Luft und Raumfahrt.

Contributed by the International Gas Turbine Institute and presented at the 33rd International Gas Turbine and Aeroengine Congress and Exhibition, Amsterdam, The Netherlands, June 5–9, 1988. Manuscript received by the International Gas Turbine Institute January 25, 1988. Paper No. 88-GT-202.

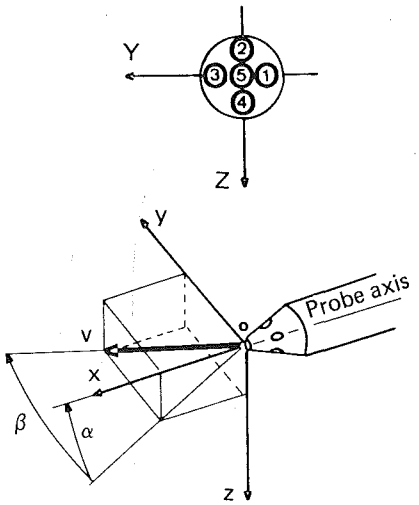

Fig. 3

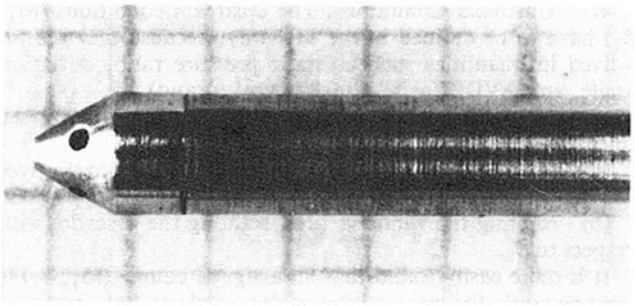

Fig. 4

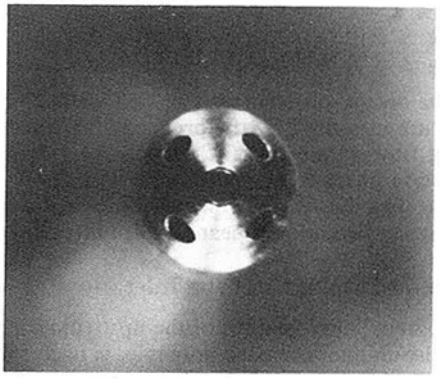

Fig. 5

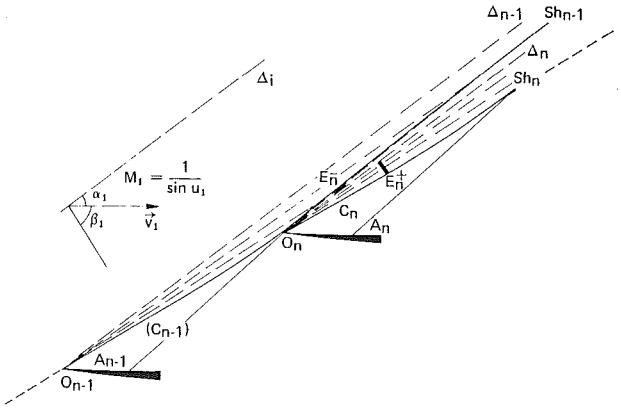

Fig. 6 Inlet flow pattern; infinite cascade

Upstream Mach Number. Three nozzles (nominal Mach numbers 1.3, 1.5, 1.7) are available. Intermediate Mach numbers are obtained by rotating the lower block of the nozzle (i.e., by reducing or increasing the sonic throat slightly). Thus the operating range is continuous from M = 1.2 to M = 1.75. The nozzle blocks are extended up to the upstream cascade front by plates that are specially designed to avoid any disturbance or blockage in the inlet flow.

Cascade. The cascade airfoils are installed between two circular ALTUGLAS windows (diameter: 400 mm), in which slots establish the cascade geometry. The windows can rotate in order to adjust the incidence angle of the flow. The number of airfoils mainly depends on the pitch chord ratio; for the ARL 19 tests, seven airfoils were used:

- Chord 83.41 mm
- Axial chord 45.44 mm
- Pitch (blade spacing) 54.28 mm

In each of the six blade-to-blade passages, and in both side walls, suction ports having an approximately rectangular shape are cut to permit controlled removal of sidewall boundary layer fluid.

Blades (numbered 1 to 7 from the section bottom to top) 1 and 7 serve as cascade endwalls with blade 1 generating an oblique wave (shock or expansion), which establishes the entrance condition for the rest of the blades (see section 4.1).

The blade-to-blade passages (numbered 1 to 6 from the bottom to the top) are similar geometrically, with passage 4 serving as the principal measurement location.

Downstream Part. A series of tailboards, beginning at the trailing edges of blades 1 and 7, are set to adjust and to control downstream periodicity; these tailboards lead to a downstream throat to adjust the cascade pressure ratio.

2.3 Instrumentation and Data Reduction System

2.3.1 Upstream and Downstream Side-Wall Instrumentation. About 60 static pressure taps (0.6 mm diameter), located on one side wall of the test section, are used to check the upstream and downstream periodicity and to estimate the cascade pressure ratio.

Measured pressures are transmitted to "Statham" transducers through a Scanivalve system. Then, data processing is monitored in real time by a dedicated computer in the test facility control room.

2.3.2 Blade Surface Instrumentation. Surface static pressure measurements are made on the suction surface of blade 4 (15 taps) and on the pressure surface of blade 5 (17 taps). Taps are perpendicular to the profile surfaces and are 0.4 mm in diameter. These measurements are processed in the same way as side-wall measurements.

2.3.3 Probe Measurements. For downstream surveys, the local flow parameters (Mach number, total pressure, pitch and yaw angles) are deduced from measurements made with a single five-hole probe.

This probe is shown on Figs. 3–5. It is a conical miniaturized probe (external diameter: 1.5 mm). Four taps (0.3 mm diameter) are perpendicular to the cone surface, and the fifth one is located at the nose.

This kind of probe obviously needs a careful calibration. During the calibration procedure (in the S5Ch wind tunnel), four parameters are assigned: Mach number, α and β angles, total pressure, and give five probe pressures (p_1 to p_5). Then, reduced coefficients are computed and stored to build a calibration matrix (Gaillard, 1983).

The operating range of such a probe is typically:

$0 \leq M \leq 3$
$-40 \text{ deg} \leq \alpha \leq +40 \text{ deg}$
$-40 \text{ deg} \leq \beta \leq +40 \text{ deg}$

When the inverse problem occurs, i.e., when five pressures (p_1 to p_5) are measured by the probe during a test, the corresponding flow parameters (M, angles, p_t) are found using the calibration matrix.

Note that the data reduction method is iterative in order to account for significant nonlinear coupled effects.

3 Theoretical Analysis of the Inlet Flow

A quick preliminary analysis of the upstream cascade flow, based on the unique incidence principle, is useful for a good understanding of the experimental results.

First consider an infinite cascade (Fig. 6) with sharp leading edges.

Let $O_{n-1}\, A_{n-1}$ be the concave fore part of the suction surface that has an influence on the upstream flow pattern. This part produces compression waves (C_{n-1}), which focus in a shock (Sh_{n-1}). The compression passes just in front of the upper leading edge where there is an expansion (E_n).

This expansion E_n can be split into two parts E_n^- and E_n^+ separated by the characteristic line Δ_n; the characteristics of E_n^- meet the shock Sh_{n-1}, those of E_n^+ the shock Sh_n.

Although these compression and expansion waves cancel each other, a uniform flow can be imagined only in the upstream infinite. Nevertheless, the cancellation is almost quite obtained when four or five expansion-compression couples are crossed in the upstream direction. Then the characteristics become the Mach lines of the uniform upstream flow and give (M_1, β_1).

A semi-infinite cascade does not have an effect on the whole upstream domain (Fig. 7). If the upstream flow (M_0, β_0) is not adapted to the cascade (i.e., if the couple M_0, β_0 does not meet the unique incidence principle), an expansion wave or an oblique shock appears at the leading edge of the first blade, in order to give a correct couple (M_1, β_1).

But even if the upstream flow is well adapted to the cascade, exact periodicity theoretically occurs at the infinite, and the following points must be emphasized.

- A blade has an influence only on the three or four upper passages,
- In the blade-to-blade passages, periodicity is obtained immediately, if the entropy drop due to the shocks is neglected.

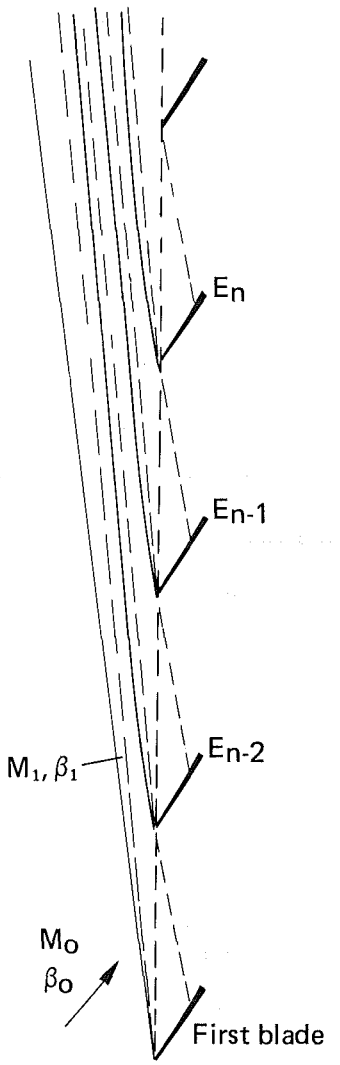

Fig. 7 Inlet flow pattern; semi-infinite cascade

4 Test Results

4.1 Upstream Conditions. The upstream conditions (M_1, β_1) have to be defined in the best way, because they are involved in quantities such as static pressure ratio, deviation angle, and AVDR (axial velocity density ratio).

As seen in section 2.2, two degrees of freedom exist for the inlet flow adjustment:

(*a*) rotating the lower nozzle block (then the nozzle gives M_0, β_0),

(*b*) rotating the windows (i.e., rotating the cascade) with respect to β_0.

It is quite easily found that an assigned couple (M_1, β_1) is obtained only for one position of the nozzle and one position of the cascade when the following criterion is met: The nozzle flow must be adapted to the cascade unique incidence. Under this condition, the disturbance coming from the first leading edge—expansion or shock—is as small as possible. Hence, at the beginning of the tests, this point is carefully checked, using the five-hole probe through the fourth blade-to-blade passage to survey the upstream flow over an axis almost parallel to the inlet flow angle β_0. Then, the probe crosses the compression and expansion waves given by the lower blades and the disturbance coming from the first leading edge. Moreover, the first part of the experimental static pressure distribution on the suction surface, where three dimensional and viscous effects are very weak, is compared to a theoretical pressure distribution given by a two dimensional Euler solver.

4.2 Overall Quantities Deduced From Detailed Wake Measurements. From the downstream survey measurements, mean quantities are computed assuming that the actual nonuniform flow and the mixed uniform mean flow have:

(*a*) the same mass flow,

(*b*) the same dynalpy (axial and tangential components).

Then one can easily find:

$\pi_s = p_2/p_1$	static pressure ratio
$\eta = p_{t2}/p_{t1}$	total pressure ratio
$\Delta\beta = \beta_2 - \beta_1$	turning angle
AVDR	axial velocity density ratio

Table 1

	π_s	η	$\Delta\beta$ (°)	AVDR	M_2
1	2.67	0.882	4.9	0.983	0.809
2	2.51	0.888	2.7	1.081	0.872
3	2.35	0.877	2.8	1.076	0.923
4	1.95	0.893	3.0	1.087	1.098
5	1.67	0.903	2.5	1.082	1.226

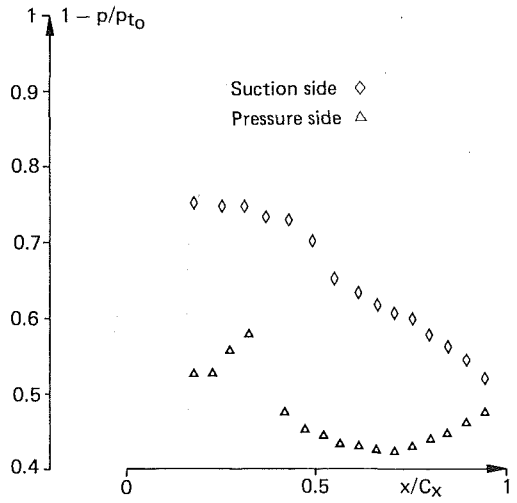

Fig. 8-1

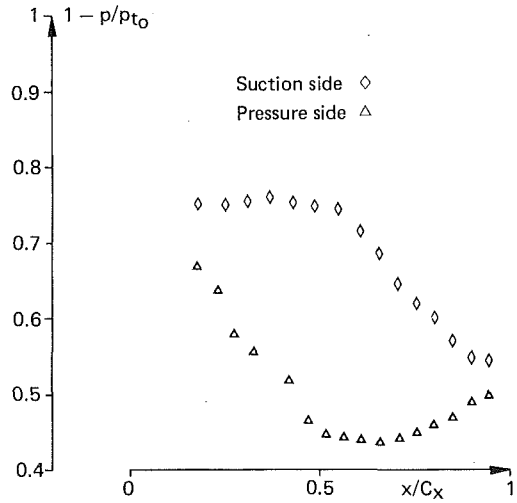

Fig. 8-2

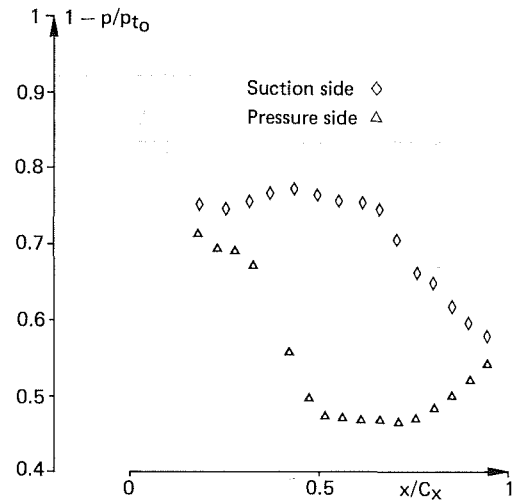

Fig. 8-3

Controlling the removal of boundary layer fluid and adjusting the downstream pressure are two independent parameters. Under these conditions, the ARL 19 cascade was tested for various values of π_s (static pressure ratio) and AVDR. Some of these tests are presented now.

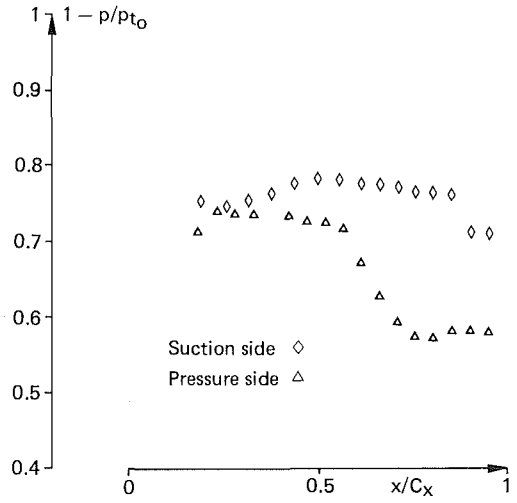

Fig. 8-4

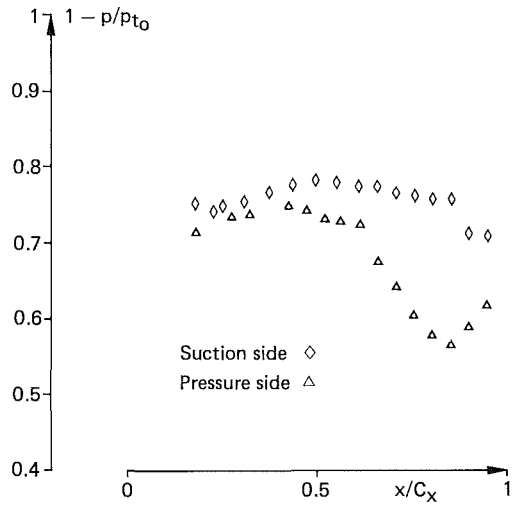

Fig. 8-5

4.3 Presentation of Experimental Results. Table 1 summarizes the results of five test cases, which have AVDR values near 1. For these tests, the upstream conditions are $M_1 = 1.66$ and $\beta_1 = 57.5$ deg.

Static pressure distributions are displayed on Fig. 8-1 to 8-5. The pressure distribution data are given on Fig. 9-1 to 9-5.

p = local static pressure
p_{t_0} = inlet total pressure (we assume that $p_{t_1} = p_{t_0}$, i.e., there are no losses through the disturbance coming from the first leading edge)
x = axial component
C_x = axial chord
M_{ise} = isentropic Mach number (computed from p/p_{t_0}).

For the highest pressure ratios (tests 1, 2, 3), the main shock is located in the blade-to-blade passage. Its impingement on the suction surface can be seen on Figs. 8-1, 8-2, and 8-3. There are strong shock–boundary-layer interactions, and the static pressure evolutions are rather smoothed. On the contrary, for the lower values of π_s (Figs. 8-4 and 8-5), the shock is attached at the trailing edge on the suction surface. Then it seems that two operating modes exist.

This remark is confirmed by detailed wake measurements (Fig. 10) where Z_G is the tangential component (positive from the bottom to the top). For the first cases (1, 2, 3), for example, the total pressure ratio evolution is smoother than for the two last cases. This is due to a large separation on both airfoil

Pressure side

Tap n°	x/C_x	p/p_{t_o}	$1 - p/p_{t_o}$	M_{ise}
1	0.180	0.477	0.523	1.086
2	0.228	0.477	0.523	1.086
3	0.275	0.444	0.556	1.142
4	0.324	0.423	0.577	1.181
5	0.372	0.419	0.581	1.187
6	0.420	0.525	0.475	1.005
7	0.468	0.550	0.450	0.965
8	0.516	0.558	0.442	0.952
9	0.563	0.568	0.432	0.937
10	0.611	0.573	0.427	0.928
11	0.659	0.577	0.423	0.923
12	0.707	0.577	0.423	0.922
13	0.755	0.572	0.428	0.929
14	0.803	0.563	0.437	0.945
15	0.851	0.554	0.446	0.958

Suction side

Tap n°	x/C_x	p/p_{t_o}	$1 - p/p_{t_o}$	M_{ise}
1	0.180	0.250	0.750	1.559
2	0.252	0.254	0.746	1.548
3	0.312	0.253	0.747	1.551
4	0.372	0.268	0.732	1.512
5	0.432	0.272	0.728	1.500
6	0.492	0.301	0.699	1.431
7	0.551	0.350	0.650	1.323
8	0.611	0.368	0.632	1.285
9	0.659	0.383	0.617	1.255
10	0.707	0.395	0.605	1.232
11	0.755	0.401	0.599	1.221
12	0.803	0.425	0.575	1.178
13	0.851	0.441	0.559	1.149
14	0.899	0.455	0.545	1.122
15	0.947	0.481	0.519	1.079

Fig. 9-1

Suction side

Tap n°	x/C_x	p/p_{t_o}	$1 - p/p_{t_o}$	M_{ise}
1	0.180	0.250	0.750	1.559
2	0.252	0.254	0.746	1.549
3	0.312	0.245	0.755	1.571
4	0.372	0.241	0.759	1.583
5	0.432	0.247	0.753	1.568
6	0.492	0.253	0.747	1.551
7	0.551	0.258	0.742	1.536
8	0.611	0.287	0.713	1.463
9	0.659	0.318	0.682	1.391
10	0.707	0.356	0.644	1.311
11	0.755	0.381	0.619	1.260
12	0.803	0.400	0.600	1.223
13	0.851	0.430	0.570	1.168
14	0.899	0.453	0.547	1.127
15	0.947	0.456	0.544	1.121

Pressure side

Tap n°	x/C_x	p/p_{t_o}	$1 - p/p_{t_o}$	M_{ise}
1	0.180	0.336	0.664	1.352
2	0.228	0.367	0.633	1.288
3	0.275	0.422	0.578	1.181
4	0.324	0.446	0.554	1.138
5	0.372	0.412	0.588	1.201
6	0.420	0.485	0.515	1.071
7	0.468	0.537	0.463	0.986
8	0.516	0.555	0.445	0.957
9	0.563	0.561	0.439	0.948
10	0.611	0.564	0.436	0.942
11	0.659	0.566	0.434	0.939
12	0.707	0.560	0.440	0.949
13	0.755	0.552	0.448	0.961
14	0.803	0.542	0.458	0.977
15	0.851	0.532	0.468	0.993

Fig. 9-2

Suction side

Tap n°	x/C_x	p/p_{t_o}	$1 - p/p_{t_o}$	M_{ise}
1	0.180	0.249	0.751	1.561
2	0.252	0.252	0.748	1.553
3	0.312	0.245	0.755	1.574
4	0.372	0.234	0.766	1.604
5	0.432	0.227	0.773	1.625
6	0.492	0.237	0.763	1.595
7	0.551	0.244	0.756	1.574
8	0.611	0.245	0.755	1.573
9	0.659	0.255	0.745	1.545
10	0.707	0.296	0.704	1.442
11	0.755	0.340	0.660	1.343
12	0.803	0.351	0.649	1.320
13	0.851	0.382	0.618	1.259
14	0.899	0.406	0.594	1.212
15	0.947	0.420	0.580	1.186

Pressure side

Tap n°	x/C_x	p/p_{t_o}	$1 - p/p_{t_o}$	M_{ise}
1	0.180	0.290	0.710	1.458
2	0.228	0.308	0.692	1.414
3	0.275	0.311	0.689	1.406
4	0.324	0.330	0.670	1.365
5	0.372	0.391	0.609	1.240
6	0.420	0.446	0.554	1.139
7	0.468	0.504	0.496	1.039
8	0.516	0.528	0.472	1.001
9	0.563	0.533	0.467	0.993
10	0.611	0.534	0.466	0.991
11	0.659	0.536	0.464	0.988
12	0.707	0.536	0.464	0.988
13	0.755	0.529	0.471	0.998
14	0.803	0.516	0.484	1.021
15	0.851	0.501	0.499	1.046

Fig. 9-3

Suction side

Tap n°	x/C_x	p/p_{t_o}	$1 - p/p_{t_o}$	M_{ise}
1	0.180	0.246	0.754	1.571
2	0.252	0.252	0.748	1.553
3	0.312	0.246	0.574	1.571
4	0.372	0.233	0.767	1.606
5	0.432	0.224	0.776	1.634
6	0.492	0.216	0.784	1.657
7	0.551	0.219	0.781	1.647
8	0.611	0.222	0.778	1.639
9	0.659	0.224	0.776	1.632
10	0.707	0.230	0.770	1.614
11	0.755	0.236	0.764	1.599
12	0.803	0.237	0.763	1.596
13	0.851	0.237	0.763	1.595
14	0.899	0.289	0.711	1.459
15	0.947	0.290	0.710	1.456

Pressure side

Tap n°	x/C_x	p/p_{t_o}	$1 - p/p_{t_o}$	M_{ise}
1	0.180	0.289	0.711	1.458
2	0.228	0.259	0.741	1.534
3	0.275	0.263	0.737	1.524
4	0.324	0.264	0.736	1.522
5	0.372	0.258	0.742	1.537
6	0.420	0.266	0.734	1.517
7	0.468	0.275	0.725	1.494
8	0.516	0.276	0.724	1.492
9	0.563	0.284	0.716	1.472
10	0.611	0.330	0.670	1.366
11	0.659	0.375	0.625	1.272
12	0.707	0.409	0.591	1.206
13	0.755	0.428	0.572	1.172
14	0.803	0.427	0.573	1.173
15	0.851	0.420	0.580	1.186

Fig. 9-4

Suction side

Tap n°	x/Cx	p/pto	1 − p/pto	Mise
1	0.180	0.248	0.752	1.564
2	0.252	0.252	0.748	1.554
3	0.312	0.245	0.755	1.572
4	0.372	0.233	0.767	1.605
5	0.432	0.224	0.776	1.633
6	0.492	0.218	0.782	1.652
7	0.551	0.221	0.779	1.643
8	0.611	0.225	0.775	1.630
9	0.659	0.228	0.772	1.620
10	0.707	0.235	0.765	1.600
11	0.755	0.239	0.761	1.590
12	0.803	0.240	0.760	1.586
13	0.851	0.240	0.760	1.585
14	0.899	0.287	0.713	1.463
15	0.947	0.292	0.708	1.452

Pressure side

Tap n°	x/Cx	p/pto	1 − p/pto	Mise
1	0.180	0.286	0.714	1.467
2	0.228	0.259	0.741	1.535
3	0.275	0.265	0.735	1.519
4	0.324	0.265	0.735	1.520
5	0.372	0.254	0.746	1.547
6	0.420	0.253	0.747	1.551
7	0.468	0.259	0.741	1.534
8	0.516	0.270	0.730	1.507
9	0.563	0.273	0.727	1.499
10	0.611	0.278	0.722	1.486
11	0.659	0.325	0.675	1.375
12	0.707	0.359	0.641	1.304
13	0.755	0.398	0.602	1.227
14	0.803	0.423	0.577	1.180
15	0.851	0.436	0.564	1.156

Fig. 9-5

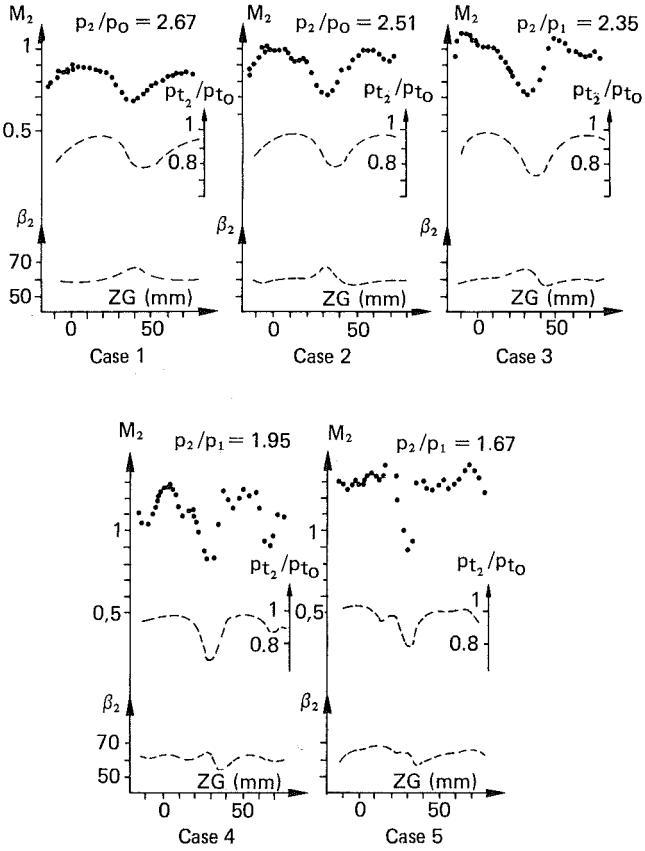

Fig. 10 Wake measurements

surfaces. Note also that the first group corresponds to a subsonic mean flow whereas the outlet Mach number of tests 4 and 5 is supersonic.

5 Conclusion

This experimental study has been conducted with a very good cooperation between ISU, DFVLR, and ONERA.

It allowed fruitful exchanges on the difficult problem of supersonic blade cascade measurements.

Tests have been done with great care, in different cascade wind tunnels, in order to compare experimental data and theoretical results. Their goal was to validate the computational methods.

Nevertheless the flow configuration analyzed experimentally on the ARL 19 cascade is a very difficult case and some remarks should be made:

- Due to the suction side geometry ("precompression" blade) and to the high value of the axial velocity, the inlet flow is not uniform even far upstream of the cascade. Thus, the conditions at the upstream infinity of the cascade are difficult to determine accurately.
- Since the Mach number reaches particularly high values in the cascade, very strong shockwave-boundary-layer interactions occur.
- The blade-to-blade channel presents a slightly convergent shape at the entrance, which can lead to unsteady regimes for some values of the back pressure.

A first attempt was made to compare the test results with a Navier–Stokes computation performed at ONERA. It displayed some problems that still remain to be solved, such as: the effect of a leading-edge detached shock wave on the initial boundary-layer profile, unsteadiness of the shock–boundary-layer interaction, transition of the boundary layer at the beginning of the interaction, and evolution of the AVDR through the blade-to-blade channel.

Thus, this very difficult case will be very useful for the validation of future sophisticated computational methods taking into account the abovementioned problems.

References

Fleeter, S., Holtman, R. L., McClure, R. B., and Sinnet, G. T., 1975, "Experimental Investigation of a Supersonic Compressor Cascade. U.S. Air Force Systems Command," Aerospace Research Laboratories, ARL TR 75-0208.

Gaillard, R., 1983, "Etalonnage et Utilisation de Sondes «Cinq Trous» ONERA," presented at Seventh Symposium on Measuring Techniques for Transonic and Supersonic Flow in Cascades and Turbomachines, Aachen, Federal Republic of Germany.

Serovy, G. K., and Okiishi, T. H., 1988, "Performance of a Compressor Cascade Configuration With Supersonic Entrance Flow—A Review and Comparison of Experiments in Three Installations," ASME Journal of Turbomachinery, Vol. 110, this issue.

Tweedt, D. L., Schreiber, H. A., and Starken, H., 1988, "Experimental Investigation of the Performance of a Supersonic Compressor Cascade," ASME Journal of Turbomachinery, Vol. 110, this issue.

Experimental Investigation of the Performance of a Supersonic Compressor Cascade

D. L. Tweedt
Turbomachinery Technology Branch,
Propulsion Systems Division,
NASA Lewis Research Center,
Cleveland, OH 44135

H. A. Schreiber

H. Starken
Institut fur Antriebstechnik,
DFVLR,
5000 Koln 90,
Federal Republic of Germany

Results are presented from an experimental investigation of a linear, supersonic compressor cascade tested in the supersonic cascade wind tunnel facility at the DFVLR in Cologne, Federal Republic of Germany. The cascade was derived from the near-tip section of a high-throughflow axial flow compressor rotor and has a design relative inlet Mach number of 1.61. Test data were obtained over the range of inlet Mach numbers from 1.30 to 1.17. Side-wall boundary layer suction was used to reduce secondary flow effects within the blade passages and to control the axial-velocity-density ratio (AVDR). Flow velocity measurements showing the wave pattern in the entrance region were obtained with a laser anemometer. The unique-incidence relationship for this cascade, relating the supersonic inlet Mach number to the inlet flow direction, is discussed. The influence of static pressure ratio and AVDR on the blade performance is described, and an empirical correlation is used to show the influence of these (independent) parameters for fixed inlet conditions on the exit flow direction and the total-pressure losses.

Introduction

The development of high-speed fans and compressors operating with supersonic relative inlet Mach numbers requires knowledge of the rotor blade performance and the flow behavior particular to these operating conditions. The linear cascade can be a useful tool for obtaining some of this information. Although the cascade model has limitations, it can nevertheless provide considerable insight into much of the relevant flow physics over a wide range of operating conditions with less time and expense than would be required to obtain similar information from an actual rotor. This form of testing allows relatively simple, but detailed flow measurement, quickly providing basic information on blade loading, losses, and flow turning. Furthermore, when the important aerodynamic boundary conditions are adequately known or controlled, the experimental cascade results are particularly well suited for the assessment and comparison of computational methods.

Results from an experimental investigation of a linear, stationary, supersonic compressor cascade are discussed in this paper. The cascade, designated here as ARL-SL19, was tested in the supersonic cascade wind tunnel facility at the DFVLR in Cologne. The cascade design originates from the Detroit Diesel Allison (DDA) Division of the General Motors Corp., which was working in the early 1970's under sponsorship of the Fluid Mechanics Research Laboratory of the Aerospace Research Laboratories (ARL) in Ohio. At DDA the cascade was designed, fabricated and tested as reported in (Fleeter, 1975). Considerable interest in this cascade has existed due to the excellent performance data obtained from the DDA cascade tests, as well as from tests conducted on the compressor stage from which the cascade was derived.

The DDA and DFVLR versions of the cascade blading are geometrically similar, but there were significant differences in the testing arrangement. These differences include the number of cascade blades, the blade aspect ratio, the sidewall boundary-layer suction system, the downstram tailboard and throttle mechanism, and the measurement instrumentation.

Cascade Blade Design

The ARL-SL19 supersonic compressor cascade has a design inlet Mach number of 1.612, with a subsonic axial flow component. The design static pressure ratio and axial-velocity-density ratio (AVDR) are 2.15 and 1.00, respectively. As discussed in (Fleeter, 1975), the cascade was intended to represent the two-dimensional aerodynamic equivalent of the rotor blade near-tip (streamline 19) section of an ARL-designed high-throughflow compressor (Wennerstrom, 1976, 1983). The rotor blade section has a positive camber angle of 4.65 degrees and a streamtube area contraction of about 11.3 percent at design. Due to the "two-dimensional" redesign of the blade suction, however, the cascade blade has a negative camber angle of −2.89 deg. Several of the cascade geometric parameters are listed in Table 1 and shown in Fig. 1 along with the cascade geometry.

The design procedure generated airfoils of arbitrary geometry, where the chamberline was related in a prescribed manner to the desired relative flow angle distribution along the chord. In order to achieve a low-loss cascade, an attempt was made to minimize pressure gradients on the airfoil, especially gradients across shock waves. The so-called precom-

Contributed by the International Gas Turbine Institute and presented at the 33rd International Gas Turbine and Aeroengine Congress and Exhibition, Amsterdam, The Netherlands, June 5–9, 1988. Manuscript received by the International Gas Turbine Institute October 1987. Paper No. 88-GT-306.

Table 1 Cascade geometry

Solidity, $\sigma = l/t$	1.5294	
Maximum blade thickness/chord, d_{max}/l	0.0255	
Leading edge radius/chord, r_{LE}/l	0.00128	
Camber angle, ϕ	−2.89	deg
Stagger angle, β_s	146.93	deg

Table 2 Supersonic cascade wind tunnel

Continuous, closed-loop operation	
Total pressure	0.3–2.5 bar
Total temperature	295–325 K
Mach number (variable nozzle)	1.3–2.4
Test section	
height, H	238.0 mm
width, b	152.4 mm
Typical blade chord, l	85.0 mm
Typical aspect ratio, l/b	1.79

pression airfoil that resulted from this procedure has an "s-shaped" camberline with negative camber in the forward portion.

The net effect of the blade shape is to reduce the average Mach number at the passage entrance to a value less than the inlet Mach number, thereby reducing shock losses and any viscous losses caused by a shock/boundary-layer interaction.

Shock losses are further minimized by the very thin leading edge ($r_{LE}/1 = 0.00128$) since the detached part of the bow shock wave is then also very small.

The approximate wave pattern in the entrance region of the cascade at the design inlet Mach number is shown in Fig. 2, where several Mach numbers are indicated in order to give an impression of the magnitudes involved. The left-running waves of the bow shocks are seen to extend out in front of the adjacent blades, as is characteristic for supersonic relative inflow with a subsonic axial component. A unique feature of the precompression airfoil is the formation of a secondary left-running shock wave, which intersects the detached bow shock of the adjacent blade. This so-called precompression shock forms from the coalescence of left-running characteristics emanating from the concave forward portion of the blade suction surface. Although this shock is relatively weak, it significantly reduces the Mach number of the flow entering the covered passage.

At the design static pressure ratio an oblique shock wave runs into the blade passage where it intersects the suction surface of the adjacent blade at about 75 percent chord. The flow incident on this oblique passage shock wave has a minimum Mach number of about 1.53 and a maximum Mach number of about 1.68 near the suction surface.

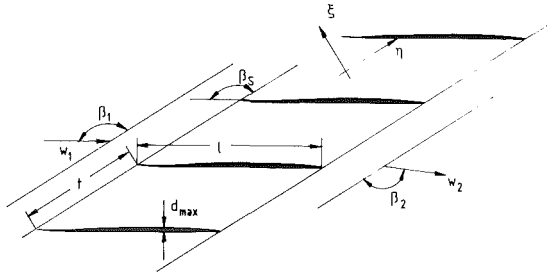

Fig. 1 Cascade geometric parameters

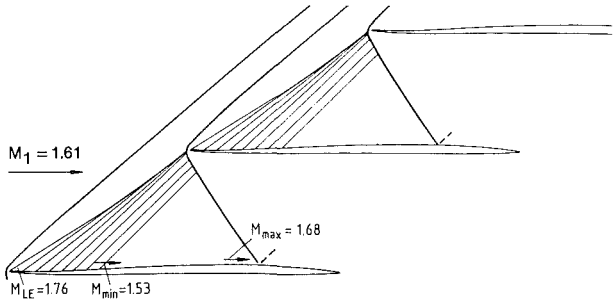

Fig. 2 Approximate wave pattern at the design inlet condition

Test Facility and Instrumentation

The supersonic cascade wind tunnel at the DFVLR in Cologne is operated as a continuous running, closed-loop test facility with several five-stage centrifugal compressors available for supplying air. These compressors can be operated in series or in parallel depending on the test cell requirements. The wind tunnel is equipped with an adjustable converging-diverging nozzle allowing a continuous variation of the test section Mach number from 1.3 to 2.4.

For the cascade results discussed here, the wind tunnel was oeprated with an upstream plenum total pressure in the range 1.0 to 1.3 bar and a total temperature between 300 and 312 K. Blade chord Reynolds numbers were in the range 1.1×10^6 to 1.4×10^6 for cascade inlet Mach numbers between 1.30 and 1.71. Some general information concerning the wind tunnel is listed in Table 2, and a cross-sectional drawing of the wind tunnel test section is shown in Fig. 3.

For the ARL-SL19 tests five cascade blades of chord length 85.0 mm and span 152.4 mm were installed in the test section, giving an aspect ratio of 1.79. The blades were mounted to

Nomenclature

AVDR = axial-velocity-density ratio $= \rho_2 w_2 \sin \beta_2 / (\rho_1 w_1 \sin \beta_1)$
b = test section width (blade span)
d_{max} = maximum blade thickness
F_u = tangential blade force
FU = dimensionless tangential blade force $= (F_u/t)/p_{t1}/((\rho_1 w_1^2/p_{t1})\sin^2 \beta_1)$
F_x = axial blade force
FX = dimensionless axial blade force $= (F_x/t)/p_{t1}/((\rho_1 w_1^2/p_{t1})\sin^2 \beta_1)$
H = test section height
l = blade chord length
M = Mach number
M_{is} = isentropic Mach number $= f(p/p_{t1})$
p = static pressure
p_t = total pressure
r_{LE} = leading-edge radius
t = blade pitch
T = static temperature
w = relative flow velocity
β = flow angle with respect to cascade front
β_s = stagger angle
η = coordinate in tangential direction
θ = dimensionless parameter $= \text{AVDR}/\tan \beta_2/(p_2/p_1)$
ν = Prandtl–Meyer flow angle
ξ = coordinate in axial direction
ρ = density
σ = blade solidity
ϕ = blade camber angle
ω = total pressure loss coefficient $= (p_{t1} - p_{t2})/(p_{t1} - p_1)$

Subscripts

ax = axial direction
LE = leading edge
N = nozzle exit conditions
1 = uniform condition far upstream of (infinite) cascade
2 = uniform condition far downstream of (infinite) cascade

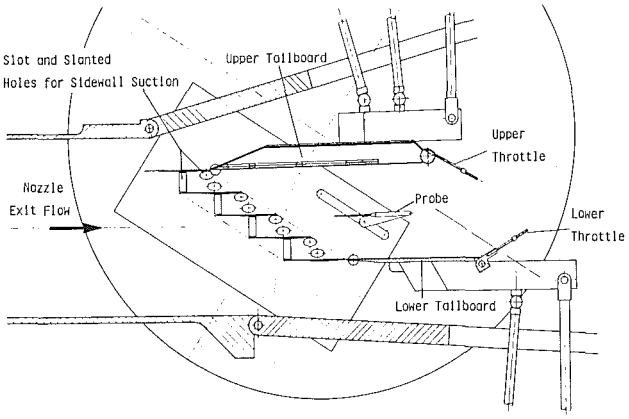

Fig. 3 Wind tunnel test section

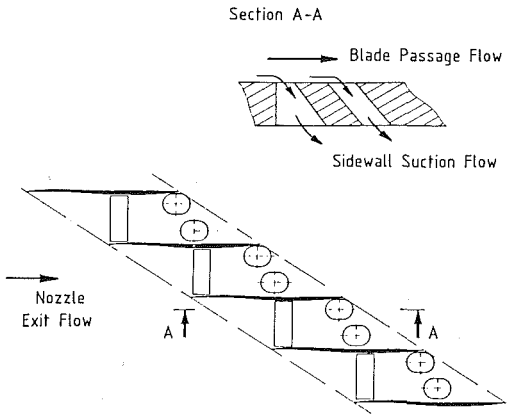

Fig. 4 Slots and holes for sidewall suction

plexiglass sidewall windows using cylindrical pins, with two pins on each side of each blade. Tailboards were hinged at the trailing edges of the upper and lower most blades, and a throttle was located at the downstream end of each tailboard. The cascade could be rotated in order to set the desired angle between the cascade inlet plane and the nozzle exit flow.

The purpose of the tailboard/throttle arrangement is to provide for adjustment of the desired exit flow conditions, which requires simultaneous adjustment of the back pressure and the blade-to-blade flow periodicity. The lower tailboard (see Fig. 3) is simply a smooth flat plate, whereas the upper tailboard consists of a thin, hollow chamber with a slotted flow surface, which is intended to allow adjustment of the static pressures at the tailboard surface.

The high static pressure ratios that were desired for this cascade could be achieved only by reducing the adverse effects caused by the sidewall boundary layers. Previus experience with transonic and supersonic cascades had shown that increasing back pressure causes considerable thickening of the side-wall boundary layers, with eventual separation, and that the flow at midspan is strongly influence. At even relatively moderate static pressure ratios the periodicity of the cascade flow is destroyed because the downstream pressure information propagates upstream through the side-wall boundary layers in the streamwise direction, instead of in the axial direction. Typically, in a supersonic compressor cascade the supersonic flow in the lower (rearmost) passage becomes unstarted by the high back pressure, while the other passages remain started. In order to reduce these adverse effects and to achieve much higher static pressure ratios across the cascade, sidewall suction was applied through slots in the forward part of the blade passages. As shown in Fig. 4, suction slots were oriented almost perpendicular to the flow direction near the passage-entrance shock wave where most of the pressure rise occurs (Leynaert, 1976). The suction system proved to be very effective in stabilizing the side-wall boundary layers at high static pressure ratios, thus allowing the attainment of much higher pressure ratios while maintaining reasonable blade-to-blade flow periodicity. As a second step toward better controlling the cascade flow conditions, two slanted holes were added at the rear of each blade passage (see Fig. 4). This was done in order to allow removal of more side-wall boundary-layer fluid, thereby providing better regulation of the axial-velocity-density ratio (AVDR).

The wind tunnel was instrumented with wall static pressure taps in the nozzle exit region, in the cascade inlet region, and in the cascade exit region. The center blade was instrumented with 10 static pressure taps on its suction surface, and the adjacent blade (below center in Fig. 3) with 10 taps on its pressure surface. Downstream blade-to-blade measurements of static pressure, total pressure, and flow direction were obtained at midspan by traversing a combination probe located at an axial distance of 26 mm ($\xi_2/l_{ax}=0.56$) downstream of the cascade exit plane. In order to reduce the adverse effects of the probe stem on the transonic exit flow field, the probe was designed with the stem displaced about 100 mm downstream of the traverse slot in the sidewall, as shown in Fig. 3.

Several flow velocity measurements were performed in the cascade inlet region using a laser transit anemometer (L2F velocimeter). These measurements were made at midspan in a plane slightly upstream ($\xi_1=1.54$ mm) of the cascade inlet plant.

A Schlieren system was used for practically all tests as a method of checking the flow periodicity and for observing the wave pattern in the cascade. Although the sidewall suction system and static pressure instrumentation severely restricted visual access to the flow field, the use of the Schlieren system was still possible. Several unobstructed Schlieren photographs of the cascade flow were taken during initial testing of the cascade before the sidewall suction system and instrumentation were installed.

Experimental Considerations

A peculiarity associated with this type of cascade is that under normal operating conditions the inlet flow is independent of the exit flow conditions, and furthermore, that the inlet flow parameters of Mach number and flow direction (or incidence) are not independent of each other. "Normal operating conditions" in this case refers to operation where the cascade passage flow is started. The started condition can exist only above a certain minimum upstream Mach number, sometimes referred to as the starting Mach number. For the ARL-SL19 cascade this starting inlet Mach number has been estimated using simple-wave theory and one-dimensional gas dynamics to be around 1.21. This estimate assumes no spanwise stream-tube contraction between the upstream flow and the passage throat.

The primary independent flow variables for the ARL-SL19 supersonic cascade were considered to be the inlet Mach number, the static pressure ratio, and the axial-velocity-density ratio (AVDR), all of which strongly influence the cascade performance. Dependent variables to be treated in the results section of this paper include the exit flow angle, the exit Mach number, and the total-pressure loss coefficient. The inlet flow angle was determined as a function of the inlet Mach number, as discussed below.

The typical procedure for generating test data was first to set the inlet Mach number at a particular value, and then increase the back pressure (i.e., the cascade static pressure ratio) incrementally from a low static pressure ratio to the maximum that could be achieved while maintaining blade-to-blade

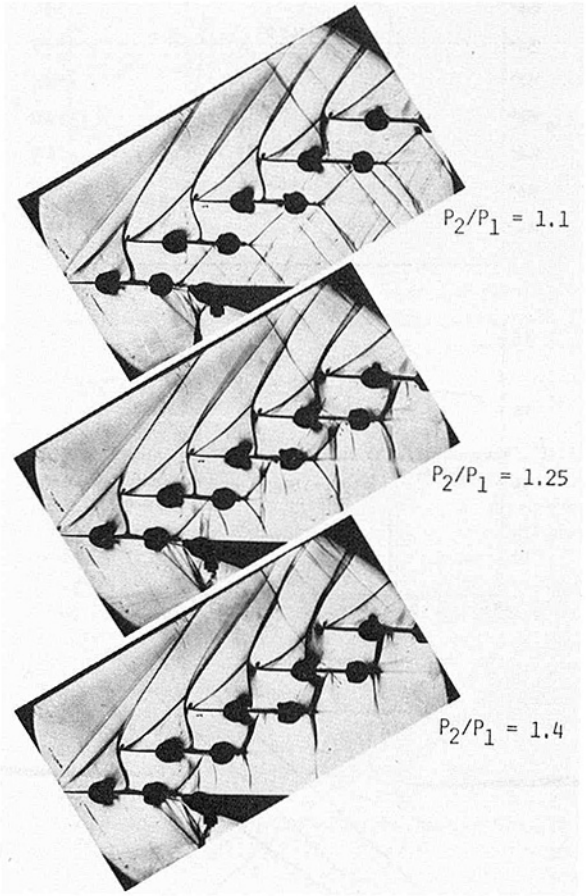

Fig. 5 Schlieren photographs of the cascade flow for $M_1 = 1.32$ and different static pressure ratios (back pressures)

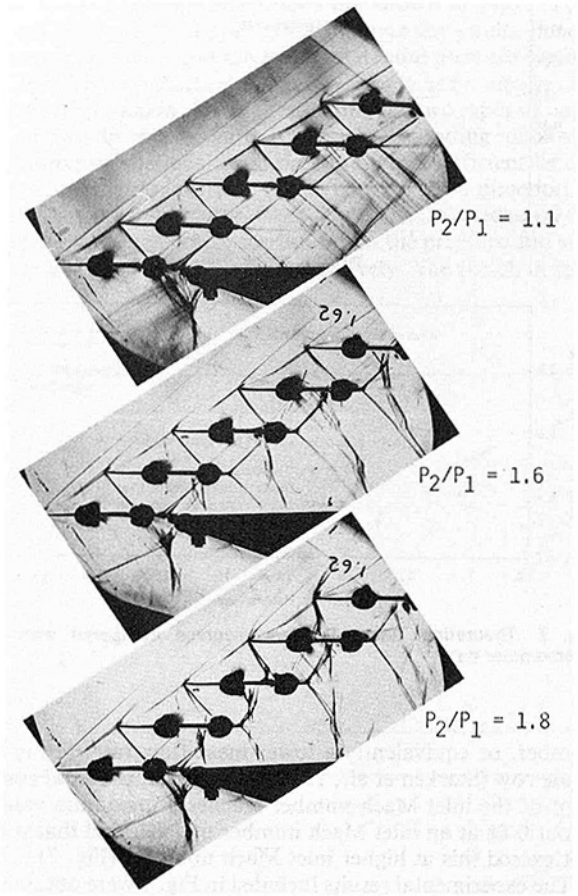

Fig. 6 Schlieren photographs of the cascade flow for $M_1 = 1.62$ and different static pressure ratios (back pressures)

periodicity. The operating line generated by this procedure is referred to here as a throttle curve.

Ideally it would have been desirable to vary the AVDR independently of the static pressure ratio, e.g., maintain a constant, prescribed AVDR along each throttle curve by controlling the amount of sidewall suction. Experimentally, however, this was not possible or practical due to a strong dependency of the AVDR on static pressure ratio; increasing the back pressure thickens the endwall boundary layers considerably causing a corresponding stream tube contraction at midspan. The application of sidewall suction stabilized the endwall boundary layers and allowed some variation of the AVDR, but for most tests in this investigation, an increase in the cascade static pressure ratio was accompanied by an increase in the AVDR.

Results and Discussion

The presentation and discussion of the ARL-SL19 cascade results is organized into four main sections: The first two sections are concerned with the cascade inlet flow and the inlet Mach number influence, and the third and fourth sections consider the influence of the static pressure ratio and AVDR, respectively, on the blade passage flow, the exit flow angle, and the total-pressure loss. Note that all blade-to-blade average quantities presented here were reduced from experimental data by using the "mixed-out" type of integration (Schimming and Starken, 1975).

Two sets of unobstructed Schlieren photographs are shown in Figs. 5 and 6 for inlet Mach numbers of about 1.32 and 1.62, respectively. In both figures the cascade back pressure is increasing from top to bottom. Only moderate static pressure ratios could be achieved under these test conditions because the side-wall suction system was not yet installed. At the inlet Mach number of 1.32 (Fig. 5) the cascade flow has what appears to be nearly a normal shock wave at the covered-passage entrance. However, the shock is not normal (over most of the covered-passage entrance), but oblique, and the cascade was started at this Mach number. At the inlet Mach number of 1.62 (see Fig. 6) the cascade was generally started, but static pressure ratios above 1.8 (approximately) caused the supersonic flow into the rearmost passages to unstart, destroying the periodicity of the cascade flow. Subsequent application of side-wall boundary layer suction permitted static pressure ratios as high as 2.47 for the same inlet Mach number of 1.62, while also greatly reducing secondary flow effects.

Cascade Inlet Flow

Supersonic cascade inlet flows with a subsonic axial velocity component involve a dependency of the inlet flow direction on the inlet Mach number. This dependency, ofter referred to as unique-incidence, is discussed in several references, e.g., Levine (1957), Novak (1967), Starken (1971), Lichtfuss and Starken (1974), and York and Woodard (1976). An approximate two-dimensional method developed by Starken (1971) for calculating the unique-incidence relationship was applied to the ARL-SL19 cascade geometry. The results of this calculation are shown in Fig. 7, were the dashed curves are included for comparison and correspond to a "no-loss" calculation. The solid curves were calculated by including approximated losses from the leading-edge bow shock waves. These losses can be seen to produce a blockage additional to that of the blade leading edges, resulting in a lower axial Mach

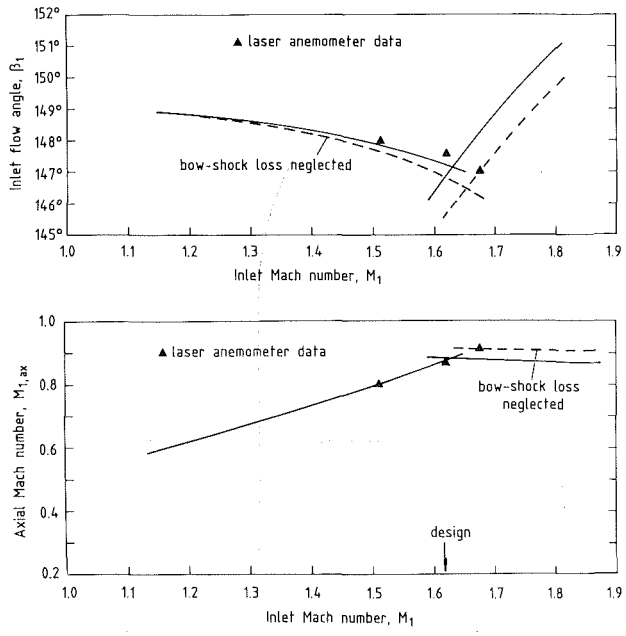

Fig. 7 Theoretical unique-incidence curves compared with laser anemometer data

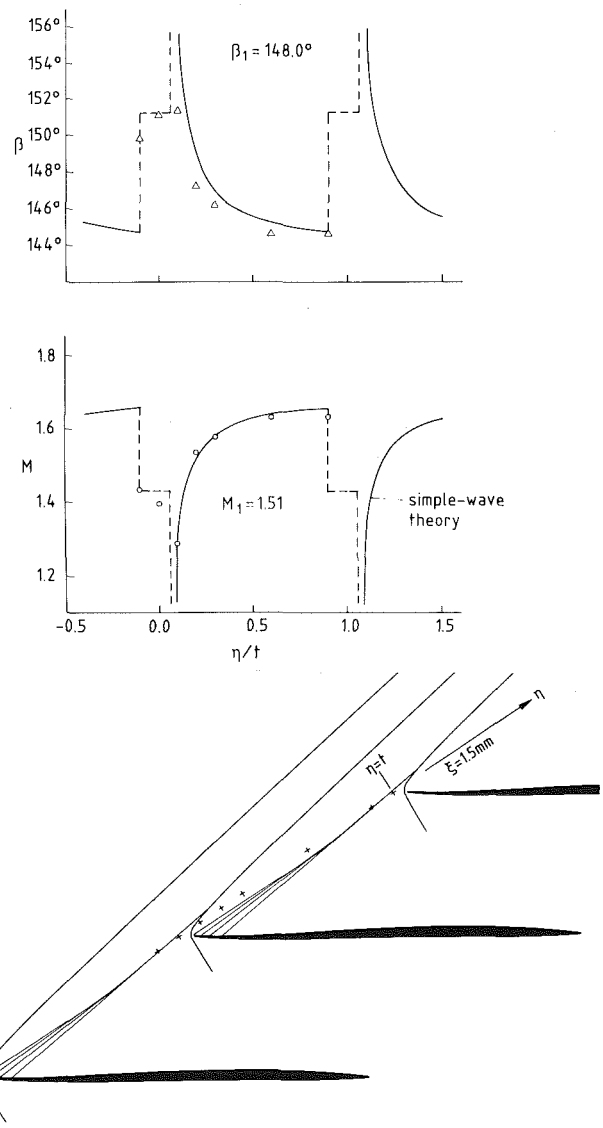

Fig. 8 Laser anemometer data and measurement locations (midspan, $\xi_1 = 1.54$ mm) for $M_1 = 1.51$

number, or equivalently a lower mass flow rate through the blade row (Starken et al., 1984). Notice that the axial component of the inlet Mach number reaches a maximum value of about 0.88 at an inlet Mach number of 1.62, and that is does not exceed this at higher inlet Mach numbers (Fig. 7).

The experimental results included in Fig. 7 were obtained by pitchwise integration of laser anemometer data measured near the inlet plane of the cascade. The L2F velocimeter (Schodl, 1980), i.e., laser transit anemometer, was used to perform velocity measurements at midspan locations 1.54 mm axially upstream of the cascade inlet plane. The measurement data and measurement locations for the two lower Mach number conditions in Fig. 7 are shown in Figs. 8 and 9. The solid curves for Mach number and flow angle represent the theoretical solution of a Prandtl–Meyer expansion around the blade leading edges, and the vertical dashed lines indicate the approximate locations where the bow shock waves (and precompression shock in Fig. 8) intersect the measurement plane. It is significant that the Prandtl–Meyer solutions were not fit to the data, but instead were calculated using the nozzle exit conditions:

$$\beta + \nu = \beta_N + \nu_N = \text{const} \tag{1}$$

The pitchwise integration of the data was done, assuming blade-to-blade periodicity, by applying the equations of motion to a control volume between upstream infinity and the measurement plane (Lichtfuss and Starken, 1974).

The theoretical simple-wave results and the experimental results in Fig. 7, 8, and 9 are in fairly good agreement indicating that the rotational flow effects, due mostly to the bow shock waves, are relatively small in the inlet region of this cascade. This is, however, not surprising considering the small leading-edge radii ($r_{LE}/l = 0.00128$).

Inlet Mach Number Influence

The inlet Mach number is the key parameter behind the static pressure rise achievable in supersonic compressor cascades. The upper graph in Fig. 10 shows the maximum static pressure ratios achieved with the ARL-SL19 cascade over the inlet Mach number range 1.23 to 1.72. Corresponding total-pressure losses are shown in the lower graph.

These results demonstrate a clear trend of increasing maximum static pressure ratio and corresponding total-pressure losses with increasing inlet Mach number. A maximum static pressure ratio of about 2.47 was obtained at the design inlet Mach number of 1.62, with a total-pressure loss coefficient of 0.13 to 0.14. At an inlet Mach number of 1.71 a static pressure ratio as high as 2.61 was achieved with a total-pressure loss coefficient of about 0.16. Based on downstream wake traverse data roughly about half of this loss is estimated to be shock loss. Note that the design static pressure ratio for this cascade is 2.15, and that an estimated design point loss coefficient of 0.225 was reported by Fleeter (1975).

Static Pressure Ratio Influence

Varying the cascade static pressure ratio—at a fixed inlet condition—alters the blade passage and cascade exit flow fields, as well as the overall cascade performance. Before discussing cascade performance in detail, however, the influence of static pressure ratio on the blade passage flow is shown by examining a typical set of blade isentropic Mach number distributions for moderate (2.12) to high (2.41) static pressure ratios and a nominal inlet Mach number of 1.58. The AVDR is almost unity in each of these test cases.

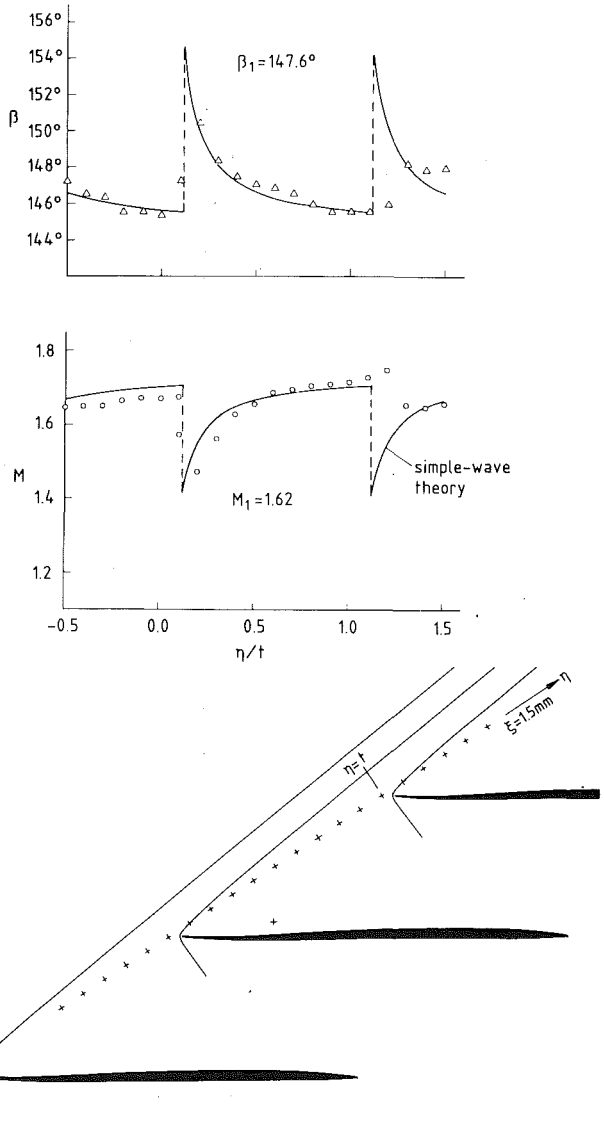

Fig. 9 Laser anemometer data and measurement locations (midspan, $\xi_1 = 1.54$ mm) for $M_1 = 1.62$

The Mach number distributions are shown in Figs. 11(*a*) through 11(*d*) in the upper graphs, where the circles denote suction surface data and the triangles denote pressure surface data. The lines connecting the data are only approximate and serve mostly to aid in visually separating the two types of data. Also shown in each figure is the corresponding pitchwise distribution of the local total-pressure loss coefficient as obtained from the downstream probe traverse. The direction of traverse was such that the "left" and "right" sides of the wake region in each graph correspond to the pressure and suction surface sides of the blade, respectively. The sketch in each

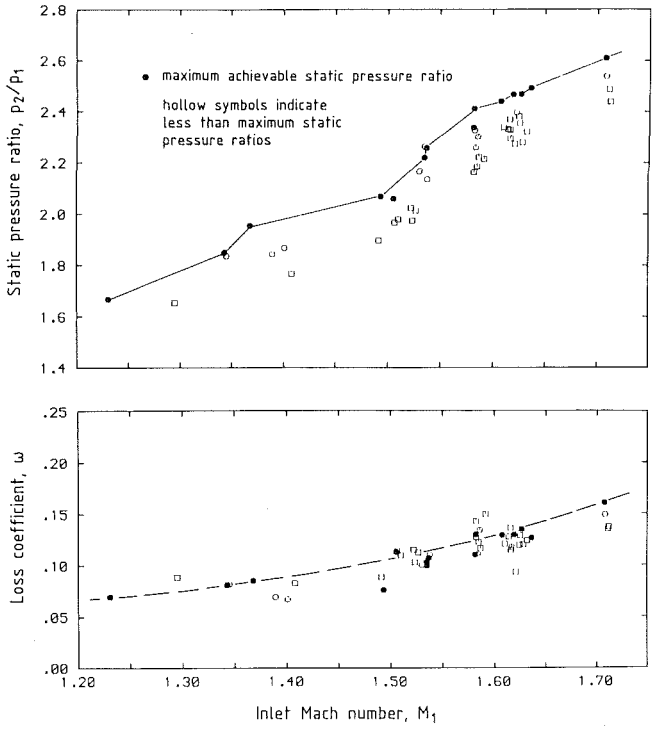

Fig. 10 Influence of the inlet Mach number on the maximum achievable static pressure ratio and the corresponding total-pressure losses

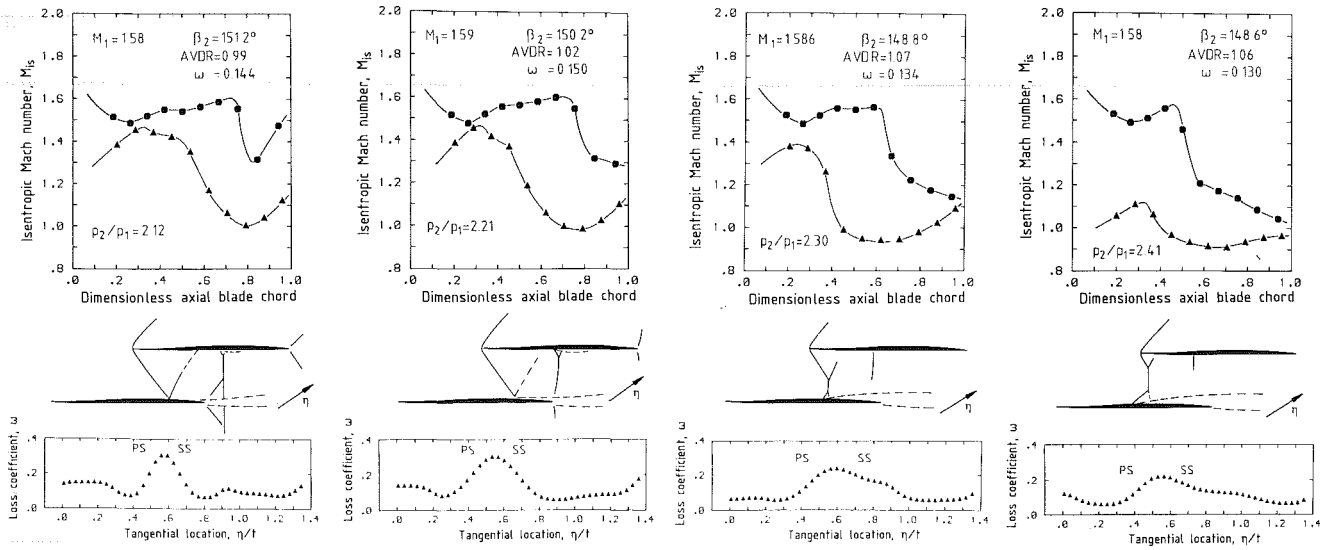

Fig. 11(*a*) Fig. 11(*b*) Fig. 11(*c*) Fig. 11(*d*)

Fig. 11 Blade isentropic Mach number distributions for a nominal inlet Mach number of 1.58; corresponding blade-to-blade losses measured downstream; sketches illustrating approximate wave pattern; (*a*) static pressure ratio 2.12; (*b*) static pressure ratio 2.21; (*c*) static pressure ratio 2.30; (*d*) static pressure ratio 2.41

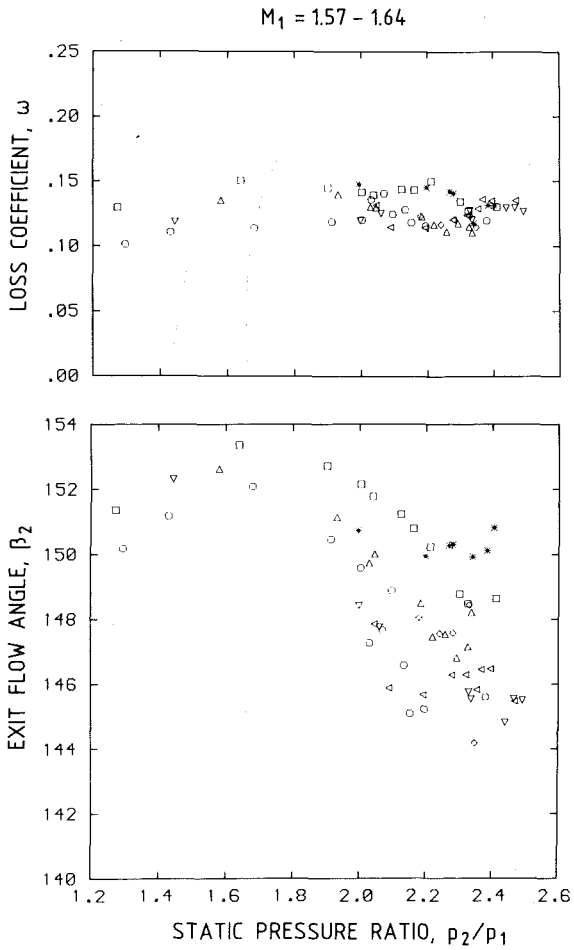

Fig. 12 Experimental data for inlet Mach numbers 1.57–1.64 showing the influence of static pressure ratio on the total-pressure losses and the exit flow angle

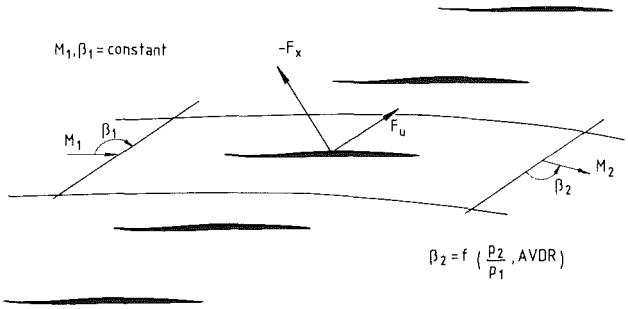

Fig. 13 Control volume used to write the equations of motion for the cascade flow

figure indicates the approximate wave pattern for that condition.

The Mach number distribution on the forward portion of the suction surface is nearly the same for all tests in Fig. 11 because the supersonic entrance region is not affected by the changes in back pressure. Although it cannot be seen in these graphs, there is actually a fairly strong deceleration along the concave part of the suction surface starting near the leading edge. This was not measured since the blades were too thin to allow static pressure tap instrumentation upstream of the first tap.

At the moderate static pressure ratio of 2.12 the trailing-edge oblique shock wave forms a so-called Mach reflection at the pressure surface of the adjacent blade, as indicated in the sketch in Fig. 11(*a*). It may be possible that his Mach reflection produces a weak boundary-layer separation, with reattachment, on the pressure surface. Increasing the back pressure moves this shock wave forward, reducing its strength until it almost disappears (around 35 percent chord on the pressure surface) for the static pressure ratio of 2.41 (see Fig. 11(*d*)). Simultaneously, the oblique shock wave at the passage entrance strengthens with increasing back pressure, eventually forming a lambda-shock system at the blade suction surface. The lambda-shock system is accompanied by full (turbulent) boundary-layer separation on the suction surface as can be partially identified in the pitchwise loss distributions (cf. loss distributions in Figs. 11*a–d*). Notice that at the moderate pressure ratios (Figs. 11 *a* and *b*) the wake region is fairly symmetric and relatively narrow, whereas at the higher pressure ratios (Figs. 11*c* and *d*) the wake region is asymmetric with a wake signature indicating boundary-layer separation on the suction surface. The losses in the extended right half of the wake region should be thought of as a combination of viscous and shock losses, as they are the result of the shock/boundary-layer interaction.

The general loss behavior observable from these four tests cases (moderate to high static pressure ratios) is that increasing back pressure causes a reduction in the shock loss, but with a corresponding increase in the viscous loss. The increase in viscous loss can be attributed mostly to a change from weak to strong suction surface boundary-layer separation.

The influence of static pressure ratio on the overall cascade performance is discussed next in terms of the exit flow angle, total-pressure loss coefficient, and the exit Mach number.

Measurement data for the exit flow angle and the total-pressure loss coefficient are shown in Fig. 12 for inlet Mach numbers in the range 1.57–1.64. The data scatter is due mostly to the concurrent variation of back pressure and AVDR during testing, although some scatter may be attributed to inlet Mach number differences. By correlating the cascade data in terms of tangential and axial blade forces, an effort was made to separate the AVDR influence from that of the static pressure ratio.

The blade forces used in the correlation were obtained by applying the conservation laws of mass, momentum, and energy to the control volume shown in Fig. 13. This control volume extends between uniform conditions far upstream and downstream of the blade row, and the momentum equations are applied in the axial and tangential directions as indicated by the blade force vectors. The control volume is quasi-three-dimensional since it includes the AVDR in the mass and momentum equations. The energy equation in this case reduces to the condition of constant total temperature over the entire flow field, and conservation of mass is equivalent to the definition of the AVDR:

$$\text{AVDR} = \rho_2 w_2 \sin\beta_2 / (\rho_1 w_1 \sin\beta_1) \tag{2}$$

Note that the inlet parameters are fixed at constant values.

A dimensionless form of the tangential momentum equations leads to the suggestion that the following dimensionless parameters might be useful for correlating the cascade data in terms of the blade forces (Schreiber and Tweedt, 1987):

Independent parameter

$$\theta = \frac{\text{AVDR}}{\tan\beta_2} \frac{1}{p_2/p_1} \tag{3}$$

Tangential blade force

$$FU = \frac{(F_u/t)/p_{t1}}{(\rho_1 w_1^2/p_{t1})\sin^2\beta_1} \tag{4}$$

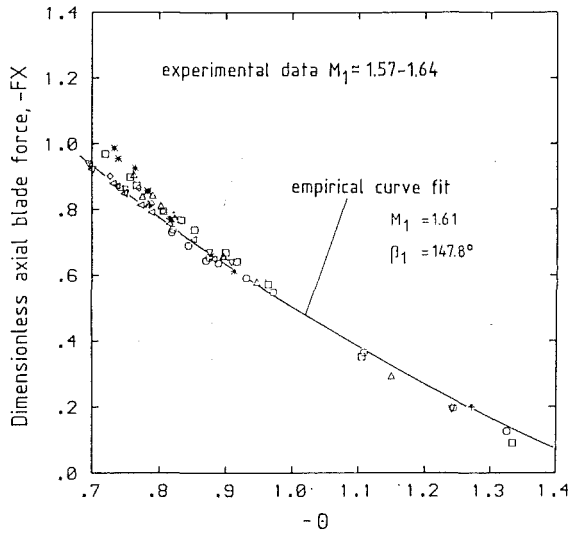

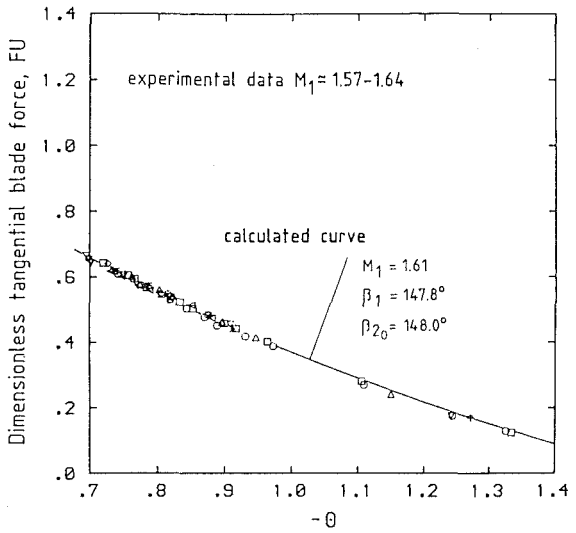

Fig. 14 Dimensionless blade force correlation using the parameter θ for an inlet Mach number of 1.61

Axial blade force

$$FX = \frac{(F_x/t)/p_{t1}}{(\rho_1 w_1^2/p_{t1})\sin^2\beta_1} \tag{5}$$

The dimensionless form of the tangential momentum equation is as follows:

$$FU = -\cot\beta_1 + \left(\frac{T_2}{T_1}\right)\theta$$

In this equation the inlet flow angle is considered to be a constant, and the temperature ratio can be expressed as a function of θ and cos β_2. The dependency of FU on β_2 is small, however, so that by approximating β_2 as a constant, $\beta_{2,0}$, the dimensionless tangential force is reduced to a function of θ only. Furthermore, the functional form is known a priori, as is verified by the correlation for an inlet Mach number of 1.61 shown in Fig. 14 (bottom). Note that the data shown in this figure are the same as those in Fig. 12.

Although the above discussion shows the reasoning behind attempting such a correlation, the usefulness of the parameter θ rests on the observation that it also correlates the axial blade force data fairly well (see Fig. 14, top). In this case the functional dependence of FX on θ is not known, and a second-order curve fit has been used.

Applying again the conservation laws of mass, momentum, and energy to the same control volume, but this time using the

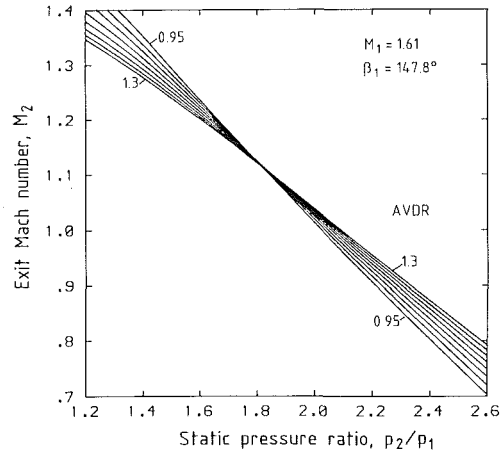

Fig. 15 Semi-empirical curves for an inlet Mach number of 1.61 showing the influence of static pressure ratio and AVDR on the cascade exit Mach number

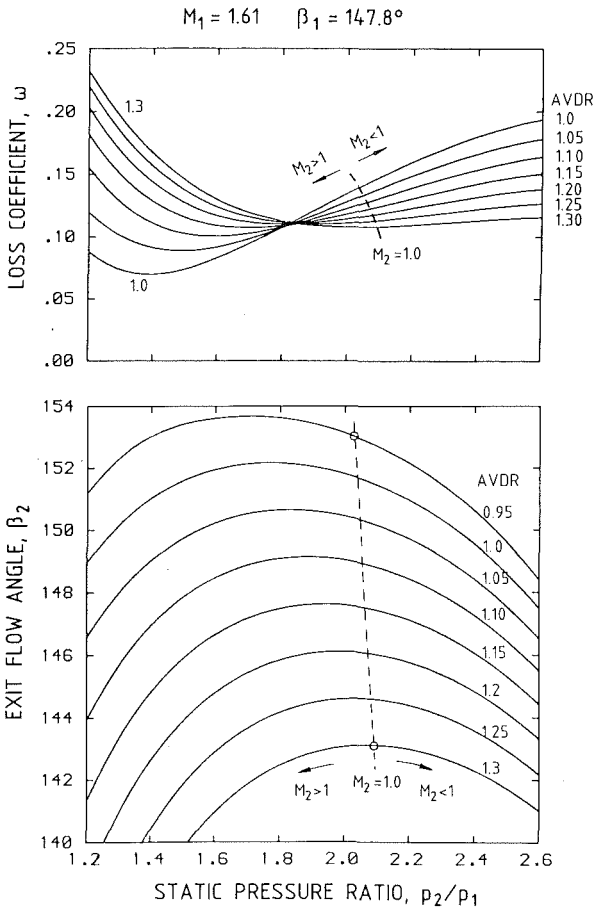

Fig. 16 Semi-empirical curves for an inlet Mach number of 1.61 showing the influence of static pressure ratio on the total-pressure losses and the exit flow angle

correlation curves as additional constraints, parameters such as the exit flow angle, exit Mach number, and the total-pressure loss coefficient can be determined as functions of the static pressure ratio and AVDR. These semi-empirical results are shown in Figs. 15 and 16 for the above correlation ($M_1 = 1.61$).

The curves in Fig. 15 show the near linear dependence of exit Mach number on static pressure ratio. Note that each curve represents a constant AVDR value, and that the increment in AVDR between each curve is 0.05. The AVDR is seen to have

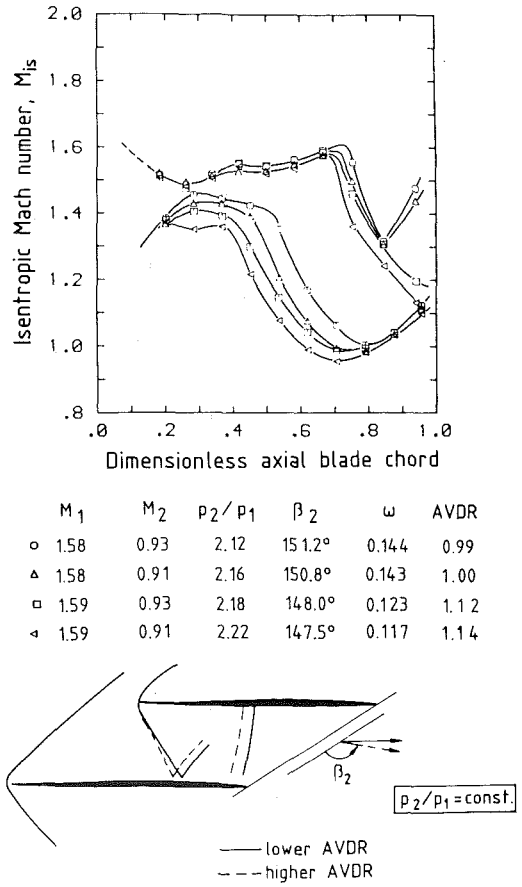

	M_1	M_2	p_2/p_1	β_2	ω	AVDR
o	1.58	0.93	2.12	151.2°	0.144	0.99
Δ	1.58	0.91	2.16	150.8°	0.143	1.00
□	1.59	0.93	2.18	148.0°	0.123	1.12
◁	1.59	0.91	2.22	147.5°	0.117	1.14

Fig. 17 Influence of AVDR on the blade isentropic Mach number distribution, for a nearly constant back pressure and an inlet Mach number of 1.58–1.59

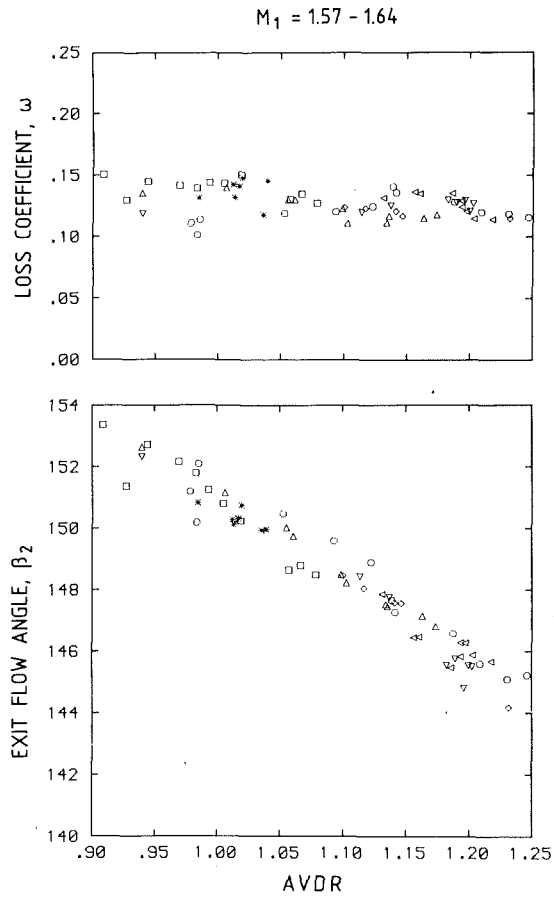

Fig. 18 Experimental data for inlet Mach numbers 1.57–1.64 showing the influence of AVDR on the total-pressure losses and the exit flow angle

only a small effect on the exit Mach number, the static pressure ratio being clearly the most dominant parameter.

The semi-empirical curves in Fig. 16 show the variations in exit flow angle and total-pressure loss with static pressure ratio. The dashed lines in this figure indicate conditions where the uniform (mixed-out) exit flow is sonic. A comparison between this figure and Fig. 12 reveals the usefulness of the correlation in helping to sort out the AVDR effects.

It can be seen in Fig. 16 that along a constant-AVDR curve a maximum exit flow angle exists at near-sonic exit conditions. This effect is well known for flat-plate cascades, e.g., Lichtfuss and Starken (1974) discuss this throttling behavior in more detail. Notice that in throttling the cascade at constant AVDR between a moderately low static pressure ratio (1.4) and a high static pressure ratio (2.5), the exit flow angle (or flow turning) can be expected to vary at most by about 2 to 3 deg, and the net change may in some cases be zero. The AVDR, on the other hand, will be shown to influence flow turning to a larger extent.

The loss-coefficient curves in Fig. 16 are especially interesting since they were in no way determined using measured loss data. These curves show what the loss values must be, assuming blade-to-blade periodicity, as determined by the equations of motion using prescribed (or measured) values of static pressure ratio, AVDR, and exit flow angle. In general, the curves show that over the typical range of moderate static pressure ratios (1.8 to 2.2) the loss coefficient can be expected to be on the order of 0.10 to 0.15, and that higher AVDR conditions should provide some reduction in the total-pressure loss. This behavior is discussed further in the next section, where measured loss data are compared for different AVDR conditions and a nearly constant static pressure ratio (about 2.17).

AVDR Influence

The AVDR influence on the blade passage flow in terms of the blade isentropic Mach number distribution is shown in Fig. 17 for a nominal inlet Mach number of 1.58. The static pressure ratio is nearly constant for the four data sets shown in this figure, although it should be noted that even the small variations in static pressure ratio contribute to and slightly exaggerate the observed trends.

The main effect of increasing AVDR is a moderate upstream shifting of the rear passage shock waves and a slight steepening of the oblique shock waves at the passage entrance, as indicated in the sketch in Fig. 17. Increased spanwise streamtube convergence tends to lower the Mach numbers in the passage, thereby reducing the shock loss and the losses from the shock/boundary-layer interaction region. As the tabulated data in Fig. 17 show, an increase in the AVDR from 1.00 to 1.14 ($p_2/p_1 = 2.16$–2.22) correspond to a decrease in the loss coefficient from 0.143 to 0.117. Also notice the relatively large decrease of 3.3 deg. in the exit flow angle (positive change in flow turning, $\beta_1 - \beta_2$).

The cascade performance data plotted against static pressure ratio in Fig. 12 are shown against AVDR in Fig. 18. Again, most of the data scatter is due to the concurrent variation of static pressure ratio and AVDR. In order to sort out the AVDR influence, the semi-empirical information contained in Fig. 16 has been rearranged and graphed against AVDR in Fig. 19. In this case each curve represents a constant static pressure ratio as indicated.

The influence of AVDR on total-pressure losses for moderate to high static pressure ratios is, as just discussed, that an increase in AVDR causes a reduction in losses. The ex-

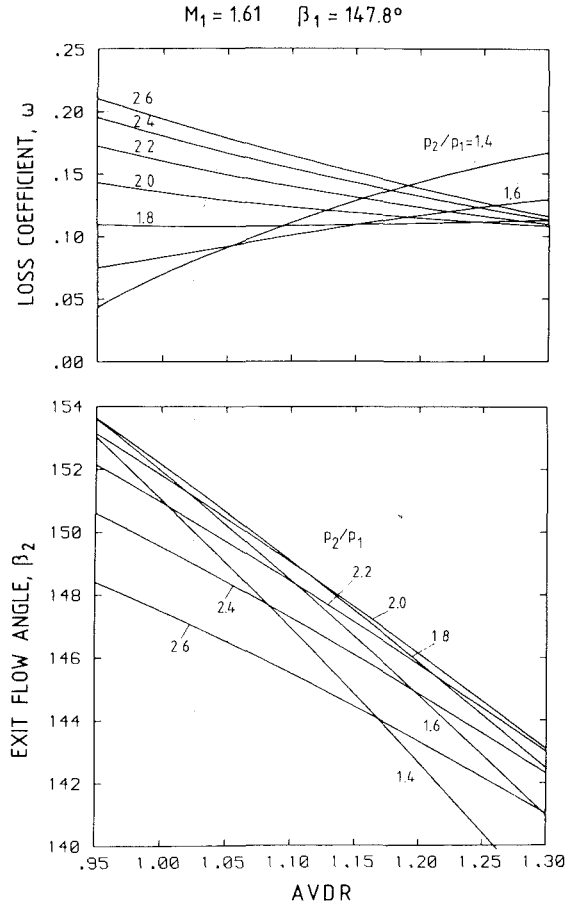

Fig. 19 Semi-empirical curves for an inlet Mach number of 1.61 showing the influence of AVDR on the total-pressure losses and the exit flow angle

tent of loss reduction, however, depends on the level of static pressure, with the loss reduction being more pronounced at higher static pressure ratios.

At low to moderate static pressure ratios (1.4 to 1.6) an increase in AVDR might be expected to cause an increase in total-pressure losses. Since sonic exit conditions occur around a static pressure ratio of 2.0 to 2.1, it is apparent that this behavior is associated with supersonic exit flow, i.e., wholly supersonic flow throughout the cascade. On the other hand, the trend of decreasing losses with increasing AVDR can be associated with sonic to subsonic cascade exit conditions. Note that any conclusions drawn for conditions of low static pressure ratio and AVDR greater than unity are, at best, uncertain. The curves for these conditions are an extrapolation from the measured data, i.e., the correlation contains no data for these conditions.

The influence of increasing AVDR on the exit flow angle (see Fig. 19) is to always reduce it and thereby increase the flow turning. The qualitative physical explanation for this effect is as follows: Maintaining a constant static pressure ratio requires that the effective exit flow area remain the same. The increased spanwise streamtube contraction for a higher AVDR necessitates that the exit flow turns to smaller values of β_2 (since β_2 is always greater than 90 deg for this cascade). Notice that this effect is considerably stronger at the lower static pressure ratios where the exit flow is supersonic.

A comparison of the relative influence of AVDR and static pressure ratio on the exit flow angle yields an interesting conclusion, namely, that the AVDR influence is more dominant.

Conclusion

The inlet condition for the ARL-SL19 cascade was measured using a laser transit (L2F) anemometer, and was found to be fairly well predicted by an approximate method for calculating the unique-incidence condition. At the (near-design) inlet Mach number of 1.62 the L2F experimental inlet flow angle was found to be 147.6 ± 0.5 deg, which yields an axial inlet Mach number of 0.87 ± 0.01. The analytically predicted inlet flow angle was 147.3 deg.

The design static pressure ratio of 2.15 for the cascade could only be achieved by applying sidewall boundary-layer suction through slots in the blade passage side walls. This suction system also allowed AVDR values near unity to be achieved, which was of considerable interest since the cascade was designed for two-dimensional flow (AVDR = 1.0). At the design point the blade passage entrance shock wave was observed to be oblique, intersecting the suction surface at about 75 percent chord. Measured design point loss coefficient values were 0.14 ± 0.01, with an exit flow angle of 151.0 ± 1.5 deg ($\beta_1 - \beta_2 = -3.4 \pm 1.5$ deg). Note that the large uncertainty in the exit flow angle includes the effects of nonperiodicity and secondary flows.

Increasing the AVDR to values above unity generally altered the blade element performance considerably. While maintaining all other independent parameters at the design values, an increase in AVDR to 1.15 was observed to decrease the loss coefficient to a value around 0.12 ± 0.01, with an accompanying decrease in the exit flow angle to about 147.5 ± 1.5 deg ($\beta_1 - \beta_2 = 0.1 \pm 1.5$ deg). The reduction in total-pressure losses is due mostly to a decrease in shock loss caused by lower blade passage Mach numbers.

A maximum static pressure ratio of about 2.47 was achieved for the design inlet conditions. At this operating point the cascade was observed to have a strong lambda-shock system in the covered passage entrance region. The passage flow downstream of this shock system is transonic/subsonic and the cascade exit flow is subsonic. Associated with the lambda-shock system is a strong shock/boundary-layer interaction with full (turbulent) boundary-layer separation on the suction surface at about 50 percent chord. Details concerning this type of shock system are described by other researchers, e.g., (East, 1976); Delery, 1986; Schreiber, 1987).

Normally in cascade testing the two parameters of static pressure ratio and AVDR are strongly coupled through side-wall boundary-layer effects, even when side-wall boundary-layer suction is being applied. The correlation discussed in this paper was an attempt to separate the effects of these two parameters in order to determine their relative influence on the cascade performance. Although care should be exercised in using the resulting curves in a quantitative manner, it is suggested that they are useful for analyzing the measured cascade results.

References

East, L. F., 1976, "The Application of a Laser Anemometer to the Investigation of Shock Wave/Boundary Layer Interactions," RAE Tech. Memo, AERO 1666; see also AGARD-CP-193, Feb. 1976.

Delery, J., and Marvin, J. G., 1986, "Shock-Wave Boundary-Layer Interactions," AGARDograph No. 280.

Fleeter, S., Holtman, R. L., McClure, R. B., and Sinnet, G. T., 1975, "Experimental Investigation of a Supersonic Compressor Cascade," ARL TR 75-0208, June 1975, Aerospace Research Laboratories, Wright-Patterson AFB, OH.

Levine, P., 1957, "Two-Dimensional Inflow Conditions for a Supersonic Compressor With Curved Blades," ASME *Journal of Applied Mechanics*, Vol. 24, No. 2, pp. 165–169.

Leynaert, J., 1976, "Cascade Test Methods in Wind Tunnel at ONERA," *Proceedings of the Symposium on Measuring Techniques in Transonic and Supersonic Cascades and Turbomachines*, Lausanne, Nov. 18–19.

Lichtfuss, H. J., and Starken, H., 1944, "Supersonic Cascade Flow," *Progress in Aerospace Science*, Vol. 15, D. Küchemann, ed., Pergamon Press Ltd., Oxford–New York.

Novak, O., 1967, "Flow in the Entrance Region of a Supersonic Cascade," Strojnicky Casopis XIX, C.2-3, pp. 138–150, Slovenskej Akademic vied Bratislava.

Schimming, P., and Starken, H., 1975, "Data Reduction of Two-Dimensional Cascade Measurements," AGARDograph No. 207, *Modern Methods of Testing Rotating Components of Turbomachines* (*Instrumentation*).

Schodl, R., 1980, "A Laser-Two-Focus (L2F) Velocimeter for Automatic Flow Vector Measurements in the Rotating Components of Turbomachines," ASME *Journal of Fluid Engineering*, Vol. 102, No. 4, 1980.

Schreiber, H. A., 1987, "Experimental Investigation on Shock Losses of Transonic and Supersonic Compressor Cascades," AGARD-CP-401, *Transonic and Supersonic Phenomenon in Turbomachines*.

Schrieber, H. A., and Tweedt, D. L., 1987 "Experimental Investigation and Analysis of the Supersonic Compressor Cascade ARL-2DPC," DFVLR IB 325-02-87.

Starken, H., Zhong, Y., and Schrieber, H. A., 1984, "Mass Flow Limitation of Supersonic Blade Rows Due to Leading Edge Blockage," ASME Paper No. 84-GT-233.

Starken, H., 1971, "Untersuchung der Strömung in ebenen Überschallverzögerungsgittern," DLR-FB 71-99.

Wennerstrom, A. J., 1983, "The Design and Evaluation of a High-Through-Flow Transonic Axial Compressor," 6th International Symposium on Air Breathing Engines, Paris.

Wennerstrom, A. J., and Frost, G. R., 1976, "Design of a 1500 ft/sec, Transonic, High-Through-Flow, Single-Stage Axial Flow Compressor with Low Hub/Tip Ratio," AFAPL-TR-76-59, Oct. Air Force Aero-Propulsion Lab/TB, Wright-Patterson AFB, OH.

York, R. E., and Woodard, H. S., 1976, "Supersonic Compressor Cascades—An Analysis of the Entrance Region Flow Field Containing Detached Shock Waves," ASME *Journal of Engineering for Power*, Vol. 98, pp. 247–257.

APPENDIX

Profile Coordinates

Suction Surface		Pressure Surface	
X_{SS}/l	Y_{SS}/l	X_{PS}/l	Y_{PS}/l
0.001389	0.001279	0.001170	-0.001274
0.012656	0.000651	0.012425	-0.002454
0.024082	0.000153	0.023844	-0.003535
0.035660	-0.000250	0.035422	-0.004518
0.047387	-0.000549	0.047164	-0.005402
0.071285	-0.000838	0.071114	-0.006885
0.095750	-0.000745	0.095653	-0.007995
0.120746	-0.000293	0.120748	-0.008761
0.146218	0.000431	0.146333	-0.009213
0.172107	0.001527	0.172342	-0.009395
0.198339	0.002990	0.198634	-0.009346
0.224836	0.004206	0.225272	-0.009132
0.251495	0.005714	0.252015	-0.008796
0.278244	0.007255	0.278317	-0.008390
0.305014	0.008783	0.305619	-0.007964
0.331755	0.010256	0.332374	-0.007536
0.358421	0.011652	0.359032	-0.007139
0.384988	0.012960	0.385573	-0.006784
0.411438	0.014149	0.411990	-0.006478
0.437768	0.015228	0.438286	-0.006219
0.463991	0.016203	0.464463	-0.005994
0.490107	0.017071	0.490544	-0.005806
0.516126	0.017836	0.516510	-0.005650
0.542037	0.018498	0.542370	-0.005524
0.567845	0.019048	0.568116	-0.005432
0.593545	0.019481	0.593746	-0.005371
0.619125	0.019797	0.619252	-0.005352
0.644583	0.019931	0.644619	-0.005370
0.669897	0.020033	0.669842	-0.005437
0.695076	0.019944	0.694920	-0.005552
0.720106	0.019713	0.719858	-0.005713
0.744997	0.019313	0.744659	-0.005884
0.769747	0.018729	0.769331	-0.006049
0.794367	0.017943	0.793885	-0.006171
0.818368	0.016949	0.818345	-0.006219
0.843268	0.015727	0.842723	-0.006164
0.867576	0.014268	0.867028	-0.005972
0.891806	0.012556	0.891284	-0.005617
0.915964	0.010575	0.915483	-0.005073
0.940058	0.008310	0.939661	-0.004310
0.964095	0.005741	0.963793	-0.003300
0.988073	0.002853	0.987909	-0.002021
1.000045	0.001233	0.999955	-0.001277

Experimental Investigation of the Three-Dimensional Flow in an Annular Compressor Cascade

H. D. Schulz
Dipl.-Ing.

H. D. Gallus
Professor Dr.-Ing.
Mem. ASME

Institut für Strahlantriebe und Turboarbeitsmaschinen,
Rheinisch-Westfälische Technische Hochschule,
Aachen, Federal Republic of Germany

A detailed experimental investigation was carried out to examine the influence of blade loading on the three-dimensional flow in an annular compressor cascade. Data were acquired over a range of incidence angles. Included are airfoil and endwall flow visualization, measurement of the static pressure distribution on the flow passage surfaces, and radial-circumferential traverse measurements. The data indicate the formation of a strong vortex near the rear of the blade passage. This vortex transports low-momentum fluid close to the hub toward the blade suction side and seems to be partly responsible for the occurrence of a hub corner stall. The effect of increased loading on the growth of the hub corner stall and its impact on the passage blockage are discussed. Detailed mapping of the blade boundary layer was done to determine the loci of boundary layer transition and flow separation. The data have been compared with results from an integral boundary layer method.

Introduction

The flow through a multistage axial compressor is very complex, being three dimensional, unsteady, and viscous. With regard to high blade loadings and lower aspect ratios, these phenomena will have an even greater effect upon the overall performance of a machine. Present design methods are barely adequate in this context since they are predominantly based on the assumption of axisymmetric flow. To improve this situation a considerable number of investigations concerning the three dimensionality of the flow field in axial-flow compressors have been conducted. Dring et al. (1982, 1983) surveyed the flow of an isolated rotor at high aerodynamic loading and low aspect ratio ($h/c = 1.0$) and Wagner et al. (1985) the rotor of a two-stage machine. They observed regions of high loss near the endwalls, the one at the hub being associated with the separation of the blade and endwall boundary layers near the end of the suction surface. Joslyn and Dring (1985) observed a stalled region of high loss fluid at the suction surface–hub endwall corner, which extended up to 75 percent span at reduced flow rates. A small casing corner stall also existed, but this diminished in size as the flow coefficient was reduced. They found the rotor hub corner stall responsible for increased incidence and hence loading on the stator, leading to the observed severe separation on the stator suction surface–hub endwall region. Dong et al. (1987) investigated the flow and loss mechanism in a single-stage low-speed axial-flow compressor. No evidence of a suction surface–endwall separation was observed in the rotor, but a separation did exist at both ends of the stator, the one at the hub being reduced by introducing a clearance between the stator vane and stationary hub.

The influence of rotor-stator interaction on boundary layer development and three-dimensional flow in axial-flow compressors has been pointed out by Gallus and Hönen (1983, 1986) and Cyrus (1986) and it is important to improve our understanding of its basic mechanism. Accordingly, a research program has been worked out where at first the flow in an annular compressor cascade at steady incoming flow is thoroughly surveyed. Special emphasis is placed upon measuring the boundary layers inside the flow passage, the wall pressure distribution, and the cascade losses at different blade loadings. These measurements will later be compared with data acquired in the presence of a rotor (wake generator) upstream of the compressor cascade to determine the differences in separation behavior of the stator with and without an upstream rotor. The long-term objective is first to get a better insight into the three-dimensional and unsteady flow phenomena present in axial compressors and to find more appropriate parameters that predict the onset and extension of boundary layer separation inside the stator flow passage. The second objective is to provide a benchmark data base for a detailed comparison with results from computational codes. This paper presents some of the experimental results acquired in the annular compressor cascade with undisturbed, steady incoming flow at increasing blade loading.

Experimental Facility

The experiments were performed in an annular cascade as shown in Fig. 1. A turbocompressor set provides a continuous airflow to the test rig. The swirl angle of the flow is varied by means of 48 adjustable inlet guide vanes (IGV). Angular momentum is conserved while the flow passes through a channel contraction to level out the wakes of the IGV. For the tests described in this paper the rotor (R) has been removed to assure an undisturbed, circumferentially uniform flow to the

Contributed by the International Gas Turbine Institute and presented at the 33rd International Gas Turbine and Aeroengine Congress and Exhibition, Amsterdam, The Netherlands, June 5–9, 1988. Manuscript received by the International Gas Turbine Institute December 18, 1987. Paper No. 88-GT-201.

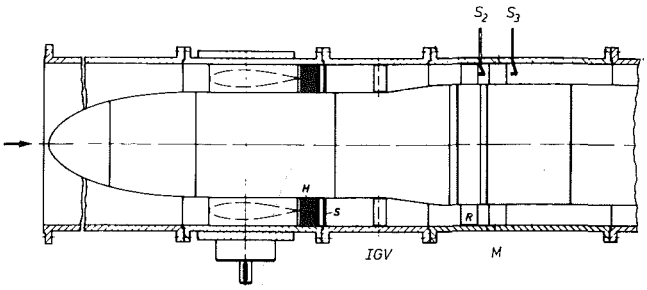

Fig. 1 Annular cascade test rig: H—honeycomb; S—screens; IGV—inlet guide vanes; R—rotor; M—measuring cascade; S_2, S_3—probe locations

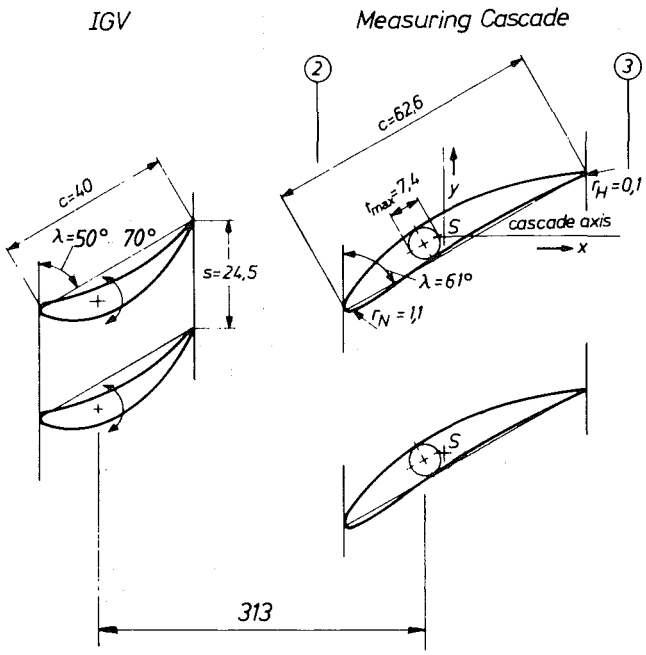

Fig. 2 Cascade geometry (midspan, units in mm)

compressor cascade (M). The cascade consists of 24 untwisted blades with a hub-to-tip ratio of 0.75. The blade profiles are radially stacked at their center of gravity. The cascade data are shown in Fig. 2 and summarized in Table 1.

The properties of the incoming flow have been surveyed using pneumatic five-hole probes at measuring station 2 (S_2) 56 percent of blade chord upstream of the vane leading edge. The circumferential uniformity of the flow has been checked and found acceptable (variation in swirl angle and velocity were less than 1 percent and 2 percent, respectively).

Table 1 Cascade geometry data

tip diameter	428	mm
hub diameter	321	mm
cascade vane number	24	
stagger angle	29°	
chord	62.6	mm
camber	29°	
max. thickness	7.4	mm
aspect ratio	0.86	
solidity at midspan height	0.78	

Test Program

The objective of this investigation is to study the three-dimensional flow phenomena occurring in an annular compressor cascade at increased loading. Accordingly, the yaw angle α_2 to the cascade has been varied from slightly negative incidence angles to high positive incidence angles (yaw angle at zero incidence $\alpha_{20} = 42.0$ deg) while the inlet Mach number, Reynolds number, and turbulence level have been kept constant. The spanwise distribution of the properties of the incoming flow are shown in Fig. 3. The five points of operation under investigation are identified by the midspan yaw angle α_2.

At these flow rates the following data have been acquired:

- flow visualization of the vane and hub surface flow
- time-averaged static pressure distribution at vane surface, hub, and casing,
- time-resolved static pressure fluctuation at the vane surface,
- pressure loss and underturning due to flow blockage at the cascade exit,
- hot-wire and hot-film measurements of the vane suction surface boundary layer.

The latter have been compared with results from an integral boundary layer method.

Results and Discussion

Surface Flow Visualization. The vane and hub surface

Nomenclature

c = blade chord
C = absolute flow velocity
Cp = pressure coefficient
D = diffusion factor
L = coordinate for the blade suction surface
LSB = laminar separation bubble
M = Mach number
P = pressure
r = radius
Re = Reynolds number
S = center of gravity
s = blade spacing
t = blade thickness
T = location of boundary layer transition
TS = location of turbulent boundary layer separation
Tu = turbulence level
U = flow velocity
x = axial direction
y = circumferential direction
z = spanwise direction
α = flow angle measured from axial direction
δ = displacement thickness
λ = stagger angle
ρ = density
τ = shear stress

Subscripts

0 = design flow angle
2 = upstream of the cascade
3 = downstream of the cascade
m = blade midspan height
t = total
s = static
ss = suction side
w = blade surface

Superscripts

(-) = mass-averaged
(′) = unsteady
(¯) = time-averaged

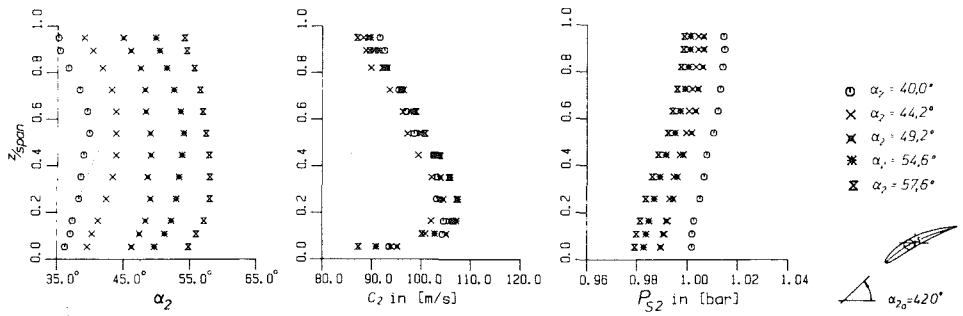

Fig. 3 Data of the incoming flow at all five points of operation

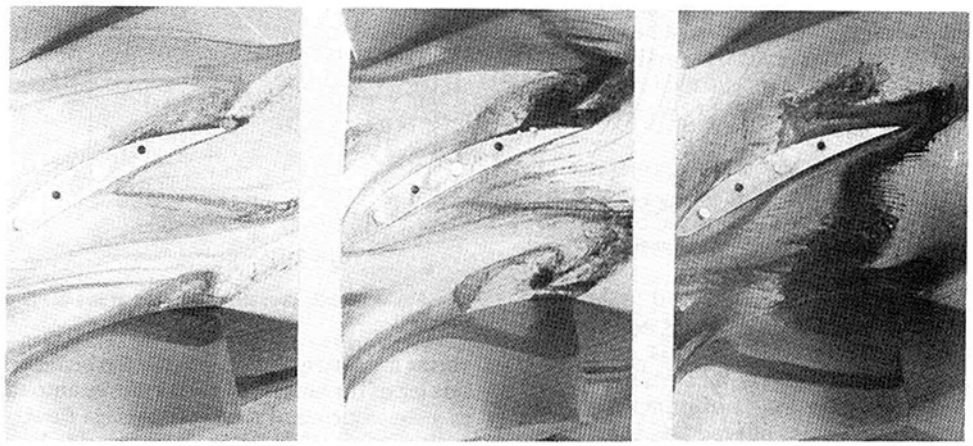

Fig. 4 Hub and vane suction side flow visualization at various blade loadings

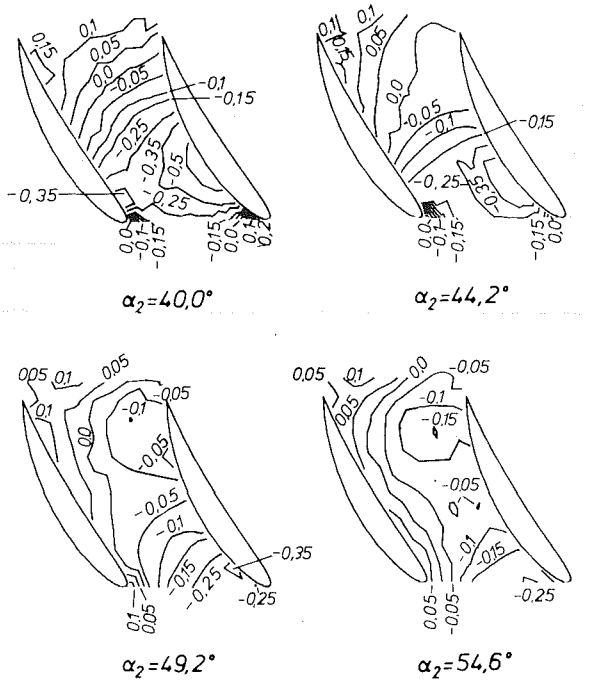

Fig. 5 Static pressure contours at the hub

flow have been visualized by means of dye injection. A mixture containing 1 percent colored ink and 99 percent acetone was injected by a small pitot tube upstream of the vane leading edge and via surface pressure taps. It was found that both methods did provide the same information, giving evidence that the disturbance of the flow due to the pitot tube was negligible. In addition the surface oil flow technique (Maltby, 1962) was applied to the vane suction and pressure surfaces to obtain information about the state of the boundary layer (Fig. 20). The results of the boundary layer measurements will be discussed later, but the oil flow visualization technique also provides useful information about the secondary flow pattern along the blade surface.

The hub and the blade suction surface flow visualization at three different angles of attack are shown in Fig. 4 (view onto the hub; one blade has been removed for photographic purposes). The most striking feature is the region of separated flow that originates near the hub endwall and the blade suction side at all three flow angles. This region extends in size with increasing angle of attack, and in case of the high incidence angle it starts at the 20 percent axial chord location and extends radially outward to 75 percent span at the trailing edge. There appears to be a large amount of radial outflow on the vane surface within and outside of the separation zone. A region of backflow, very similar to that seen by Joslyn and Dring (1985) and Dong et al. (1987), is also visible within the separated flow region on the suction surface and on the hub. Some of the backflow originates in the pressure surface boundary layer, turns around the trailing edge, and moves upstream toward the leading edge. On the hub endwall, it can be seen that the stagnant flow region entends to some 70 percent of the pitch away from the suction surface at $\alpha_2 = 57.6$. The flow visualization shows a significant overturning of the hub boundary layer flow by the cross-passage pressure gradient, more pronounced at high angles of attack. Close to the suction surface the cross-passage flow moves upstream into the separation region, joining the back flow and generating a vortex with a clockwise orientation. The center of this vortex

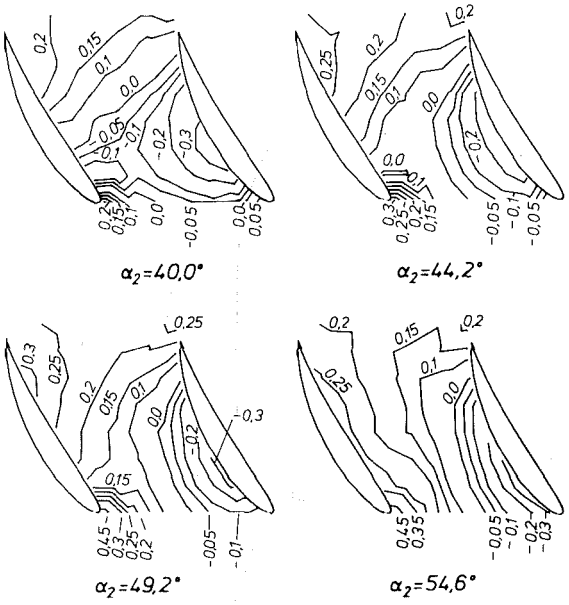

Fig. 6 Static pressure contours at the casing

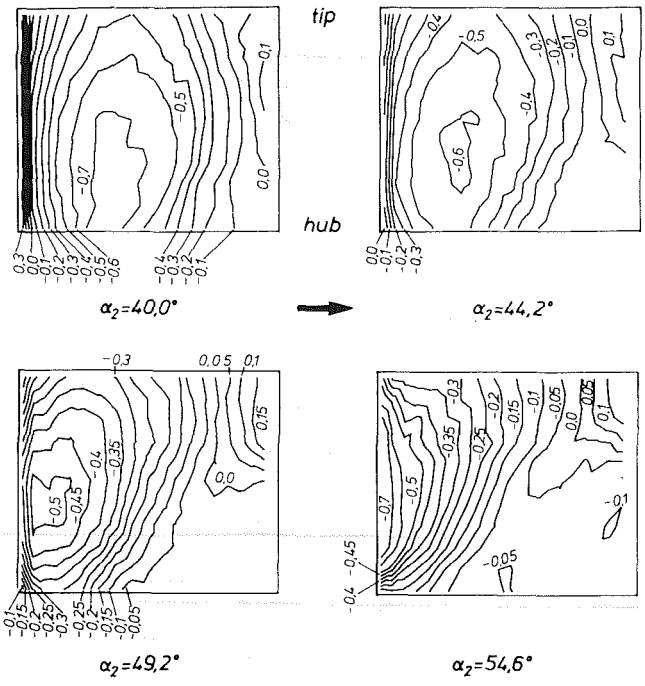

Fig. 7 Static pressure contours at the blade suction side

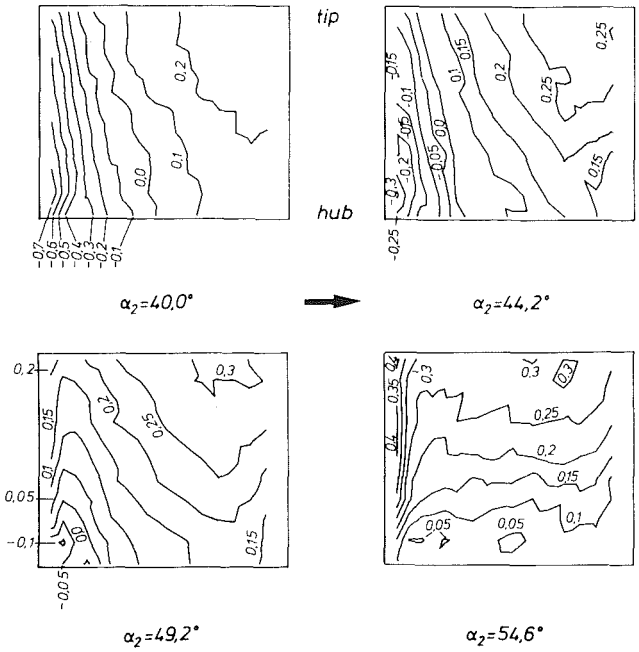

Fig. 8 Static pressure contours at the blade pressure side

appears as a low-pressure region in the contour plots of the hub static pressure (Fig. 5) discussed below. A similar significant cross passage flow has been observed by Dong et al. (1987), Gallus and Hönen (1986), and Wisler et al. (1987).

The oil flow technique (Fig. 20) reveals on the blade suction surface a small region of separated flow near the outer casing. At increasing angle of attack the separation diminishes due to the increased blockage created by the hub corner stall. This is coherent with the results of Joslyn and Dring (1985). In contrast to the situation on the suction surface, the visualization proved that the flow was essentially two dimensional at the pressure surface.

Where the hub boundary layer meets the leading edge of the blades, the dye injection in Fig. 4 indicates that a horseshoe vortex is formed. The separation lines associated with this vortex are clearly visible. Within the blade passage the suction side leg of the horseshoe vortex moves onto the suction surface as a consequence of the cross-passage flow. At the high angle of attack $\alpha_2 = 57.6$ deg the pressure side leg of the vortex appears to be swept toward the pressure side due to the blockage created by the hub corner stall.

In summary, the dominant feature seen in the cascade flow visualization is the suction surface–hub flow separation. With increasing angles of attack the hub corner stall grows and the observed small stall at the tip corner contracts even more. At the hub a significant cross-passage flow transports low-energy fluid toward the suction surface, generating a vortex close to the hub–suction side corner. All these phenomena have been observed in motion by means of video camera equipment.

Surface Static Pressure Distribution. To provide a benchmark data base for detailed comparison with computed results and to investigate the effect of the abovedescribed flow phenomena on the pressure field, all surface static pressure distributions have been measured at the flow rates under investigation.

They are given in terms of *Cp* contours in Figs. 5, 6, 7, and 8. The local static pressure was measured relative to the cascade inlet static pressure at midspan. This pressure difference has been normalized with the midspan dynamic head at the cascade inlet. Since the static pressure remains constant downstream of the location where the flow separates, generally regions of separated flow can be identified by regions of constant pressure. On the blades, in particular, flow separation can be detected by the "flattening" of the blade pressure distribution.

Figures 5 and 6 show the static pressure contour plots along the hub and along the casing, respectively. The measurements were taken via a matrix array of 56 pressure taps at the casing and 114 pressure taps at the hub. Comparing Figs. 5 and 6 the flow appears to be very similar at the hub and at the casing at $\alpha_2 = 40$ deg, and there appears to be only a very little hub–suction side corner separation. At increasing angle of attack the hub static pressure distribution clearly shows the increase in extent of the hub–suction side separation. Due to the blockage of the flow, diffusion is inhibited, and there is no further increase in static pressure along the suction surface as soon as the boundary layer separates. The subsequent deflection of the

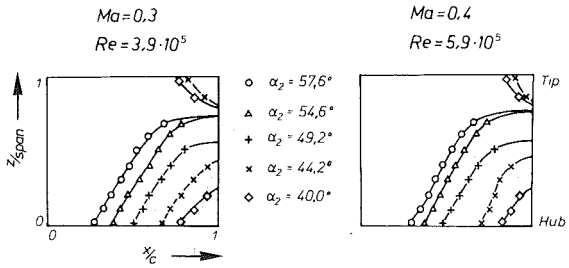

Fig. 9 Separation lines along the blade suction side

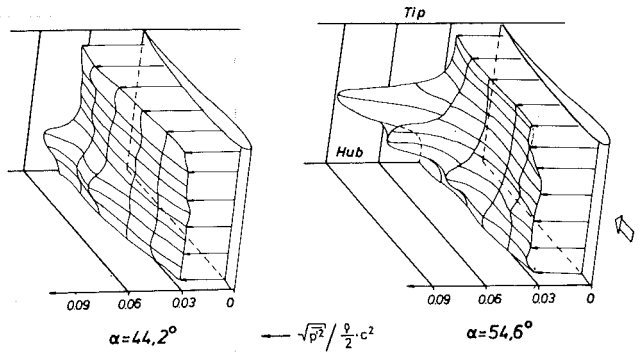

Fig. 10 Topological presentation of the static pressure fluctuation along the blade suction surface

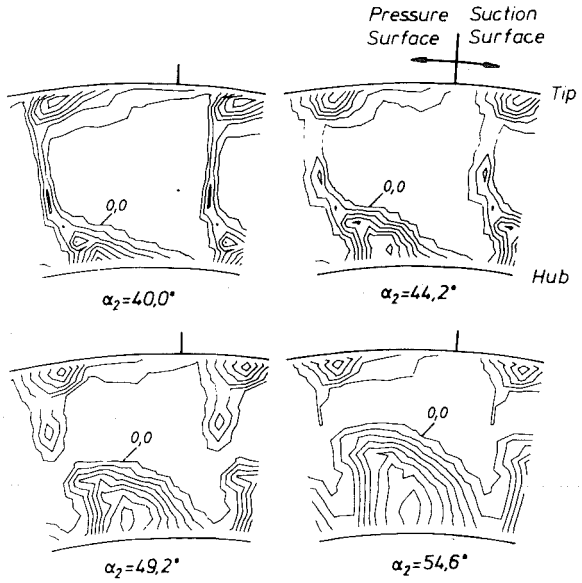

Fig. 11 Cascade exit total pressure $Cp_{t3} = (\bar{P}_{t2} - P_{t3})/(\bar{P}_{t2} - \bar{P}_2)$ contours; contour interval $\Delta Cp_{t3} = 0.1$

main flow increases the cross-passage pressure gradient, thus giving rise to an even more severe secondary flow on the hub. The abovementioned low-pressure region, visible in the pressure contours, coincides with the core of the vortex seen in Fig. 4. On the contrary, the static pressure distribution along the casing shows no evidence of boundary layer separation. With increasing angle of attack the loci of maximum static pressure at the pressure side move upstream toward the leading edge, thus increasing cross-passage pressure gradient and secondary flow inside the flow passage.

Since the blades of the compressor cascade are untwisted, an elongated blade has been instrumented with 19 pressure taps along the suction side and 15 taps along the pressure side. The blade has been radially traversed by a specially designed mechanism. Subsequently, the row of pressure taps moved to different positions along the span. The blade surface pressure distribution was measured at eleven span positions. The static pressure contours along the suction side and the pressure side are shown in Figs. 7 and 8, respectively. The striking feature at the suction side again is the separation close to the hub and the blade trailing edge, which grows in extent at increasing angle of attack as can be seen in the surface flow visualization (Figs. 4 and 20) as well as in the static pressure distribution at the hub (Fig. 5). The "shell-like" shape of the pressure contours at midchord position is a result of the reduction in inlet swirl due to the development of the hub and casing boundary layers downstream of the inlet guide vanes and the development of secondary flow in the front part of the flow passage. At the blade pressure side the lines of constant pressure are deflected from radial to axial direction with increasing swirl angle (Fig. 8). The pressure gradient in radial direction grows as a consequence of the high inlet swirl angle, and due to the blockage of the flow at $\alpha_2 = 54.6$ deg there is hardly any diffusion in axial direction.

In summary, the surface pressure distribution reveals the impact the hub–suction side flow separation has on the pressure field inside the flow passage. Figure 9 shows the lines of separation on the blade suction side, deduced from the chordwise *Cp* distribution at various span positions (not shown here). It is apparent that the extent of separation largely depends on blade loading and that the flow is highly three dimensional. In the scope of this investigation the flow separation did not depend on Mach number or Reynolds number, which is not surprising, since the flow can be considered incompressible and beyond the critical Reynolds number.

In this context, it should be mentioned that in order to determine the separation point, one can not rely upon the pressure distribution only, but must have additional information like flow visualization, hot-wire measurements, etc., to aid in its interpretation. For example, the pressure distribution at the casing (Fig. 6) suggests that there is no flow separation at the casing–suction side corner whereas the flow visualization reveals that a small region of backflow exists. The static pressure distribution only gives evidence of flow separation if the pitchwise extent of the separated region is large enough to affect the pressure field of the passage flow.

Pressure Fluctuation Along the Blade Suction Side. A blade similar to the one described above has been instrumented with 11 semiconductor pressure transducers (six on the suction side, five on the pressure side). The normalized root mean square of the static pressure fluctuation along the span and along the chord of the blade suction surface are shown in Fig. 10 in terms of a topological presentation.

Especially at the high angle of attack, it can be seen that there are local maxima of the pressure fluctuation. They become more pronounced toward the trailing edge. A comparison with Fig. 9 reveals that the loci of these maxima coincide with the blade separation line. Simpson et al. (1981a, 1981b) investigated two-dimensional separated boundary layers using the LDA technique. He observed that the maximum turbulence production is at the boundary of the separated region. These large-scale disturbances retain their coherence while diffusing downstream (Willmarth, 1975), thus increasing the turbulence level in addition to the local turbulence production. The pressure fluctuation was determined to be as high as 12 percent of the dynamic head at cascade inlet. The level of fluctuation within the attached boundary layer was some 3 percent of dynamic head, which is in accordance with Lim (1971) for boundary layers under the effect of an adverse pressure gradient. A local maximum in the distribution of the turbulent energy along the separation line was also observed by Gallus and Hönen (1986).

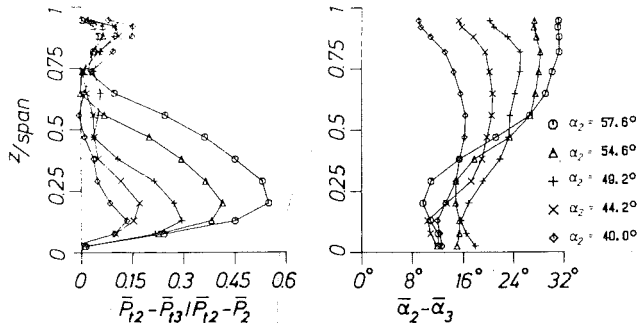

Fig. 12 *Circumferentially mass-averaged total pressure loss and flow turning*

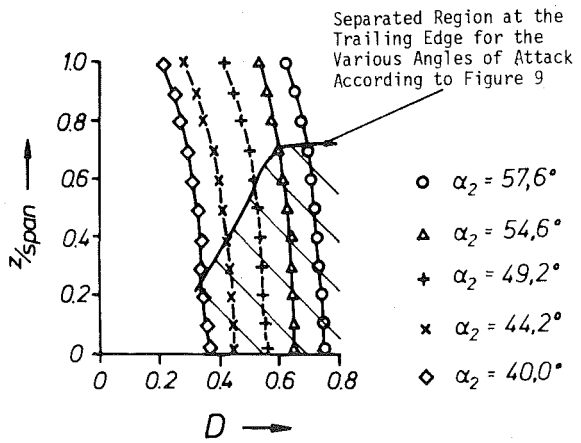

Fig. 13 **Spanwise distribution of diffusion factor at various angles of attack α_2 (from potential flow calculation)**

Pneumatic Probe Measurements at Cascade Exit. Detailed radial-circumferential measurements of the total and static pressure and the flow direction (yaw and pitch) were made at the cascade inlet plane (56 percent of axial chord ahead of the cascade leading edge) and at the cascade exit plane (35 percent of axial chord downstream of the cascade trailing edge). Pneumatic five-hole probes with a probe head diameter of 2.6 mm have been used. The uncertainty of the probe measurements was about ±2 percent in *Cp* and ±1 deg in flow angle. A description of the probe and its calibration is given by Bohn and Simon (1975).

Contour plots of the total pressure results at the cascade exit plane are shown in Fig. 11 at four angles of attack. The total pressure was measured relative to the cascade inlet total pressure at midspan. This pressure difference has been normalized with the midspan dynamic head at the cascade inlet. At $\alpha_2 = 40.0$ deg, the low total pressure regions are confined to the wakes and to the hub and tip regions adjacent to the suction surface. These low total pressure regions are the result of the secondary flow observed in Fig. 4 and the corner stall. The displacement of the wakes with respect to the physical location of the trailing edges in Fig. 11 is due to the remaining swirl of the flow at the cascade exit. Increasing angle of attack results in a spanwise and pitchwise growth of the hub corner stall region. It extends radially to approximately 65 percent at the trailing edge and gapwise to nearly a full pitch at the hub. The size of the low total pressure region at the tip is greatly reduced at the angle of attack increases. This is due to the displacement of the flow by the increased hub corner stall, which also has a major impact on the wake region.

The circumferentially mass-averaged spanwise distribution of total pressure loss, normalized with the dynamic head at the according spanwise position at cascade inlet and the turning of the flow, is shown in Fig. 12. High loss regions are located near the hub and near the tip. These regions are primarily due to the hub and tip secondary vortex flow and corner stall. At the high angles of attack the losses near the hub progressively grow as one would have expected from the total pressure contours and the flow visualization. The resulting redistribution of the flow inside the cascade passage due to the increased hub corner stall causes the small tip corner stall to contract even more. Regions of negative loss (total pressure rise) appeared because measurements were taken at constant radii rather than on constant streamsurfaces and also because of the mixing that occurs due to the strong secondary flow as described by Wisler et al. (1987). The spanwise variation of the flow angle $\alpha_2 - \alpha_3$ shows that while there is still a considerable amount of turning toward axial and thus diffusion at the tip, there is quite a bit of underturning close to the hub at higher angles of attack. This is due to the deflection of the flow caused by the blockage of the separated flow region. From that one can deduce the major impact the hub corner stall has on the cascade exit flow angle profile.

The results of the probe measurements are in good agreement with those of Joslyn and Dring (1985). However, the flow on the hub differs in that the present results show significant cross-passage secondary flow while their results showed no such large effects. This might be due to the lack of skew at the cascade inlet and the difference in aspect ratio, although large cross-passage secondary flows also have been found by Dong et al. (1987), Cyrus (1986), and Wisler et al. (1987).

Inviscid Flow Calculation. In order to examine the loading of the cascade in the case of inviscid flow, and to provide the pressure distribution along the blade as input for the boundary layer code discussed below, a potential flow calculation has been run on the cascade flow. The quasi-three-dimensional computational code solves the potential flow equation on S_1-S_2 surfaces and is described by Lücking (1982). From the area-averaged results at cascade inlet and cascade exit the spanwise diffusion factors (Lieblein, 1959) have been calculated as shown in Fig. 13. Also indicated is the boundary of the separated region at the trailing edge as deduced from Fig. 9 and from flow visualization tests (Fig. 20). Taking into account the well-known limit for diffusion factor of $D = 0.6$ (Lieblein, 1959) one can see from Fig. 13 that there should be no flow separation up to an angle of attack of $\alpha_2 = 49.2$ deg. Therefore it should be noticed that although the diffusion factor indicates the increased loading on the cascade, it does not predict the onset of flow separation properly. This is not surprising, since the diffusion factor is deduced from two-dimensional cascade data and the major reasons for the flow separation in the compressor cascade described above are three-dimensional flow effects. This suggests that in order to provide an approximate tool for the designer of axial compressors in terms of diffusion factor, three-dimensional effects like radial pressure gradient and flow blockage somehow have to be taken into account.

Suction Surface Boundary Layer Investigations. As has been seen in the abovementioned investigations, a major source of the loss in the compressor cascade is due to the separation of the suction surface boundary layer. The development of the boundary layer and determination of the loci of its transition and separation are therefore of great interest. Hot-wire measurements are a well-known technique to survey boundary layers and it has been established by Hodson (1983) that they also reliably can detect separated flow and boundary layer transition. Here, the results of the hot-wire measurements have been supplemented by hot-film measurements and an oil flow visualization technique. The measured velocity profiles were fitted through a log-wall type of approximation, and the wall shear stress and the integral

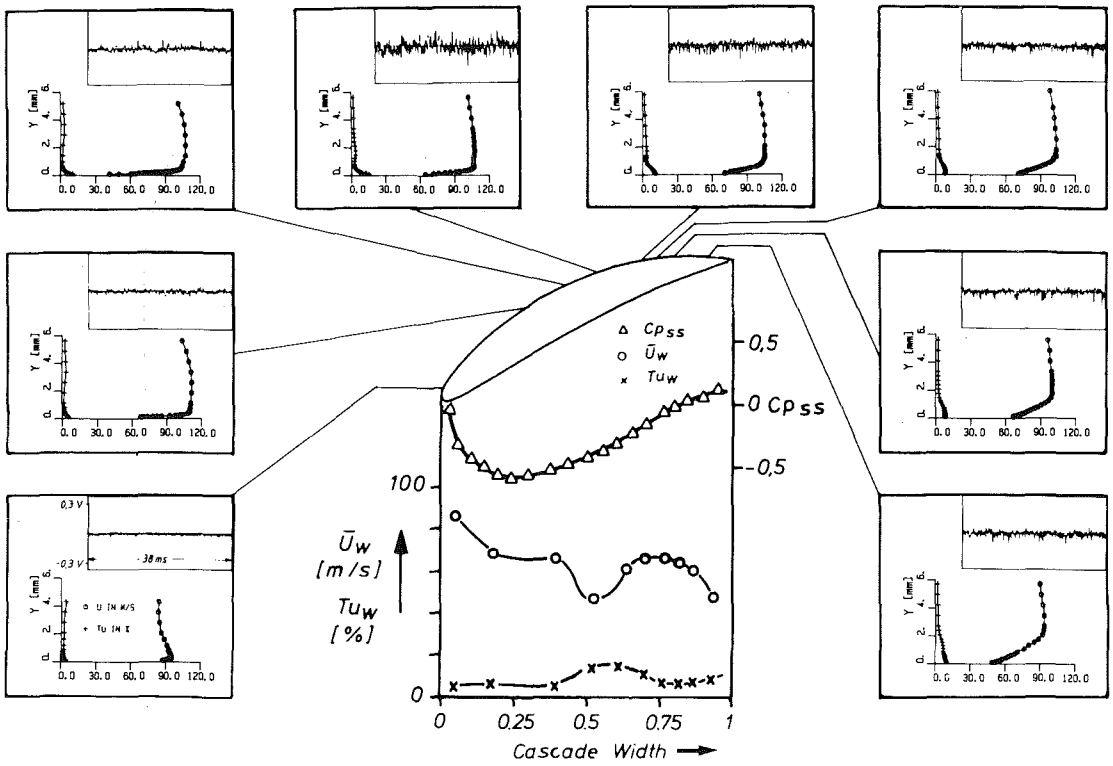

Fig. 14(*a*) Midspan

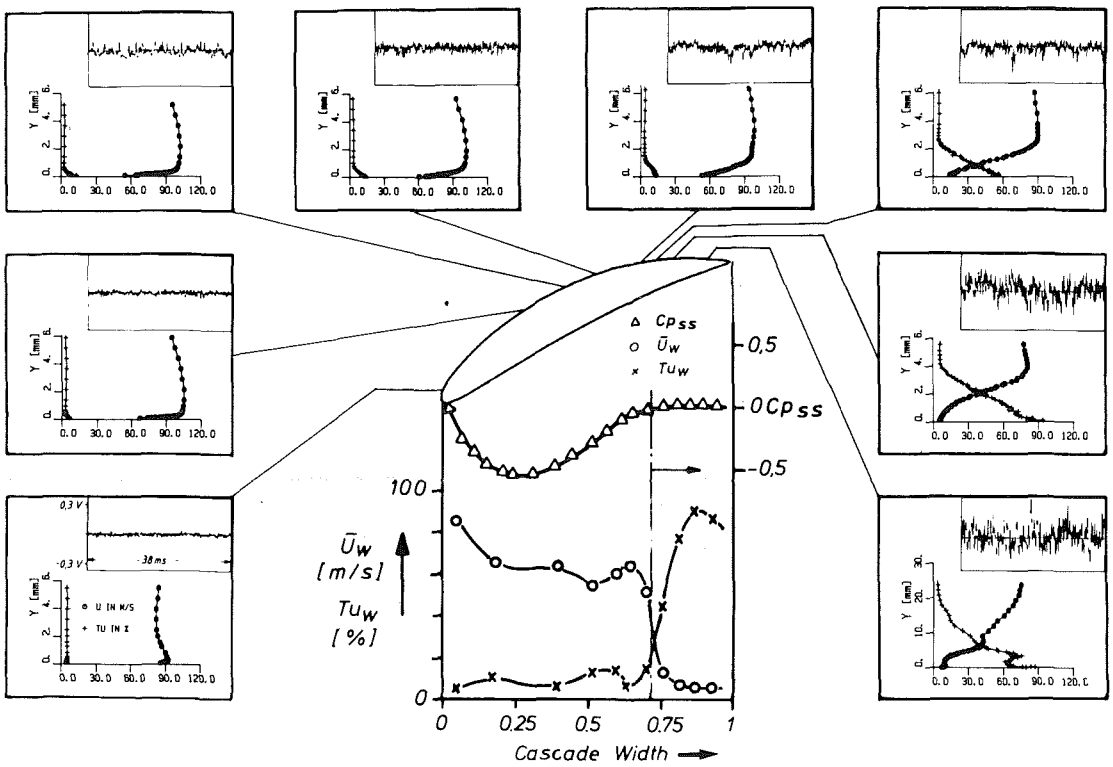

Fig. 14(*b*) 13 percent span

Fig. 14 Hot-wire measurements of the blade suction side boundary layer (including real time traces close to the blade surface), angle of attack $\alpha_2 = 44.2$ deg; leading plots contain the legend for all other plots

values of the boundary layer were deduced from there. All results have been compared with an integral boundary layer prediction method.

Hot Wire Measurements. The boundary layer has been scanned by a single-wire boundary layer probe at various chordwise and spanwise positions. The probe has been moved along the blade suction side by a newly designed mechanism, which allows the continuous, remote-controlled axial, radial, and circumferential traversing of a probe inside the flow

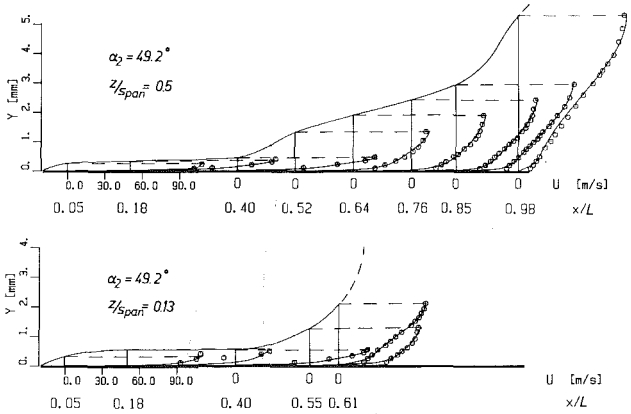

Fig. 15 Comparison of measured velocity profiles and a log-wall approximation

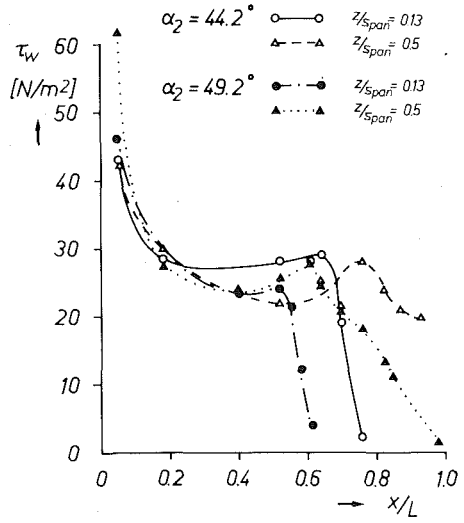

Fig. 16 Deduced wall shear stresses

passage. The probe also is a special design, incorporating an additional prong, which causes the stepmotor to stop if it touches the blade, thus positioning the probe at exactly 0.15 mm away from the surface. The hot wires were calibrated in a low-turbulence wind tunnel. A least-squares-error criterion was used to decide upon the best fit for the general form of King's law through the calibration points. Based on the investigations of Oka and Kostic (1980) and our own experiments, the influence of wall proximity on the hot-wire measurements has been negligible because of the high free-stream velocity (100 ms). Due to directional insensitivity of the hot wire, errors in measuring the averaged flow velocity and velocity fluctuation occur if the degree of turbulence exceeds 30 percent. Unfortunately these errors largely depend on the structure of turbulence, i.e., the probability density distribution of the velocity fluctuations, and according to Bradbury (1976) and Tutu and Cevray (1975) there is no sensible approach to correcting the hot-wire results. Therefore, care has to be taken when interpreting the boundary layer measurements at high turbulence level, especially in the presence of backflow. In general, the average flow velocity will be measured too high and the velocity fluctuation too small (Dengel and Vagt, 1983). In spite of these restrictions and the inability of the single hot wire to resolve the radial flow component, the measurements provide a good insight into the development of the boundary layer and the locus of its separation.

Figure 14 presents the boundary layer profiles along the chord at midspan and close to the hub. The midspan angle of attack is $\alpha_2 = 44.2$ deg. Also shown are the measured velocity (U_w), the degree of turbulence (Tu_w), and the hot-wire real time traces 0.15 mm away from the blade surface. The measured Cp distribution is indicated for comparison. At midspan (Fig. 14*a*) it is apparent that the boundary layer remains attached along the whole blade chord. The boundary layer is very thin (0.3 mm) close to the leading edge due to the acceleration of the flow, and accurate measurements are difficult. The boundary layer increases in thickness toward the trailing edge (up to 2 mm) because of the adverse pressure gradient. Figure 14(*b*) shows similar development of the boundary layer close to the hub at the first 70 percent of chord. At 75 percent chord there is a marked increase in turbulence level and the velocity drops to nearly zero. The degree of turbulence close to the wall got as high as 95 percent, indicating flow separation and intermittent backflow. As discussed above, the hot-wire measurement can not detect backflow due to signal rectification, and therefore the region where the turbulence level exceeds 30 percent is indicated through a dashed line. However, the locus of flow separation could be accurately determined and coincides with the one indicated by the Cp distribution.

There is an apparent drop in velocity and a rise in turbulence level close to the wall between 45 percent and 60 percent of chord. This is due to transition, occurring in the decelerating part of the boundary layer. Another indication of transition has been given by the hot-wire real time traces, showing typical turbulent bursts occurring at about 50 percent of chord. Also visible are the breakdown of the flow and high velocity fluctuations close to the hub when the flow separates beyond 75 percent of chord.

The measured velocity profiles prior to separation have been fitted through a split law of the wall approximation. Close to the wall, up to a dimensionless distance from the wall y^+ less than 50, the formula deduced by van Driest (1956) has been used, and for $y^+ > 50$ the law of the wall–law of the wake formulation (Kline et al., 1983) based on the empirical correlation by Coles (1956) has been incorporated

$$Y^+ < 50; \quad U^+ = \int_0^{Y^+} 2dy^+ / (1 + 4(K - Y^+)^2(1 - \exp(-Y^+/A^+))^2)^{0.5})$$

$$Y^+ > 50; \quad U^+ = 1/K \ln Y^+ + C + \pi(x)/K \cdot (1 - \cos(\pi Y/S))$$

$$K = 0.41, \quad C = 5.0$$

The shear stress velocity U^+, the van Driest damping factor A^+, and the wake parameter $\pi(x)$ have been varied to get the best fit through the measured velocity values. Figure 15 shows a comparison of the hot-wire measurements and the approximation.

As long as the errors in the measurement due to rectification effects of the hot wire are small, i.e., if the flow is not separated, an excellent fit of the approximation to the measurements is achieved. From Fig. 15 it is apparent that for $\alpha_2 = 49.2$ deg at midspan the boundary layer separates at the trailing edge, indicated by a marked increase in boundary layer thickness and by the shape of the velocity profile. Close to the hub it separates just beyond 61 percent of chord, which is coherent with Fig. 9. In the future it will be investigated whether the deduced values of A^+ and $\pi(x)$ follow some kind of law in order to find an indication for separation and whether the approximation can also be applied to the velocity profiles in separated flow. So far the approximation has been used to evaluate the integral boundary layer values and to get a more accurate description of the wall shear stress development, which is shown in Fig. 16. From there it can be seen that the wall shear stress decreases from its maximum at the leading edge toward a local minimum where the boundary

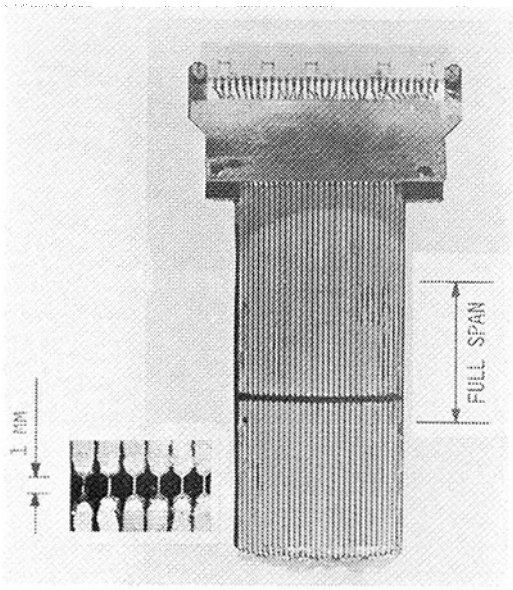

Fig. 17 Instrumented elongated blade incorporating 31 surface-mounted hot films along the suction side (the inset is a blowup of the sensor area)

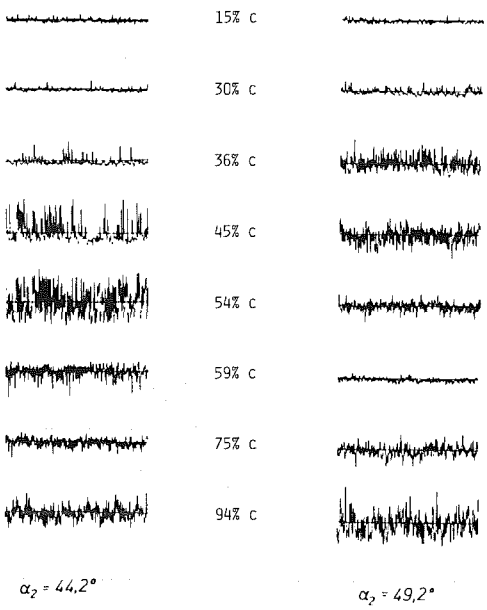

Fig. 18 Hot-film real time traces at blade suction surface (midspan)

layer undergoes transition and the wall shear stress rises again. It then decreases due to the deceleration of the flow and falls to zero once the flow approaches separation.

Surface-Mounted Hot-Film Measurements and Oil Flow Visualization. In order to define the location of the boundary layer transition more accurately, an oil film technique (Maltby, 1962) and surface-mounted hot-film probes were applied. The hot-film sensors have a reasonably high temporal resolution, and therefore it is possible to identify the state of the boundary layers by examining their output signals. An elongated blade similar to the one being used to measure the blade surface pressure distribution was instrumented with 31 hot-film sensors along the blade suction side (Fig. 17) and then traversed radially across the span.

Their output signals were analyzed using a transient recorder and a fast Fourier analyzer. The unsteady heat

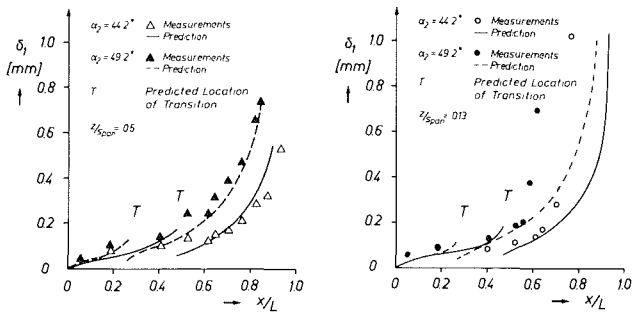

Fig. 19 Comparison of measured and calculated displacement thickness (*T* denotes the predicted location of the boundary layer transition)

transfer signals of the hot-film sensors at blade midspan are shown in Fig. 18. To aid the interpretation, an oil flow visualization technique has been applied to the blade suction surface (Fig. 20). The hot film traces at $\alpha_2 = 44.2$ deg show that the first two signals contain relatively low-frequency fluctuations interspersed with very little bursts of larger amplitude, higher frequency fluctuations. They indicate the intermittent change from laminar to turbulent flow, where the shear stress is higher than in the laminar case. This generation of turbulence continues and the turbulent spots coalesce until the boundary layer is fully turbulent 59 percent downstream of chord.

Interpreting Fig. 20, it can be observed that a laminar separation bubble occurs between 35 percent and 60 percent of chord. Therefore it must be concluded that the boundary layer is being kept laminar by the acceleration of the outer flow, even if it is on the verge of transition, up to 54 percent of chord. The low-frequency fluctuation of the second signal might also result from the diffusing boundary layer's inability to quench any disturbances that may naturally arise (Hodson, 1985) and to the overall turbulence level of the free stream, which was measured to 1.2 percent at midspan cascade inlet. When increasing the incidence by 5 deg ($\alpha_2 = 49.2$ deg) the separation bubble moves farther upstream as a result of the earlier onset of diffusion (Fig. 20). The hot-film traces show a high intermittency of turbulent spots already at 30 percent of chord, and the boundary layer undergoes transition at about 45 percent chord. At 94 percent chord the large amplitudes of the heat transfer fluctuation indicate—like the hot-wire traces in Fig. 14(*b*)—the onset of boundary layer separation.

The oil flow visualization in Fig. 20 indicates the chordwise and spanwise extent of the laminar separation bubble on the suction and on the pressure side. It can be deduced that the profile boundary layer close to the hub and to the casing are already turbulent due to mixing with the endwall boundary layer. Although dye injected into the bubble through pressure taps did not spread out in spanwise direction (not shown here), the oil traces indicate that no natural transition occurs, but there is transition via a separation bubble, which is most likely at these free-stream turbulence conditions (Hoheisel et al., 1987). However, the laminar separation bubble can not extend very far normal to the blade surface, since it is barely visible in the measured Mach number distribution at midspan (Fig. 20) and in the hot-wire measurements (Fig. 14).

Boundary Layer Prediction Technique. Prediction of the blade surface boundary layer development has been made using a boundary layer integral method described by Truckenbrodt (1952). Additional empirical criteria given by Dunham (1972) have been incorporated to predict boundary layer transition and turbulent separation. The measured and predicted Mach number distributions from the inviscid flow calculation discussed earlier were used as input data. Figure 20 displays the predicted location of transition (T) and of turbulent

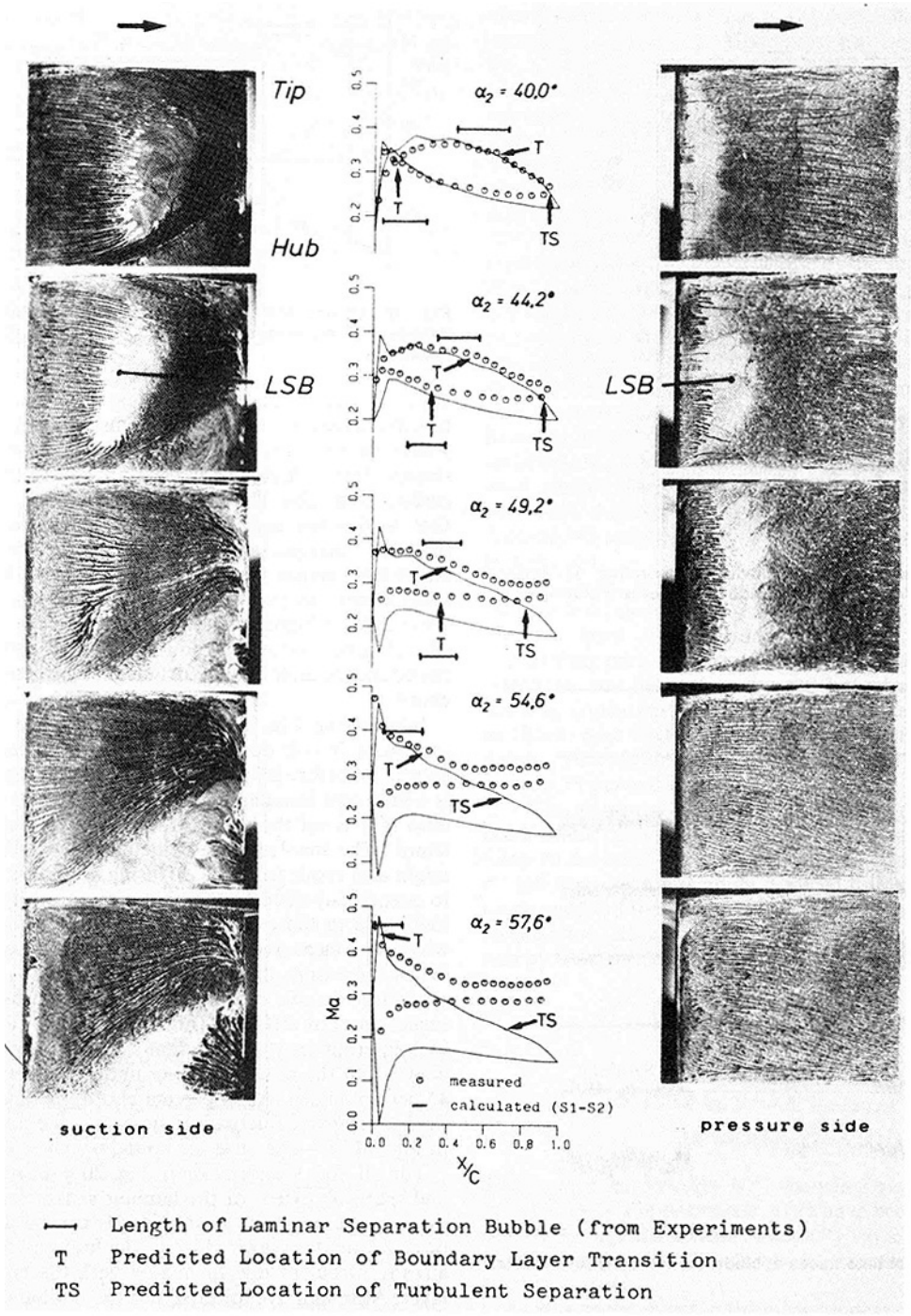

Fig. 20 Oil flow visualization and comparison with prediction at midspan

separation (*TS*) and the chordwise extent of the laminar separation bubble (⊢⊣) deduced from the flow visualization and hot-film measurements. If the measured Mach number distribution is used as input data, the boundary layer code is very accurate in predicting the location of transition on the suction and pressure sides. The code also predicts transition to occur always via a laminar separation bubble. At the existing free-stream turbulence level of 1.2 percent, the predicted location of boundary layer transitions deduced from both applied criteria did not vary more than 4 percent from each other.

However, the code failed in predicting the location of the turbulent separation when using the measured Mach number distribution as input data. This is because of the influence the separation has on the pressure field of the core flow. Since the severe blockage due to the separated flow inhibits a further diffusion of the flow, the pressure remains constant downstream of the separation, and the code fails in predicting turbulent separation. By using the calculated inviscid Mach number distribution as input data (from the $S_1 - S_2$ calculation), the boundary layer method predicted a turbulent separation due to the calculated ongoing diffusion in the absence of separation. The inviscid flow calculation does not take into account blockage due to boundary layer buildup, and therefore the results largely deviate from the measured values with increasing angles of attack. However, at midspan in the cases of light blade loading ($\alpha_2 = 44.2$ deg and $\alpha_2 = 49.2$ deg) the agree-

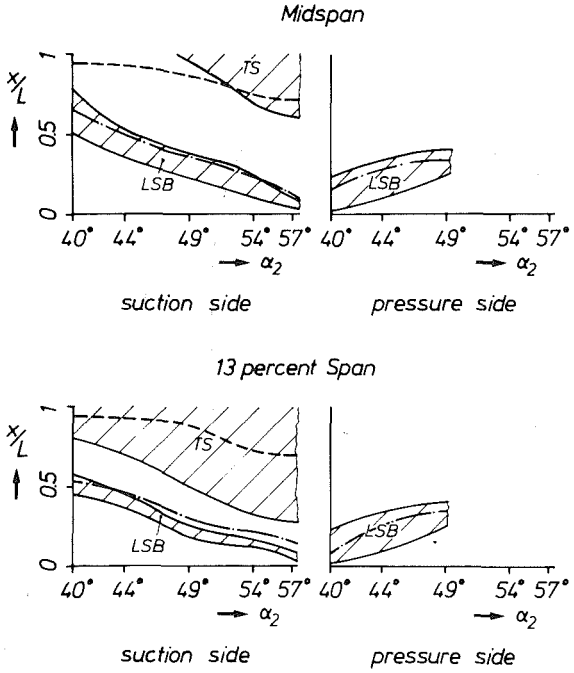

Fig. 21 Summary of boundary layer investigation

ment of the predicted integral boundary layer values with measured values is excellent (Fig. 19*a*). The predicted distribution of boundary layer integral values close to the hub (Fig. 19*b*) did not vary much from those at midspan. The measurement values show a good agreement up to 50 percent of chord, but large deviations downstream of midpassage. This is due to the early onset of separation, caused by the three-dimensional effects inside the compressor cascade discussed earlier, which could not effectively be simulated by the calculation.

The results of the boundary layer measurements and calculations are summarized in Fig. 21.

The extent of separated flow in the chordwise direction is indicated versus angle of attack at midspan and close to the hub (13 percent span). Regions of separated flow determined from experiments are hatched. The laminar separation bubble (LSB), predicted using the measured data as input, is indicated by a dashed and dotted line. The onset of turbulent separation (*TS*), predicted using the calculated Mach number distribution, is indicated by a dashed line. At midspan, where the flow is nearly two dimensional for most of the angles of attack under investigation, i.e., α_2 less than 50 deg, the laminar separation bubble and the turbulent separation could be predicted very accurately. At the suction side the onset of laminar separation moves upstream with increasing angle of attack and the chordwise extent of the bubble decreases. From measurements turbulent separation at midspan starts at angles of attack greater than 49 deg. It has been predicted to be too far downstream at α_2 greater than 52 deg because of the growing influence of the hub–suction side corner separation. At 13 percent span the laminar separation bubble decreases in size because of the higher turbulence level due to the influence of the hub boundary layer. While the prediction of the laminar separation bubble is still reasonable, the boundary layer method fails in predicting the onset of separation, due to the influence of the secondary flow and the hub–suction side corner separation.

The flow at the pressure side has been found to be nearly two dimensional. The laminar separation bubble moves upstream with increasing angle of attack and vanishes beyond α_2 greater than 49 deg. The flow was found then to be laminar along the whole blade chord in the experiments and in the calculations.

Conclusions

Experiments have been performed in a subsonic annular compressor cascade operated at various blade loadings. The paper has presented some results of an ongoing detailed experimental study, including airfoil and endwall surface flow visualization, surface static pressure contour plots, total pressure and flow angle distributions at the cascade exit, blade pressure fluctuations, and hot-wire and hot-film measurements along the blade suction surface. The blade boundary layer data have been compared with predictions from an inviscid throughflow analysis and an integral boundary layer method.

The suction surface–endwall corner separation was the primary three-dimensional feature of the flow. It did exist at all points of operation under investigation, the one at the hub growing and the smaller one at the casing diminishing with increasing angle of attack.

The surface flow visualization suggested significant secondary flows, which are partly responsible for the suction side–hub corner separation. The cross-passage flow at the hub moves upstream close to the suction surface and generates a vortex with a clockwise orientation. The low-pressure region in its center was clearly visible in the hub static pressure distribution. The separations in the suction surface–hub endwall corner and the secondary flows were responsible for the high loss found downstream.

Significant fluctuations of the static pressure have been observed along the blade suction separation line. Their maximum root mean square values were observed to be as high as 12 percent of the dynamic head at the cascade inlet.

Boundary layer transition appears to be always coupled with a laminar separation bubble in the Reynolds number range and turbulence level of interest. The bubble moves upstream along the suction side and downstream along the pressure side with increasing angle of attack.

While the prediction of the boundary layer transition appeared to be very accurate using the applied calculations, it failed in predicting the onset of separation in the presence of three-dimensional flow.

In experiments to come the development of the hub boundary layer and the influence of rotor wakes generated upstream of the cascade will be investigated.

Acknowledgments

The work reported herein was supported within the framework of research programs of the "Deutsche Forschungsgemeinschaft." Permission for publication is gratefully acknowledged. The authors are also indebted to R. Loesch-Schloms and A. Beckers for their help in carrying out these investigations.

References

Bohn, D., and Simon, H., 1975, "Mehrparametrige Approximation der Eichräume und Eichflächen von Unterschall- bzw. Überschall-5-Loch-Sonden," ATM *Meßtechnische Praxis*, Lieferung 470.

Bradbury, L. J. S., 1976, "Measurements With a Pulsed Wire and a Hot Wire Anemometer in the Highly Turbulent Wake of a Normal Plate," *Journal of Fluid Mechanics*, Vol. 77, Part 3, pp. 473–497.

Coles, D., 1956, "The Law of the Wake in the Turbulent Boundary Layer," *Journal of Fluid Mechanics*, Vol. 1, pp. 379–389.

Cyrus, V., 1986, "Experimental Study of Three-Dimensional Flow in an Axial Compressor Stage," ASME Paper No. 86-GT-118.

Dengel, P., and Vagt, J. D., 1983, "A Comparison Between Hot Wire and Pulsed Wire Measurements in Turbulent Flows," *Proceedings 4th Turbulent Shear Flow Conference*, Karlsruhe.

Dong, Y., Gallimore, S. J., and Hodson, H. P., 1987, "Three-Dimensional Flows and Loss Reduction in Axial Compressors," ASME JOURNAL OF TURBOMACHINERY, Vol. 109, pp. 354–361.

Dring, R. P., Joslyn, H. D., and Hardin L. W., 1982, "An Investigation of Compressor Rotor Aerodynamics," ASME *Journal of Engineering for Power*, Vol. 104, pp. 84–96.

Dring, R. P., Joslyn, H. D., and Wagner, J. H., 1983, "Compressor Rotor Aerodynamics," *AGARD-CP-351*, Ref. 24.

Dunham, J., 1972, "Prediction of Boundary Layer Transition on Turbomachinery Blades," *AGARDograph* No. 164, pp. 55–71.

Gallus, H. E., and Hönen, H., 1986, "Experimental Investigations of Airfoil and Endwall Boundary Layers in a Subsonic Compressor Stage," ASME Paper No. 86-GT-143.

Gallus, H. E., and Hönen, H., 1983, "Measurements of 3D Unsteady Flow Downstream of Rotor and Stator Blades in Axial-Flow Compressors," GTSJ Paper No. 83-Tokyo-IGTC-68.

Hodson, H. P., 1983, "The Detection of Boundary Layer Transition and Separation in High Speed Turbine Cascades," *Proceedings 7th Symposium on Measuring Techniques in Transonic and Supersonic Flow in Cascades and Turbomachines*, Aachen.

Hodson, H. P., 1985, "Boundary-Layer Transition and Separtion Near the Leading Edge of a High-Speed Turbine Blade," ASME *Journal of Engineering for Gas Turbines and Power*, Vol. 107, pp. 127–134.

Hoheisel, H., Kiock, R., Lichtfuss, H. J., and Fottner, L., 1987, "Influence of Free-Stream Turbulence and Blade Pressure Gradient on Boundary Layer and Loss Behavior of Turbine Cascades," ASME JOURNAL OF TURBOMACHINERY, Vol. 109, pp. 210–219.

Joslyn, H. D., and Dring, R. P., 1985, "Axial Compressor Stator Aerodynamics," ASME *Journal of Engineering for Gas Turbines and Power*, Vol. 107, pp. 485–493.

Kline, S. J., Bardina, J. G., and Strawn, R. C., 1983, "Correlation of the Detachment of Turbulent Boundary Layers," *AIAA Journal*, Vol. 21, No. 1.

Lieblein, S., 1959, "Loss and Stall Analysis of Compressor Cascades," ASME *Journal of Basic Engineering*, pp. 387–397.

Lim, K. B., 1971, "A Study of Pressure Fluctuations in Turbulent Shear Flows Under the Effect of Mean Pressure Gradients," Ph.D. Thesis, University at Adelaide.

Lücking, P., 1982, "Numerische Berechnung der dreidimensionalen reibungsfreien und reibungsbehafteten Strömun durch Turbomaschinen," Ph.D. Thesis, Rheinisch-Westfälisch Technische Hochschule, Aachen.

Maltby, R. L., 1962, "Flow Visualization in Wind Tunnels Using Indicators," *AGARDograph* 70.

Oka, S., and Kostic, Z., 1980, "Influence of Wall Proximity on Hot Wire Velocity Measurements," DISA-Information 25.

Simpson, R. L., Chew, Y. T., and Shivaprasad, B. G., 1981a, "The Structure of a Separating Turbulent Boundary Layer. Part 1: Mean Flow and Reynold Stresses," *Journal of Fluid Mechanics*, Vol. 113, pp. 23–51.

Simpson, R. L., Chew, Y. T., and Shivaprasad, B. G., 1981b, "The Structure of a Separating Turbulent Boundary Layer. Part 2: Higher Order Turbulence Results," *Journal of Fluid Mechanics*, Vol. 113, pp. 53–73.

Truckenbrodt, E., 1952, "Ein Quadraturverfahren zur Berechnung der laminaren und turbulenten Reibungsschicht bei ebener und rotationssymmetrischer Strömung," *Ingenieur Archiv*, Vol. 4.

Tutu, N. K., and Cevray, R., 1975, "Cross Wire Anemometry in High Intensive Turbulence," *Journal of Fluid Mechanics*, Vol. 71, pp. 785–800.

van Driest, E. R., 1956, "On Turbulent Flow Near a Wall," *Journal of Aerospace Science*, Vol. 23, pp. 1007–1036.

Wagner, J. H., Dring, R. P., and Joslyn, H. D., 1985, "Inlet Boundary Layer Effects in an Axial Compressor Rotor: Part 1—Blade-to-Blade Effects," ASME *Journal of Engineering for Gas Turbines and Power*, Vol. 107, No. 2, pp. 374–380.

Willmarth, W. W., 1975, "Pressure Fluctuations Beneath Turbulent Boundary Layers," *Annual Rev. Fluid Mechanics*, Vol. 7, pp. 13–28.

Wisler, D. C., Bauer, R. C., and Okiishi, T. H., 1987, "Secondary Flow, Turbulent Diffusion, and Mixing in Axial-Flow Compressor," ASME JOURNAL OF TURBOMACHINERY, Vol. 109, pp. 455–482.

D. G. Gregory-Smith
School of Engineering and
Applied Science,
University of Durham,
Durham DH1 3LE, United Kingdom

J. A. Walsh
Logica Space and Defence Systems Ltd.,
London W1A 4SE, United Kingdom

C. P. Graves
Gilbert Gilkes and Gordon Ltd.,
Cumbria LA9 7BZ, United Kingdom

K. P. Fulton
Rolls-Royce plc,
Derby DE2 8BJ, United Kingdom

Turbulence Measurements and Secondary Flows in a Turbine Rotor Cascade

This paper presents results for turbulence measurements that have been made using hot-wire anemometry in the endwall region of a high turning rotor blade cascade. It is shown that the levels of turbulence are very high in the regions of the flowfield containing the passage vortex and its associated loss core. A comparison with the total pressure loss measurements illustrates the mechanisms of loss generation within the cascade. The growth of turbulent kinetic energy was much less than the growth of loss indicating significant viscous dissipation.

Introduction

Secondary flows are transverse velocity components produced when a nonuniform flow is turned. In a turbine cascade secondary flows are often considered to be the difference between the primary, or ideal, flow direction and that measured in the cascade. The reason for studying secondary flows is that they produce a spanwise variation of outlet angle in a cascade and that the secondary losses, due to the action of the secondary flows, may constitute a major portion of the losses within a blade row. Belik (1972) has stated that for low-aspect-ratio blading the secondary losses may be as large as the profile losses. In steam turbines the secondary flows are the source of undesirable concentrations of wetness and water film. Gaugler and Russell (1984) have shown, by a comparison of flow visualization and heat transfer measurements, that local peaks in heat transfer correspond to the secondary flow regions.

A comprehensive review of recent developments in the experimental study of secondary flows in axial turbines has been given by Sieverding (1985). However there is very little information available concerning the role of turbulence in the loss generation process in turbomachines. Although several workers have presented results of turbulence measurements for duct flows and for the downstream planes of cascades, the experimental techniques used have not always lent themselves to taking measurements within the blade row.

Turbulent flows in a strongly curved rectangular duct have been investigated by Humphrey et al. (1981), and further by Taylor et al. (1982), using the technique of laser-Doppler anemometry (LDA).

Results for the downstream planes of compressor cascades have been presented by Kiock (1973) and Raj and Lakshminarayana (1973). The latter found that the maximum turbulence intensity was located on the wake centerline close to the blade. Additional data for rotating blade wakes has been presented by Raj and Lakshminarayana (1976). An important finding was that in the rotating case all of the turbulence parameters were greater than those measured in the stationary cascades.

The endwall boundary layer in a turbine nozzle cascade was investigated by Senoo (1958). Instantaneous hot-wire traces were presented for the mainstream and endwall boundary layer flows. Langston et al. (1977) presented hot-wire results for the flow within the endwall boundary layer just upstream of the trailing edge plane of a turbine cascade. Although the turbulence intensities were found to increase as the endwall was approached, there were no data presented for the cascade bulk flowfield.

A large-scale turbine nozzle passage was investigated by Bailey (1980) using LDA with the leading edge vortex and blade wake suppressed. It was found that large regions of the passage vortex were of low turbulence intensity. It was suggested that this was a surprising result since it was thought that the passage vortex was composed mainly of turbulent inlet boundary layer fluid.

Moore et al. (1987) presented hot-wire results for a downstream plane of a turbine cascade that was geometrically similar to that of Langston et al. (1977). They were able to identify two mechanisms that could act to produce total pressure loss. There is a deformation work term that acts to produce mean kinetic energy from turbulent kinetic energy. There is also a reversible pressure work term that can exchange mean kinetic energy among its three components. The combined effect of these two mechanisms was found to offset the loss production rate caused by the shear of the primary flow in the endwall boundary layer. Zunino et al. (1987) have

Contributed by the International Gas Turbine Institute and presented at the 33rd International Gas Turbine and Aeroengine Congress and Exhibition, Amsterdam, The Netherlands, June 5–9, 1988. Manuscript received by the International Gas Turbine Institute June 24, 1987. Paper No. 88-GT-244.

Table 1 Cascade design data

Inlet flow angle	42.75 deg
Inlet blade angle	52.25 deg
Exit flow angle	−66.60 deg
Exit Blade angle	−67.50 deg
Blade chord	216 mm
Blade axial chord	175 mm
Span	457 mm
Pitch	191 mm
Aspect ratio	2.6
Zweifel loading coefficient	1.07
Reynolds number (based on chord and exit velocity)	5×10^5

Table 2 Inlet boundary layer data

Estimated 99 percent thickness	102.0 mm
Displacement thickness	12.1 mm
Momentum thickness	9.9 mm
Free-stream turbulence intensity	1.4 percent

presented measurements of the turbulent kinetic energy of the flowfield in a large-scale, high turning, steam turbine rotor cascade.

A program of work at Durham University is studying both experimental and theoretical aspects of secondary flows in high turning turbine rotor blade cascades with the aim of improving prediction and design procedures. Results for the mean velocity flowfield have been presented by Gregory-Smith and Graves (1983) and by Gregory-Smith et al. (1988). The objectives of the work presented in this paper were:

(*a*) to obtain details of the turbulence in the flowfield

(*b*) to relate the turbulence to the loss generation

(*c*) to provide data for the development of prediction techniques.

Apparatus

Hot-wire anemometry measurements have been made in a large-scale low-speed linear cascade consisting of blades scaled from the midspan section of a high-pressure turbine rotor design. The main geometric parameters for the cascade are given in Table 1.

Angles are measured relative to the axial direction and there is no tip clearance.

The cascade was constructed with slots at ten axial locations as shown in Fig. 1. Results will be presented for measurements taken at slots 1, 5, 6, 7, 8, and 10.

The turbulence measurements were carried out using two miniature crossed hot-wire sensors (DISA 55P53 and DISA 55P54). The measuring plane of the two sensor types differed by 90 deg relative to the sensor support (DISA 55H24). For one probe the measurement plane of the crossed wires was parallel to the endwall, and the probe was approximately aligned with the mean flow direction (the U–V plane). The measurement plane for the other probe was formed by the radial direction and the mean flow direction (the U–W plane). In order to obtain second-order correlations the flowfield was traversed separately using each of the two sensors.

The instrumentation used for hot-wire anemometry is very complex and great care has to be taken in order to obtain good quality results. The data collection technique, which used DISA 55M01 Constant Temperature Bridges and PROSSER 6130 Linearisers, has been fully described by Walsh (1987).

The measurements were recorded using a data acquisition system controlled by a microcomputer. The data were then

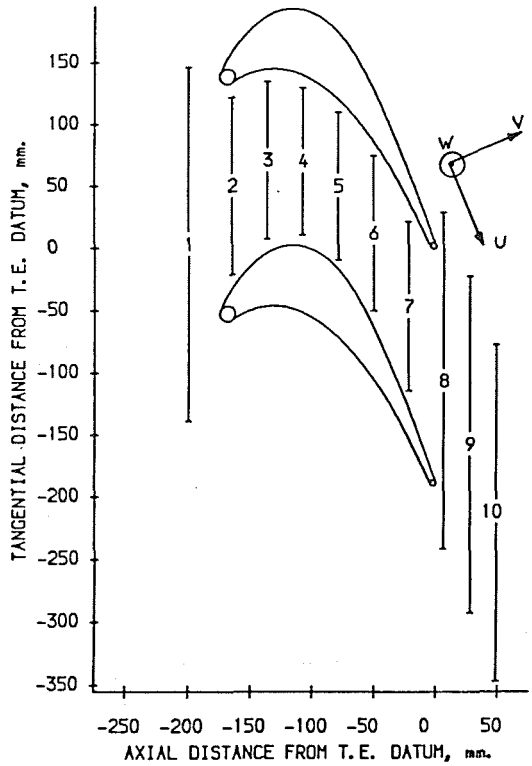

Fig. 1 Location of measurement planes

transferred to a mainframe computer for analysis and plotting. The method that was used to obtain the flow angles, the velocities, and the turbulence parameters from the recorded data has been described by Graves (1985). Hot-wire sensors need to be calibrated in a region of flow in which the velocity can be varied over the range that is to be measured. During this research two different hot-wire calibration techniques were used. Initially Graves (1985) calibrated his sensors in a jet of compressed air. However it is sufficient, if not preferable, to calibrate the sensors at a low turbulence position in the rig in which the measurements will be taken (Perry, 1982). An alternative technique of calibrating the sensors in the downstream slot (slot 10) of the cascade between the blade wakes was therefore adopted by Walsh (1987). Other steps taken to reduce experimental errors included filtering the air at inlet to the wind tunnel, frequent calibration checks, and the selection of amplifier gains and offsets to minimize the digitization errors.

Results

Inlet Flow. The inlet flow conditions are summarized in Table 2.

These data were obtained at slot 1, 14 percent of an axial chord upstream of the cascade. The high free-stream turbulence intensity was due to the honeycomb flow straightener placed upstream of the cascade. No attempt was made to simulate the very high turbulence levels experienced by turbine rotor blades placed downstream of stator blades.

Passage Flow. The area plots for slot 5, 55 percent of an axial chord from the leading edge of the blade, are presented in Fig. 2. The total pressure loss, turbulent kinetic energy, and

Nomenclature

U, V, W = velocity components in the streamwise, cross-passage, and radial (or spanwise) directions, respectively

u', v', w' = fluctuating velocity components

S_n = Strouhal number

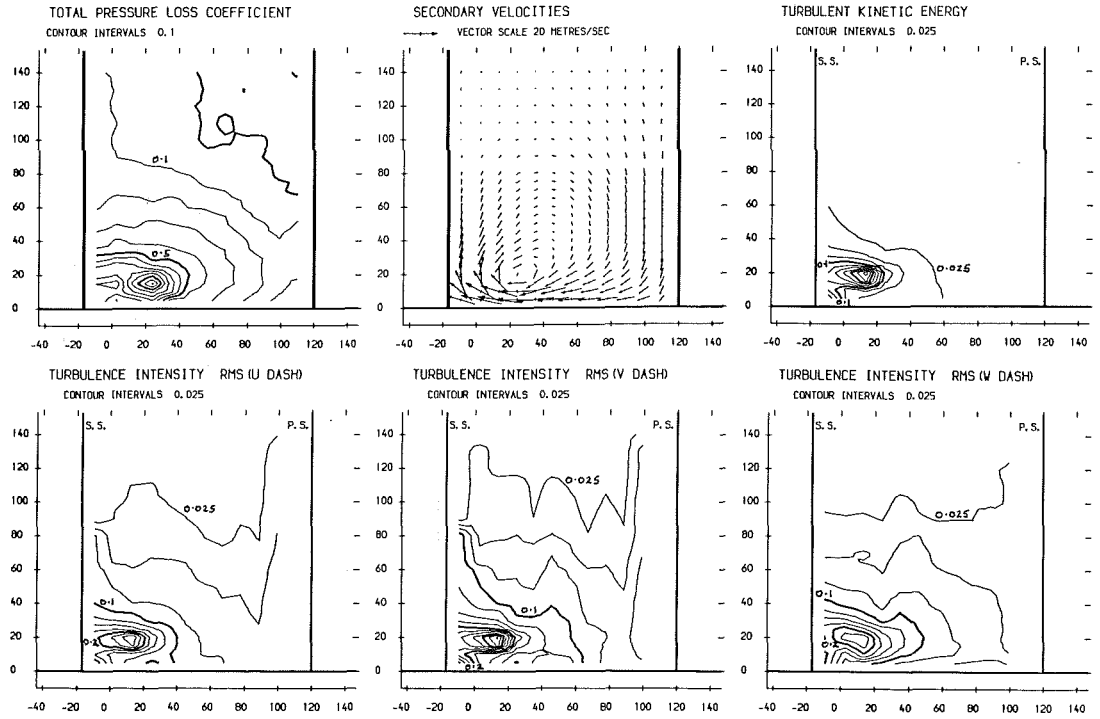

Fig. 2 Results for slot 5

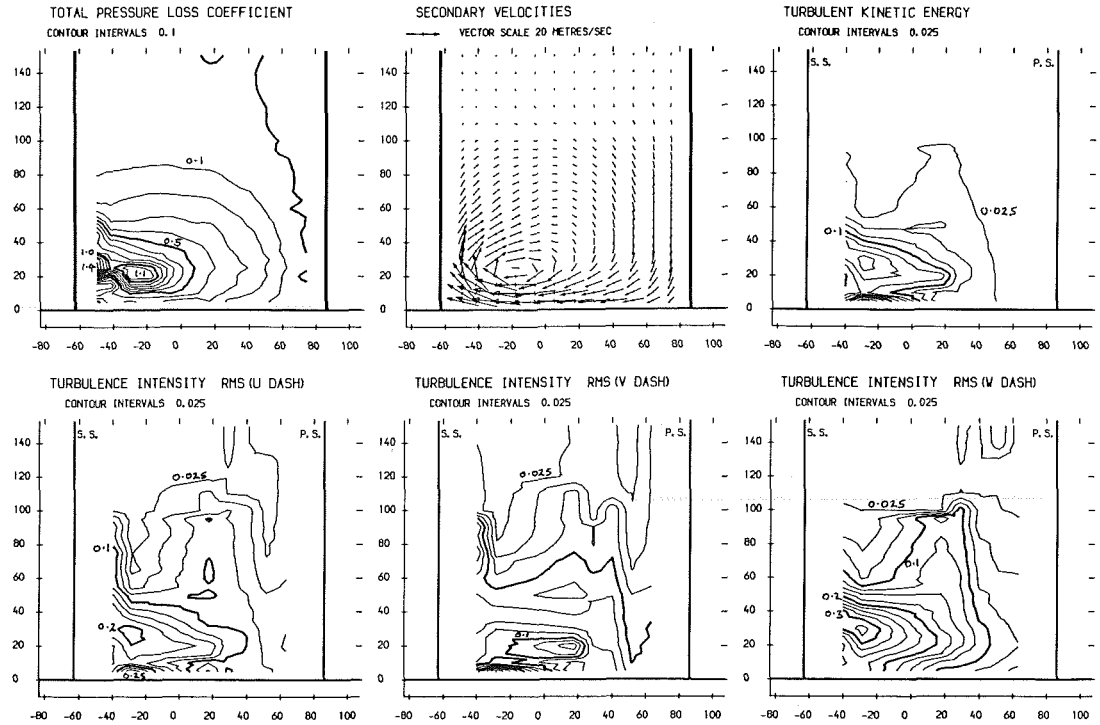

Fig. 3 Results for slot 6

rms turbulence intensities are normalized with respect to the inlet free-stream velocity. The secondary velocity vectors show the developing passage vortex. The turbulent kinetic energy contours may be compared with the total pressure loss contours that were obtained with a five-hole pressure probe. This is an interesting comparison since the production of turbulence is the first step in losing energy from the (steady) flow, if that flow is turbulent. In particular it can be seen that the center of the loss core appears further from the suction surface than the location of the peak turbulent kinetic energy value. However the location of this peak turbulent kinetic energy value does appear to be close to the center of the passage vortex as indicated by the secondary velocity vectors. Although the turbulence intensity contours appear to be similar, which would indicate isotropy, the v' component is larger than the other two components.

The area plots for slot 6, 71 percent of an axial chord from the leading edge of the blade, are presented in Fig. 3. The secondary velocity vectors show the continued development of the passage vortex and its migration up the suction surface of

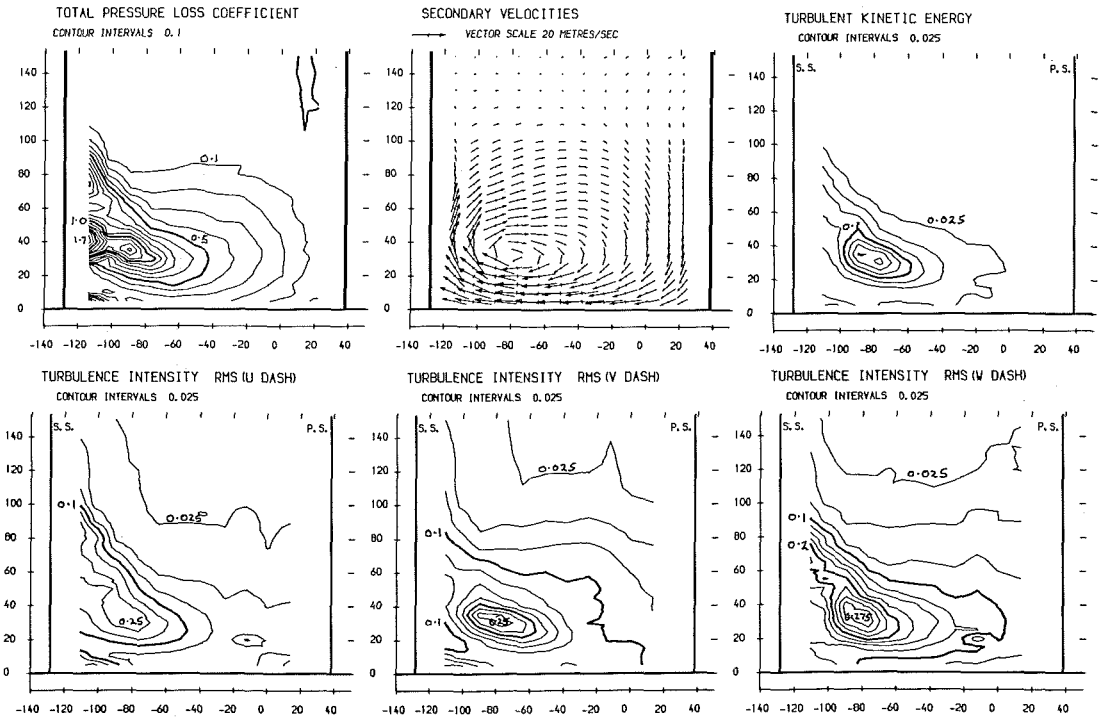

Fig. 4 Results for slot 7

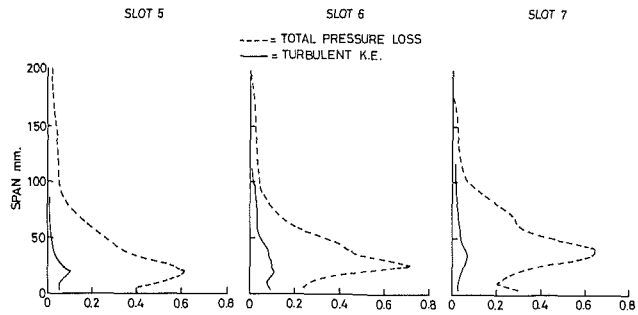

Fig. 5 Pitch-averaged through-passage results

the blade. A comparison of the turbulent kinetic energy contours with the total pressure loss contours again shows the noncoincidence of their respective peak values. The peak value of turbulent kinetic energy is located above and nearer the suction surface side of the loss core. Both the peak values of turbulent kinetic energy and total pressure loss have moved away from the endwall. Although the turbulence intensity contours show similar qualitative features for each of the velocity components it can be seen that the w' (spanwise) component has the largest peak value.

The area plots for slot 7, 87 percent of an axial chord from the leading edge of the blade, are shown in Fig. 4. The secondary velocities have increased in magnitude and the vectors show the continued development of the flow field. The passage vortex is seen to be migrating toward the suction surface of the blade and away from the endwall as a result of its growth in size. The peak value of turbulent kinetic energy is now found on the pressure surface side of the peak value of total pressure loss in the loss core. Although the turbulence intensity contours indicate a fair degree of isotropy, the w' component appears to have a slightly larger peak value than the other two components.

The pitch-averaged results for slots 5, 6, and 7 are shown in Fig. 5. The results for slot 5 show the peaks of turbulent kinetic energy and total pressure loss occurring at the same spanwise location from the endwall. This same feature is seen in the results for slot 6. The results for slot 7 show a broader loss peak. The countervortex causes the high loss and turbulent kinetic energy close to the endwall.

Downstream Flow. The area plots for slot 8, 3 percent of an axial chord downstream of the trailing edge plane of the cascade, are presented in Fig. 6. The secondary velocity vectors show the fully developed passage vortex and also the significant endwall counter vortex. When compared to the total pressure loss contours the turbulent kinetic energy contours show high values in regions associated with high total pressure loss. However there is poor repeatability of one blade wake compared to the other due to an insufficient number of probe traverses within the thin blade wakes. The repeatability within regions away from the blade wakes is much better. The peak value of turbulent kinetic energy is seen to lie in the wake region. However there is also a peak value in the region associated with the loss core but on the suction surface side of the passage vortex. Although poor wake-to-wake repeatability is a feature of the flowfield, the turbulence intensity contours, in the regions outside of the wake, show a fair degree of isotropy but with the v' intensity generally higher. The peak intensities are seen to occur in the regions occupied by the wake and also the passage vortex and its associated loss core.

The area results for slot 10, 28 percent of an axial chord downstream of the trailing edge plane of the cascade, are presented in Fig. 7. The secondary velocity vectors show the passage vortex and endwall counter vortices. The relatively weak counter vorticity on the midspan side of the passage vortex can also be seen. The loss contours show the blade wakes somewhat diffused near midspan compared to slot 8. However below the loss core the passage vortex has washed out the wake. A loss region near the endwall is associated with the endwall boundary layer loss being fed into the flow by the corner counter vortex. A striking feature of the turbulent kinetic energy contours is the dissipation in the blade wakes, whereas within the vortex core the turbulence has actually increased from slot 8. The loss from the endwall is associated with only a very low level of turbulence. The turbulence intensity contours show a reasonable degree of isotropy but with the v' intensity higher in the vortex core region.

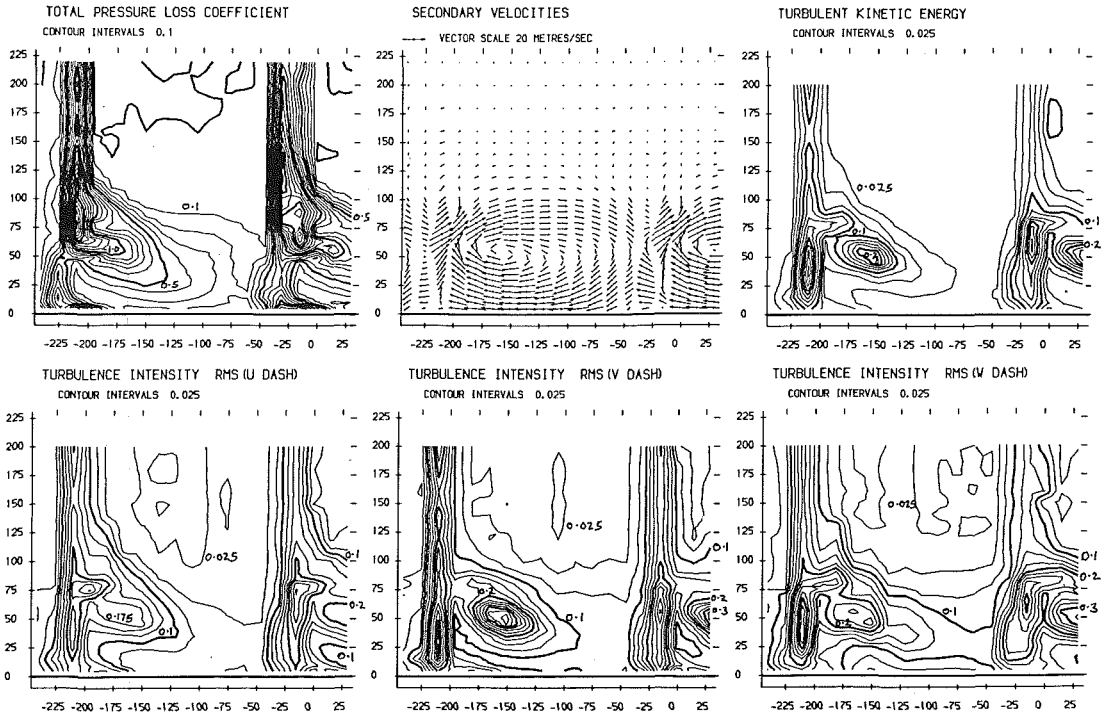

Fig. 6 Results for slot 8

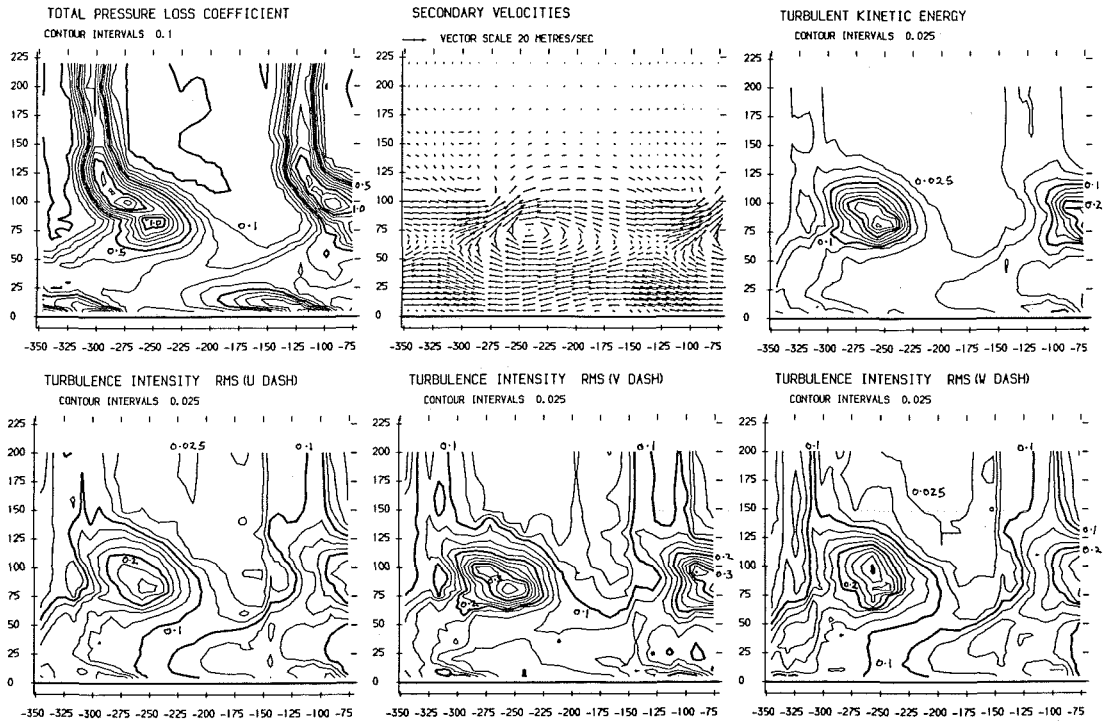

Fig. 7 Results for slot 10

The pitch-averaged results for the downstream planes are presented in Fig. 8. The results for slot 8 are similar to those presented for slot 7. Although the distributions of the total pressure loss and the turbulent kinetic energy are similar, there is an offset between them due to the addition of the turbulent kinetic energy in the blade wakes. The results for slot 10 show the loss and turbulence in the loss core convected further from the endwall. The endwall loss is seen to grow from slot 8 to slot 10 with no corresponding increase in turbulence.

Spectral Analysis. Because such high levels of turbulence were detected within the loss core a limited spectral analysis of the data has been carried out. A typical spectrum for the center of the loss core at slot 10 is presented in Fig. 9. At slots 1 and 6 it was difficult to identify any dominant frequencies in the range analyzed. The spectra for these slots showed that the turbulence activity was equally spread over all frequencies and may therefore be considered to be random in nature. However at slot 10 the frequency containing the most energy in the spectrum is in the band 27.5 Hz to 32.5 Hz. This cannot be due to vortex shedding from the trailing edge of the blade. For a trailing edge thickness of 5 mm, an exit velocity of 30 m/s, and a

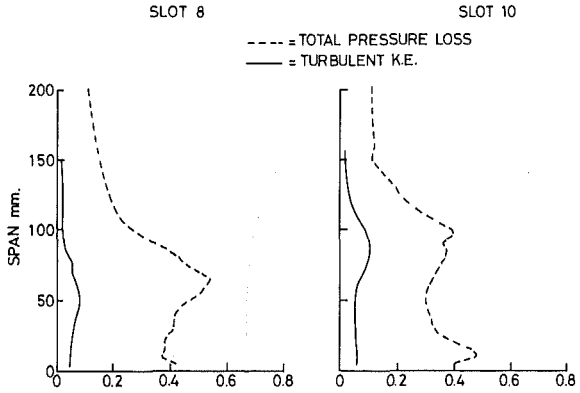

Fig. 8 Pitch-averaged downstream results

Strouhal number (S_n) of 0.2, a frequency of 1200 Hz would be expected as a result of the shedding of trailing edge vortices. Working back the other way by fixing the frequency at 30 Hz, a "thickness" of 200 mm is obtained (i.e., a dimension close to the blade chord or pitch). This result indicates a bulk unsteadiness of the fluid within the blade passage that may be associated with the movement of the passage vortex.

Development Through the Cascade. Area-averaged results are presented in Fig. 10 that compare the growth of total pressure loss and turbulent kinetic energy through the cascade. The error bands that are given for slots 1, 8, and 10 were obtained by integrating over different regions of the plane for pitch averaging. The error bands give a measure of repeatability and in the case of slot 8 the poor repeatability was due to the sparseness of traverse points in the wake regions. The total pressure loss is seen to grow throughout the cascade with a jump at the trailing edge. The loss is seen to continue to grow downstream of the blades due to the presence of the endwall. The turbulent kinetic energy grows steadily through the cascade although the value at slot 6 seems high. There is a jump in value across the trailing edge with a small growth downstream. Overall there is about a tenfold increase in turbulent kinetic energy. However it is clear that most of the loss is not going into turbulent kinetic energy and is therefore dissipated by viscous action.

Discussion

The flowfield of a large-scale low-speed linear cascade has been traversed with hot-wire probes. The results that have been obtained illustrate the link between total pressure loss growth and the production and dissipation of turbulent kinetic energy.

Although it is not possible to estimate the cumulative effect of experimental errors, steps were taken to ensure that errors were minimized at each stage of the experiments. Yavuzkurt (1984) has shown that ±5 percent is a reasonable estimate of the level of uncertainty for the velocity and normal Reynolds stresses for a slant wire in a two-dimensional flat plate boundary layer. Due to the similarity of the calibration techniques it is therefore assumed the results presented in this paper are subject to a similar level of uncertainty in the regions where the probe is reasonably aligned with the flow. However, since the probe could only be adjusted in the (U, V) plane the accuracy may be lower where high radial velocities exist. Such velocities occur from slot 6 onward, particularly near the suction surface of the blade. The shear stresses are more sensitive to experimental error than the normal stresses. So although the shear stresses in the (U, V) and (U, W) planes were calculated, the quality of the results was not sufficient to warrant their presentation here.

The upstream turbulence intensity level for the wind tunnel

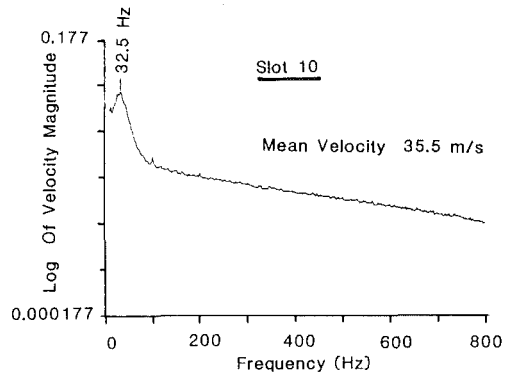

Fig. 9 Spectral analysis results

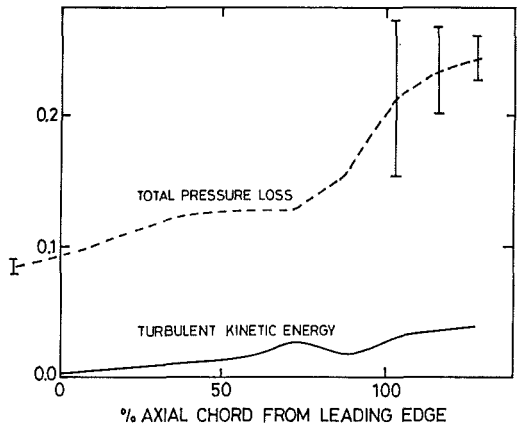

Fig. 10 Development of loss and turbulent kinetic energy

was at a higher level than quoted for most other comparable facilities. It can be argued that a high level of free-stream turbulence is more representative of the conditions that would be found in a real machine. The short spectral study did not detect discrete frequencies that could be associated with the blade passing frequency of the fan that was used to supply the air. It was therefore assumed that the cause of the high levels of turbulence was the honeycomb flow straightener that was placed at the entrance to the working section of the wind tunnel. The spectral study did detect a discrete frequency component downstream of the cascade that was associated with the passage vortex. The presence of such a frequency may indicate that such gross features should not be treated as random in nature.

Detailed traversing through the cascade with twin hot wires has shown that in all of the measurement planes there was a fair degree of isotropy. It has also been shown that the regions of high turbulent kinetic energy were associated with regions of high total pressure loss.

The levels of turbulence intensity found are higher than those of Moore et al. (1987) and Zunino et al. (1987). The former give a maximum local value downstream of 0.18, and the latter give a value of 0.07. These are to be compared with the maximum value of 0.275 at slot 10. These workers also report total pressure losses that were significantly lower than those measured in the Durham cascade. Compared to the Durham cascade, Moore et al. (1987) used a much lower aspect ratio (1.0) so that the two passage vortices strongly interacted resulting in a very different flow pattern. Although Zunino et al. (1987) had an aspect ratio of 2.5, their boundary layer at inlet was relatively thin. Both had low inlet free-stream turbulence (<0.5 percent) and neither reported the gross unsteadiness shown by the spectral study. Thus it is likely that the high inlet turbulence and gross unsteadiness were causing higher loss and a consequent generation of turbulence.

Another difference with Moore et al. (1985) is that they used a boundary layer trip on their blades, whereas Gregory-Smith et al. (1988) observed a laminar separation on the suction surface between slots 5 and 6. This may have affected the results at slot 6 near the suction surface and may be linked with the gross unsteadiness. Clearly more work is required to determine the exact effects of the separation and unsteadiness.

Within the blade passage the location of the peak value of turbulent kinetic energy did not coincide with the center of the loss core associated with the passage vortex. However the peak value of turbulent kinetic energy appears to be fairly mobile relative to the center of the loss core. Only far downstream do the two features actually coincide. The large difference between the loss growth and the growth of turbulent kinetic energy implies that the action of viscous dissipation was very important. This may be partly due to the possible laminar nature of the highly skewed endwall boundary layer, which is formed as a result of the rapid acceleration of the flow, and of the action of the passage vortex in sweeping the inlet boundary layer into the loss core. Also the wake turbulence caused by the blade profile was seen to dissipate rapidly downstream. Cleak (1987) has found that in calculating the flow through a similar cascade the best loss predictions are obtained when the flowfield is assumed to be substantially laminar. However there was a large increase in turbulent kinetic energy that was seen to be contained mainly in the loss core at slot 10, and that contained a dominant low frequency. It would appear that the passage vortex is creating the high turbulence and that the oscillation of its position may also contribute to the high turbulence that was measured.

The results that have been presented are an indication of the importance of turbulence in the loss generation process. It is clear that a good model of turbulence, and also of transition, will be necessary if the three-dimensional viscous flow calculation methods are required to give accurate predictions of loss. The data that have been presented will provide an exacting test case for any such methods.

Conclusions and Recommendations

A detailed experimental investigation of the flowfield of a large-scale low-speed linear cascade of turbine blades using hot-wire anemometry has shown that:

- Regions of high turbulent kinetic energy are associated with regions of high total pressure loss.
- The growth of turbulent kinetic energy through the cascade follows a pattern similar to that for the growth of total pressure loss, but the values are much lower. The action of viscous dissipation is therefore very significant.
- There was a discrete frequency present in the turbulence spectrum of the downstream flow associated with the passage vortex suggesting that such gross features should not be treated as random in nature.
- Data have been presented that will be very useful in developing and evaluating the new three-dimensional viscous flow calculation methods, and their associated turbulence models.

There is clearly further work that needs to be done. In particular the effects of free-stream turbulence need to be investigated since the role of turbulence in the loss generation process is not fully understood. The effect of free-stream turbulence on transition is also likely to be important. An investigation of the boundary layers on the surfaces of the blades will provide a useful contribution to the development of a model of transition.

Acknowledgments

This work has been carried out with the support of the Procurement Executive of the Ministry of Defence. The authors gratefully acknowledge additional support from Rolls-Royce plc and their permission to publish this paper. The authors are also grateful for the support that they received from the Science and Engineering Research Council.

Apology

The original paper in preprint form (No. 88-GT-244) contained some errors that affected the magnitude of the turbulence. The authors apologize for any inconvenience or confusion that this may have caused.

References

Bailey, D. A., 1980, "Study of Mean and Turbulent Velocity Fields in a Large-Scale Turbine-Vane Passage," ASME *Journal of Engineering for Power*, Vol. 102, pp. 88–95.

Belik, L., 1972, "Secondary Flow in Blade Cascades of Axial Turbomachines and the Possibility of Reducing its Unfavourable Effect," *Proceedings of the 2nd International JSME Symposium on Fluid Mechanics and Fluidics*, Tokyo.

Cleak, J. G., 1987, unpublished work at Durham University.

Gaugler, R. E., and Russell, L. M., 1984, "Comparison of Visualized Turbine Endwall Secondary Flows and Measured Heat Transfer Patterns," ASME *Journal of Engineering for Gas Turbines and Power*, Vol. 106, pp. 168–172.

Graves, C. P., 1985, "Secondary Flows and Losses in Gas Turbines," Ph.D. Thesis, Durham University.

Gregory-Smith, D. G., and Graves, C. P., 1983, "Secondary Flows and Losses in a Turbine Cascade," in: *Viscous Effects in Turbomachines*, AGARD-CP-351.

Gregory-Smith, D. G., Graves, C. P., and Walsh, J. A., 1988, "Growth of Secondary Losses and Vorticity in an Axial Turbine Cascade," ASME JOURNAL OF TURBOMACHINERY, Vol. 110, pp. 1–8.

Humphrey, J. A., Whitelaw, J. H., and Yee, G., 1981, "Turbulent Flow in a Square Duct With Strong Curvature," *Journal of Fluid Mechanics*, Vol. 103, pp. 443–463.

Kiock, R., 1973, "Turbulence Downstream of Stationary and Rotating Cascades," ASME Paper No. 73-GT-80.

Langston, L. S., Nice, M. L., and Hooper, R. M., 1977, "Three-Dimensional Flow Within a Turbine Cascade Passage," ASME *Journal of Engineering for Power*, Vol. 99, pp. 21–28.

Moore, J., Shaffer, D. M., and Moore, J. G., 1987, "Reynolds Stresses and Dissipation Mechanisms Downstream of a Turbine Cascade," ASME JOURNAL OF TURBOMACHINERY, Vol. 109, pp. 258–267.

Perry, A. E., 1982, *Hot-Wire Anemometry*, published by OUP.

Raj, R., and Lakshminarayana, B., 1973, "Characteristics of the Wake Behind a Cascade of Aerofoils," *Journal of Fluid Mechanics*, Vol. 61, pp. 707–730.

Raj, R., and Lakshminarayana, B., 1976, "Three-Dimensional Characteristics of Turbulent Wakes Behind Rotors of Axial Flow Turbomachinery," ASME *Journal of Engineering for Power*, Vol. 98, pp. 218–228.

Senoo, Y., 1958, "The Boundary Layer on the Endwall of a Turbine Nozzle Cascade," *Transactions of the ASME*, Vol. 80, pp. 1711–1720.

Sieverding, C. H., 1985, "Recent Progress in the Understanding of Basic Aspects of Secondary Flow in Turbine Blade Passage," ASME *Journal of Engineering for Gas Turbines and Power*, Vol. 107, pp. 248–257.

Taylor, A. M., Whitelaw, J. H., and Yianneskis, M., 1982, "Curved Ducts With Strong Secondary Motion: Velocity Measurements of Developing Laminar and Turbulent Flow," ASME *Journal of Fluids Engineering*, Vol. 104, pp. 350–359.

Walsh, J. A., 1987, "Secondary Flows and Inlet Skew in Axial Flow Turbine Cascades," Ph.D. Thesis, Durham University.

Yavuzkurt, S., 1984, "A Guide to Uncertainty Analysis of Hot-Wire Data," ASME *Journal of Fluids Engineering*, Vol. 106, pp. 181–186.

Zunino, P., Ubaldi, M., and Satta, A., 1987, "Measurements of Secondary Flows and Turbulence in a Turbine Cascade Passage," ASME Paper No. 87-GT-132.

Effects of Incidence on Three-Dimensional Flows in a Linear Turbine Cascade

A. Yamamoto

H. Nouse

National Aerospace Laboratory,
Chofu, Tokyo, Japan

The paper describes effects of the incidence on cascade three-dimensional flows and on the associated loss mechanisms occurring in a low-speed linear turbine rotor cascade. For each of five nominal incidences ranging from 7.2 to −53.3 deg, the cascade flow was surveyed at 15 or 16 planes located axially throughout the cascade. Blade-to-blade flows at the cascade midspan and near the endwalls, meridional flows along the blade surfaces, and static and total pressures within the cascade were analyzed in detail. The results were represented by two- or three-dimensional tomograms, on the surfaces of which the cascade flows were drawn by vectors, scalar contours, and streaklines, and from which one can easily understand the extraordinarily complicated cascade flows and the loss generation mechanisms. The present study will not only give new insight into the incidence effects, but will also contribute many solid experimental facts of a quantitative nature to our current knowledge of turbine cascade flows.

Introduction

The turbine blade row operates at various inlet flow angles (i.e., incidences), due to the change of rotational speeds of the preceding blades or of the blades in question. The incidence is one of the most important factors affecting turbine performance. The overall loss tendency with incidence variation, however, is well known, as shown for example by Ainley's correlation curves (e.g., Fig. 67 in Ainley, 1948) and such curves have been widely used in turbine designs. The flow mechanisms causing the loss tendency may be fairly well understood or speculated in relation to, for example, flow separation on the blade surfaces and increase or decrease of secondary flows due to the incidence variation. The understanding or speculation, however, is based mainly on flow surveys made only upstream and downstream of cascades.

Recently, many flow surveys within turbine cascades have been made in order to understand the cascade internal flows and the loss generation mechanisms in more detail (e.g., Sjolander, 1975; Langston et al., 1977; Marchal and Sieverding, 1977; Carrick, 1977; Bindon, 1980; Gregory-Smith, 1983; Boletis et al., 1983; Hodson and Dominy, 1987a, 1987b; Yamamoto, 1986, 1987a, 1987b). Most of the surveys, however, were made only at design or near-design incidences but not at off-design incidences. Detailed studies aimed at the incidence effects on turbine internal flows seem to be very scarce except for the following: Langston et al. (1977) presented ink-trace flow visualizations in a low-speed linear cascade for two incidences (about zero and +11.8 deg) and showed that a saddle point of the cascade inlet endwall flow separation moved to the suction side of the cascade passage as the incidence was increased. Hodson and Dominy (1987b) have recently discussed internal flow mechanisms of a high-speed linear cascade under various off-design conditions and presented oil-flow visualization pictures for two incidences: The low-momentum endwall fluids migrated more intensely onto the blade suction surface as the incidence increases from −20 to +8.6 deg. Yamamoto (1988a) showed, based on flow surveys in a rotor cascade with tip clearance at six nominal incidences ranging from 7.2 to −68.7 deg, that flow separation easily occurs from the pressure side of the blade leading edge, and the associated loss gradually dominates the whole cascade passage as the incidence decreases. Detailed experimental studies are still too few to reveal fully the cascade internal flows and the loss mechanisms under various incidence conditions, specifically in a quantitative manner.

The primary objectives of the present paper are to supply a set of detailed and quantitative data obtained within a cascade for large incidence variation and to present the results in such a way that one can easily understand or visualize the cascade internal flows and the loss mechanisms at both design and off-design incidences. The present experimental results will also be helpful to understand or verify numerical results by advanced computer programs currently being developed for turbomachines with Euler or Navier–Stokes equations.

Test Facilities and Test Methods

Low-Speed Linear Cascade Facility. Figure 1 shows the test section of the present linear rotor cascade (see also Yamamoto, 1987b). The major specifications are given here:

Contributed by the International Gas Turbine Institute and presented at the 33rd International Gas Turbine and Aeroengine Congress and Exhibition, Amsterdam, The Netherlands, June 5–9, 1988. Manuscript received by the International Gas Turbine Institute January 9, 1988. Paper No. 88-GT-110.

- Blade chord, $C = 73.5$ mm
- Axial blade chord, $Cax = 72.6$ mm
- Blade pitch, $S = 61.42$ mm
- Aspect ratio, $H/C = 1.37$
- Solidity, $C/S = 1.20$
- Blade maximum thickness/$C = 0.257$
- Blade LE radius = 8.17 mm, TE radius = 4.08 mm
- Number of blades, $N = 6$
- Cascade camber angle, inlet = 49.8 deg
  outlet = −63.5 deg
- Design cascade turning angle = 113.3 deg
- Design flow angles, inlet = 43.6 deg
  outlet = −63.5 deg
- Design turning angle of flow = 107.1 deg

Two pairs of inlet guide plates and outlet guide plates are installed upstream and downstream of the cascade, respectively. The former is used to change the incidence (see Fig. 1 in Yamamoto, 1988b for more detail).

Traverse Measurements. Figure 2 shows the test setting angles of the inlet guide plates (IGP) and the traverse measuring planes (named S3-planes). The angle is indicated by $\theta_{y,g}$ or $i_{,g}$ where $\theta_{y,g}$ shows the angle measured from the cascade axial direction, and $i_{,g}$ from the direction of the cascade inlet camber line. Periodicity of the cascade inlet and the outlet flows was checked by adjusting the inlet and the outlet guide plates; however, fairly good periodicity, enough for the present purposes (typically as seen in Fig. 5), was attained without any special adjustment of these plates: For each test incidence the inlet guide plates were set parallel to each other, while the outlet ones were fixed in a constant direction irrespectively to the incidence change.

The test outlet Reynolds number ($Re_{,c}$), based on the mass-averaged outlet velocity at Plane 12 ($Z/Cax = 1.24$) and the blade chord, was about 1.8×10^5. The value is the same order

Fig. 1 Test section of the cascade

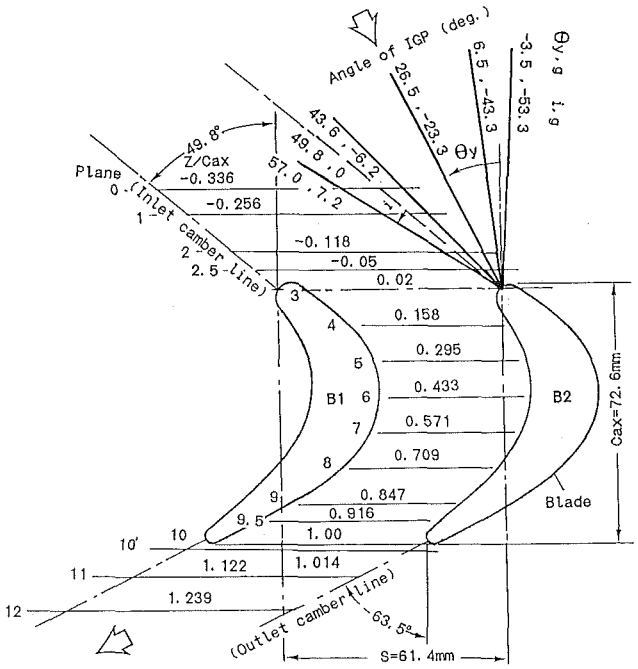

Fig. 2 Traverse S3 planes and test conditions

Nomenclature

Cax = axial blade chord
CPs = static pressure coefficient based on mass-averaged velocity at Plane 12, $\bar{\bar{V}}_{m,12}$ $= (Ps - \bar{\bar{P}}t_{,0})/(0.5 \times \rho \times \bar{\bar{V}}^2_{m,12})$
CPt = total pressure loss coefficient based on $\bar{\bar{V}}_{m,12}$ $= (Pt_{,0} - Pt)/(0.5 \times \rho \times \bar{\bar{V}}^2_{m,12})$
CVm = dimensionless resultant velocity normalized by $\bar{\bar{V}}_{m,12}$
H = span of cascade passage
i = incidence
Ps = static pressure
Pt = total pressure
Vm = resultant flow velocity
Vs = magnitude of secondary flow vector normal to the local midspan flow directions
Vs' = magnitude of secondary flow vector normal to the mass-averaged flow direction
Vz = meridional velocity
W = velocity component projected onto the endwall
Y = spanwise distance from hub endwall
Z = axial distance from blade leading edge
Δ = interval of contour plot
θ_y = yaw flow angle measured from cascade axial direction
ρ = density

Subscripts

0–12 = number of traverse measuring (S3) planes
g = inlet guide plates
mid = midspan
net = net
z = axial

Superscripts

$\bar{}$ = pitchwise mass-averaged value
$\bar{\bar{}}$ = overall mass-averaged value

as the typical Reynolds number of 2×10^5 used in Ainley's cascade data correlations (Ainley, 1948) but is lower by about an order of magnitude than engine conditions. However, this does not mean the present cascade cannot simulate the flows in real machines: In the author's opinion, although Reynolds number effects have still been one of the most profound problems in turbomachinery studies, the Reynolds number difference to this extent over the present Reynolds number level would not be so important as to change the flow mechanisms significantly.

All traverse measurements were made using a miniature five-hole pitot tube with a head-size of 1.5 mm, with a ratio to the axial blade chord of about 48. The pitot tube was fixed in a constant yaw direction during each traverse measurement and absolute yaw angles of the flows were then determined with calibration data obtained in advance.

Experimental Results and Discussion

Cascade Inlet and Outlet Flow Conditions. To show the test conditions, some selected velocities and yaw angles are given in Figs. 3 and 4. Figure 3 shows the cascade inlet velocity profiles at Plane 0. Since the outlet velocity far downstream from the cascade was maintained at a constant value through the present serial tests, the inlet velocity varies with the incidence change with the minimum value near the test $i_{,g}$ of -43.3 deg that corresponds roughly to the axial flow direction (or to the maximum flow area). Inlet boundary layer parameters on both tip and hub endwalls calculated at Plane 1 were given in the previous paper (Yamamoto, 1988a) to vary with the setting angle of IGP: The tip-side boundary layer is a little thicker than the hub-side and is of transitional state, while the hub-side one is always fully turbulent regardless of the setting angles.

Figure 4 compares the spanwise yaw angle distributions for three incidences. Since any upstream traverse planes were not far enough upstream from the cascade leading edge, the inlet flows obtained there are already disturbed by the cascade and the measured inlet yaw angles of the flows do not necessarily coincide with the setting angle of IGP: At Plane 1, for example, the mass-averaged inlet flow angle is smaller than the IGP setting angle $i_{,g}$ by 7 to 12 deg corresponding to $i_{,g}$ of -53.3 to 7.2 deg, respectively (Yamamoto, 1988a). Therefore, the IGP setting angles ($i_{,g}$) rather than the actual inlet flow angles will be used as nominal incidences through the present paper except for Fig. 18.

Two local maximum peaks on the spanwise yaw angle profiles are caused by the passage vortices, which gradually increase their strength in the cascade passage. At a larger incidence (i.e., a larger cascade turning), the peaks start to grow at earlier axial stations than at a smaller incidence. The mass-averaged values at downstream Plane 12 ($Z/Cax=1.24$), however, are nearly constant between -60.4 and -60.7 deg, regardless of the present incidence change.

Incidence Effects on Midspan and Downstream Flows. Figure 5 shows midspan blade-to-blade flows W for five test incidences with corresponding downstream flows at Plane 12. The vector W is a projection of a resultant velocity onto the midspan blade-to-blade (S1-) plane parallel to the endwall. The downstream vectors Vs and contours CPt indicate the secondary flows and the total pressure loss coefficient. The vector Vs is defined as the velocity component normal to the local midspan flow at the same pitchwise location. To show the secondary flows clearly, the scale of Vs is increased to ten times that of W.

The pneumatic probe presently used cannot detect back flows if they exist. However, the vectors W clearly show by very small velocities that as the incidence decreases, a flow separation originates from the blade pressure-side leading edge and reattaches onto the blade pressure surface. Due to the blockage effect of this leading-edge separation, the flows within the cascade passage are, in general, more accelerated as the incidence decreases. The incidence variation affects the midspan flows strongly in the cascade passage, but little downstream of the cascade.

The passage vortex seen at the downstream plane is strongest at the maximum incidence. With decrease of incidence, it gets rapidly weaker and the amount of low-energy fluid on the suction surface decreases rapidly. The loss due to the leading-edge separation starts to diffuse from the pressure side to the midpassage. The diffused loss finally dominates nearly the whole cascade passage at the minimum test incidence. The detailed diffusion process occurring within the cascade passage will be seen later in Fig. 12.

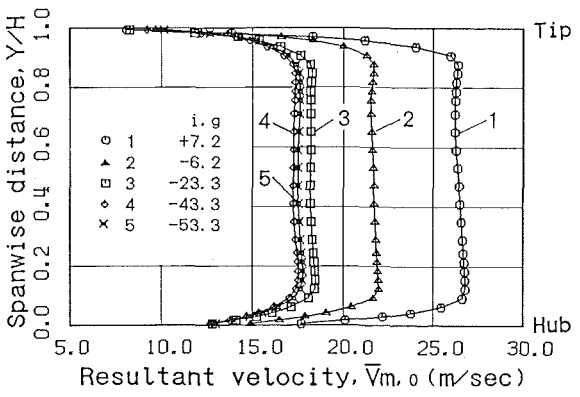

Fig. 3 Pitch-averaged inlet velocity profiles at S3 plane 0 for various test incidences

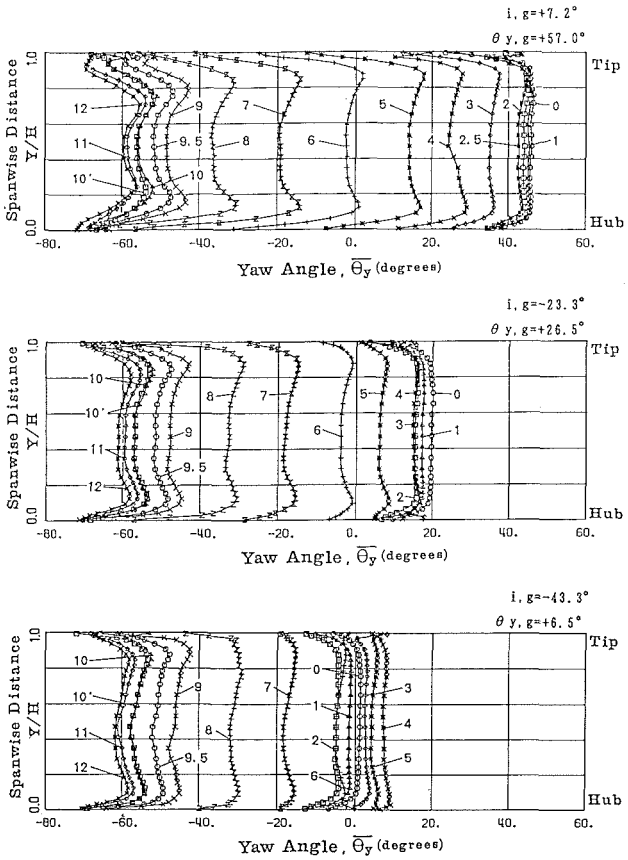

Fig. 4 Pitch-averaged yaw flow angles at various S3 planes for three inlet guide angles

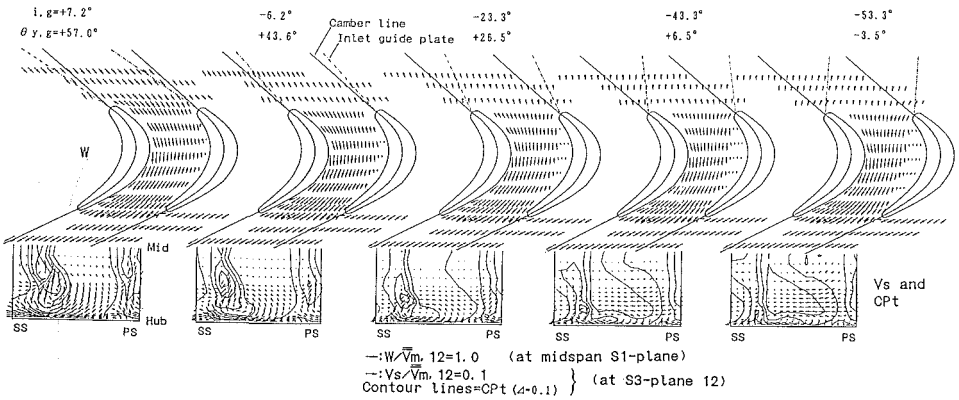

Fig. 5 Midspan flows and downstream secondary flows/loss contours for five inlet guide angles tested

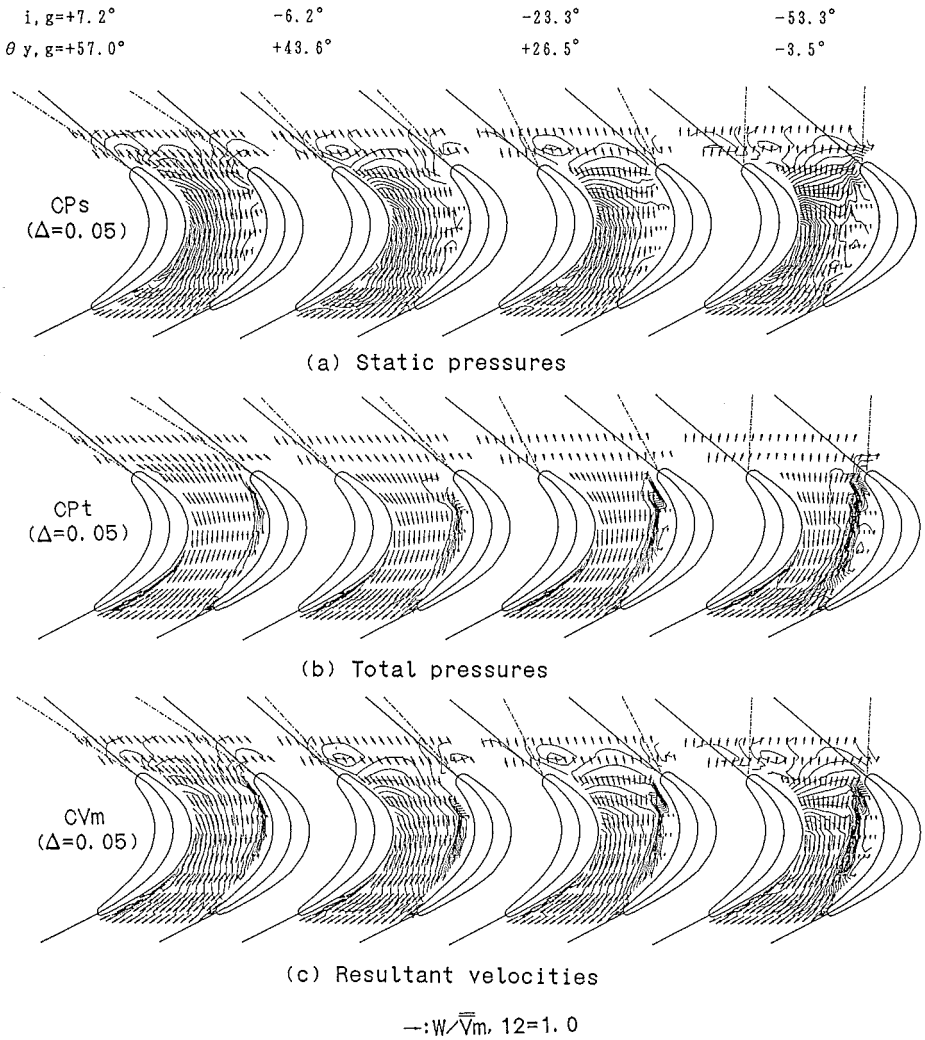

Fig. 6 Three types of contour: static pressures, total pressures, and velocity at midspan S1 plane with vectors *W* for four inlet guide angles

Incidence Effects on Midspan Static and Total Pressures, and Velocity. Figure 6 shows variation of the midspan static pressure *CPs*, total pressure loss *CPt*, and velocity *CVm* with incidence change. *CPs* is very sensitive to the incidence change particularly in the front half of cascade passage, where the blade loading, i.e., the pitchwise pressure difference, decreases significantly as the incidence decreases.

CPt shows two high-loss regions: One is located near the suction surface, starting from a little upstream of the cascade throat where the boundary layer can easily develop due to the adverse pressure gradient there, as shown in the previous *CPs* contours. The region seems to be insensitive to the incidence change. The other high-loss region is located near the pressure surface and is apparently caused by the leading-edge flow separation as discussed previously. The region is very sensitive to the incidence change. The separation (loss) is seen to occur even at the maximum incidence, originating from a small separation region with adverse pressure gradient located near

the pressure side of leading edge. The small separation was also visualized by oil smoke; a strong spanwise flow from the endwall corner toward the midspan along the pressure-side leading edge was seen. The region could be recognized also by atmospheric dust left on the pressure surface after the long runs of the present serial tests.

CVm gives cascade internal velocity fields, which reveal two regions with large velocity gradients corresponding to the insensitive suction surface boundary layer and the sensitive leading-edge flow separation to the incidence change. A region with locally decreased velocities can also be recognized ahead of the suction side of leading edge, corresponding to the region with locally high static pressures as shown in the previous figures (*a*) of *CPs*.

Incidence Effects on Endwall Flow Vectors. Figure 7 shows detailed endwall flows close to the hub for three incidences. As the incidence increases, the flows within the cascade passage migrate more strongly toward the blade suction surface, as expected from flow visualizations available. This is due to the increased pitchwise pressure gradient, particularly in the front half of the cascade passage, as seen previously. At the maximum incidence, most of the vectors between Z/Cax of 0.7 (Plane 8) and Z/Cax of 1.0 (Plane 10), except in a small region near the pressure surface, face almost normal to the axial direction. The separation from the leading edge is significantly reduced near the endwall, compared to that seen at the midspan (Fig. 5). Effects of the incidence on the endwall flows decrease rapidly downstream; at the downstream Plane 12 (i.e., $Z/Cax = 1.24$), the endwall flows are quite insensitive to the incidence variation, as seen also in the midspan flows.

Incidence Effects on Static Pressures Near Endwalls and Near Blade Surfaces. Figure 8 shows three-dimensional tomograms of static pressures *CPs*, obtained by cutting the cascade flows with a blade-to-blade (S1-) plane at 1.2 percent of span away from the tip, a meridional (S2-) plane near the blade suction surface, and a traverse (S3-) plane at the cascade exit ($Z/Cax = 1.0$). The figures are again superimposed with *W* and *Vs* to be able to visualize the flow mechanisms easily. At the maximum test incidence, some tip endwall flows *W* nearly stagnate ahead of the pressure side of the leading edge. These stagnated flows were not seen in Fig. 7 of the hub endwall

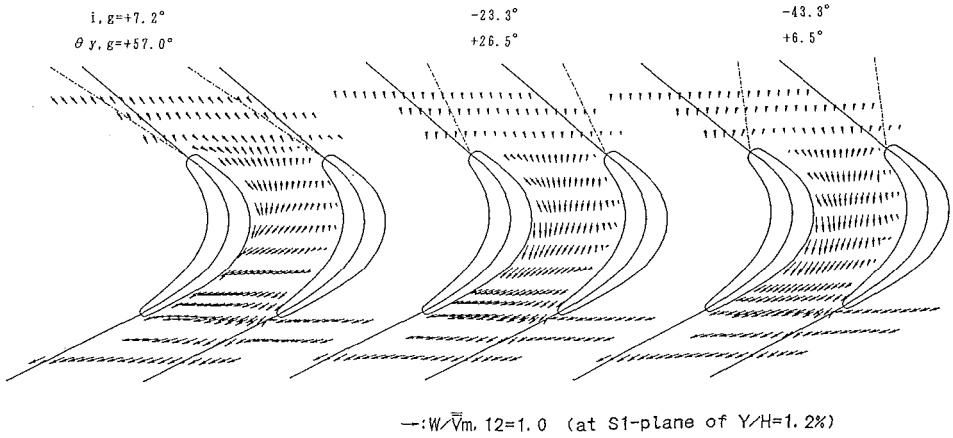

Fig. 7 Hub endwall flow vectors for three inlet guide angles

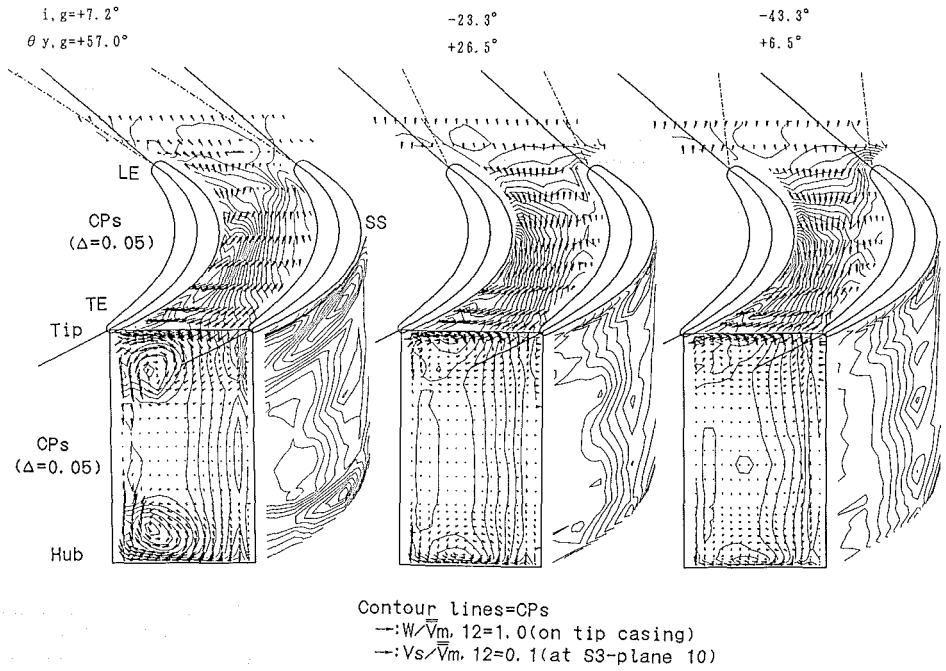

Fig. 8 Three-dimensional representation of static pressure contours with vectors *W* and *Vs* for three inlet guide angles

flows measured at the same 1.2 percent of span; the appearance of the stagnated flows depends on the boundary layer thickness. A distinct minimum pressure point is seen fairly apart from the suction surface due to the strong passage vortex at the maximum incidence. As the incidence decreases, the point moves upstream and close to the suction surface. The static pressures on the cascade exit plane are significantly affected by the passage vortices, particularly at the maximum test incidence. The vortex centers nearly coincide with the minimum static pressure point. Pressure contours over the suction surface are also affected by the passage vortices, and at the maximum incidence, both separation and reattachment lines of the vortices on the surface are clearly shown by the densely distributed contours.

Figure 9 shows the static pressures near the hub endwall and near both blade surfaces, with some streaklines or particle path lines starting upstream or at the leading edge of the cascade. The streaklines can show movements of the endwall flows and the blade surface flows more visually than the vectors. The streaklines analytically obtained from the traverse data resemble cascade flow visualization results using, for example, oil or ink flows (e.g., Sjolander, 1975; Langston et al., 1977; Marchal and Sieverding, 1977; Langston and Boyle, 1982; Bindon, 1980; Gaugler and Russell, 1984; Hodson, 1985; Hodson and Dominy, 1987a, 1987b). At the maximum incidence, a point of the minimum pressure is generated downstream of the inlet endwall fluids, which were completely swept out from the endwall and rolled up onto the blade suction surface. As clearly seen, the rolling-up height of the inlet endwall flows on the suction surface decreases very rapidly as the incidence decreases, and the flows over the suction surface become two dimensional. Note that all endwall streaklines coming from the cascade inlet tend to gather into a single line, keeping a relatively wide space between the line and the blade suction surface until the line reaches the suction surface. A countervortex (*Hs*) exists in this space without diminishing, as will be seen later in Figs. 11 and 12.

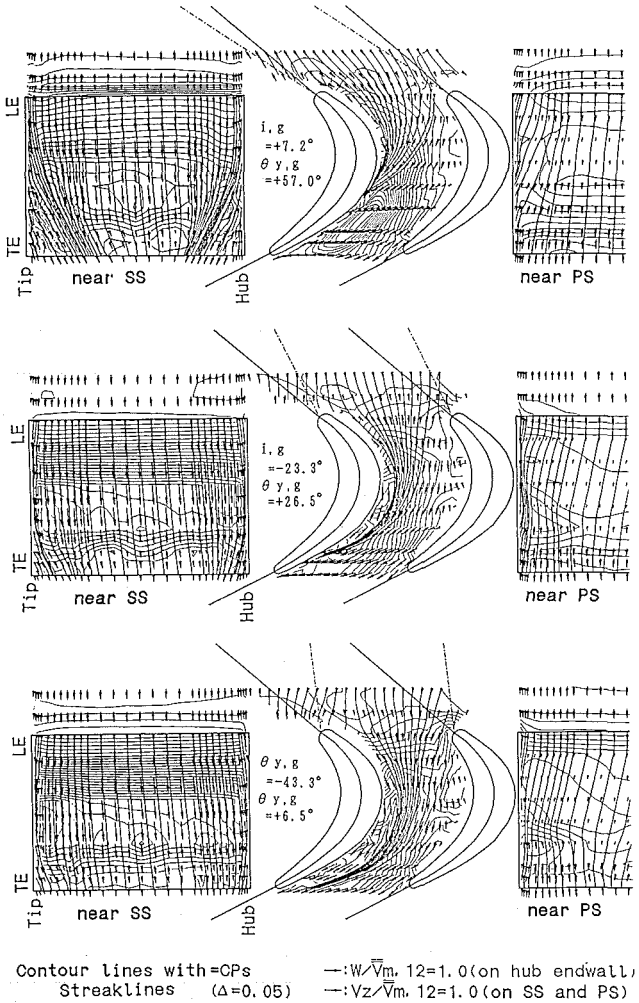

Fig. 9 Static pressure contours, streaklines on SS and on hub endwall with vectors *W* (on hub casing) and *Vz* (on SS) for three inlet guide angles

Incidence Effects on Midspan and Endwall Streaklines. Figure 10 gives the streaklines at three blade spans to demonstrate skewness of so-called "streamlines" in the cascade passage. The inlet streaklines at the midspan shown in the three figures tend to pass the passage nearly parallel to each other. The midspan streakline closest to the suction surface separates from the rear half of the surface due to the boundary layer development there, which is not seen in inviscid streamline computations (e.g., in Fig. 12 of Bario et al., 1982). The streaklines are more highly skewed at larger incidence and nearer the endwall; the streaklines are highly skewed both at 1.2 and 3.6 percent of the span at the maximum incidence, but only at 1.2 percent of span at the other incidences.

Figure 11 gives the pitch angle contours of the flows at 3.6 percent of span away from the hub endwall in order to show the spanwise flows, since the actual streaklines do not always remain on one blade-to-blade (S1-) plane parallel to the endwalls, except on S1 planes at the midspan and very close to the endwalls, and generally move in the spanwise direction. A relatively large region with solid lines (denoted by *A*) exists along the blade suction surface at the maximum incidence. The solid lines indicate rolling-up flows from the hub toward the midspan. As the incidence decreases, the region moves apart from the suction surface toward the midpassage and an

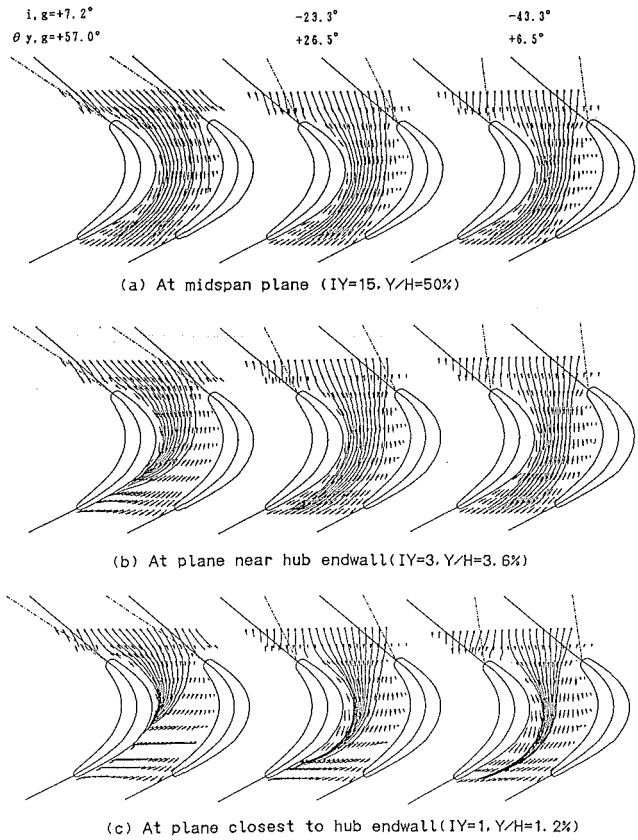

Fig. 10 Streaklines of inlet flows on three S1 planes for three inlet guide angles

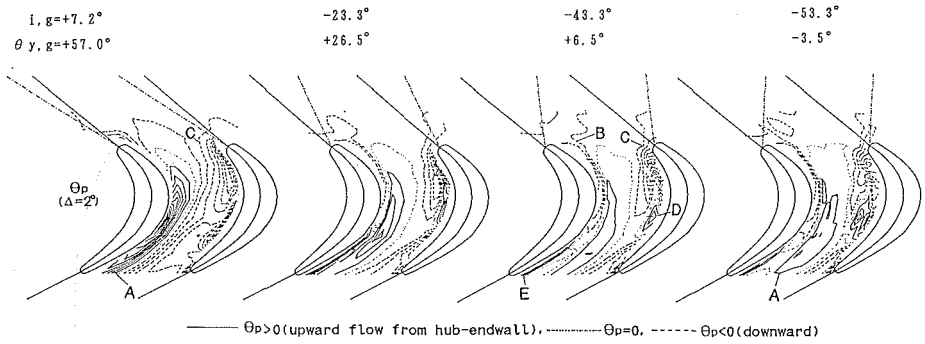

Fig. 11 Pitch angle contours near hub endwall (*Y/H* = 3.6 percent) for four inlet guide angles

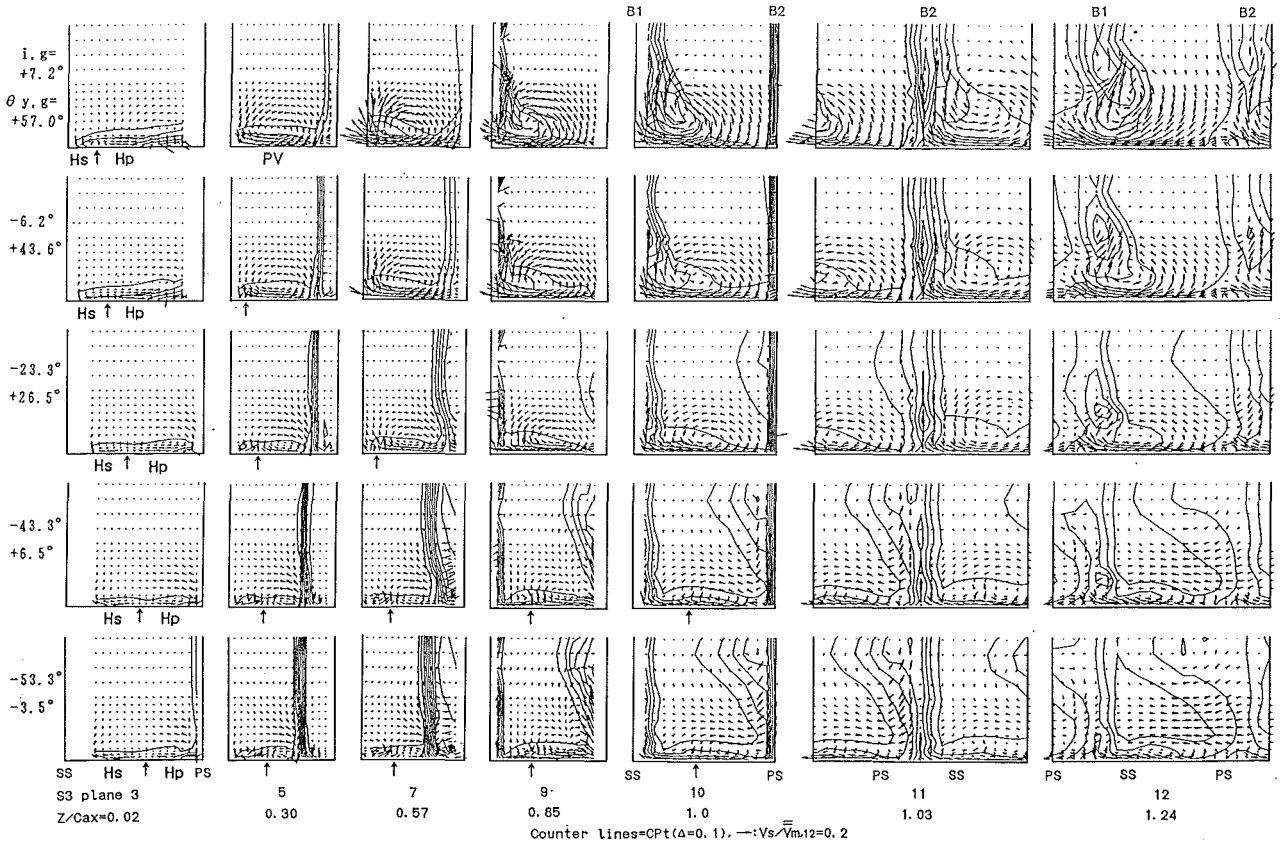

Fig. 12 Development of secondary flows and total pressure losses at various S3 planes (hub-side halves are presented)

area of dotted lines (*B*) appears instead between area *A* and the suction surface. The flows in this region *B* are rolling-down flows toward the hub and correspond to the counter-vortex (*Hs*), as will be seen in the next section. The inlet end-wall fluids did not enter region *B* as seen in Fig. 10. Near the blade pressure surface, other rolling-down flows (*C*) also exist. Therefore, two contrarotating vortices may exist at both sides of the solid area *A*. Another small area of rolling-up flows (*D*) is also recognized to be included in region *C*. Note that at the three negative incidences shown here, a very thin area with solid lines (*E*) is also recognized to remain very close to the suction surface downstream of the cascade throat, showing that there is a rolling-up corner flow at the suction surface/endwall corner.

Incidence Effect on Development of Secondary Flows and Losses. Figure 12 shows details of the development process of secondary flows and losses under various incidence conditions. Some of the traverse planes are chosen and only the hub-side halves are presented here. Special attention is given to identification of various vortices within the cascade passage: the passage vortex, the pressure-side leg (*Hp*) and the suction-side leg (*Hs*) of the horseshoe vortex, and other "new" secondary flows caused by the leading-edge separation.

At cascade inlet Plane 3 ($Z/Cax = 0.02$), both *Hs* and *Hp* can be seen under all incidence conditions, and the intersection point between *Hs* and *Hp*, indicated by an arrow, moves from the suction side to the pressure side of the cascade passage as the incidence decreases. At Plane 5 ($Z/Cax = 0.3$), it is already difficult to distinguish the *Hp* (principally caused by the span-wise pressure gradient) from the passage vortex (caused by the cascade pitchwise pressure gradient), because both *Hp* and the passage vortex rotate in the same sense. When the incidence decreases, for example, less than −43.3 deg, however, the vortex at the pressure side must be attributed more to the *Hp* rather than to the passage vortex, since the pitchwise pressure

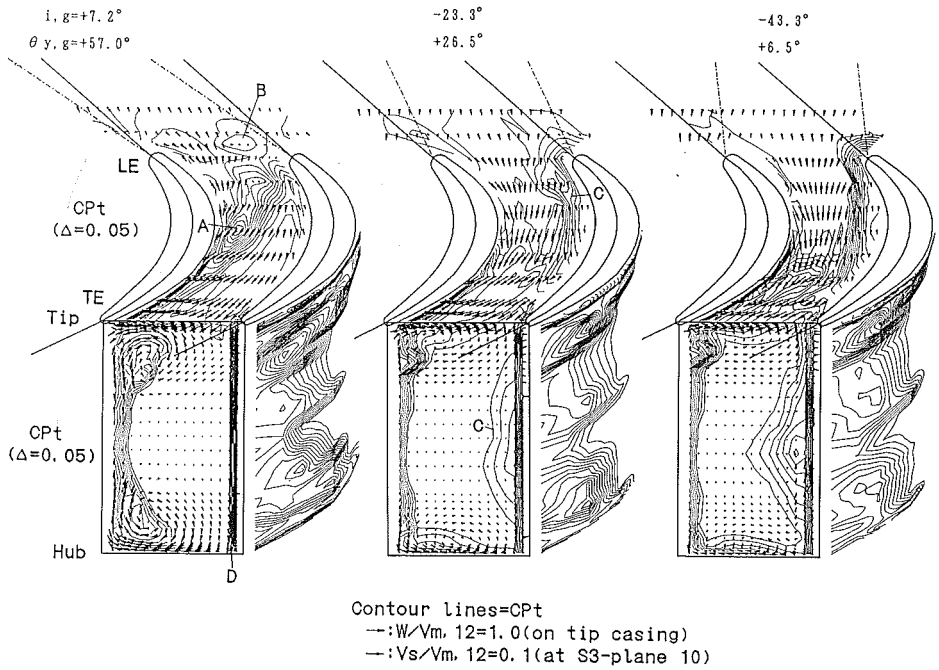

Fig. 13 Three-dimensional representation of total pressure loss contours with vectors *W* and *Vs* for three inlet guide angles

gradient is considered not large enough to cause the passage vortex. As shown here and in some other workers' results, the degree of the merging of *Hs* with the passage vortex depends largely on the cascade incidence or flow turning: Bario et al. (1982) showed the absence of *Hp* in their highly loaded cascade with a turning of 125 deg even at the cascade entrance region, while Langston (1977) and Marchal and Sieverding (1977) showed the existence of *Hp* as well as *Hs* in their moderately loaded cascades. For all of the present test incidences except the maximum incidence, the countervortex *Hs* can be clearly recognized at Plane 5. At incidences less than -43.3 deg, the *Hs* can be seen even at the cascade exit Plane 10 ($Z/Cax=1.0$). Close inspection of the endwall flow vectors reveals that for all incidences, the endwall flows downstream from Plane 9 ($Z/Cax=0.85$) very close to the wall (i.e., at the first traverse line $IY=1$) always move from the pressure side to the suction side. This is the case even at large negative incidences less than -43.3 deg, where the contrarotating vortices (*Hs*, and *Hp* or the passage vortex) exist over the endwall flows at $IY=1$.

At two larger incidences ($i_{,g}=7.2$ and -6.2 deg), the strength of the passage vortex increases rapidly with the axial distance *Z/Cax*, and the center of the vortex gradually separates from the endwall. At the other three incidences, however, the center nearly remains at a constant span, as was seen also in a linear stator cascade with moderate turning (Yamamoto, 1987a). The loss contours at Plane 5 show that leading-edge separation occurs near the blade pressure surface uniformly along the whole span. The separation loss then begins to diffuse from the pressure side toward the midpassage as the flow goes downstream. In this diffusion process, some amounts of high-energy fluid from the free stream are fed to the separation near the pressure-surface/endwall corner by the countervortex *Hp* and/or the passage vortex which, in other words, scrapes some of the low-energy fluids from the separation region and accumulates them onto the endwall, making the width of the separation region thinner near the corner. As the incidence decreases, some of the fluids toward the corner turn their direction to the separation region away from the endwalls, causing "new" secondary flows, which roll up onto

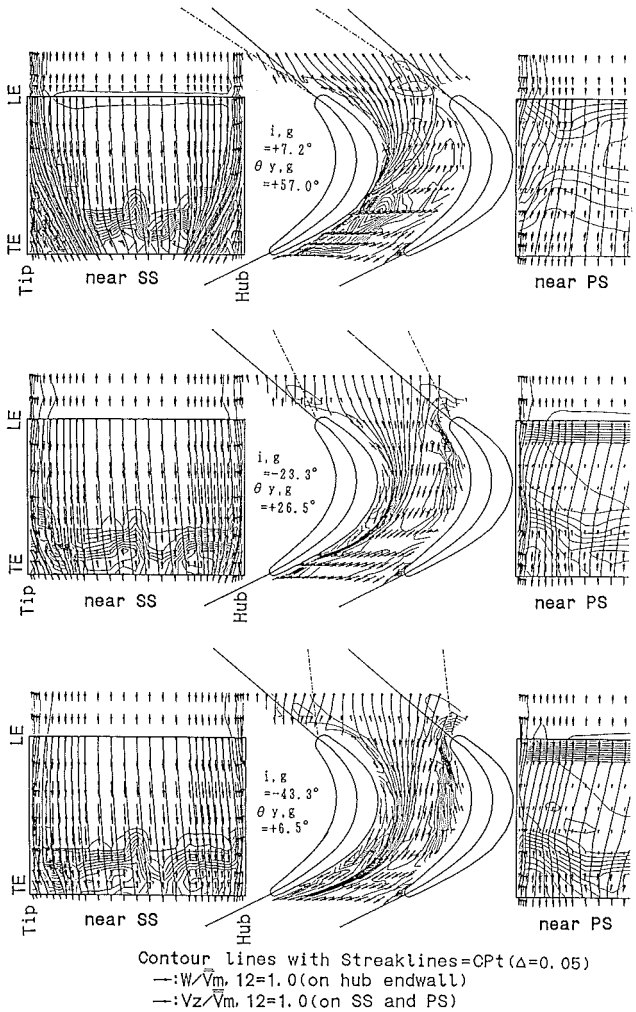

Fig. 14 Total pressure contours, streaklines on SS and on hub endwall with vectors *W* (on tip casing) and *Vz* (on SS) for three inlet guide angles

the pressure surface. This leading-edge separation plays a major role in the cascade loss generation at these negative incidences.

Incidence Effects on Total Pressure Losses Near Endwalls and Blade Suction Surface. Figure 13 shows three-dimensional tomograms of total pressure losses, analyzed in the same manner as used for Fig. 8. The cascade exit loss corresponds to the net loss, which is generated purely in the cascade passage between Planes 0 ($Z/Cax = -0.34$) and 10 ($Z/Cax = 1.0$). Generation mechanisms of the cascade exit loss could be visually understood with the help of the endwall loss and the near-suction surface loss shown in the same figure. The endwall loss contours shown here are more complicated than the midspan ones shown in Fig. 6(b).

At the maximum incidence, a high-loss region with a peak (A) extends from the pressure side of the leading edge toward the rear suction surface of the adjacent blade. Another loss peak (B) can be seen upstream of the leading edge. At the cascade exit plane, the boundary layer fluids on both endwalls are swept out onto the suction surface completely, without leaving any low-energy fluids on the endwalls except near the suction surface. The exit loss seen on the blade suction surface, therefore, consists of the rolled-up endwall loss and the suction surface boundary layer loss (profile loss), which develops on the suction surface and is accumulated near the midspan. On the pressure surface, any boundary layer can hardly develop at the maximum incidence; only the trailing-edge wake loss (D) is seen.

As the incidence decreases, another loss C shown on the tip endwall is generated due to the leading-edge flow separation, which extends around the leading edge more widely than that at the midspan (Fig. 6b). Considering from the diffusion process of the loss C previously discussed, one can see that the loss that spreads over the rear half of the endwall consists

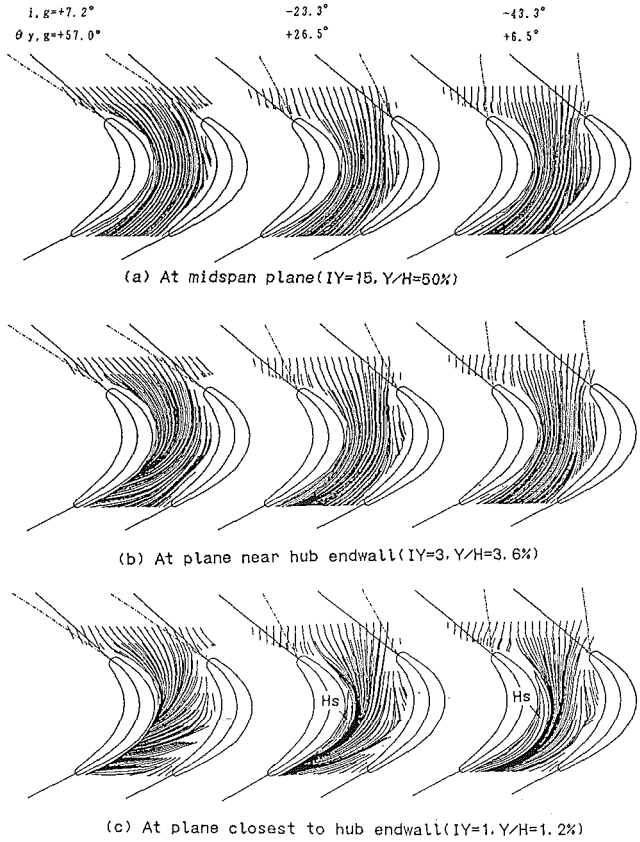

Fig. 15 Streaklines at three S3 planes

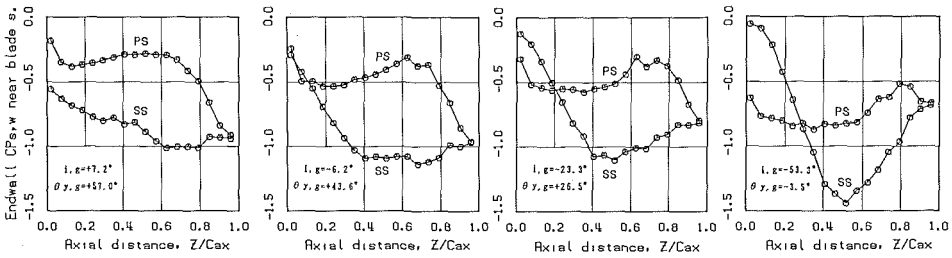

Fig. 16 Tip endwall static pressure around blade surface

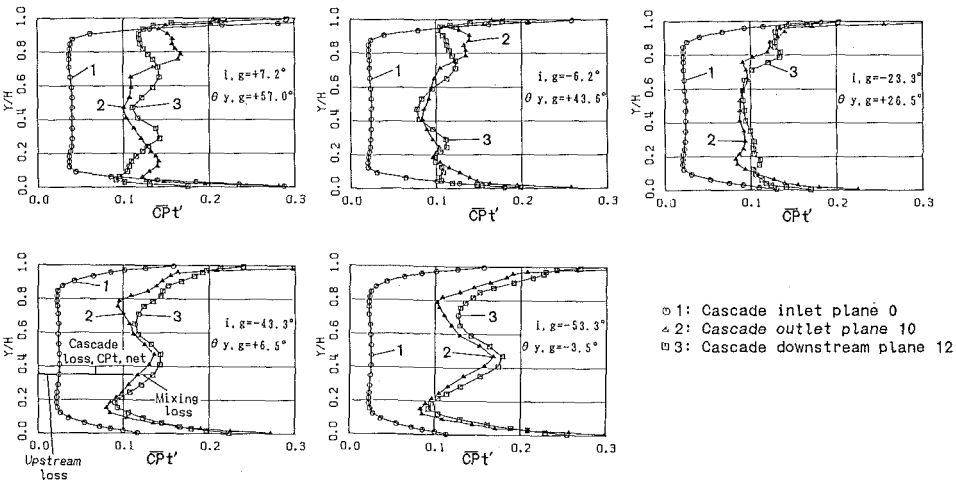

Fig. 17 Evolution of pitch-averaged total pressure loss at three axial locations for five inlet guide angles

mainly of the inlet endwall loss and some amount of the separation loss *C*. The rest of the separation loss is seen as a large exit loss *C* shown on the pressure surface, being driven by the new secondary flows. Due to the reduced pressure gradient in the cascade pitchwise direction, the inlet boundary layer fluids are not yet swept completely onto the suction surface at the cascade exit and some part of the fluids remain over the whole endwalls. The amount of low-energy fluid on the suction surface, therefore, decreases. Along the tip and the hub endwall corners on the suction surface, the corner losses are clearly shown by some dense contours (or dark lines) along the corners.

Figure 14 shows the loss contours with streaklines on the hub endwall and on both blade surfaces. At the maximum incidence, the inlet flows are entirely swept out from the endwall at about half axial chord from the leading edge and move onto the suction surface. The flows then move to about 1/4 span away from the endwall at the trailing edge. On the hub endwall downstream of the inlet flows, which were already swept out, a minimum loss peak is generated by the passage vortex. At the two negative incidences shown here, the minimum loss peak disappeared from the endwall, while a corner loss appears to cover a relatively wide endwall area along the endwall/suction surface corner. It is considered that the corner loss corresponds to the cascade inlet endwall loss migrated to the corner plus a loss newly generated by the vortex *Hs*.

Quantitative Flow Visualization. Figure 15 shows more detailed streaklines at three incidences and three S1 planes: The streaklines were drawn as if oil dots or oil smoke were injected from all traverse measuring points. The most interesting behavior of the streaklines is seen in the figures (*c*) closest to the hub endwall: Between the pressure surface and the streaklines coming from the inlet, new boundary layer flows arise, containing the fluids coming from the midspan side. The new boundary layer also migrates toward the suction surface. At the two negative incidences, the new boundary layer cannot reach the suction surface beyond the accumulation line (or region) of the inlet boundary layer fluids, and between the suction surface and the accumulation line, a corner flow (*Hs*) is clearly visible.

Incidence Effects on Blade Loading at Tip. Figure 16 shows the incidence effect on blade loading at the blade tip obtained from tip-endwall static pressures measurements (see Yamamoto, 1988b for details). As the incidence decreases, the front part of the cascade passage becomes unloaded. Regions with adverse pressure gradient (where *CPs* increases with increase of *Z/Cax*) can be seen on both blade surfaces and are significantly affected by the incidence change. These regions are attributed to the flow separations and the associated loss generation.

Incidence Effects on Overall Loss. Figure 17 shows spanwise distributions of pitchwise mass-averaged loss obtained at three S3 planes for five incidences. The loss coefficients *CPt'* here were calculated based on the atmospheric pressure far upstream of the cascade inlet and on the mass-averaged velocity at the downstream Plane 12. The loss indicated by 1, therefore, corresponds to the loss due to the natural boundary layer that develops on the endwall up to the cascade inlet. The difference between two losses 1 and 2 corresponds to the net loss generated within the cascade. The net loss, however, does not include the whole wake loss generated by the trailing edge, but does include the majority of the wake loss, as seen in Figs. 12 or 13. The difference between the losses 2 and 3 corresponds to the mixing loss occurring downstream of the trailing edge between *Z/Cax* of 1.0 and 1.24. At three incidences larger than −23.3 deg, both positive and negative mixing losses can be seen along the span. Two loss peaks seen on the loss profiles of 2 and 3 are apparently due to the passage vortices and move away from the walls as the flow goes downstream. At negative incidences of −43.3 and −53.3 deg, the mixing loss is positive and nearly uniform along the whole span, and the loss peak near the midspan corresponds to the leading-edge separation, as was already discussed.

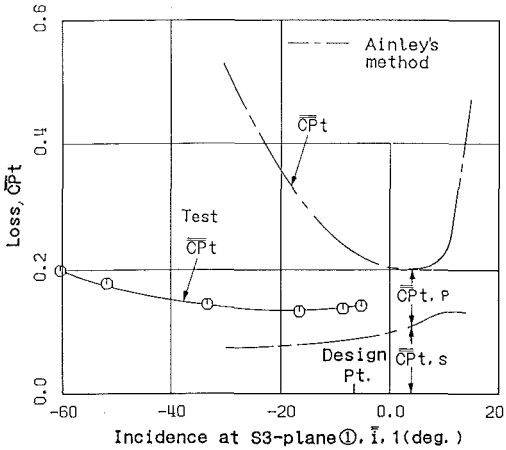

Fig. 18 Overall loss characteristics obtained at S3 plane 12

Information on the loss growth through cascades is very important as was found by several workers for design or near-design incidence conditions (e.g., Langston et al., 1977; Marchal and Sieverding, 1977; Gregory-Smith and Graves, 1983; Yamamoto, 1987a, 1987b). In the present study with large incidence variation, however, it was difficult to obtain accurate mass-averaged losses at traverse planes with the leading-edge separation, because of the difficulty in mass-average computation of the separated flows. Therefore, only the overall loss characteristics obtained at the downstream Plane 12 are shown here in Fig. 18 with the characteristics predicted by the Ainley/Mathieson method (1951). The horizontal axis shows mass-averaged incidence of the flow at Plane 1. The test loss curve shows smaller loss values as well as a very small loss variation with the incidence change, compared to the loss curves predicted by the A/M method. For the present cascade with thick leading and trailing edges and high turning, it was likely that the A/M method tends to overestimate the profile loss $\overline{CPt,p}$. Further discussion on individual losses may be found in Yamamoto (1988a).

Conclusions

The present study describes detailed effects of the incidence on three-dimensional flows and the loss generation mechanisms in a linear turbine rotor cascade. The results are briefly summarized here:

1 Three-dimensional representations used in the study clearly and easily visualize extraordinarily complicated flows in the cascade and the associated loss mechanisms at both design and off-design incidences.

2 As the incidence increases, the migration of endwall low-energy fluids to the suction surface and the associated passage vortices rapidly becomes intense due mainly to the increase of blade loading (pitchwise pressure difference) in the front part of the cascade. The vortex promotes the spanwise accumulation of low-energy fluids on the rear part of the blade suction surface, making the suction surface flows three dimensional. The loss accumulated on the suction surface is the main loss at larger (or positive) incidence.

3 As the incidence decreases, the front part of the cascade becomes unloaded and the flows passing on the suction surface become two dimensional, while the cascade flows near the pressure surface separate easily. The associated separation loss is diffused downstream within the cascade passage by the new secondary flows that are rolling up from the endwall and pil-

ing up a large part (not all) of the separated low-energy fluids onto the pressure surface. The separation is a main cause in the cascade loss generation mechanisms at negative incidence.

4 Each vortex occurring within the cascade is sensitive to the incidence change. Both the suction-side and the pressure-side legs of the leading-edge horseshoe vortex exist at the cascade inlet at all incidences tested, but the former leg can remain up to the cascade exit plane only at large negative incidences and forms a part of the cascade exit secondary flows. The loss by this former leg, however, can be recognized as a corner loss along the suction surface/endwall corner and is negligibly small compared to the other losses generated in the cascade. The latter leg, on the other hand, merges with the passage vortex and the degree of merging depends on the incidence or the cascade turning. The cascade inlet endwall fluids migrate toward a single line beside which both of the legs and/or the passage vortex exist. The secondary flow vectors very close to the endwall downstream from about 85 percent of the axial blade chord always direct from the pressure side to the suction side at any incidences tested even when contrarotating vortices exist over the vectors.

5 For the present cascade with blunt leading and trailing edges and high turning, the test overall loss characteristics with incidence change show smaller loss values as well as a smaller loss variation with the incidence change, compared to the ones predicted by the Ainley/Mathieson Method.

References

Ainley, D. G., 1948, "The Performance of Axial Flow Turbines," *Proc. IMechE.*, Vol. 159, p. 235, Fig. 67.

Ainley, D. G., and Mathieson, G. C. R., 1951, "A Method of Performance Estimation for Axial-Flow Turbines," British ARC, RM2974.

Bario, F., Leboeuf, F., and Papailliou, K. D., 1982, "Study of Secondary Flows in Blade Cascades of Turbomachines," ASME *Journal of Engineering for Power*, Vol. 104, pp. 497–509.

Bindon, J. P., 1980, "Exit Plane and Suction Surface Flows in an Annular Turbine Cascade With a Skewed Inlet Boundary Layer," *Int. J. Heat and Fluid Flow*, Vol. 2, pp. 57–66.

Boletis, E., Sieverding, C. H., and Van Hove, W., 1983, "Effects of a Skewed Inlet End Wall Boundary Layer on the 3-D Flow Field in an Annular Turbine Cascade," *Viscous Effects in Turbomachines*, AGARD-CP-351.

Carrick, H. B., 1977, "Secondary Flow and Losses in Turbine Cascade With Inlet Skew," *Secondary Flows in Turbomachines*, AGARD-CP-214.

Gaugler, R. E., and Russell, L. M., 1984, "Comparison of Visualized Turbine Endwall Secondary Flows and Measured Heat Transfer Patterns," ASME *Journal of Engineering for Gas Turbines and Power*, Vol. 106, pp. 168–172.

Gregory-Smith, D. G., and Graves, C. P., 1983, "Secondary Flows and Losses in a Turbine Cascade," *Viscous Effects in Turbomachines*, AGARD-CP-351.

Hodson, H. P., 1985, "Boundary-Layer Transition and Separation Near the Leading Edge of a High-Speed Turbine Cascade," ASME *Journal of Engineering for Gas Turbines and Power*, Vol. 107, pp. 127–134.

Hodson, H. P., and Dominy, R. G., 1987a, "Three-Dimensional Flow in a Low-Pressure Turbine Cascade at Its Design Condition," ASME JOURNAL OF TURBOMACHINERY, Vol. 109, pp. 177–185.

Hodson, H. P., and Dominy, R. G.., 1987b, "The Off-Design Performance of a Low-Pressure Turbine Cascade," ASME JOURNAL OF TURBOMACHINERY, Vol. 109, pp. 201–209.

Langston, L. S., Nice, M. L., and Hooper, R. M., 1977, "Three-Dimensional Flow Within a Turbine Cascade Passage," ASME *Journal of Engineering for Power*, Vol. 99, No. 1, pp. 21–28.

Langston, L. S., and Boyle, M. T., 1982, "A New Surface Streamline Flow Visualization Technique," *Journal of Fluid Mechanics*, Vol. 125, Dec., pp. 53–57.

Marchal, P., and Sieverding, C. H., 1977, "Secondary Flows Within Turbomachinery Bladings," *Secondary Flows in Turbomachines*, AGARD-CP-214.

Sjolander, S. A., 1975, "The Endwall Boundary Layer in an Annular Cascade of Turbine Nozzle Guide Vanes," Carleton University, TR ME/A 75-4.

Yamamoto, A., and Yanagi, R., 1986, "Production and Development of Secondary Flows and Losses Within a Three-Dimensional Turbine Stator Cascade," *International Journal of Turbo and Jet-Engines*, Vol. 3, No. 1, pp. 79–90.

Yamamoto, A., 1987a, "Production and Development of Secondary Flows and Losses in Two Types of Straight Turbine Cascades: Part 1—A Stator Case," ASME JOURNAL OF TURBOMACHINERY, Vol. 109, pp. 186–193.

Yamamoto, A., 1987b, "Production and Development of Secondary Flows and Losses in Two Types of Straight Turbine Cascades: Part 2—A Rotor Case," ASME JOURNAL OF TURBOMACHINERY, Vol. 109, pp. 194–200.

Yamamoto, A., 1988a, "Interaction Mechanisms Between Tip Leakage Flow and the Passage Vortex in a Linear Turbine Rotor Cascade," ASME JOURNAL OF TURBOMACHINERY, Vol. 110, pp. 329–338.

Yamamoto, A., 1988b, "Endwall Flow/Loss Mechanisms in a Linear Turbine Cascade With Blade Tip-Clearance," ASME JOURNAL OF TURBOMACHINERY, in press. Paper No. 88-GT-235.

Experimental Investigation of Secondary Flow and Mixing Downstream of Straight Turbine Cascades

A. Mobarak
Professor.

M. G. Khalafallah
Professor.

A. M. Osman
Research Assistant.

Cairo University,
Cairo, Egypt

H. A. Heikal
Professor,
Helwan University,
Cairo, Egypt

The purpose of this paper is to investigate the flow field downstream of turbine cascades of low aspect ratio, often used in vehicles and small turbomachines. Experimental investigation was carried out to study the flow downstream of three sets of turbine cascades having the same blade turning angle of about 83 deg but different profiles. The total energy losses were measured at several planes downstream of the cascade of blades in order to determine the changes in gross secondary flow loss coefficient and the growth of the mixing loss with distance downstream. Influence of inlet boundary layer thickness, aspect ratio, and exit Mach number on the nature of the flow at the exit plane of the cascade and total energy loss were studied. The tests were performed with four values of aspect ratio: 1.16, 0.8, 0.5, and 0.25. Some new correlations were deduced that predict energy loss coefficients as a function of distance downstream, aspect ratio, and exit Mach number as well as the upstream boundary layer thickness. The test results compare well with other published correlations.

Introduction

A problem that arises in the design of axial turbines and in the analysis of their performance is the understanding of the nature of secondary flows and their influence on the associated losses. Based on the current state of the art, secondary flow may be defined as the "unexpected three-dimensional flow effects in a turbine that lead to unexplained losses." A more complete understanding of the complex three-dimensional flow and of losses and their origin would certainly prove helpful in any attempt to make improvements in turbine performance. In the last ten years, detailed studies of flows in turbine cascades have been carried out by various investigators.

One such area, where the loss mechanism is not at all clearly understood, is the flow region downstream of the trailing edge of blades. From data available in the literature, it is clear that an appreciable part of energy loss takes place downstream of the trailing edge in addition to that occurring within the blade row. For example, Langston et al. (1977) show about one-third to one-half of the losses occurring downstream presumably due to mixing out of a nonuniform flow at the blade exit. Other investigators (Came et al., 1974; Marchal and Sieverding, 1977; Gregory-Smith and Graves, 1983) also reported increases in losses behind the trailing edge plane. However as Sieverding and Wilputte (1981) and Moore and Adhye (1985) pointed out, "the way in which the losses mix out is entirely unclear."

Came (1973) and Chen and Dixon (1985) show that the secondary flow and mixing process downstream of the cascade are affected by the inlet boundary layer thickness.

Analysis of cascade loss data by Sharma and Butler (1987) has demonstrated that inlet boundary layer losses convect through the passage without causing additional loss and can be distinguished from the passage loss. This means that the inlet boundary layer losses are additive and hence the total energy loss can be considered as the sum of inlet loss contained within the cascade inlet boundary layer and passage loss generated within the cascade passage.

This paper presents the results of experimental work carried out to determine the effect of trailing edge thickness, aspect ratio, and inlet boundary layer thickness on the mixing processes and total energy losses developed by a flow through high deflecting turbine blade cascades.

Experimental Facility

Testing of blade cascades was conducted using a high-speed wind tunnel exhausting directly to the atmosphere at the cascade exit. The compressed air is supplied by a 300 kW screw compressor with a maximum pressure ratio of 4 and mass flow rate of 1 kg/s. The wind tunnel test section is 224 × 64 mm (Figs. 1 and 2). The height of the test section may be changed by inserting wooden plates of known thickness and fixing them to the lower endwall.

The main geometric details of the three tested blade

Contributed by the International Gas Turbine Institute and presented at the 33rd International Gas Turbine and Aeroengine Congress and Exhibition, Amsterdam, The Netherlands, June 5–9, 1988. Manuscript received by the International Gas Turbine Institute September 1987. Paper No. 88-GT-8.

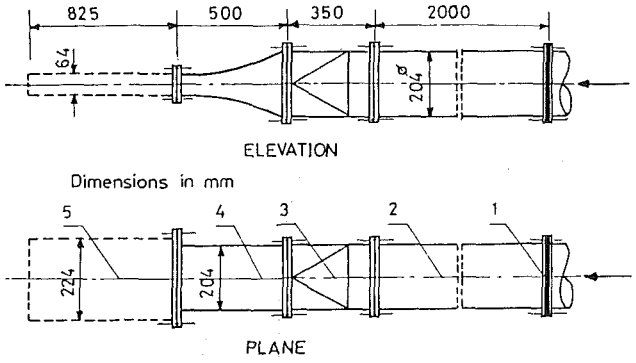

1- Honeycomb
2- Developing pipe.
3- First stage area conversion section.
4- Nozzle 5- Main wind tunnel element.

Fig. 1 Schematic of the test rig

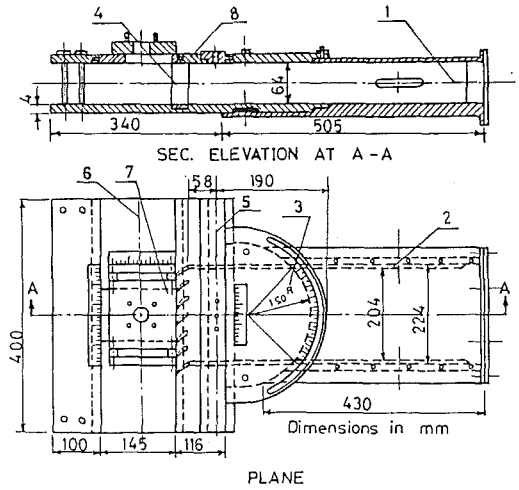

1- Rectangular duct
2- Side walls
3- Protractor.
4- Blade cascade.
5- Upstream traversing plate.
6- Downstream pitchwise traversing plate.
7- Downstream axial traversing plate.
8- The upper cover of the cascade.

Fig. 2 Layout of main wind tunnel element

Table 1 Geometry of the turbine cascades

Cascade No.	1	2	3
Blade chord length, c(mm)	55	60	55
Blade axial chord, b,(mm)	43	45	43
Leading edge radius, r_o(mm)	3.0	3.0	3.5
Blade height, h(mm)	64	64	64
Blade aspect ratio, h/c	1.16	1.07	1.16
Pitch/chord ratio, S/c	0.61	0.61	0.61
Maximum thickness to chord ratio, t/c	0.236	0.25	0.264
Trailing edge thickness to pitch ratio, t_e/S.	0.0441	0.027	0.0147
Inlet blade angle, β_1'	83°	83°	83°
Outlet blade angle β_2'	14°	14°	14°
Blade turning angle, ϵ $\epsilon = 180 - (\beta_1' + \beta_2')$.	83°	83°	83°

cascades are given in Table 1. The second cascade consists of six blades; the other two cascades each consist of seven blades. Each cascade was chosen to have a pitch-to-chord ratio of 0.61, which is the optimum value corresponding to the tested values of blade exit angle and deflection of the cascade (Abdel Hafiz, 1982).

Instrumentation and Measurements

At the upstream station, the parameters to be measured are the total pressure, static pressure, and total temperature. These parameters were measured at a distance of 58 mm upstream from the leading edge in the undisturbed flow (Fig. 3). This distance is usually of the order of eight to ten times the blade leading edge diameter (Mansour, 1982). The upstream total pressure in the mainstream was measured with a three-hole probe (Cobra type) having a tip height of 1 mm and width of 3 mm. The inlet boundary layer was measured with a boundary layer probe 0.5 mm in diameter. The inlet turbulence intensity at the central passage was measured using a hot-wire anemometer probe for different values of the tested parameters and it was found to vary within 2-3 percent, which is a typical value for actual machines (Mansour, 1982). Precautions were taken before each test to be sure that these parameters are uniform in the inlet measuring plane.

Measurements of flow parameters were performed at four different planes downstream of the cascade by using a five-hole probe 3 mm in diameter. The measuring probes were calibrated with respect to a total pressure probe of the shielded type, which has a unity recovery factor through a range of

Nomenclature

AR = h/c = blade aspect ratio
b = axial chord length
C = absolute velocity
c = blade chord length
H = shape factor
h = static enthalpy or blade height
h_0 = stagnation enthalpy or reference blade height = 64 mm
i = incidence angle
k = isentropic index
l = distance from trailing edge in streamwise direction
M = Mach number
m = index in power law of the inlet boundary layer-velocity profile expression
P = pressure
R_a = arithmetic average height
r_0 = leading edge radius
S = blade pitch
t = maximum thickness
t_e = trailing edge thickness
Z = spanwise coordinate measured from the cascade lower endwall
β = flow angle measured from tangential direction
β' = blade angle measured from tangential direction
δ = boundary layer thickness
δ^* = displacement thickness
ϵ = blade turning angle
θ = momentum thickness
ξ = enthalpy loss coefficient
ξ_p = profile loss coefficient
ξ_{p0} = profile loss coefficient at $t_e/S = 0.0147$

Subscripts

0 = stagnation condition
1 = inlet to the cascade
2 = outlet from the cascade
ms = midspan values
s = isentropic

Superscripts

$\bar{}$ = pitch-averaged values
$\tilde{}$ = pitch and span averaged values

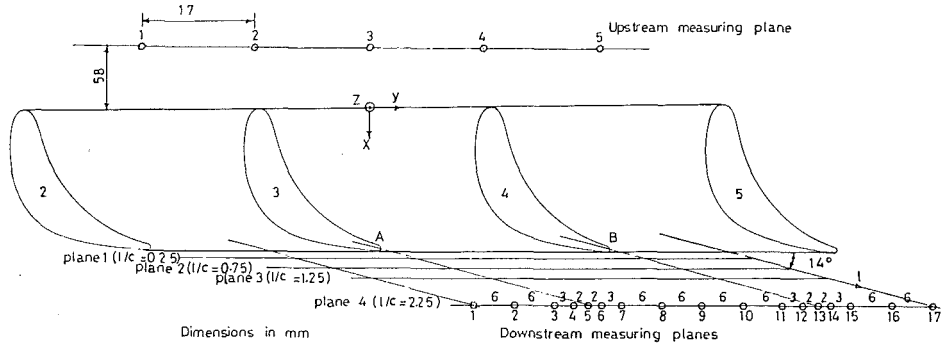

Fig. 3 Inlet and exit measuring stations as distributed in the pitchwise direction

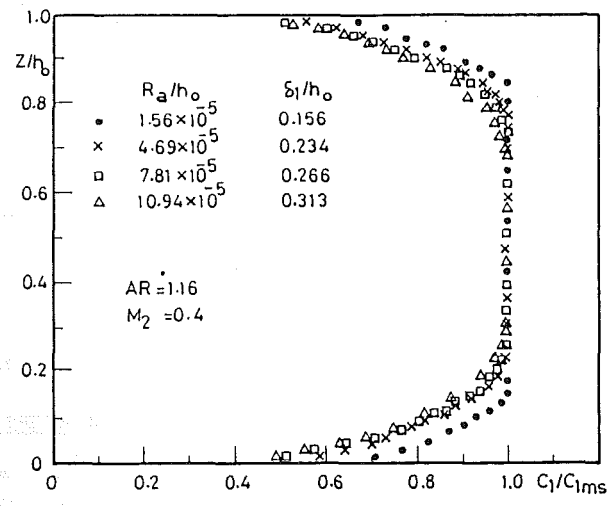

Fig. 4 Spanwise distribution of the inlet boundary layer velocity profiles

±30 deg of yaw angle. The distances of the measuring planes from trailing edge were measured in the streamwise direction and these planes are located at l/c = 0.25, 0.75, 1.25, and 2.25, where l is the streamwise distance (Fig. 3). The pitchwise measuring stations were chosen such that the exit area of the central passage AB and half of each of the adjacent passages are covered completely by 17 measuring stations (Fig. 3).

Spanwise traversing of the inlet and exit planes of the cascades were carried out by using two traversing mechanisms with stepper motors. Betz manometers having an accuracy of 0.2 mm mercury were used in measuring pressure heads.

Testing was conducted at an air speed such that the blade chord Reynolds number was varied from 2.2×10^5 to 5.5×10^5 based on the average outlet velocity, which is relatively high; thus the effect of Reynolds number on loss coefficient can be neglected (Kacker and Okapuu, 1982). Local values of total energy loss coefficient corresponding to each exit measuring station were calculated using the relation

$$\xi = \frac{h_2 - h_{2s}}{h_{02} - h_{2s}} = \frac{(P_{01}/P_{02})^{\frac{k-1}{k}} - 1}{(P_{01}/P_2)^{\frac{k-1}{k}} - 1} \tag{1}$$

The pitch-averaged and passage-averaged energy loss coefficients were calculated on a mass-averaged basis.

The test program of the investigated cascades comprised the determination of the optimum incidence angle, which is found to be zero deg for all the different conditions. Tests were carried out for different values of inlet boundary layer thickness, which was changed by sticking sandpaper on the upper and lower endwalls. Figure 4 shows the shape of the inlet velocity and boundary layer profiles for different values of relative arithmetic-average heights (R_a/h_0). The velocity profile is described by the relation

$$\frac{C_1}{C_{1ms}} = (Z/\delta_1)^m \tag{2}$$

The values of boundary layer parameters may be obtained as given in Table 2.

Table 2 Inlet boundary layer properties for AR = 1.16 and M_2 = 0.4

R_a/h_o	δ_1 (mm)	m	δ_1/h_o	δ_1^* (mm)	Θ_1 (mm)	h_1	δ_1^*/c
1.56×10^{-5}	10	0.215	0.156	1.77	1.237	1.43	0.042
4.96×10^{-5}	15	0.220	0.234	2.70	1.878	1.44	0.049
7.81×10^{-5}	17	0.216	0.266	3.02	2.109	1.43	0.055
10.94×10^{-5}	20	0.210	0.313	3.47	2.440	1.42	0.063

Results and Discussion

For high-aspect-ratio blades, the midspan pitch-averaged loss is taken as the profile loss, but for low-aspect-ratio blades differentiation between the profile and secondary loss was not possible. Sieverding and Wilputte (1981) used the midspan loss as profile loss for testing a rectilinear cascade of blades having an aspect ratio of 0.83. Sharma and Graziani (1983) concluded that existing two-dimensional boundary layer calculation methods can substantially underestimate the midspan boundary layer losses in low-aspect-ratio cascades. One of the main sources quoted by Sharma and Graziani is the work of Langston et al. (1977) in which the aspect ratio was the relatively low value of 0.8077. In the present work, the tested cascades of blades had AR greater than one and the flow at the midspan may be considered two dimensional. Therefore, the measured midspan energy loss may be considered to be the same as the profile energy loss.

It is clear from Fig. 5 that the midspan energy loss coefficient shows a rising trend with the increase of l/c and with the increase of the ratio t_e/S (trailing edge thickness to pitch ratio). The increase in energy loss with l/c is due to flow mixing together with the additional loss caused by the skin friction on the endwalls (Chen and Dixon, 1985). For the higher t_e/S values, the midspan energy loss coefficient is greatly influenced by the mixing process, while this is not the case for lower t_e/S, where the loss coefficient stabilizes at lower values of l/c. Of course for a thicker trailing edge, the trailing edge wake becomes wider, and hence there is a greater tendency toward mixing behind the blade.

The data given in Fig. 5 may be correlated as follows:

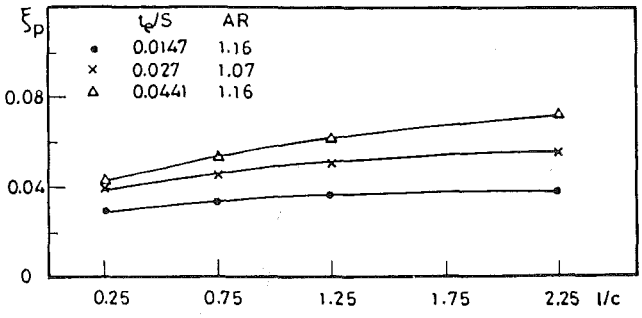

Fig. 5 Variation of midspan energy loss coefficient with *l/c* at δ_1/h_0 = 0.156 and M_2 = 0.4

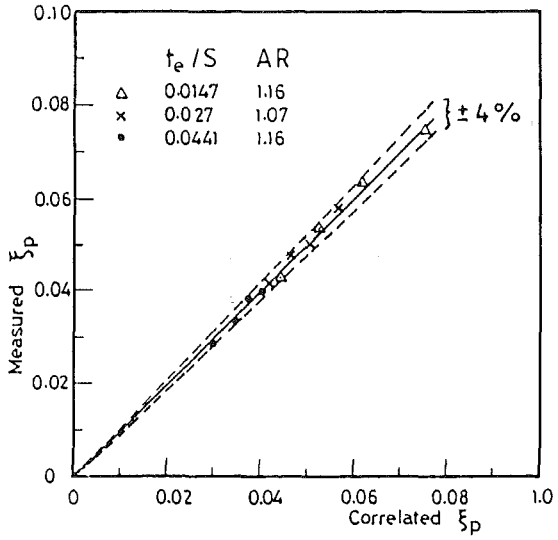

Fig. 6 Correlated profile loss shows good agreement with the present data

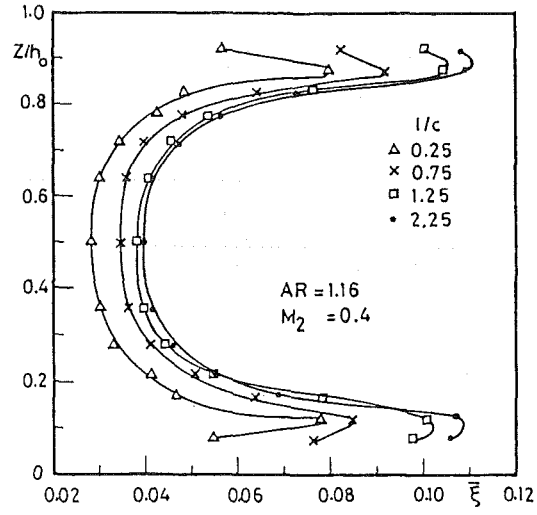

Fig. 7 Spanwise distribution of the pitch-averaged loss coefficient at δ_1/h_0 = 0.156

$$\xi_p = \xi_{p0} + A_1\left(\frac{t_e}{S} - 0.0147\right)^{A_2} \tag{3}$$

where ξ_{p0} is the midspan energy loss coefficient at t_e/S = 0.0147; given as function of l/c

$$\xi_{p0} = 0.0123 + 0.0235(l/c)^{0.22} \tag{4}$$

A_1 and A_2 are constants, each of which depends on l/c.

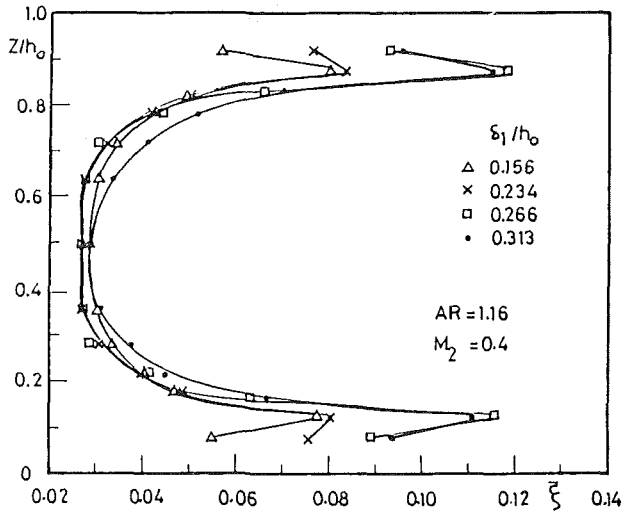

Fig. 8 Spanwise distribution of the pitch-averaged loss coefficient at *l/c* = 0.25

$$A_1 = 0.0184 + 0.166(l/c)^2 \tag{5}$$

$$A_2 = 1.691(l/c)^{0.2} - 1.08 \tag{6}$$

According to the above equations, the midspan loss coefficient can be put in the form

$$\xi_p = 0.0123 + 0.0235(l/c)^{0.22} + [0.0184 + 0.166(l/c)^2]\left[\frac{t_e}{S} - 0.0147\right]^{[1.691(l/c)^{0.2} - 1.08]} \tag{7}$$

Correlation (7) fits the data given in Fig. 5 within ±4 percent deviation, as shown in Fig. 6.

It is important to mention that this correlation is applicable to the tested cascade under the conditions mentioned above and it is difficult to decide its generality except after comparing experimental data for other cascades. However, it is difficult to find a generalized correlation for energy loss prediction that could be applied for any blade cascade. This was pointed out by Denton (1973) as he discussed seven methods for predicting the profile loss from simple blade parameters. Denton compared these methods with 79 cascade results and he found that none of them predicted the loss accurately.

Further information about the pattern of cascade losses is obtained by plotting the averaged loss coefficients of each pitchwise traverse against distance along the span of the most efficient blade cascade (cascade No. 3, Table 1).

Figure 7 shows the typical evolution of the pitch-averaged total loss distribution with distance downstream. It is clear from this figure that the regions of low energy (which are characterized by two peaks of energy loss) lie near the upper and lower endwalls. The expected increase in loss coefficient in boundary layers at the endwalls was not investigated, as the measurements did not include the boundary layer. This figure indicates that as the downstream distance (l/c) increases, the pitchwise-averaged losses increase continuously and the rate of decrease of the two peaks toward the endwalls diminishes. This effect is to be expected from the growth of the mixing loss with the distance downstream.

Figure 8 shows that the values of profile loss coefficient ($\bar{\xi}$ at midspan) may be considered constant, about 0.028 for all values of δ_1/h_0, but the pitchwise-averaged losses away from the midspan increase continuously as δ_1/h_0 increases. It is clear that the two peaks occur at the same distance from the endwalls (at Z/h_0 = 0.125 and 0.875) irrespective of the value of δ_1/h_0 as this distance depends on the aspect ratio and turning angle (Moustapha et al., 1985).

The effect of AR on the pitch-averaged loss coefficient is shown in Fig. 9. It is clear that the two peaks of energy loss

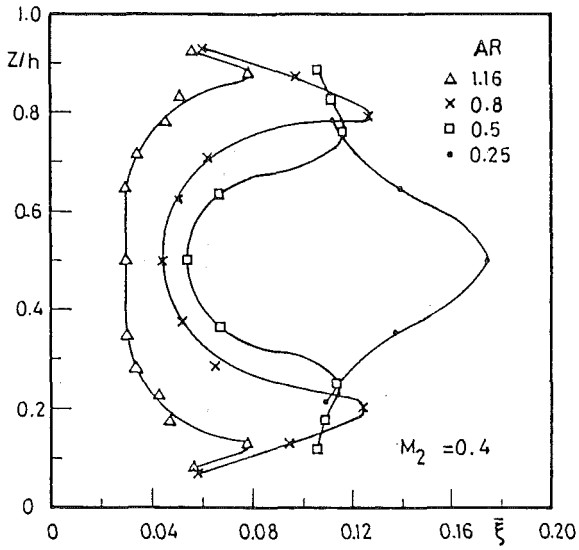

Fig. 9 Spanwise distribution of the pitch-averaged loss coefficient at $l/c = 0.25$ and $\delta_1/h_0 = 0.156$

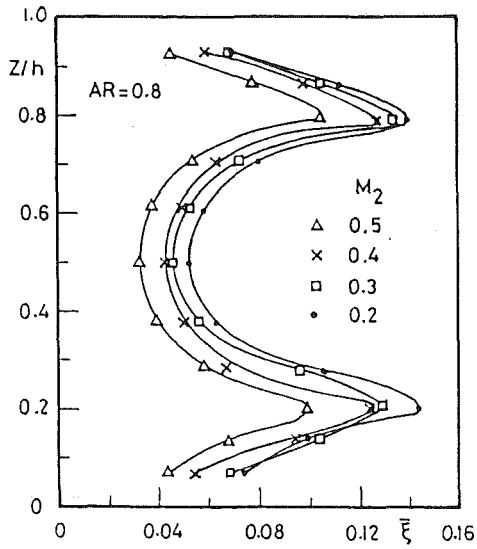

Fig. 10 Spanwise distribution of the pitch-averaged loss coefficient at $l/c = 0.25$ and $\delta_1/h_0 = 0.156$

coefficient approach each other by reducing the blade aspect ratio to 0.5. With further reduction of aspect ratio (AR = 0.25), the two peaks combine to form a single strong peak at midspan. Moreover, the continuous increase of the mean value of loss coefficient with decreasing aspect ratio can be remarked. This means that the influence of secondary vortices becomes more noticeable at the midspan of blades as the aspect ratio decreases.

Figure 10 shows that the increase of exit Mach number decreases the energy loss coefficient as it reduces the possibility of stagnation near endwalls by increasing the momentum of fluid particles.

Mixing of Downstream Flow

The mixing process that takes place downstream of the blade cascade is accompanied by an increase in losses due to the wake effect and the motion of vortices. To evaluate the effect of mixing on the energy loss coefficient the passage-averaged loss coefficient is calculated as a function of downstream distance l/c and plotted as given in Figs. 11, 12, and 13 for different values of δ_1/h_0, AR, and M_2.

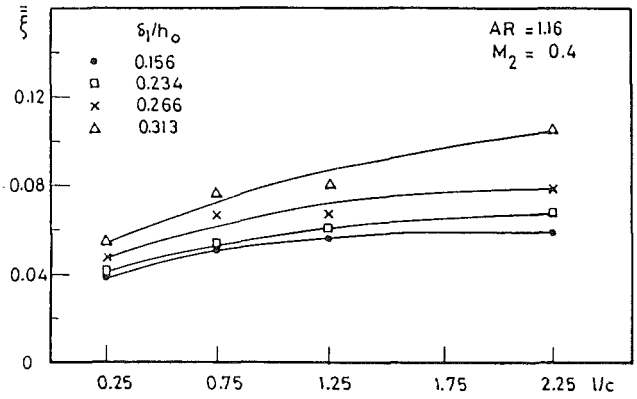

Fig. 11 Variation of passage-averaged loss coefficient with l/c

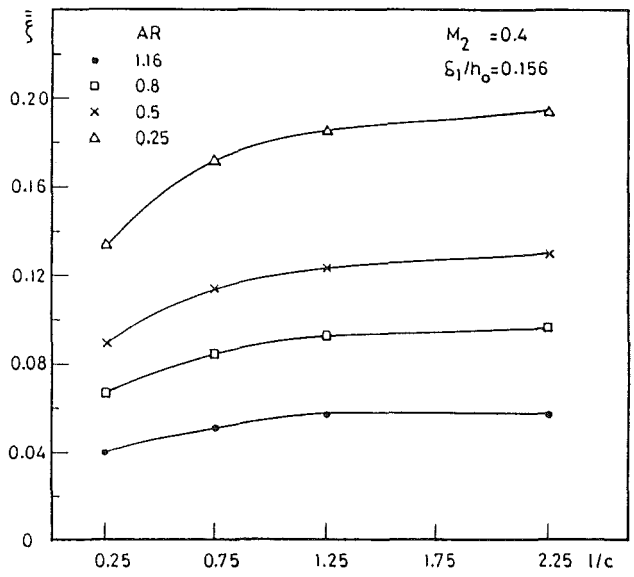

Fig. 12 Variation of passage-averaged loss coefficient with l/c

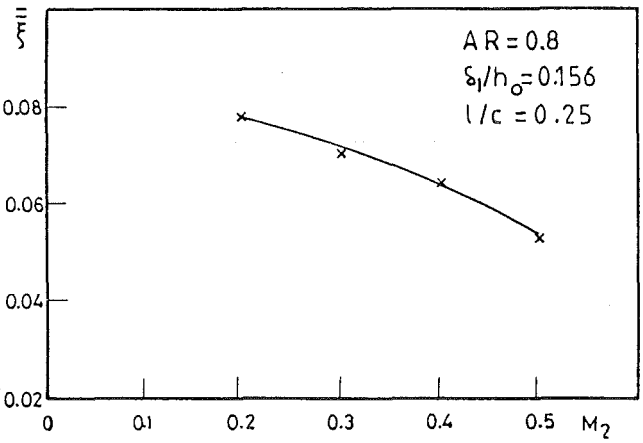

Fig. 13 Variation of the passage-averaged loss coefficient with M_2

Figure 11 indicates that as the values l/c increase the total energy loss coefficient increases rapidly with increasing inlet boundary layer thickness. It is important to mention that increasing δ_1 increases the spanwise extent of the zone behind the cascade in which the secondary loss vortex dominates. Dunham (1970) and Came (1973) both demonstrated increased losses when the upstream wall boundary layer thickness was artificially thickened.

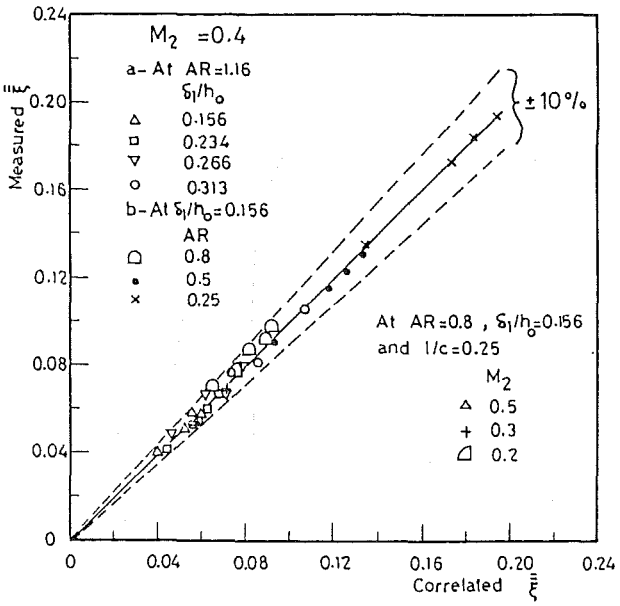

Fig. 14 Correlated $\bar{\xi}$ shows good agreement with measured $\bar{\xi}$

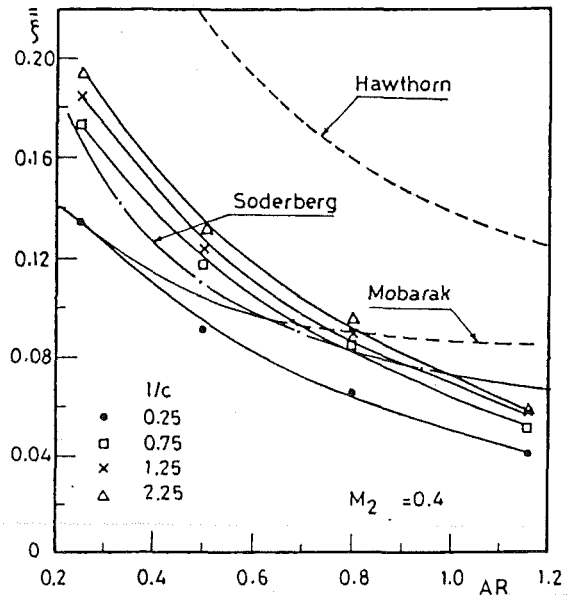

Fig. 15 Variation of passage-averaged loss coefficient with *AR*

Figure 12 shows that the energy loss coefficient increases with l/c for all aspect ratios. This increase in loss is due to flow mixing together with an additional loss due to the skin friction on the endwalls. This additional loss may be significant because of the effect of the large velocity gradients produced near the endwall by the action of the secondary flows near cascade exit. Also, it is clear from Fig. 12 that the energy loss coefficient, for all aspect ratios, increases rapidly until l/c = 0.75 and then it slightly increases with further increase of l/c. This behavior is due to the fact that most of the mixing process takes place until l/c = 0.75. It is important to mention that for aspect ratios 1.16 and 0.8, the loss coefficient exhibits a rising trend up to l/c = 1.25 and then becomes approximately constant. For aspect ratios lower than 0.8, the energy loss coefficient increases until l/c = 2.25. This is due to the growth of the additional loss (mentioned before), which appears more for a lower *AR* than for higher ones.

Figure 13 shows that the total energy loss coefficient decreases with increasing Mach number. This is a well-known behavior for subsonic flow as the increase of Mach number reduces the possibility of stagnation near walls by increasing the fluid particle acceleration.

According to the above discussion, it is clear that the passage-averaged total energy loss coefficient depends on inlet boundary layer thickness, aspect ratio, and exit Mach number. Therefore, a general correlation was deduced from Figs. 11–13 immediately to relate the passage loss coefficient with these parameters

$$\bar{\xi} = \left[K_1 + K_2\left(\frac{\delta_1/h}{K_4}\right)^{K_3}\right] \times K_5 \tag{8}$$

where K_1, K_2, K_3, K_4, and K_5 are constants that depend on different aerodynamic parameters.

The coefficient K_1 represents the passage-averaged total energy loss coefficient when the inlet boundary layer thickness tends to zero. The region of the endwall boundary layer is assumed to be very small compared to the blade height and the flow conditions in this region are assumed to be the same for all blade heights. It is obvious that the value of K_1 represents the profile loss coefficient, which in turn is a function of profile shape, space to chord ratio, incidence, Reynolds number, Mach number, and distance downstream to chord ratio (l/c).

The relation between K_1, l/c, and M_2 is given by

$$K_1 = 0.0718 - \frac{0.008}{(l/c)^{0.7}} - 0.07M_2^2 \tag{9}$$

The constants K_2 and K_3 represent the growth of mixing losses and depend mainly on l/c, while the constants K_4 and K_5 represent the effect of the secondary flow on passage-averaged total energy loss coefficient and depend on *AR*. The suggested relations for K_2, K_3, K_4, and K_5 are given by

$$K_2 = 2.389 + 3.102(l/c)^{1.565} \tag{10}$$

$$K_3 = 4.35 + 0.2(l/c) \tag{11}$$

$$K_4 = 0.8345 + (0.192/AR) \tag{12}$$

$$K_5 = 20.212 - 18.971(AR)^{0.085} \tag{13}$$

Of course, relation (8) is valid for the ranges of M_2 in which the loss coefficient increases with the decrease of M_2.

It is clear from Fig. 14 that correlation (8) agrees quite well with the present data within ±10 percent deviations.

Soderberg and Hawthorne's correlations (Horlock, 1966) are processed and compared with the suggested correlation on Fig. 15 for the same values of turning angle and maximum thickness to chord ratio. It is important to mention that the positions of the downstream planes at which these correlations were deduced are not given.

Although both Hawthorne's correlation and the present correlation have the same trend, there is a large difference in values of $\bar{\xi}$. This difference may be due to the fact that Hawthorne obtained his relation for high aspect ratio (higher than three). This fact makes the Hawthorne relation open to criticism at low values of *AR*.

The differences between the present and Soderberg's correlations may be due to the fact that Soderberg tested actual turbines of *AR* higher than one in which other losses exist, such as tip clearance losses and those due to the effect of rotation. Also, one can add the effect of blade shape and regime of operation. But for *AR* lower than one Soderberg's correlation agrees quite well with the present correlation due to the effect of growth of the additional losses that appear for lower *AR*, which compensates the effect of other losses in actual machines.

Mobarak et al. (1985) obtained a correlation at l/c = 0.4 for a straight turbine cascade having aspect ratios in the range of 0.654 to 0.145. It is clear from Fig. 15 that Mobarak's correlation agrees with the present correlation for lower values of *AR*.

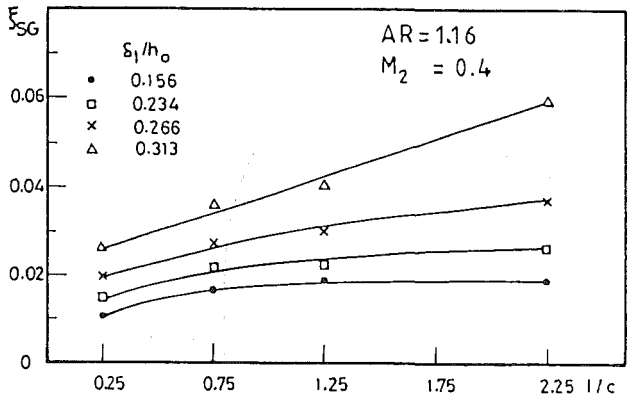

Fig. 16 Variation of gross secondary loss with *l/c*

The gross secondary losses are determined by subtracting the measured midspan pitchwise-averaged loss coefficient from the passage-averaged loss coefficient. For low-aspect-ratio blades used in the present tests, the differentiation between the profile and the secondary loss is difficult due to the merging of vortices (Moustapha et al., 1985). Therefore, the gross secondary loss will be estimated for $AR = 1.16$ only.

Figure 16 shows the variation of the gross secondary loss coefficient with the downstream distance to chord ratio (l/c) for different values of relative upstream boundary layer thickness at $AR = 1.16$ and $M_2 = 0.4$. It is clear that the gross secondary loss coefficient increases with the increase of l/c and with the increase of the value δ_1/h_0. Also, it is evident that the loss coefficient increases rapidly with l/c for higher values of δ_1/h_0. This behavior is attributed to growth of additional loss due to the skin friction on the endwalls. This additional loss may be significant for high values of δ_1/h_0 because of the effect of large velocity gradients produced near the endwalls.

Conclusions

From the previous results and discussion the following conclusions can be drawn:

1 The shapes of the three examined blade cascades do not affect the loss coefficient appreciably; however, the main parameter that has a measurable effect on the midspan energy loss coefficient is the trailing edge thickness.

2 Increasing inlet boundary layer thickness increased the spanwise extent of the zone behind the cascade in which the secondary loss vortex dominates and in turn the gross secondary loss and total energy loss coefficients increase.

3 The results show an increasing rate of energy loss with decreasing aspect ratio due to the contraction of the low loss core (potential core) of the flow and the increase of endwall effects.

4 A new correlation giving the midspan energy loss as a function of distance downstream and with t_e/S is determined for the cascades tested (correlation (7)).

5 A general correlation was deduced that predicts the passage-averaged energy loss coefficient as a function of distance downstream, aspect ratio, and exit Mach number as well as the upstream boundary layer thickness (correlation (8)).

References

Abdel Hafiz, A., 1982, "Investigation of Flow in Axial Turbines," Ph.D. Thesis, Cairo University, Cairo, Egypt.

Came, P. M., 1973, "Secondary Loss Measurements in a Cascade of Turbine Blades," *IMechE Conference Publication 3*, pp. 75–83.

Came, P. M., and Marsh, H., 1974, "Secondary Flow in Cascades: Two Simple Derivations for the Components of Vorticity," *J. Mechanical Engineering Science*, Vol. 16, pp. 391–401.

Chen, L. D., and Dixon, S. L., 1985, "Growth of Secondary Flow Losses Downstream of a Turbine Blade Cascade," ASME Paper No. 85-IGT-35.

Denton, J. D., 1973, "A Survey and Comparison of Methods for Predicting the Profile Loss of Turbine Blades," *IMechE Conference Publication 3*, pp. 204–212.

Dunham, J., 1970, "A Review of Cascade Data on Secondary Losses in Turbines," *J. Mechanical Engineering Science*, Vol. 12, pp. 48–59.

Gregory-Smith, D. G., and Graves, C. P., 1983, "Secondary Flows and Losses in a Turbine Cascade," *AGARD Conference Proceedings No. 351 on Viscous Effect in Turbomachines*, Copenhagen, Denmark.

Horlock, J. H., 1966, *Axial Flow Turbines*, Butterworths Publishers, London, Chap. 3.

Kacker, S. C., and Okapuu, U., 1982, "A Mean Line Prediction Method for Axial Flow Turbine Efficiency," ASME *Journal of Engineering for Power*, Vol. 104, pp. 111–119.

Langston, L. S., Nice, N. L., and Hooper, R. M., 1977, "Three-Dimensional Flow Within a Turbine Cascade Passage," ASME *Journal of Engineering for Power*, Vol. 99, pp. 21–28.

Mansour, M. L., 1982, "Influence of Low Aspect Ratio on Total Energy Loss and Flow Pattern in Linear Accelerating Cascade," M.Sc. Thesis, Cairo University, Cairo, Egypt.

Marchal, Ph., and Sieverding, C. H., 1977, "Secondary Flows Within Turbomachinery Bladings," *AGARD Conference Proceedings No. 214 on Secondary Flows in Turbomachines*, The Hague, The Netherlands.

Mobarak, A., Khalafallah, M. G., and Lotayef, M., 1985, "Effect of Aspect Ratio on Energy Loss in Nozzle Blades of Small Power Turbines," *International Journal of Turbo and Jet-Engines*, Vol. 2, pp. 299–305.

Moore, J., and Adhye, R. Y., 1985, "Secondary Flows and Losses Downstream of a Turbine Cascade," ASME *Journal of Engineering for Gas Turbines and Power*, Vol. 107, pp. 961–968.

Moustapha, S. H., Paron, G. J., and Wade, J. H. T., 1985, "Secondary Flows in Cascades of Highly Loaded Turbine Blades," ASME *Journal of Engineering for Gas Turbines and Power*, Vol. 107, pp. 1031–1038.

Sharma, O. P., and Butler, T. L., 1987, "Predictions of Endwall Losses and Secondary Flows in Axial Flow Turbine Cascades," ASME JOURNAL OF TURBOMACHINERY, Vol. 109, pp. 229–236.

Sharma, O. P., and Graziani, R. A., 1983, "Influence of End Wall Flow on Airfoil Suction Surface Midheight Boundary Layer Development in a Turbine Cascade," ASME *Journal of Engineering for Power*, Vol. 105, pp. 147–155.

Sieverding, C. H., and Wilputte, Ph., 1981, "Influence of Mach Number and End Wall Cooling on Secondary Flows in a Straight Nozzle Cascade," ASME *Journal of Engineering for Power*, Vol. 103, pp. 257–264.

Detection of Separation Bubbles by Infrared Images in Transonic Turbine Cascades

W. Bräunling
DFVLR, Institute for Experimental Fluid Mechanics, Göttingen, Federal Republic of Germany

A. Quast
DFVLR, Institute for Design Aerodynamics, Braunschweig, Federal Republic of Germany

H.-J. Dietrichs
Motoren und Turbinen Union München GmbH, Munich, Federal Republic of Germany

In a test facility for straight cascades, equipped with profiles designed for a highly loaded gas turbine rotor of a high-pressure stage, experiments were conducted to clarify some effects of shock wave–boundary layer interactions. The specific aim was to determine both the position and strength of compression shocks originating from profile wake flows and the position and extent of separation bubbles. The latter are most often detected by visualization methods like surface oil flow patterns or Schlieren photographs, as well as by typical properties in wall pressure distribution curves. In addition, the infrared image technique, which has found many applications in a wide range of technical activities in the recent years, may also be used. Compared with other methods, this technique has distinct advantages in fluid mechanics applications. The whole model can be observed without disturbing the boundary layer by tappings, measuring materials, or probes. Some typical infrared images are presented and interpreted using results of pressure distribution measurements, hot-film measurements, and surface oil flow visualizations.

Introduction

One of the main trends in the development of modern turbomachinery components for aircraft engines is the reduction of the number of stages without compromising the efficiency levels. This leads to a considerable increase of the aerodynamic loading of the blade rows. The loss produced in the transonic flow fields within the blade row passages is counterproductive to the desired efficiency targets. Therefore, a profound understanding of the flow phenomena in transonic flow fields is necessary to enable optimization of the blade profiles for specific flow conditions. A typical flow field in a straight transonic rotor cascade is shown in Fig. 1. The transonic flow phenomena are essentially controlled by trailing edge shocks (*a*), separation bubbles (*b*), and expansion waves (*c*), (*d*) (Dietrichs et al., 1987).

The shock wave–boundary layer interaction has been studied by many investigators. A current review of the most important experimental and theoretical works of the last few years is given by Delery and Marvin (1986). Nevertheless, the understanding of the physical phenomena is not complete yet. This is especially true in turbine flows where both laminar and turbulent boundary layer conditions are present along with transition zones. The problems resulting from that are not completely clear. In order to achieve a better understanding of these physical phenomena MTU München and the Institute for Experimental Fluid Mechanics of the DFVLR conducted a joint investigation of the shock wave–boundary layer interaction in a highly loaded turbine cascade. The experimental part of this scientific cooperation consisted of measurements applying several techniques: wake flow measurements using a pneumatic probe, surface pressure distribution measurements on the profile and on the side wall with a higher number of tappings than usual, boundary layer measurements with hot-

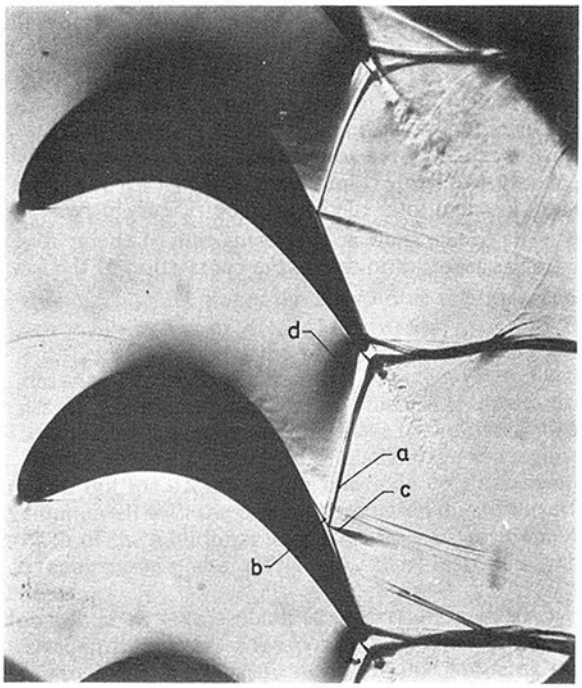

Fig. 1 Transonic rotor cascade at an isentropic outlet Mach number $M_{2S} = 1.25$

Contributed by the International Gas Turbine Institute and presented at the 33rd International Gas Turbine and Aeroengine Congress and Exhibition, Amsterdam, The Netherlands, June 5-9, 1988. Manuscript received by the International Gas Turbine Institute October 1, 1987. Paper No. 88-GT-33.

film sensors, and finally flow visualizations using Schlieren photography, liquid crystal techniques, and oil flow patterns. Oil flow visualization was performed on both the profile surfaces and the side walls. The goal of applying all these techniques was to determine the shock structures, their intensity, and the interaction mechanism with the suction side boundary layer. This gives the desired information about both the position and the extent of separation bubbles.

In cooperation with the DFVLR Institute for Design Aerodynamics an additional visualization method was used, the infrared image technique. It had already been successfully applied to studies on single airfoils at this institute (Quast, 1987).

The infrared image technique is a very simple method for detection of processes connected with heat transfer, like transition and separation, where changes in the local shear stresses result in corresponding changes in the local heat transfer. If a temperature difference between the fluid and the wall exists, the heat transfer is low in laminar boundary layers, very low in separation regions, and high in turbulent boundary layers.

Transition lines and separation zones are usually detected by well-known methods like oil flow patterns or sublimation techniques. These methods have the disadvantage that the flow quality may be affected by the presence of the materials used. Other methods, such as hot wires or hot films, give only point-by-point information. Moreover, these methods are time consuming and therefore costly. The infrared image technique is able to eliminate these disadvantages completely.

Application of the infrared image technique in a transonic wind tunnel for straight turbine cascades is described here. The results will be compared with those from other techniques mentioned earlier.

Analogy Between Heat Transfer and Skin Friction

For boundary layer flows a relationship between heat transfer and skin friction (c'_{fx}) exists, which was first discovered by O. Reynolds and which is therefore known as the Reynolds analogy. According to this, especially in the case of the similar solutions of the boundary layer equations, and neglecting the free-stream turbulence, the local heat transfer coefficient α_x can be written in the following form (Schlichting, 1968):

$$\alpha_x = \frac{c'_{fx}}{2} \cdot U_x \cdot \frac{k}{\nu}$$

It should be noted that the Reynolds analogy is only valid for established laminar or turbulent flows. Moreover, it remains approximately true in cases when the streamwise pressure gradient is different from zero without being too large. It is not valid in transitional or separated flows. The above formula explains the well-known fact that heat transfer in a laminar boundary layer is small because skin friction is small and that heat transfer in a turbulent boundary layer is much higher due to a higher skin friction. For example, on a flat plate the skin friction coefficient increases along the transition region by more than a factor of 10 (Quast, 1987). According to the Reynolds analogy, the heat transfer also changes by the same factor.

If there is a temperature difference between the fluid and the profile surface, the model surface will adopt different temperatures, whether the boundary layer is laminar or turbulent. Thus, in turbulent flow, and especially just behind the transition, the heat transfer is high and the model will adopt nearly the temperature of the fluid. On the other hand, the model temperature will remain nearly unchanged in the laminar boundary layer just upstream of the transition location, where the wall shear stress is low.

Infrared Measurement Technique

In a wide range of technical applications, the infrared measurement technique has made considerable progress in the last two decades, especially for no-contact temperature measurements. Logically, its use in fluid mechanics is also appropriate for processes connected with heat transfer, like transition and separation.

Infrared Spectral Range. Above absolute zero any material emits thermal radiation in all its aggregate states. Below a few thousand Kelvin this radiation is caused by oscillating atoms in the lattice space of solid bodies or by oscillating and rotating atoms or molecules in substances of gaseous state. At higher temperatures dissociation and ionization are governing. For solid bodies and liquids these different modes of origin produce either continuous spectra or spectra with a wide range of wavelengths, whereas gases radiate either with discrete spectra or spectra in very small regions of wavelengths.

The infrared spectral range is only a very small part of the whole range of the electromagnetic radiation spectrum. It reaches from the end of the visible spectral range with a wavelength of roughly 0.78 μm up to wavelengths of 1 mm. Without any physical reasoning a more or less arbitrary classification in four sectors is usual: near infrared (0.78–1.5 μm) mean infrared (1.5-6–60 μm), far infrared (6.0–40 μm) and ultrafar infrared (>40 μm). In colloquial usage, the terms thermal radiation and infrared radiation are used synonymously, although they are only identical in a confined region, because the former reaches from the of the visible wavelength zone up to the end of the far infrared.

Emissivity. To determine the temperature by a radiation measurement, the emissivity is of central importance. The emissivity of an arbitrary thermal radiator is defined by the ratio of its emitted radiation to that of a black body with the same temperature. The range of the emissivity reaches from zero for nonemitting radiators up to unity for the black body. The position of an arbitrary thermal radiator inside this range depends on its material, the character of its surface, its temperature, and the direction of observation. That means materials like plastic, wood, or rubber have an emissivity near unity, just like materials coated with black lusterless paint,

Nomenclature

c'_f = skin friction coefficient
E = time-averaged thin-film signal
k = thermal conductivity
l = length
M = Mach number
p = pressure
U = mean velocity
x = coordinate along the profile surface
α = heat transfer coefficient
β = flow angle
ϑ = separation angle
ν = kinematic viscosity
τ = wall shear stress

Subscripts

0 = at zero flow conditions
1 = homogeneous inlet flow
2 = homogeneous outlet flow
c = profile chord
p = pitch
ps = pressure side
S = isentropic
ss = suction side
st = staggered
w = profile surface
x = location on the profile along the surface

whereas materials with polished metal surfaces are near to the other end of the emissivity scale. For example, a plastic surface with flush-mounted polished metal spots and a homogeneous thermal distribution has an inhomogeneous radiation distribution due to the different local emissivities. Therefore, an infrared system, which measures the emitted radiation, would interpret the metal spots as cooler regions compared to the surrounding plastic surface. This illustrates the importance of material selection for infrared measurements in wind tunnels. Good results may always be expected by emissivities near unity.

Also of importance are the radiation properties of the different materials in respect to the radiation incidence angle (Quast, 1987). Nonmetallic substances have a wide range of incidence angles where the emissivity is nearly constant. On the other hand metals have an astonishing increase of emissivity with decreasing incidence angles. Therefore, infrared measurements on highly curved surfaces are extremely difficult.

Infrared Detectors. The most important element of any infrared measurement instrument is the radiation detector, which changes the radiant energy received due to infrared radiation into electrical energy or controls an electrical subsidiary circuit. There are essentially two types of infrared detectors: the thermal detector and the photon detector.

The thermal detector measures the absorbed energy per unit of time. This means that the detector changes its temperature due to the absorption of electromagnetic radiation. In principle, the output signal of such a thermal detector is independent of the radiation wavelength. Unfortunately, the detector surface has different coefficients of absorption at different wavelengths. Therefore, such independence is not completely present.

The process of the temperature change of a thermal detector is relatively slow and therefore its time constant is correspondingly high and lies in general in the millisecond range. The time constant is the time that the detector needs to produce a utilizable electrical output signal. The salient advantage of such a thermal detector is its capability to enable high thermal resolutions up to 0.1 K.

The main difference between a photon and a thermal detector is the reaction to absorbed radiation. A photon detector counts the number of absorbed photons per unit of time. This process is based on the physical principle of photoelectric emission. Because the energy of the photons is inversely proportional to the electromagnetic wavelength, a critical wavelength exists at which the energy level is too low to maintain the photoelectric emission. For modern detectors this critical wavelength is roughly 14 μm. Above this value infrared measurements using photon detectors are not possible. Corresponding to Planck's radiation law, a black body with a temperature of 300 K has its maximal specific emission at a wavelength of roughly 10 μm. This is within the so-called atmospheric window of the infrared spectral range, which reaches from 8 μm up to 14 μm. Therefore, infrared detectors working with this wavelength are of great interest, especially for experiments in noncryogenic wind tunnels. Furthermore, these detectors are very fast, with time constants in the microsecond range. Due to the restricted resolving power for the received infrared radiation only a temperature resolution of 2 K is possible at best. One of today's most important photon detectors is the cadmium-mercury-telluride ($Cd_xHg_{1-x}Te$) detector, often used in infrared cameras for observing dynamic processes. The critical wavelength of this detector increases with decreasing operation temperatures. Best results are achieved at 77 K. Therefore, such a detector is nitrogen cooled.

Single Detector Infrared Image System. Most commercially available infrared cameras today, including the one used in the present work, operate with a single-element infrared detector. An opto-mechanical scanner system consisting of a rotating polygonal (12,500 rpm) and an oscillating plane mirror scans the object line by line (Walther and Gerber, 1983). The detector measures the emitted radiation from each point on the object surface and changes it into an electrical signal. After amplification this signal is used to control the intensity of an electron ray, which is deflected in a cathode-ray tube synchronously to the movements of the scanner system. This results in the development of a picture in grey tones on the screen. This is the so-called thermogram. The local brightness of such a picture is proportional to the temperature of each corresponding point on the object surface.

The advantage of using a single-element detector is that each point on the object is measured by the same detector, and therefore an incorrect representation of the thermogram due to differences in the detector sensitivities by using a multi-element system does not occur.

When observing emitting temperature fields with a single-element system the scanning rate depends on the time constant of the detector and the dynamic behavior of the opto-mechanical scanning system. Picture frequencies between 10 Hz and 50 Hz are necessary to observe dynamic temperature fields with an acceptable resolution of roughly 30,000 scanning points on the screen. This requires the use of photon detectors with time constants in the microsecond range.

The infrared image system used (AGEMA-Thermovision 782) is capable of measuring dynamic processes with a picture frequency of 25 Hz. The screen of the imaging system has 280 lines with 100 pixels in each line. The camera is equipped with a nitrogen-cooled ($Cd_xHg_{1-x}Te$) detector working in the spectral range from 8 μm to 12 μm. Its time constant is approximately 1.5 μs. The operation range of the camera lies normally between 253 K and 1173 K and allows a selection of the temperature resolution in nine steps from 2 K up to 1000 K.

The thermogram produced is composed of continuous grey tones between white and black. Under normal conditions regions of small emissivity are shown darker. When the screen option of inverse picture reproduction is used, the regions of small emissivity will be lighter. The temperature level for the beginning of the grey tone scale can be adjusted continuously by hand or automatically. The selected temperature resolution is indicated on the screen. By using a photo-camera triggered by the scanner system an inscribed thermogram can be produced. As in the present work qualitative results can be obtained without any subsequent data processing.

Conditions for the Test Setup. Past experiences have shown (Quast, 1987) that in most wind tunnels temperature differences between the model and the flow exist and thus the basic requirement to enable the application of the infrared image technique at all is satisfied. In general the model will not have the flow temperature because of convection, conduction, and especially radiation between the model and the more voluminous tunnel side walls and the holding device. Therefore, no internal or external heating of the model surface is necessary. In cases where this precondition is not fulfilled, the requirements can be met by using wind tunnel cooling equipment.

The measurements were conducted in a test facility for straight cascades. An updated description of this cascade tunnel is given by Heinemann (1983). Therefore, only some salient features are highlighted here.

The tunnel is of semicontinuous suck down type. Atmospheric air passes through a dryer, a settling chamber with honeycombs, a rectangular inlet duct, the cascade test section enclosed in a plenum chamber, a choking diffuser, and finally through a butterfly valve into a big vacuum vessel.

The test setup for measurements is shown schematically in Fig. 2, where the area covered by the infrared camera is also

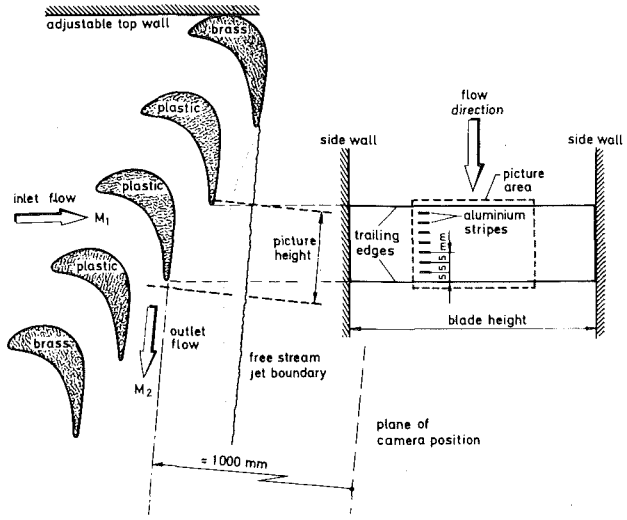

Fig. 2 Test setup

indicated. A highly loaded gas turbine rotor cascade of a high-pressure stage was used for testing. The profile shape was designed by MTU München (Dietrichs at al., 1987). For the wind tunnel test the chord length was 60 mm and the blade height 125 mm. During the measurements described here nine blades were in the flow. Infrared pictures were taken from the central blade. The camera position was roughly one meter behind the cascade outlet plane. To minimize emissivity errors, the optical axis and the rear part of the suction side were approximately perpendicular to each other. By this setup the camera and its holding device could not affect the flow quality and the camera itself was not exposed to high dynamic pressures in the supersonic outlet flow. The central blade and the two adjacent ones were manufactured of fiber-reinforced plastic, which has a higher emissivity than the other blades made of brass. Moreover, reflection problems between the adjacent blades and the central one were also minimized. Marks on the model surface, which may be used as a helpful tool to interpret the results, were made by flush-mounted polished aluminum strips (Fig. 2). As explained earlier they are quite easily visible on an infrared picture due to their lower emissivity.

Shock Wave–Boundary Layer Interaction

General Results. For an inlet flow angle of $\beta_1 = 120.8$ deg the profile surface Mach number distributions versus the dimensionless distances along both the suction and the pressure side for three different isentropic outlet Mach numbers M_{2S} are shown in Fig. 3. The Reynolds number was 0.8×10^6 based on the exit conditions and the chord length for all three cases. The total temperature of the inlet flow was 305 K and the temperature of the test setup was 292 K.

For the first case, $M_{2S} = 0.6$, all local Mach numbers on the surface are subsonic. The next exit Mach number itself is still subsonic, $M_{2S} = 0.9$, whereas some local Mach numbers on the suction side are already supersonic. The third case with $M_{2S} = 1.25$ represents the typical case of transonic flow conditions and corresponds to the Schlieren picture in Fig. 1. In the rear part, a short distance behind the suction maximum for all three Mach number distribution curves, characteristic features indicate a separation bubble. This statement is supported by both the Schlieren picture Fig. 1 and the oil flow patterns in Fig 4. In both cases the bubbles are very clearly visible. Moreover, the shapes of the Mach number distributions around the trailing edge are quite remarkable. These distributions are obtained by using more tappings than usual, partly arranged in blade height direction. The distance between the

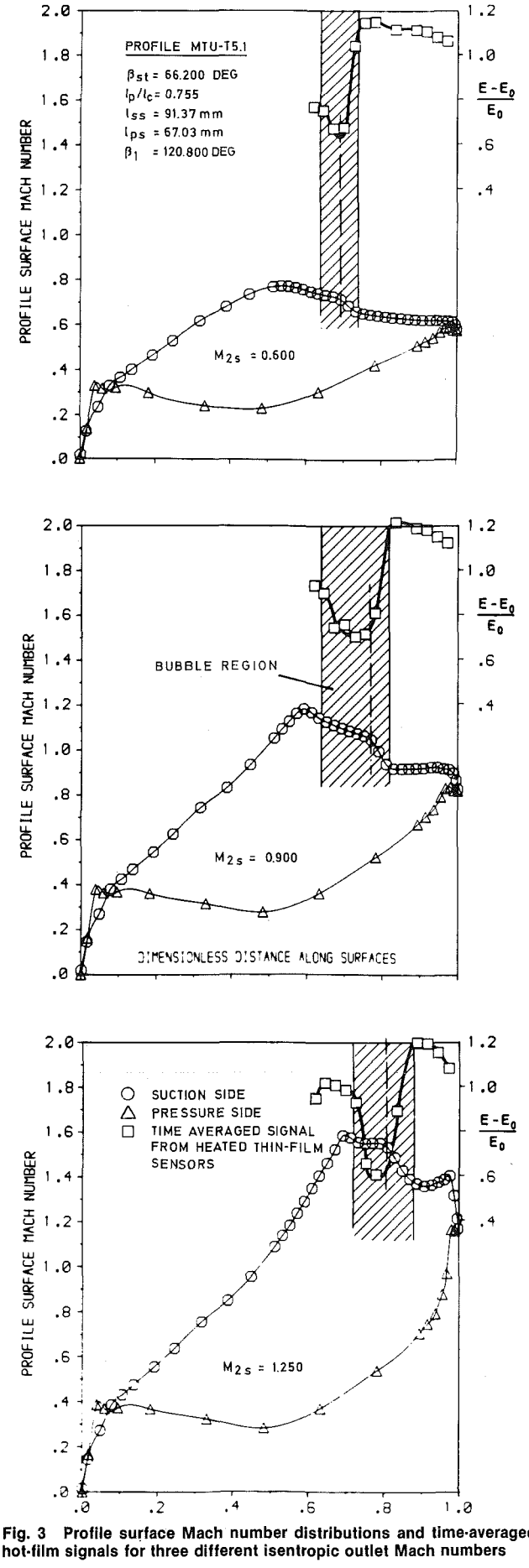

Fig. 3 Profile surface Mach number distributions and time-averaged hot-film signals for three different isentropic outlet Mach numbers

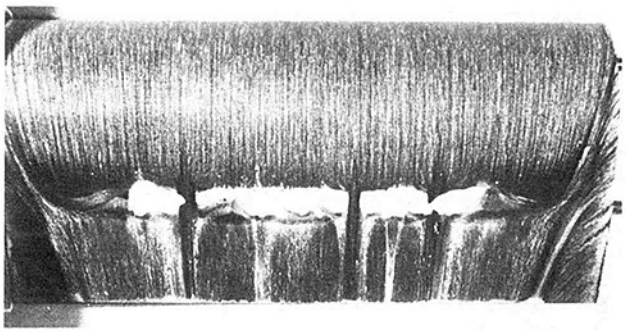

Fig. 4 Suction side oil flow patterns: β_1 = 120.8 deg, M_{2S} = 0.6

extreme holes was roughly 10 mm in the blade height direction. As this section of the blade height is almost at the center of the channel, there can be no influence due to three-dimensional effects. The influence of the large number of tappings themselves on the results was tested by comparison with an additional blade with the usual number of tappings at a few identical conditions. Comparison of such results with the ones presented here did not show any significant differences.

Another considerable indication of the existence of the bubble and its extent is given by the curves plotted additionally to the Mach number distributions in Fig. 3. These curves represent the time-averaged signals of measurements with flush-mounted heated thin-film sensors. They were manufactured by MTU München and an application to a single airfoil is described by Pucher and Göhl (1987).

The signals of the thin-film measurements are evaluated separately for the DC and AC components. Here only the proportion E of the DC voltage corresponding to the time-averaged heat transfer is taken into account. Changes in the local wall shear stress result in changes of the local thin-film heat transfer, which is indicated by changes of the voltage E.

The distinct jump in the thin-film curves can only be due to the separation bubble, because in this region the wall shear stresses are less than or equal to zero. Also a considerable difference in the E levels exists in front of and behind the bubble region. This indicates different boundary layer conditions. Together with additional information from the AC voltage, which is not discussed here due to limited length of the present paper, the assumption that the boundary layer changes from laminar to turbulent along the bubble region in all cases presented here is appropriate.

Physical Interpretation. The fully subsonic case in Fig. 3 is discussed first. On the suction side the flow is accelerated up to a velocity maximum. Slightly farther downstream the gradient of the Mach number distribution curve is inverted and the surface Mach number decline is small and continuous up to that point where the gradient becomes distinctly steeper. Thereby the typical hump in the distribution curve is formed indicating a bubble. Such a curve shape could not be obtained by inviscid predictions (Dietrichs at al., 1987).

When the development of the boundary layer is taken into account this phenomenon can be explained. Due to the continuous acceleration of the flow on the front part of the suction side the boundary layer remains laminar up to the point just downstream of the velocity maximum where the adverse pressure gradient leads to a laminar separation. In the following separated region an exponential decrease of the slope of the pressure curve is observed, for both the laminar and turbulent cases. In general the laminar case has weaker pressure gradients, often approximated by constant pressure.

The separated flow, which behaves like a boundary layer, is thickening continuously in streamwise direction and loses the capability to decelerate. This is the reason for the weak pressure rise region. Near the peak of the hump the separated

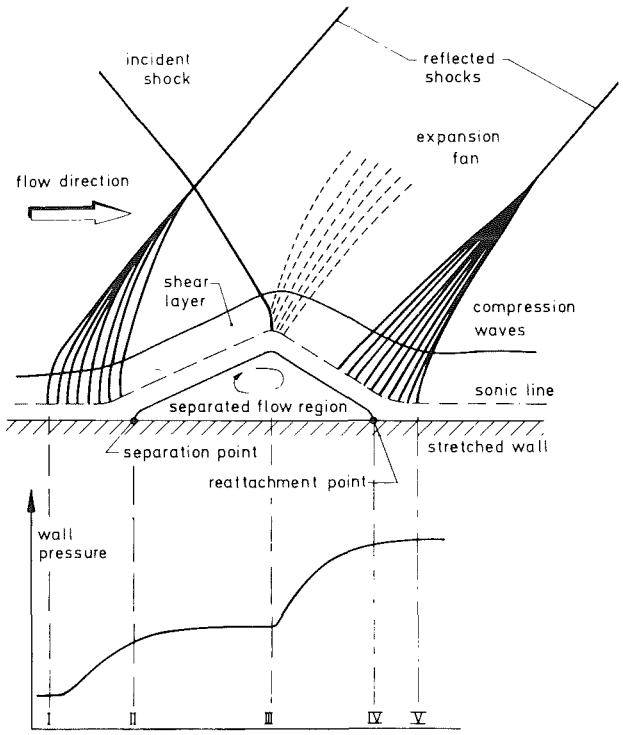

Fig. 5 Laminar shock boundary layer interaction; schematic representation of the flow field and the wall pressure distribution

shear layer turns turbulent. In turbine flow the rearrangement of the shear layer seems to happen quite rapidly, as is obvious by the steep gradient of the pressure distribution curves. The turbulent flow has a much stronger diffusion capability than the laminar one. Therefore, the turbulent flow reattaches a short distance downstream of the transition zone. Thus in the subsonic case the transition can be detected by the shape of the pressure distribution curves only.

At first sight the experimental results of the transonic case downstream of the velocity maximum appear to exhibit a similar behavior to the subsonic ones. However, a comparison with inviscid predictions shows quite different pressure distributions in this region (Dietrich et al., 1987). The reasons for such differences are explained with the help of Fig. 1. Interferences between oblique shocks originating from trailing edge wake flows and the suction side boundary layers are obvious. Unfortunately, the resulting sharp change of the pressure gradient is visible in both nontransitioning laminar flows and fully turbulent flows. This change is imposed by the turning of the flow due to an incident shock impinging onto the boundary layer. Evidently, in transonic flows the identification of transition, using the pressure distribution only, is not possible as it is in subsonic flows, because both boundary layer conditions may occur independently. It is safe to assume that more complicated interactions exist, making the interpretation of test results entirely difficult.

In the following section the phenomenon of shock wave–boundary layer interaction will be discussed in more detail by using Fig. 1, Fig. 3, and the additional Fig. 5. The latter figure is a scheme of the real flow field of Fig. 1. Up to the velocity maximum the flow is assumed to be laminar. Together with displacement effects of the boundary layer the incoming flow may be assumed parallel. Due to the impingement of the incident shock a pressure discontinuity is produced that the viscous flow can not follow immediately. Therefore, the imposed pressure jump is spread along a finite distance upstream and downstream of the shock impingement point. In this process, the information about the shock-produced pressure disturbance is propagated upstream

through the subsonic part of the boundary layer. The principle of energy conservation prevents a boundary layer possessing small momentum from passing through a shock wave. As this is the case for the laminar viscous layer approaching an incident shock wave, an additional supply of momentum is necessary. The latter is mainly provided by the mixing of the external flow with the boundary layer, whose thickness then increases rapidly until it separates from the wall. Hence, the velocity profile will fill up before the boundary layer reaches the shock impingement point. The resulting deflection of the boundary layer outward from the wall causes a compression at station I in Fig. 5, and a marked rise in pressure occurs up to the shock impingement point. The interaction of the streamline curvature resulting from the growth of the displacement thickness and the camber of the profile wall contour produces the pressure rise in the so-called free interaction region from station I to station II. Because of the weak pressure gradients and the corresponding weak density gradients in laminar boundary layers, such a flow detail cannot be resolved by either the Schlieren optic or the static pressure measurements. Therefore, it may be suggested that the free interaction length in laminar turbine flow is relatively short.

Up to here, very close to separation point II, the flow has the strongest adverse pressure gradient that the laminar boundary layer can endure. Then it separates from the wall, approximately with the separation angle ϑ, given by Oswatitsch (1958)

$$\vartheta = \arctan\left[-3\,\frac{\partial\tau/\partial x}{\partial p/\partial x}\right]$$

This equation is a solution of the Navier–Stokes equations and is valid for compressible, two-dimensional steady-state flows with arbitrary Reynolds numbers. From the above equation it is obvious that, although a high-pressure gradient $\partial p/\partial x$ is required for boundary layer separation, the separation angle is inversely proportional to the pressure gradient. This angle will decrease farther downstream of the separation point as explained by Oswatitsch (1958) and Katzer (1985). Similarly to the subsonic case mentioned above the shear layer is thickening in streamwise direction. This leads to a continuously decreasing pressure gradient, in the separated flow region. The streamline curvature is formed by an adaption process to the recirculating region. By this process compression waves are induced, which in turn produce the pressure distribution required by the shear layer. At this the shear layer is lifted so far from the profile surface that the resulting displacement effect gives the streamlines the required curvature. As the pressure gradient approaches the shock impingement point, it tends asymptotically to zero, the compression waves become weaker, and the flow becomes more parallel to the profile surface. Not far from the shear layer edge the compression waves are combined to build the first reflected shock.

At station III the incident oblique shock reaches the edge of the free shear layer. Up to now the discontinuity inherent in the shock has been considerably weakened due to its interaction with the compression waves in the flow. The oblique shock turns the flow toward the wall. At the shear layer this turning has to be accomplished by an expansion wave at station III, which may be identified quite clearly in the Schlieren picture in Fig. 1. This expansion takes place along a very short distance. This indicates the presence of a Prandtl–Meyer expansion. Therefore, the pressure remains continuous through the incident shock and the following induced expansion. Unfortunately, the pressure gradient downstream of station III is significantly stronger than the upstream one, although the latter equals the limit for the separation at point II. Nevertheless, behind station III the shear layer tends to reattach. Assuming that the flow is still laminar such a phenomenon cannot be explained in terms of Prandtl's boundary layer theory.

Downstream of the expansion fan the pressure distribution

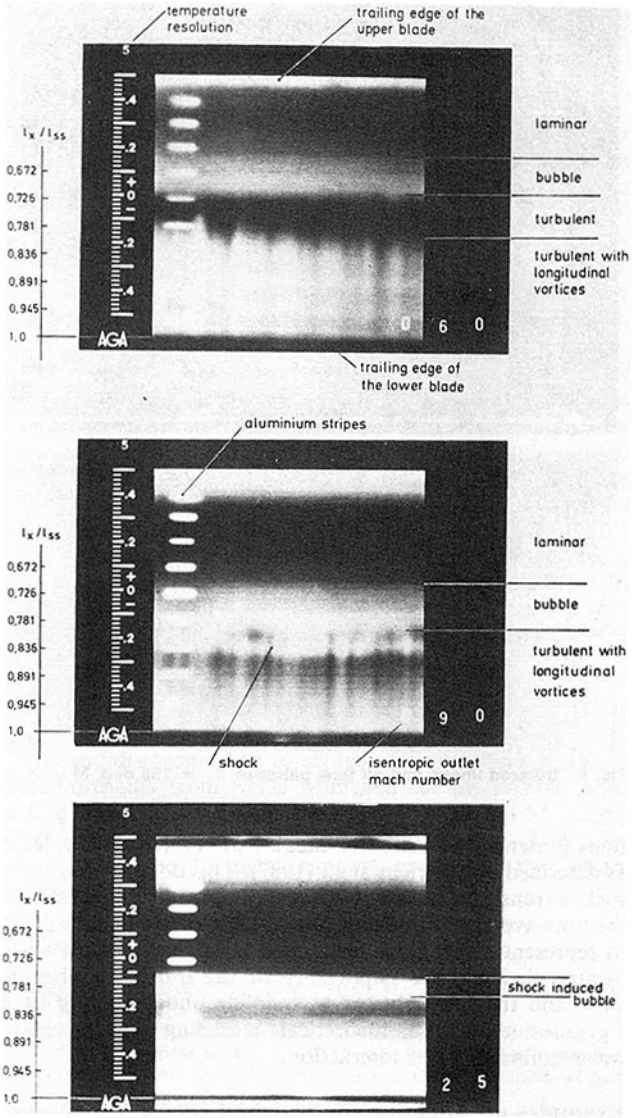

Fig. 6 Infrared images for three different isentropic outlet Mach numbers

shape is again coupled with the development of the free shear layer, which leads to a second weak continuous compression. The compression waves are combined again to form a second reflected shock. Downstream of the reattachment point at station IV the compression waves are weaker because of the lower pressure gradients. Parallel flow is assumed downstream of station V.

The characteristic features explained by Fig. 5 are applicable to both fully laminar and fully turbulent flows. The essential difference between these cases is the considerably higher pressure gradient for the turbulent case (Delery and Marvin, 1986). Therefore, in transonic cases no typical criteria exist to identify transition by interpreting the pressure distributions only.

The occurrence of transition from laminar to turbulent flow along the interaction zone leads to a substantially higher complexity of the problem and has an extreme importance for the performance of turbine bladings. Such a development has the distinct advantage that the reattaching problems mentioned for the fully laminar shock wave-boundary layer interaction can be eliminated. A schematic description of such a process with the transition zone immediately downstream of the shock impingement point is explained in more detail by Dietrichs at al. (1987). The Schlieren pictures and the pressure distribu-

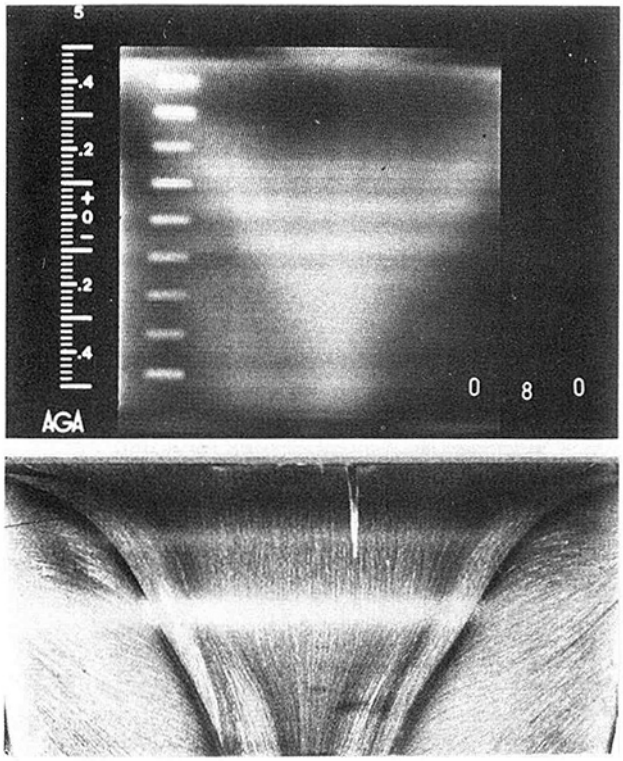

Fig. 7 Infrared image and oil flow patterns: $\beta_1 = 155$ deg, $M_{2S} = 0.8$

tions presented here are not capable of resolving such details as described by Dietrichs at al. (1987). This does not mean that such a transition does not happen. The additional curves of the time-averaged hot-film signals in Fig. 3 can be interpreted to represent a turbulent reattached boundary layer. This indicates distinctly the importance of the transition phenomenon and the necessity for a complete understanding of it, e.g., for a precise theoretical modeling of the shock wave-boundary layer interaction.

Examples of Applying the Infrared Image Technique

The infrared images corresponding to the profile surface Mach number distributions in Fig. 3 are presented in Fig. 6. For the infrared images presented the screen option of inverse picture reproduction was used. Therefore, regions of lower emissivity are light and those of higher emissivity are dark.

In the case of $M_{2S} = 0.6$ a zone with a distinct black coloring is visible. When looking in the flow direction (Fig. 2), this region begins roughly at $l_x/l_{ss} = 0.73$. This value is determined using the position of the aluminum stripes visible in Fig. 6 and the calculated suction side length l_{ss} in Fig. 3, which starts at the current stagnation point. A comparison of the value $l_x/l_{ss} = 0.73$ with those of the abscissa in Fig. 3 shows that the beginning of the black zone corresponds to the end of the bubble region, which itself begins at $l_x/l_{ss} = 0.63$. From here up to $l_x/l_{ss} = 0.73$ a light region is visible. As explained earlier, the total temperature of the flow was 13 K higher than the temperature of the plastic blade. According to this the light region mentioned can be identified as the bubble zone because in this separated region the initial temperature of the blade is dominating. Consequently, the black area behind this zone, which is darker than the black area in front of the bubble, represents the turbulent boundary layer. At first glance this agrees quite well with the physical arguments explained earlier. Unfortunately, this black region is shorter than expected, because a light region streaked with dark stripes follows. A relaminarization due to an acceleration of the flow is not probable as shown by the Mach number distribution. Also, the time-averaged hot-film signals do not give a definite indication, although the values behind the bubble do decrease after reaching a maximum. Rather, the assumption that the turbulent boundary layer falls apart and builds longitudinal vortices is true. This was already described by Ginoux (1969) for reattaching laminar and transitional high-speed flows. Using several measurement techniques, he observed spatially periodic patterns of counterrotating streamwise vortices. On infrared images the presence of vortices can be deduced from the light areas when the flow is warmer than the model. An illustration of this is presented in Fig. 7. By considerably increasing the inlet flow angle β_1, distinct passage vortices were produced, which are extended up to the half blade height. The corresponding infrared picture shows the typical flow patterns of the vortices by a V-shaped light area. The oil flow pattern in Fig. 7 does not show the presence of a laminar separation bubble. Due to the great inlet flow angle an overexpansion of the suction side flow near the leading edge is produced with a following turbulent reattachment. Although a considerable acceleration follows no indication of a relaminarization is obvious. The boundary layer is fully turbulent up to the trailing edge. Therefore, no laminar separation bubble is visible.

The case of $M_{2S} = 0.9$ shows a similar result to the previous one. From the infrared picture presented the beginning of the bubble cannot be identified clearly, whereas its end is easily visible at approximately $l_x/l_{ss} = 0.79$. For the presentation here only those pictures were selected that are of high contrast at the rear part of the suction side. Contrary to the previous infrared picture, typical traces due to the streamwise vortices start now directly behind the bubble region. It is clearly visible that the vortex periodicity has changed. The vortex traces are crossed by a distinct but relatively small light region produced by dominating local suction side shock, which is quite visible in Fig. 8. The other shocks visible in this figure are weaker and cannot be identified by the infrared system.

The presence of such streamwise vortices leads to a periodic variation of the slope of the velocity profiles at the model surface along the blade height and implies similar variations of the skin friction. By Reynolds analogy spanwise variations of the heat transfer coefficient are therefore expected.

Small free-stream nonuniformities, which are unavoidable under practical conditions, can trigger small disturbances in the boundary layer. As the flow separates and reattaches, a stability machanism organizes the nonuniformities into regular patterns, resulting in a spanwise variation of boundary layer properties demonstrated in the infrared images shown.

Given the existence of streamwise vortices in reattaching high-speed flows, spanwise variations of the boundary layer properties will be induced. Consequently the question arises: Do they affect the streamwise properties of the reattaching flow? As explained earlier, the pressure rise at reattachment associated with the ability of the shear layer to reattach to the wall is dominated by the diffusion rate between the shear layer and the main flow. Thus it is possible that the streamwise vortices in the boundary layer modify this diffusion and affect the wall static pressure distribution. To clarify this and also the effects of the streamwise vortices on transition in turbine cascade flow more research is required.

An additional difference between the cases $M_{2S} = 0.6$ and $M_{2S} = 0.9$ in Fig. 6 is noticeable. Behind the bubble at $M_{2S} = 0.6$ a dark region exists indicating turbulent boundary layer conditions. This dark region disintegrates due to the development of the streamwise vortices. The case $M_{2S} = 0.9$ does not show such a closed dark zone. Here the vortices are developed close behind the bubble. The reason for that could be that for the production of streamwise vortices small perturbations in the free stream or leading edge imperfections are necessary (Ginoux, 1969). These weak and certainly irregularly spaced disturbances exist already upstream of the separation. They will be amplified by the turbulent boundary layer after reat-

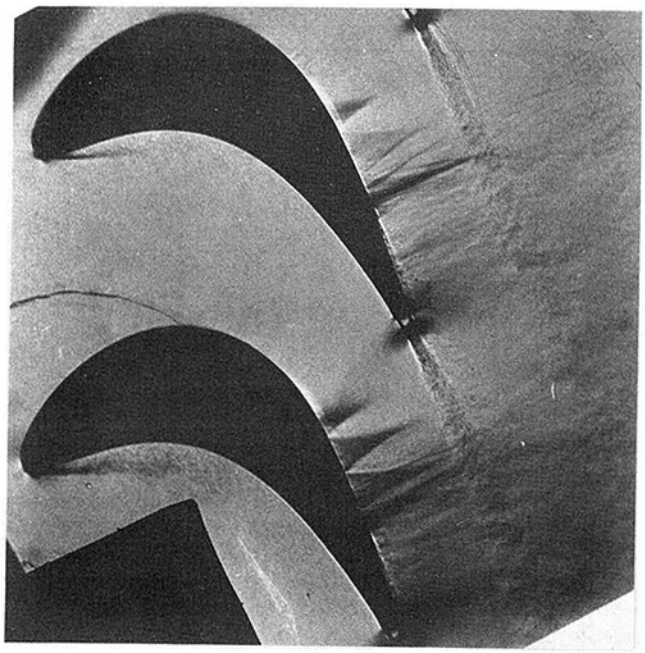

Fig. 8 Schlieren picture: $\beta_1 = 120.8$ deg, $M_{2S} = 0.9$

taching and then become spatially periodic. For the case $M_{2S} = 0.9$ such an amplification occurs earlier due to the presence of weak shocks as visible in Fig. 8.

The last case, $M_{2S} = 1.25$, in Fig. 6 corresponds to Fig. 1 and represents pure transonic conditions. Behind a distinct black region a small white zone follows indicating the shock-induced separation bubble. This white area is followed by a moderate dark one indicating the presence of a turbulent boundary layer. The dark region then changes again to a light-colored region in the flow direction. Such a development corresponds to the one at the case of $M_{2S} = 0.6$. But the presence of streamwise vortices could not be clearly proved, although many attempts were made. There is reason to suppose that the temperature resolution of the infrared camera, which depends on the resolving power of the infrared detector, was too low to resolve the present flow processes.

For all three cases in Fig. 6, the change of the dark coloring of the areas upstream of the separation bubbles with increasing Mach numbers agrees well with the hot-film signals in Fig. 3. This is also true for the intensity of the light zones in the bubble regions. Due to the boundary layer conditions the areas behind the bubbles have to be darker than those in front of them. This requirement is fulfilled only at $M_{2S} = 0.6$ if the effects of the development of streamwise vortices are neglected. Further interpretation of the infrared imaging results of the other two cases, especially the comparison with the results of the hot-film measurements, cannot be undertaken. It is likely that more information is required. But is should be pointed out that Ginoux (1969) has reported measurements of the recovery temperature along a model surface in the presence of streamwise vortices, which show the same tendencies as the hot-film signals presented here.

Conclusions

The phenomenon of shock wave–boundary layer interaction in transonic turbine cascades has been investigated. Some results of profile surface pressure distribution measurements and flow visualizations using Schlieren photography and oil flow patterns were presented, discussed, and finally complemented by some time-averaged signals of hot-film measurements. Moreover, a relatively new measurement method, the infrared image technique, was explained. Its results were compared with the others mentioned above.

A physical interpretation of the phenomenon investigated was given. It was explained that the presence of both laminar and turbulent boundary layers increases the complexity of the flow and makes it rather difficult to give a complete interpretation of the test results. No answer could be given to the very interesting question of whether the viscous interaction on the profile suction side causes boundary layer transition.

An analysis of the infrared images compared with results from literature led to the assumption that during and after the reattachment spatially periodic streamwise vortices are produced. For a more detailed and complete interpretation of the infrared images more investigations are necessary.

Acknowledgments

The authors would like to express their gratitude to Dr. J. Hourmouziadis from MTU München for his efforts in initiating this scientific cooperation between MTU München, DFVLR Göttingen, and DFVLR Braunschweig. They also acknowledge the financial support given by the Federal Ministry for Research and Technology.

References

Delery, J., and Marvin, J. G., 1986, "Shock-Wave Boundary Layer Interactions," AGARDograph No. 280.

Dietrichs, H. J., Hourmouziadis, J., Malzacher, F., and Bräunling, W., 1987, "Flow Phenomena in Transonic Turbine Cascades. Detailed Experimental and Numerical Investigation," *Proceedings of the 8th International Symposium on Air Breathing Engines* (*ISABE*), Cincinnati, OH.

Ginoux, J. J., 1969, "On Some Properties of Reattaching Laminar and Transitional High Speed Flows," Technical Note No. 53, Von Karman Institute for Fluid Dynamics, Rhode-Saint-Genese, Belgium.

Heinemann, H.-J., 1983, "The Test-Facility for Rectilinear Cascades (EGG) of the DFVLR," DFVLR report No. IB 222 - 83 A 14.

Katzer, E., 1985, "Numerical Study of Laminar Shock/Boundary Layer Interaction," Doctor of Engineering Thesis, University of Karlsruhe, Federal Republic of Germany; DFVLR-FB 85-34.

Oswatitsch, K., 1958, "Die Ablösebedingung von Grenzschichten," IUTAM Symposium 1957, *Boundary Layer Research*, H. Görtler, ed., Springer-Verlag, Berlin–Göttingen–Heidelberg, pp. 357–367.

Pucher, P., and Göhl, R., 1987, "Experimental Investigation of Boundary Layer Separation With Heated Thin-Film Sensors," ASME JOURNAL OF TURBOMACHINERY, Vol. 109, pp. 303–309.

Quast, A., 1987, "Detection of Transition by Infrared Image Technique," *Proceedings of the ICIASF-Record International Congress on Instrumentation in Aerospace Simulation Facilities*, Williamsburg, VA, pp. 125–133.

Schlichting, H., 1968, *Boundary Layer Theory*, 6th ed., McGraw-Hill, New York.

Walther, L., and Gerber, D., 1983, *Infrarotmesstechnik*, 2nd ed., VEB Verlag Technik, Berlin, German Democratic Republic.

Influence of Deposit on the Flow in a Turbine Cascade

A. Bölcs

O. Sari

Ecole Polytechnique Fédérale de Lausanne, Lausanne, Switzerland

An experimental study on a gas turbine cascade operating under transonic flow conditions is presented. The flow is compared for airfoil shapes corresponding to the design geometry and the geometry taken from a rotor blade, in an industrial gas turbine burning heavy oil, after a few thousand hours of operation. Steady-state data have been obtained in a linear cascade over a range of isentropic exit Mach numbers from 0.6 to 1.6. The flow field was determined by static pressure measurements on the side walls up- and downstream of the cascade, on one side wall in the blade passage, and on the blade surface at midspan. Furthermore, the flow was visualized by the methods of Schlieren and laser holography. The results show that the choked flow conditions are reached at different steady-state isentropic outlet Mach numbers for the two blade shapes. The deposit, typical for a gas turbine, does not however significantly modify the boundary layer separation point. The flow visualization indicates that the shock wave fluctuations have not been significantly influenced by the important roughness and thickness of the deposit. The experimental results on the two cascades are also compared with two-dimensional time-marching calculations after Denton. In the subsonic regime, good agreement was found for the "clean" blade. For the profile with deposit, the flow cannot be correctly predicted by the time-marching calculation, even in subsonic flow condition. The sonic line calculated by the numerical model under transonic outlet conditions ($0.9 < M_{2S} < 1.20$) does not agree with the laser holography measurements for either of the two cascades.

Introduction

In industrial gas turbines, nonrefined fuel is often used. The combustion process with such heavy fuels produces solid particles, which then go through the turbine and can stick to the blades. The blade geometry and surface roughness may thus after a few thousand running hours be significantly different from the designed blade shape. During the design process of a new blade geometry a tremendous effort is made to ensure high efficiency and flow stability. The question which then arises is how the deposit affects the flow conditions.

It is evident that the efficiency of the turbine decreases and the centrifugal forces on the blade increase with growing deposit (Felix and Balser, 1982; Zaba, 1980). The influence of the deposit on the stability of the shock waves in transonic flow is however not well known, although this may have a significant influence on the aeroelastic behavior of the blade row (Bölcs and Sari, 1984).

An example of the change in the rotor blade shape by a deposit after a few thousand running hours is given in Fig. 1. This figure shows that the main deposit is on the pressure surface, where the geometry is considerably altered, and that only a small number of particles stick to the suction surface. The main influence here is thus on the blade surface roughness.

The most important flow effects in the transonic operating region are due to a decrease in the throat area and a significant change in the shape of the trailing edge. This variation can alter the configuration and stability of the shocks in the transonic and supersonic operating regimes.

The main objective of the present experimental study is to clarify how the shock wave configurations and their stability

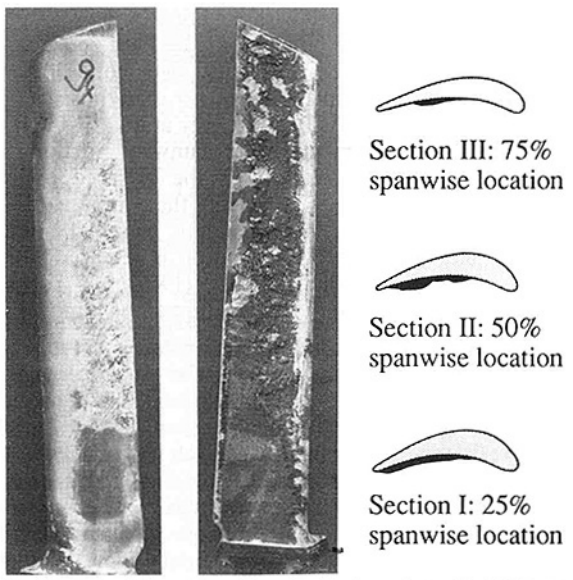

Fig. 1 Example of deposit on the rotor blade surface after 2000 running hours with heavy fuel

Contributed by the International Gas Turbine Institute and presented at the 33rd International Gas Turbine and Aeroengine Congress and Exhibition, Amsterdam, The Netherlands, June 5–9, 1988. Manuscript received by the International Gas Turbine Institute July 29, 1987. Paper No. 88-GT-207.

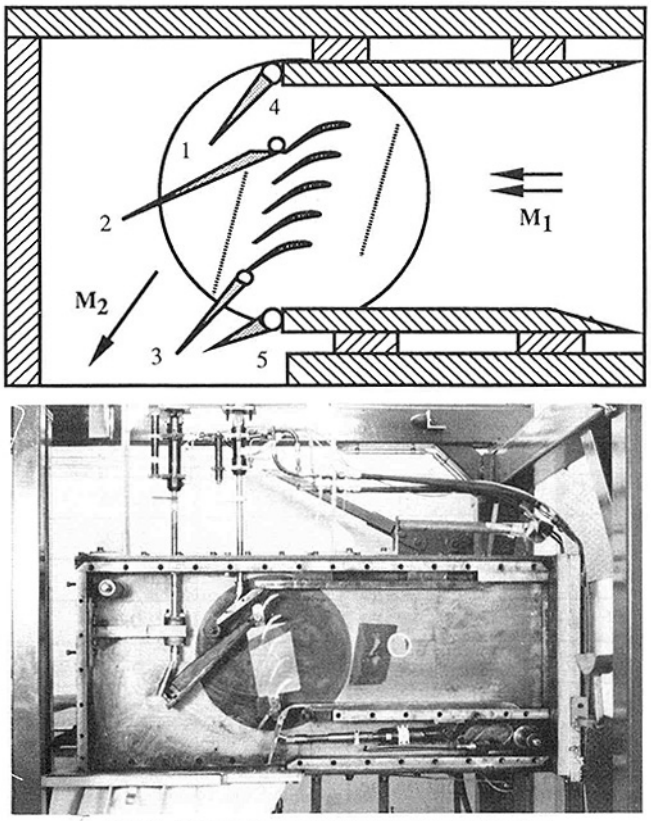

Fig. 2 Schematic view of the linear test facility

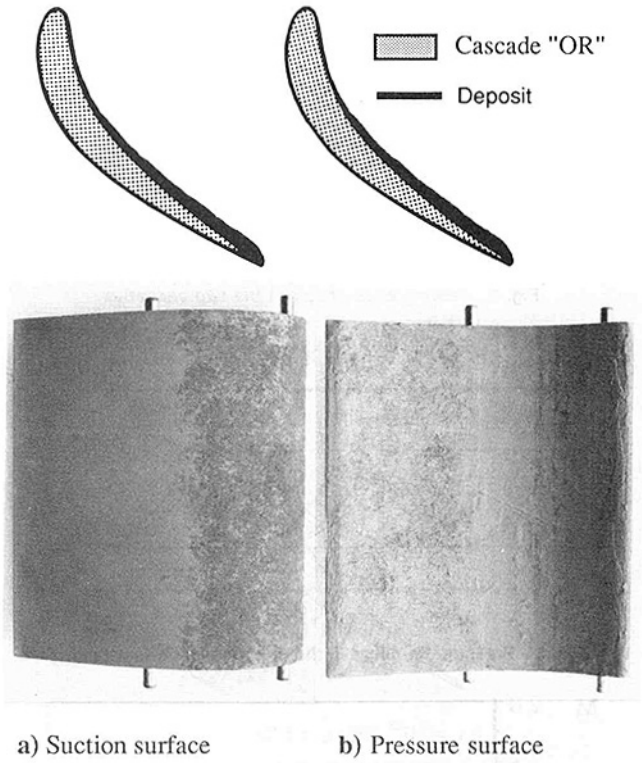

Fig. 3 Cascade *DE* (cascade with deposit)

are influenced by the deposit. The boundary layer separation is not measured but visualized by optical methods.

A systematic experimental investigation has been performed in the linear test facility at the Laboratoire de Thermique Appliquée et de Turbomachines ("LTT"). The experiments were carried out at different downstream flow velocities ($0.6 \leq M_{2S} \leq 1.60$) with three different inlet flow angles.

In the present paper, we describe only the measurements at a nominal inlet incidence flow angle $\beta_1 = +10$ deg, as the behavior of the flow was similar throughout the $-7 \leq \beta_1 \leq +25$ deg range.

Linear Test Facility and Model Cascade

The experiments were performed in the linear test facility at the LTT. This test facility is fed from a continuously running air source, which delivers a mass flow of 10 kg/s, with a pressure ratio of 3.5 (Bölcs and Sari, 1986a).

The experimental setup for the present study in the linear test facility consists of five blades. The inlet flow angle β_1 can be adjusted with the rotation of the disk on which all profiles are suspended ("1" in Fig. 2).

The isentropic exit Mach number (M_{2S}) as well as the downstream flow periodicity is regulated by two tailboards, "2" and "3." The upper of these ("2") is slotted to minimize shock reflections, while the lower ("3") is solid. A further regulation of the flow periodicity is made with the two vanes "4" and "5" (Fig. 2). Although only five profiles are present in the cascade, an acceptable flow periodicity is obtained (Bölcs and Sari, 1986a).

The original blades (cascade "OR") were fabricated in aluminum, with a surface treatment (surface oxidation processing) in order to protect the blade surface. The deposit (cascade "DE") was put on using a plastic cement on the pressure surface of the profiles (Fig. 3) according to a print made of the blades removed from a gas turbine (section I in Fig. 1). Furthermore, a thin layer was put on the forward 40

Nomenclature

A = surface, mm^2
A^* = throat area, mm^2
CLA = center line average (roughness coefficient), μm
d = thickness, mm
e = distance, mm
h = span, mm
L = profile chord, mm
M = isentropic Mach number, defined with the local static pressure and the upstream stagnation pressure
n = number of fringes
p = pressure, bar
R = gas constant (for air: R = 287), J/kg K
Re = Reynolds number $= \dfrac{W \cdot L \cdot \rho}{\mu}$
T = static temperature, K
W = velocity, m/s
t = blade pitch, mm
h/L = aspect ratio
t/L = pitch-to-chord ratio
x/L = dimensionless (with chord) chordwise coordinate
β = flow angle from axial (Fig. 5), deg
γ = stagger angle (Fig. 5), deg
δ = trailing edge angle (Fig. 4), deg
ϵ = angle (Fig. 5), deg
η = dynamic viscosity, kg/m•s
κ = specific heat ratio (for air: κ = 1.4)
ρ = density, kg/m^3

Subscripts

1 = inlet
2 = outlet
ch = choked flow
eff = effective (with losses)
s = isentropic
te = trailing edge
w = stagnation
OR = ORiginal profile (without deposit)
DE = DEposit on the pressure side (large) and suction surface (small)

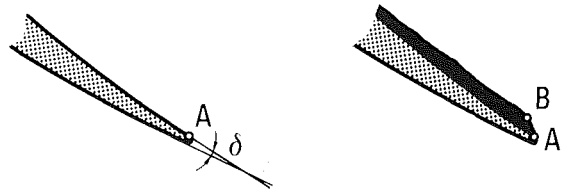

a) Reference blade (= blade "OR")

b) Blade with deposit (= blade "DE")

Fig. 4 Trailing edge shape of the two cascades

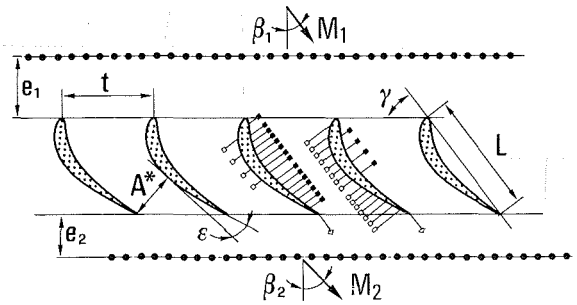

Fig. 5 Pressure tappings in the linear cascade test facility

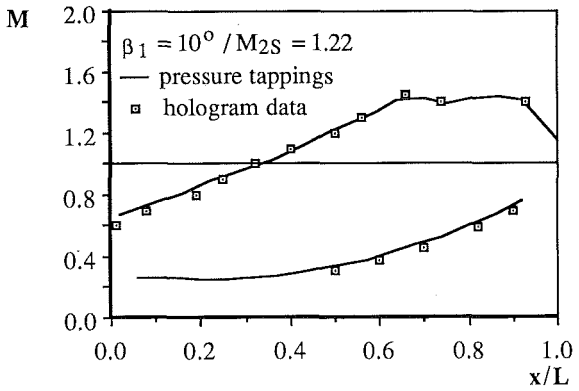

Fig. 6 Comparison of blade surface Mach number distribution from hologram with those from blade surface static pressure tappings

percent of the suction surface, also corresponding to the traces on the used blade. The surface roughness of the original blades is 3 μm. The blades with deposit have instead a roughness of 7–12 μm.

The cascade DE consists of, as previously mentioned, five blades. Out of these five blades, only the two center ones have been modified with the deposit. The other three profiles in the cascade correspond to the original one. The blade represented in Fig. 3 indicated that the cascade with the deposit has a throat section that is approximately 5 percent smaller than the original one.

Due to the deposit on the blade pressure surface the shape of the trailing edge has been considerably modified. Instead of the rounded trailing edge, in the original version, it is 60 percent thicker and cut off at about 45 deg (Fig. 4).

Measuring Equipment and Data Reduction

The inlet flow conditions are measured by a wedge probe situated 1.20 axial chord lengths upstream of the cascade leading edge plane. The flow periodicity is checked by the side wall pressures up (30 pressure tappings) and downstream (30 pressure tappings) of the cascade (Fig. 5, Table 1). The blade surface pressures are measured at midspan on two neighboring profiles on the suction and pressure side, respectively, and on both trailing edges.

The side-wall pressures were measured in one blade passage

Table 1 Specifications of the test cascades

Cascade		" OR "	" DE " with plastic cement
Re	(x 10^{-6})	1.4 - 2.1	1.4 - 2.1
Tu	(-)	1%	1%
T_w	(K)	320.	320.
CLA	(μm)	~3	~7 - 12
L	(mm)	85.47	85.47
Camber	(deg)	49.	49.
γ	(deg)	37.76	37.76
δ	(deg)	6.2	~45.0
A*/L	(-)	0.38	0.36
d/L	(-)	0.117	0.124
d_{te}/L	(-)	0.0147	0.0374
e_1/L	(-)	0.61	0.61
e_2/L	(-)	0.36	0.36
h/L	(-)	1.17	1.17
t/L	(-)	0.747	0.747
Pressure tappings on the blade suction surface		19	19
Pressure tappings on the blade pressure surface		19	0
Pressure tappings in blade trailing edge		2	2

(180 pressure tappings in a grid 5 × 5 mm (Bölcs and Sari, 1986a)), and the flow was visualized with Schlieren and laser holography techniques. In the cascade with deposit only the suction surface and the trailing edge are instrumented; on the blade with deposit the surface is rough and uneven, and the use of pressure tappings would not give an accurate result. For this reason, the blade surface pressures were evaluated in an indirect way. This was performed with the aid of the fringe system of the laser holography images (Bryanston-Cross et al., 1984) and verified with the side-wall pressure tappings in the blade passage.

The hologram (see example in Fig. 7) consists of isodensity lines with a constant density step $\Delta\rho$ between the fringes, defined by the optical system (Oldfield et al., 1985). The Mach number on the fringes is evaluated by the upstream stagnation pressure (p_w) and temperature (T_w) and the local density ρ.

The intersection of the interference fringes with the profile gives the blade surface Mach numbers. The Mach number distribution on the fringe system, starting from the reference line, can be determined within ± 1 fringe, which in the present case gives an average error of $\Delta M = \pm 0.03$. Short duration Schlieren images were used to determine any eventual boundary layer separations and the stability of the shock waves.

Experimental Results and Discussion

Measurements on the Reference Blade. The measurements on the original design cascade have the following objectives:

- validation of the indirect technique for evaluation of the blade surface pressures from the laser holography images,
- evaluation of the flow in the original cascade,
- comparison with numerical computations.

Figure 6 shows a comparison of the blade surface Mach number distributions in the transonic flow region, determined by pressure tappings and laser holography. It is concluded that both methods give the same blade surface Mach number distribution. In Figs. 7 and 8 the flow field, obtained from the Schlieren and hologram photos, is compared with the pressures determined from the side-wall pressure tappings.

From Fig. 7 it is noted that the shock position is represented identically by the Schlieren and laser holography methods. Figure 8 shows a good agreement between the iso-Mach lines as determined from the holography technique and the static pressure tappings, except in the shock wave region. It is noted that the laser holography visualization technique gives good results in comparison with pressure measurements, and so it can be used to determine the Mach number distribution on the blade with deposit.

From the measurements on the reference cascade the following conclusions can be drawn:

- no boundary layer separation is found on the blades;
- the shock configurations are identical in the Schlieren and laser holography visualizations (see example in Fig. 7) and

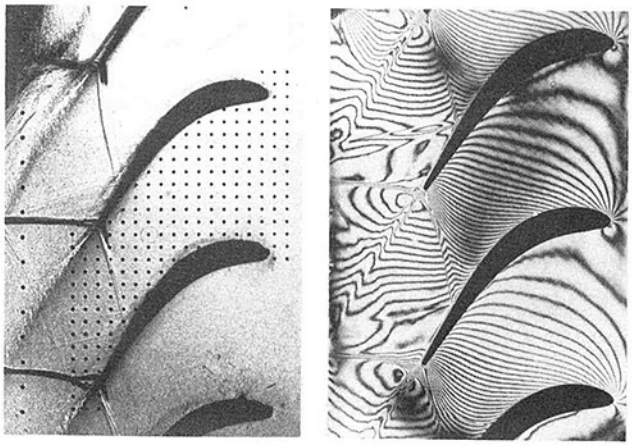

Fig. 7 Comparison of the Schlieren and hologram pictures at β_1 = +10 deg/M_{2S} = 1.22

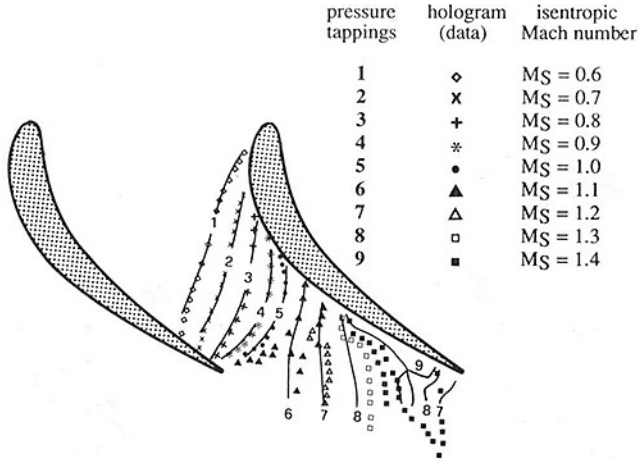

Fig. 8 Comparison of isodensity lines from a hologram with iso-Mach lines from side-wall pressure tappings at β_1 = 10 deg/M_{2S} = 1.22

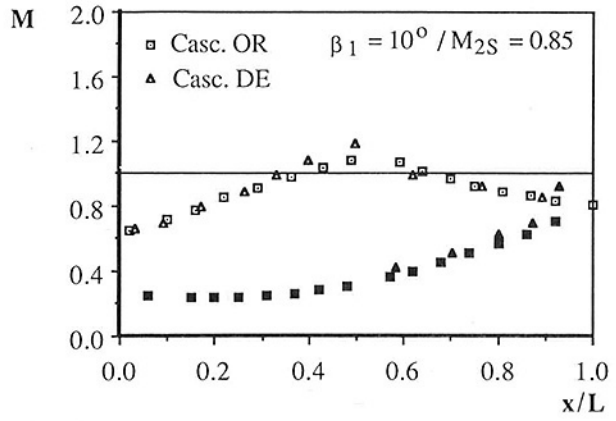

a) Mach number distribution on the profile

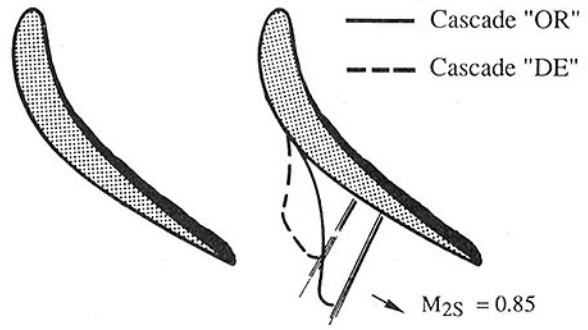

b) Sonic line distribution in the inter-blade passage

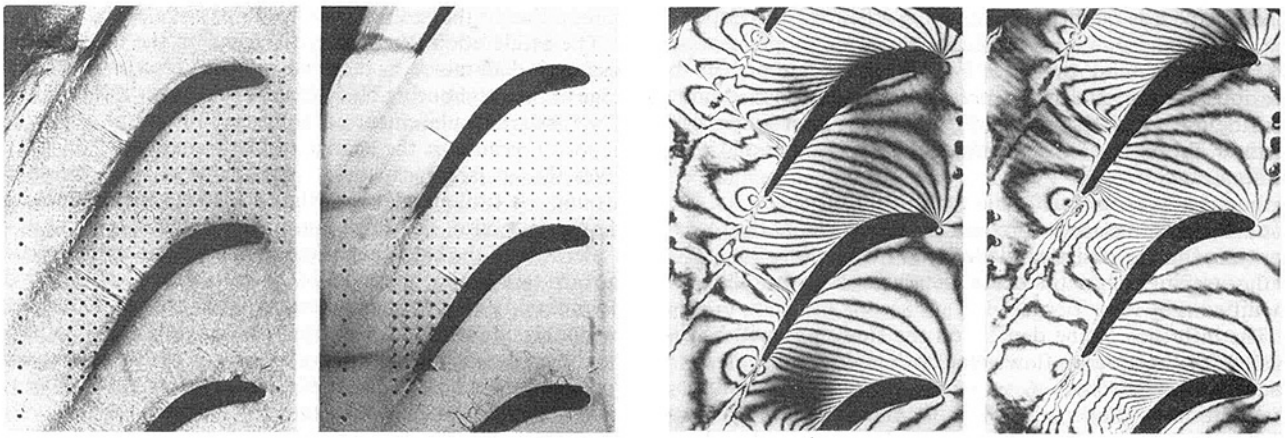

Fig. 9 Cascade flow at β_1 = 10 deg/M_{2S} = 0.85

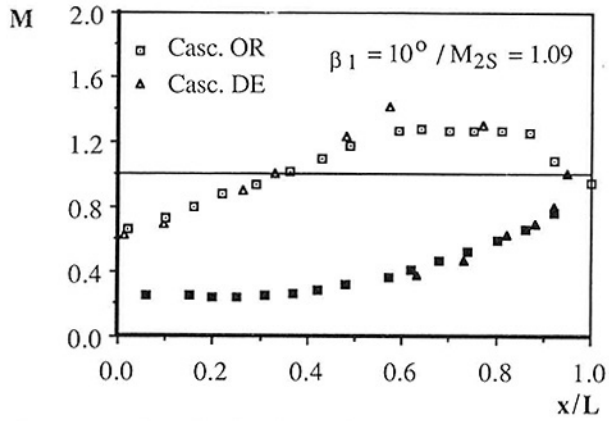

a) Mach number distribution on the profile

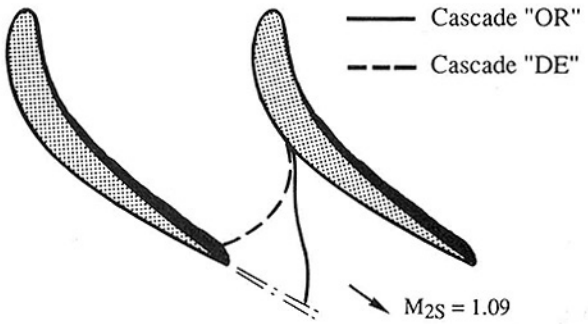

b) Sonic line distribution in the inter-blade passage

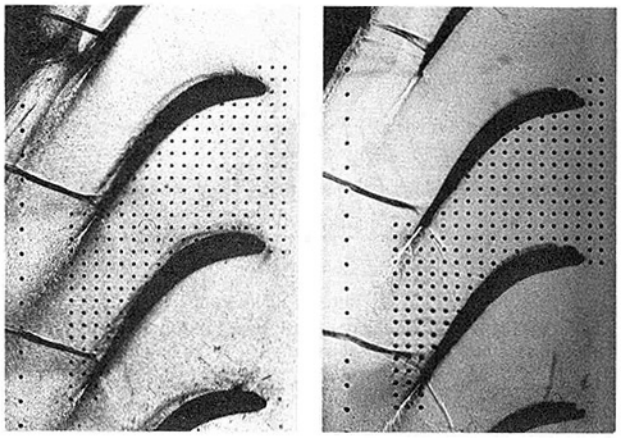

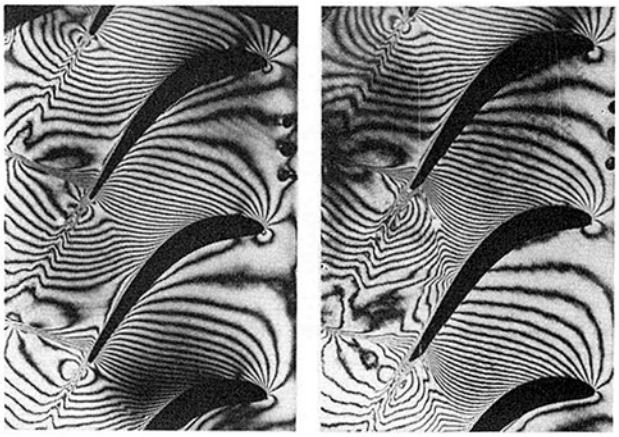

Fig. 10 Cascade flow at β_1 = 10 deg/M_{2S} = 1.09

their position agrees well with the one determined from the blade surface pressure measurements;

- the flow can be considered two dimensional;
- the interaction of the shock with the boundary layer gives, for outlet flow velocities close to sonic velocity, a considerable increase in the boundary layer thickness at the foot of the normal shock. The shock system is fairly stable;
- at higher isentropic outlet Mach numbers, the oblique shock system does not show any boundary layer effects and the shock position is also here stable.

Measurements on the Blade With Deposit. The original blade shape was modified by applying a deposit, corresponding to a print from a gas turbine rotor blade (approximately 2000 hours running time, see Fig. 1). As mentioned in the previous section, the blade pressure surface Mach number distribution was determined indirectly by the laser holography method. From the used gas turbine blade (Figs. 1 and 3) it can be seen that:

- the blade pressure surface is rough and uneven,
- the interblade passage is reduced ($\sim$ 5 percent at the throat) compared to the designed blade,
- the trailing edge thickness increases and its shape is modified (Fig. 4).

The influence of the deposit on the flow field will be discussed for three outlet flow velocity domains (subsonic, near sonic, and supersonic). A selection of typical Mach number distributions in these regimes is represented in Figs. 9, 10, and 11. In these figures the inlet flow angle is identical and corresponds to the design condition ($\beta_1 = +10$ deg). It is noted that, although the blade shape is different from the original cascade, the blade pressure surface Mach numbers show remarkable deviation only close to the throat, i.e., near the trailing edge (Figs. 9*a*, 10*a*, 11*a*). This can be explained by the facts that a small change in flow area gives large differences in Mach numbers close to the sonic velocity, and that the sonic point on the pressure surface must be advanced (from point "A" to "B" in Fig. 4) to accommodate the increase in flow area downstream of the throat (point "B") on the cascade with deposit.

Similarly, on the blade suction surface, the Mach number distribution is only slightly influenced by the applied deposit in the region between the leading edge and the sonic point (Figs. 9*a*, 10*a*, 11*a*). However, the sonic point is slightly advanced due to the reduction in blade passage area.

The acceleration after the sonic point on the blade suction surface is determined by the expansion centered on the trailing edge of the neighboring blade (points "A" and "B" in Fig. 4). The forward displacement of the sonic point in the case of the deposit (because of the change in blade shape and thickness) gives thus a larger expansion, for identical back pressures, around the trailing edge and thus a higher Mach number on the blade suction side upstream of the shock.

Because of the high roughness of the deposit on the suction surface (see photo of model blade with deposit, Fig. 3), the boundary layer becomes turbulent and thicker almost immediately downstream of the leading edge. This larger boundary layer thickness stays along the whole suction side (compare laser holograms in Figs. 9*d*, 10*d*, and 11*d*). On the pressure surface there is no significant change in the boundary layer thickness between the reference and "deposit" blades. Obviously, the increase in blade and boundary layer thicknesses gives a thicker wake with larger recirculation zones and thus higher losses.

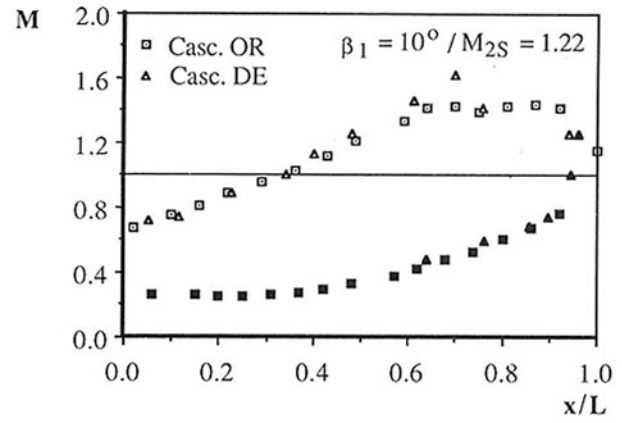

a) Mach number distribution on the profile

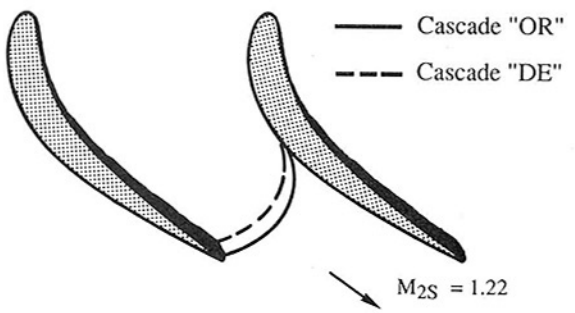

b) Sonic line distribution in the inter-blade passage

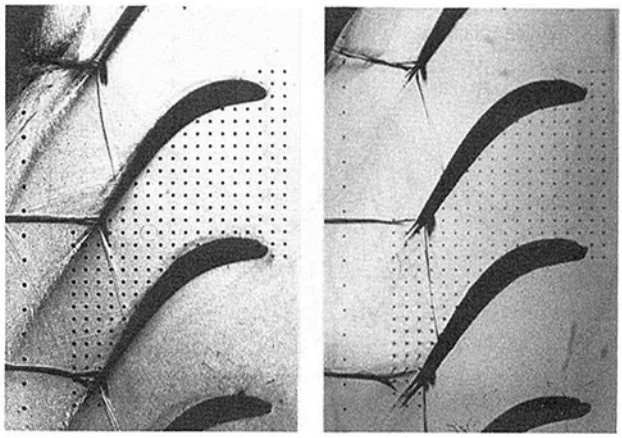

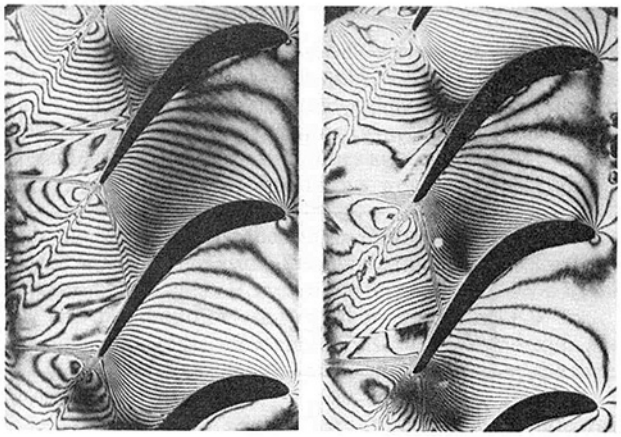

Fig. 11 Cascade flow at β_1 = 10 deg/M_{2S} = 1.22

In the *high subsonic range* ($M_{2S} \sim 0.8$, Fig. 9) the high-speed Schlieren films show that without deposit the shock is unstable but remains in principle as one main shock with a few weaker ones. In the case with deposit the unsteady shock decomposes into several small ones. This is due to the fact that the larger boundary layer thickness gives a higher postshock expansion at the outer edge of the boundary layer, which thus again can give a second shock (Bohning and Zierep, 1980) (compare the shock structures for the reference and "deposit" blade in Fig. 9*c*). This modification of the shock structure does not however appreciably affect the stability of the shock. In both cases the main shock is slightly unstable, with an appearance of smaller shocks in a distance of approximately $\Delta x/L \sim 0.31$ around a mean position $x/L \sim 0.67$. This slight instability in the shock position also explains why the blade suction surface pressure distribution does not show a sharp decrease in Mach number at the expected time-averaged shock position (Fig. 9*a*).

In both cases, the boundary layer thickness increases considerably in the shock region, and because of the higher turbulence in the boundary layer *a*, the blade wake is more unstable in the case with deposit than without.

For *transonic outlet flow velocities* ($M_{2S} \sim 1.1$, Fig. 10) the normal shock on the reference blade is positioned just before the suction side trailing edge and is only slightly unstable as indicated both by the pressure measurements and the high-speed Schlieren films. Both the blade surface Mach number distribution and the holograms (Figs. 10*a*, 10*d*) indicate that the flow velocity on the suction side is constant between $0.6 \leq x/L \leq 0.85$ and that the flow velocity is below the sonic value along the whole pressure side. The sonic line departs from the suction surface but is not connected directly with the pressure side of the neighboring blade for the reference cascade. It goes instead into the wake (Fig. 10*b*). The flow visualization shows that the shock in the neighborhood of the profile is influenced by the shock boundary layer interaction and that it opens itself to a compression wave, which reaches the main shock a small distance from the blade surface.

With the deposit, the flow in this Mach number region changes drastically. As noted before, the boundary layer is thicker along the whole suction side. The sonic line extends now from the suction side to the pressure surface, where it departs from the shoulder of the trailing edge (Fig. 10*b*, see also point "B" in Fig. 4).

An expansion is thus centered at point "B," where a significantly higher preshock Mach number is reached on the suction surface, compared to the reference cascade. The high expansion ends with a lipshock departing from the blade pressure surface trailing edge (Bölcs and Sari, 1986b). This shock impinges, fairly localized, on the suction side without any noticeable increase in boundary layer thickness. The postshock Mach number distribution and structure of the normal shock at the trailing edge are not remarkably different for the blades with and without deposit, with the exception of the shock boundary layer interaction. It is noted that in this velocity range the shocks are only slightly unstable, both with and without deposit.

For the *supersonic outlet velocity range* ($M_{2S} \sim 1.2$, Fig. 11) the sonic line occupies, as is expected, the throat of the cascade. The reference blade shows that the sonic line departs from the pressure surface trailing edge (point "A" in Fig. 4*a*). At the corner of the trailing edge a small expansion starts, which is ended by a weak shock (Figs. 11*a*, 11*d*). This shock impinges and is reflected on the suction side at $x/L \sim 0.72$

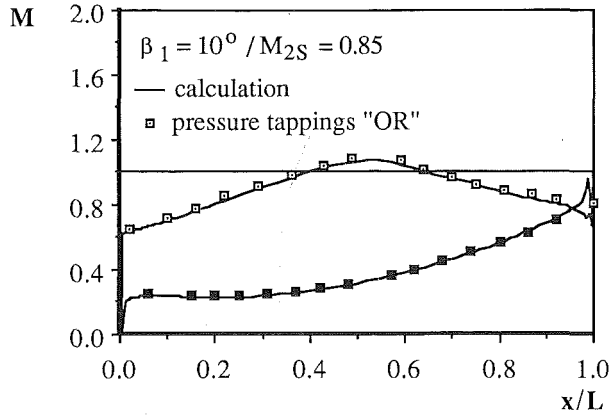

a) Mach number distribution on the profile

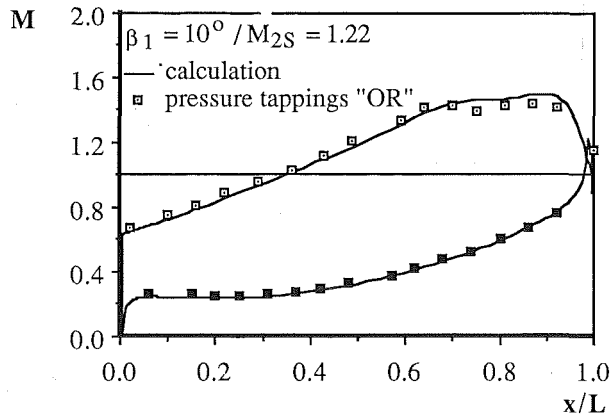

c) Mach number distribution on the profile

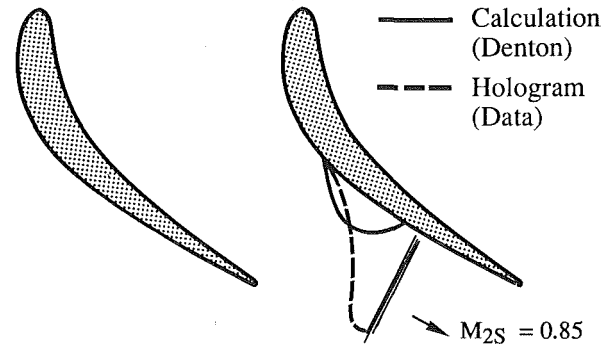

b) Sonic line distribution in the inter-blade passage

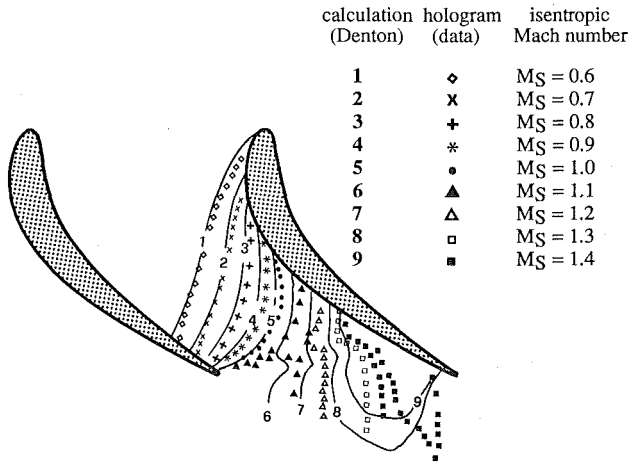

d) Comparison of isodensity contours from hologram with time-marching prediction

Fig. 12 Comparison between experimental and numerical results at β_1 = 10 deg

(Figs. 11*a*, 11*c*, 11*d*), whereafter the Mach number distribution shows a slight acceleration of the flow velocity up to the suction side trailing edge. At this point a strong shock departs, with a boundary layer separation at the foot.

The cascade with deposit shows, as for the previous velocity ranges discussed, a higher expansion on the blade suction surface. This is again due to the change in trailing edge shape of the blade pressure surface. As this shock is now stronger, a thicker postshock boundary layer is found in the cascade with than without deposit. However, the postshock blade suction surface Mach number distribution is identical in the two cascades.

As the sonic line again departs from the shoulder of the trailing edge pressure side (point "B" in Fig. 4) the last 5 percent of the blade pressure surface shows large supersonic velocities. As in the transonic velocity range, the shocks remain stable.

From the comparisons of the cascade with deposit toward the reference cascade, the following conclusions can be drawn:

- the stability of the shock systems does not change;
- as the pressure surface trailing edge is now cut in a different way the expansion on the blade suction surface is different. The preshock Mach numbers on the blade suction surface are higher;
- the sonic point on the suction side is slightly advanced;
- the wake is thicker, with a larger recirculation zone;
- the shock structure for high subsonic outlet flow velocities ($M_{2S} \sim 0.85$) changes. The main shock that appeared on the reference cascade is decomposed into several smaller unstable shocks, with postshock expansions between each;
- the structure at the foot of the normal shocks remains approximately the same, but extends farther out in the flow field as the boundary layer is thicker;
- the cascade reaches its choking limit at a lower outlet flow velocity.

Comparisons With Numerical Calculations

In order to establish whether the flow field in a cascade with deposit can be accurately predicted numerically, the experimental results have been compared to numerical calculations, obtained with a program by Denton (1982, 1983). The calculations were performed with a grid (100 points in the axial and 13 points in the tangential direction, respectively) with 13 points clustered in the last 10 percent of the blade.

Two calculations performed on the reference cascade are presented in Fig. 12. It is concluded that the program can accurately predict the blade surface Mach numbers at subsonic outlet velocities (Fig. 12*a*). The sonic line and thus the choking limits are however not correctly captured at high subsonic outlet flow velocities (Fig. 12*b*). At transonic and supersonic flow velocities, the oblique shock system is not captured (Figs. 12*c*, 12*d*). The sonic line, as the flow is now choked, is well predicted.

As the purpose of this numerical investigation is to validate the computations for a blade with deposit, the true geometry from this cascade (Fig. 4) was introduced into the time-marching program. The calculated Mach number distribution on the blade pressure surface is thus fairly uneven (Fig. 13).

As the trailing edge is now much thicker and with a different

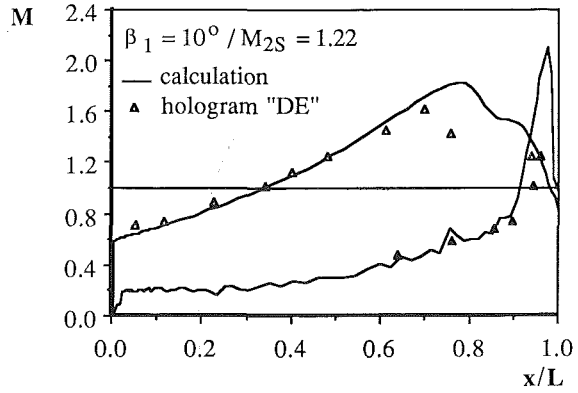

c) Mach number distribution on the profile

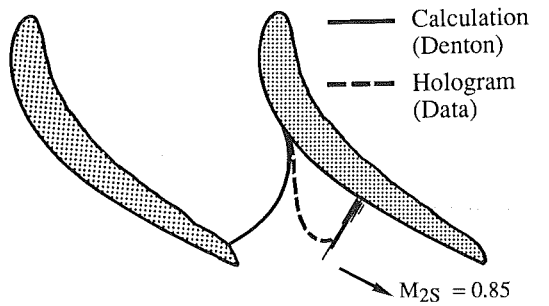

b) Sonic line distribution in the inter-blade passage

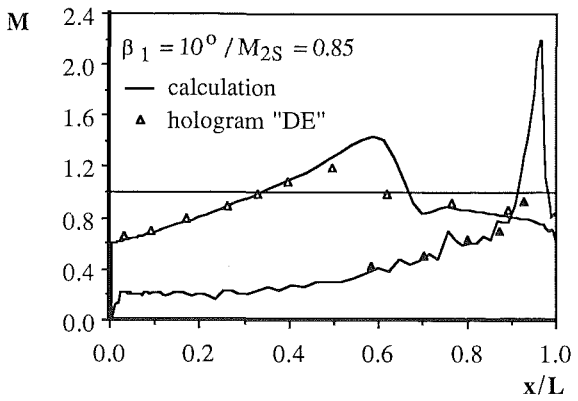

a) Mach number distribution on the profile

Fig. 13 Comparison between experimental and numerical results at β_1 = 10 deg

shape, the expansion from the pressure surface is not captured correctly. Thus the Mach number distribution close to the trailing edge at the pressure surface is very different, and the preshock suction surface Mach numbers are remarkably different. It should be pointed out that, for the calculations presented in Fig. 13, the numerical grid had 28 points more in the trailing edge region, in order better to capture the expansion, than the calculations for the reference cascade (grid mesh with deposit 200 × 20). From the comparisons between the measurements and the computations the following conclusions can be drawn:

- for the design cascade, an excellent agreement is noted. Differences are found in the position of the sonic line close to choking conditions and in the shock structures;
- the computed results do not agree well for the cascade with deposit. This is mostly due to the change in expansion at the pressure surface trailing edge.

Conclusions

The results obtained are representative for a special rotor gas turbine cascade and are not descriptive for all other cascades. The experimental results allow however some general conclusions.

- The suction surface boundary layer is thicker with deposit than without.
- The expansion on the suction surface is larger in the cascade with deposit than on the reference profile. This is due to the larger thickness and different shape of the trailing edge on the neighboring blade. This fact changes the departure of the sonic line on the blade pressure surface.
- The shock positions remain approximately the same for both cascades.
- There is no dramatic change in the shock structure, or on the boundary layer separation point.
- The stability of the shock waves is not significantly influenced.
- If the original blade is of a "good" design (i.e., shock waves are stable, no large overexpansions, no large flow separations, . . .) it is not expected that a deposit will significantly change the unsteady aerodynamic or aeroelastic behavior of the blading. However, if instabilities are found in the "clean" blading, even worse flow conditions would probably appear with deposit on the profiles.
- For the reference cascade, an excellent agreement is noted between the two-dimensional time-marching calculations and the experimental data. However, differences are found in the sonic line distribution close to choking conditions.
- At supersonic outlet flow conditions, the shock position and the subsequent flow cannot be correctly predicted by the time-marching calculation.
- The computed results do not agree well for the cascade with deposit. This is mostly due to change in expansion at the pressure surface trailing edge. However the subsonic part of the flow can be predicted.

In general, a carefully designed blading will not significantly change its flow properties in a soiled condition.

Acknowledgments

The present investigation was carried out as part of a research project subsidized by Brown Boveri & Cie, Baden, Switzerland. This support and the authorization to publish the results are kindly acknowledged.

References

Bohning, R., and Zierep, J., 1980, "Normal Shock-Turbulent Boundary Layer Interaction at a Curved Wall," AGARD Conference Proceedings No. 291.

Bölcs, A., and Sari, O., 1984, "Unsteady Flow Measurements in a Turbine Cascade in Stalled Transonic Flow," *Unsteady Aerodynamics of Turbomachines and Propellers*, Symposium Proceedings, Cambridge.

Bölcs, A., and Sari, O., 1986a, "Experimental Study of the Transonic Flow Through a Gas Turbine With Deposit on the Blades," Internal Report No. EPFL/LTT-6-86.

Bölcs, A., and Sari, O., 1986b, "Etude de l'Ecoulement dans une Grille de Turbine à Gaz aux Bords de Fuite Tronqués," Internal report No. EPFL/LTT-1986.

Bryanston-Cross, P. J., Beretta-Piccoli, F., and Ott, P., 1984, "Implementation of the Ruby Pulse Laser Holography at the LTT/EPF-L," Internal report No. EPFL/LTT-TM-16-84.

Denton, J. D., 1982, "Two Dimensional Time-Marching Program for Turbomachine Blade Rows," Private Communication.

Denton, J. D., 1983, "An Improved Time-Marching Method for Turbomachinery Flow Calculation," ASME *Journal of Engineering for Power*, Vol. 105, pp. 514–524.

Felix, P., and Basler, B., 1982, "Modern Base Load Gas Turbines Running on Crude Oil: Long Time Effects and Experience," ASME Paper No. 82-GT-115.

Oldfield, M. L. G., Bryanston-Cross, P. J., Nicholson, J. H., and Scrivener, C. T. J., 1985, "A Study of Passage Flow Through a Cascade of Turbine Blades Using Image Plane Holographic Interferometry," Private Communication.

Zaba, T., 1980, "Verlust bei Gasturbinen durch Ablagerunder auf des Beschfelung," Brown Boveri Mitteilungen 12-80.

R. L. Davis
Senior Research Engineer,
Computational Fluid Dynamics Group,
United Technologies Research Center,
East Hartford, CT 06108

D. E. Hobbs
Research Engineer,
Fan and Compressor Technology Group,
Mem. ASME

H. D. Weingold
Senior Research Engineer,
Fan and Compressor Technology Group,
Mem. ASME

Pratt and Whitney,
East Hartford, CT 06108

Prediction of Compressor Cascade Performance Using a Navier-Stokes Technique

An explicit, time marching, multiple-grid Navier-Stokes technique is demonstrated for the prediction of quasi-three-dimensional turbomachinery compressor cascade performance over the entire incidence range. A numerical investigation has been performed in which the present Navier-Stokes procedure was used to analyze a series of compressor cascade viscous flows for which corresponding experimental data are available. Results from these calculations show that the current viscous flow procedure is capable of predicting cascade profile loss and airfoil pressure distributions with high accuracy. The results from this numerical investigation in the form of comparisons between the predicted profile loss, exit gas angle, and pressure distributions with experimental data are presented in this paper. Results from a grid refinement study are also shown to demonstrate that the Navier-Stokes solutions are grid independent.

Introduction

Computational fluid dynamics has grown in use by airframe and gas turbine engine manufacturers to the point where various numerical procedures are now an integral part of their design systems. Among these procedures are the Reynolds-averaged Navier-Stokes techniques, which are playing an increasing role in the analysis and design of various aerodynamic components. Navier-Stokes numerical procedures are currently being used either as an analysis tool to increase the engineer's understanding of a given flow phenomena, or as a design tool to improve aerodynamic geometries. The primary focus has been to use Navier-Stokes methods to predict the viscous effects on the pressure loading distributions of aerodynamic bodies as well as to determine the existence and extent of separated and secondary flow regions within the flow path. For the most part, the Navier-Stokes techniques available have met this goal.

For internal flows, particularly those within the compressor and turbine components of gas turbine engines, several Navier-Stokes procedures have been developed for both two- and three-dimensional flows. For three-dimensional flows, the numerical schemes developed by Rai (1987), Hah (1986), Rhie (1986), Nakahashi et al. (1987), Weinberg et al. (1986), and Subramanian et al. (1987) are currently being used to improve the understanding of the flow physics, in particular, the secondary and radial flow effects within the blade passages. Several two-dimensional schemes have also recently been developed including those of Chima (1987), Norton et al. (1984), Shamroth et al. (1984), Schafer et al. (1986), and Davis et al. (1987). Some of these schemes are currently used routinely as part of the design systems of various manufacturers primarily to predict the viscous effects on the pressure distribution of cascades and the determination of the presence of separated flow regions.

One of the ultimate goals for which Navier-Stokes procedures are needed, however, is the prediction of performance. For internal cascades flows, performance is usually measured in terms of flow turning and entropy rise (or total pressure loss) through the cascade passage as opposed to lift and drag, which are typically used as indicators of performance for external flows. In terms of gas turbine compressor and turbine cascade design systems, Navier-Stokes procedures should have the ability to predict performance in order to optimize cascade designs over their entire operating range. Very little work has been performed thus far in terms of applying Navier-Stokes procedures to predict performance. The inability to predict performance accurately up to this time with these numerical procedures has been largely due to the fact that numerical smoothing errors within the central differenced algorithms as well as the truncation error within the upwind differenced algorithms add an artificial viscosity effect, which results in diffusive solutions and erroneously high levels of predicted total pressure loss. Numerical smoothing and/or upwinding techniques are usually required in most Navier-Stokes procedures to capture shocks and to eliminate solution oscillations brought about by the convection terms of the governing equations. Thus, in order to obtain stable, converged solutions for many of these schemes, it has been necessary to sacrifice the ability to predict performance accurately.

The significance in the ability to predict performance with a Navier-Stokes procedure is that turbomachinery designers can use such a numerical tool to predict cascade performance over a much wider range of flow conditions than more approximate

Contributed by the International Gas Turbine Institute and presented at the 33rd International Gas Turbine and Aeroengine Congress and Exhibition, Amsterdam, The Netherlands, June 5-9, 1988. Manuscript received by the International Gas Turbine Institute December 15, 1987. Paper No. 88-GT-96.

numerical procedures allow. Thus, cascade designs can be optimized with a Navier–Stokes procedure over their entire operating range rather than in a narrow region around their design point condition. In practice, one-pass direct boundary layer procedures using edge conditions from a potential flow or Euler calculation with standard wake mixing procedures have been and will continue to be successfully used to predict cascade performance at near-design point conditions. As the flow conditions move away from the design point, inviscid/viscous interaction techniques can be used to improve these one-pass direct calculations to predict performance. However, as the flow conditions become significantly different from the design point, these techniques break down due to their inherent limitations and cannot be used to determine either the performance or provide an accurate description of the physics of the flow field. At this point, Navier–Stokes procedures should be used to predict the effects of separation on the loading distribution as well as the performance of cascades to establish their viable operating range. For compressor geometries, this prediction capability is particularly important since compressors operate over a wide range of flow conditions from low to high inlet Mach number as well as at high positive and negative incidence angles. It is essential to establish the operating range of a compressor airfoil section in order to avoid compressor stall during transients in the flight cycle.

An investigation has recently been performed in which the quasi-three-dimensional Navier–Stokes procedure, VISCAS (VIScous CAScade), developed by Davis et al. (1987), was used to determine the ability of this technique to predict cascade performance over a wide range of flow conditions. During this investigation, a series of turbine and compressor cascades for which detailed pressure distribution and performance data existed over a wide incidence range were analyzed with the VISCAS procedure to determine the accuracy and reliability of this technique to predict performance. In addition, the effect of computational grid spacing and numerical smoothing on the predicted loss levels was also determined. The results of this investigation have shown that the VISCAS Navier–Stokes procedure is capable of accurately predicting cascade total pressure loss over the entire incidence range. In addition, the results from this investigation show that this procedure is capable of predicting the onset of stall for both positive and negative incidences. These results are very encouraging in that they demonstrate that the present procedure can be used by gas turbine compressor and turbine designers to optimize cascade designs over a wide range of flow conditions and to determine the limits of stable operation of the cascade.

This paper will present the results of this investigation and review the numerical techniques used in the VISCAS procedure that allow it to predict cascade total pressure loss. Due to the large volume of results to be shown, this paper will restrict itself to compressor cascade geometries. Similar results for turbine cascades will be presented in the future.

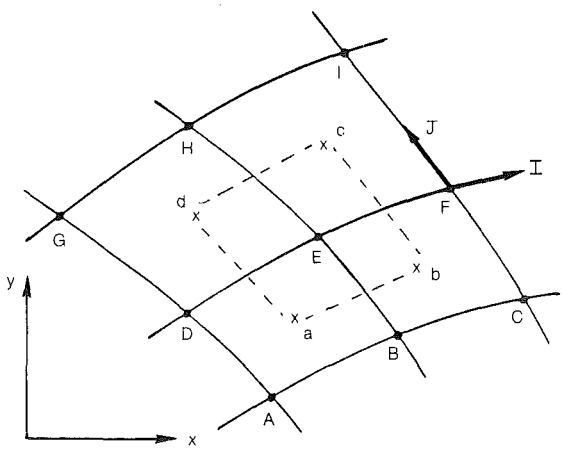

Fig. 1 Computational cell

Numerical Procedure

The two-dimensional, time-dependent Navier–Stokes equations are solved in conservative form in the Cartesian coordinate system as described by Davis et al. (1987). Quasi-three-dimensional effects due to varying streamtube height in the spanwise direction are also included using the assumption that the streamtube height varies linearly between the leading and trailing edges of the cascade. Upstream of the leading edge and downstream of the trailing edge, the streamtube height is assumed to be constant.

An explicit, time marching, control volume, multiple-grid procedure (Davis et al., 1987) is used to iteratively solve the Navier–Stokes equations in pseudo-time until a steady-state solution is obtained. The flow variables are updated in time using the local time step according to a second-order Taylor series approximation. In this procedure, the Euler equations are integrated around primary control volumes defined by the computational mesh (i.e., ABED as shown in Fig. 1) to give the first-order inviscid time rate change in the flow variables at the control volume centers (such as point *a*). These first-order inviscid time rate changes are then distributed from the primary control volume centers to the computational nodes (at A, B, E, D), where the flow variables are stored, using a distribution formula developed by Ni (1982). This distribution formula consists of two steps. This first step determines the flow variable first order time rate changes at the nodes (for example, at E) by averaging the primary control volume center values (at *a* through *d*). The second step determines the second-order time rate changes at the nodes through a piecewise integration of the time derivative of the Euler equations around secondary control volumes (i.e., *abcd*), which have their corners at the primary control volume centers. Viscous effects are included by integrating the shear stress and conduction terms of the Navier–Stokes equations around the secondary control volumes. The flow variables are then up-

Nomenclature

H_1 = inlet streamtube spanwise height
H_2 = exit streamtube spanwise height
M_1 = inlet Mach number
M_2 = exit Mach number
P = static pressure
P_{T1} = inlet stagnation pressure
P_{T2} = exit stagnation pressure
Re_1 = free-stream inlet reference Reynolds number
V = velocity
x = axial Cartesian coordinate
y = tangential Cartesian coordinate or normal distance from wall
β_1 = inlet gas angle referenced from lower tangential
β_2 = exit gas angle referenced from upper tangential
μ = coefficient of viscosity
ρ = density
τ = normal shear stress
ω = vorticity

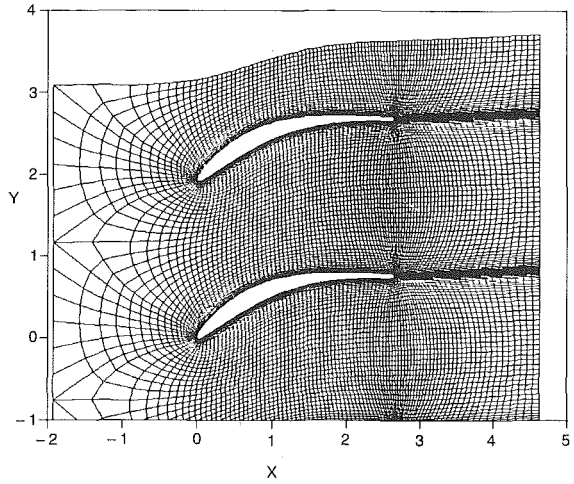

Fig. 2 Computational mesh for transonic compressor cascade

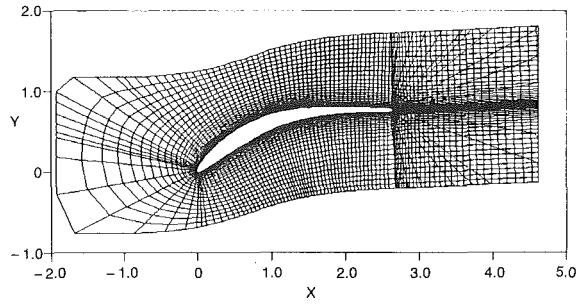

Fig. 3 Body-normal turbulence model mesh for transonic cascade

dated in time and the Ni (1982) multiple-grid scheme is used to accelerate convergence to a steady-state solution. When the viscous effects are eliminated, the current numerical procedure reduces to the multiple-grid Euler technique developed by Ni (1982) for inviscid flows. Further details of this numerical procedure are described by Davis et al. (1987).

During the development of this procedure, particular attention was given to the accuracy of the numerical scheme as compared with boundary layer theory. Several unique numerical techniques are used in this procedure that provide high accuracy and the ability to predict total pressure loss. Among these techniques are the computational grid generation procedure, the numerical smoothing algorithm, and the turbulence model implementation. These techniques are reviewed in the following paragraphs.

The VISCAS Navier–Stokes procedure uses a "periodic" C-grid, which is generated using an elliptic Poisson equation solution procedure similar to those of Thompson et al. (1974) and Sorenson (1980). An example of this "periodic" C-grid is shown in Fig. 2 for a transonic compressor cascade to be discussed in the Results section. A periodic boundary condition along the midgap boundary of the C-grid allows the computational mesh to adjust itself in both directions from the initial guess during the solution of the Poisson equations in order to make the mesh as orthogonal as possible in this region. As a result, the computational grid metrics remain continuous across the periodic boundary, which should reduce the truncation error of the Navier–Stokes scheme. In addition, it has been found that the errors associated with numerical smoothing on skewed grids are reduced considerably. For viscous calculations, an algebraically generated fine grid is patched into a relatively coarse Euler grid near the airfoil surface and along the wake centerline. The viscous grid is generated in this manner in order to minimize the computational time to generate the grid and to provide for greater control of the grid point distribution in the viscous part of the flow field. The "periodic" C-grid generation procedure has been found to be applicable to a wide range of compressor and turbine geometries and eliminates the need for complicated dissimilar, noncontinuous patched grid systems (Rai, 1987; Norton et al., 1984; Nakahashi et al., 1987), which require interpolation schemes to pass information between grid zones.

A combination of second and fourth-difference numerical smoothing is used in the present Navier–Stokes procedure to avoid spatial oscillations in the flow variables in regions where gradients are high and the grid spacing is relatively coarse. A detailed numerical study involving different smoothing strategies has shown that the second and fourth-difference smoothing of the axial and tangential velocity components must be reduced to zero in the boundary layer region in order to obtain good agreement with boundary layer theory. This is accomplished in the present analysis through the use of exponential decay functions, which reduce the numerical smoothing of the velocity components to zero in both directions through the boundary layer. This technique is similar to the methods used by Shamroth et al. (1984), Rhie (1986), and others in which the smoothing coefficient is based upon the local cell Reynolds number. The major difference between the decay function technique used in the current approach and the cell Reynolds number based method is that the current method is independent of the computational grid spacing. Many comparisons (Davis et al., 1987) have been made between the current Navier–Stokes procedure and a finite difference boundary layer technique for flows over complex geometries as a demonstration of the accuracy of the present Navier–Stokes analysis.

In order to reduce the numerical smoothing within the boundary layer region to zero and to eliminate spurious errors in the algebraic turbulence model, it is advantageous to determine the location of the edge of the boundary layer. In the present analysis, the edge of the boundary layer is located using three basic consecutive criteria. The first criterion consists of a search from the wall to the outer computational boundary for the minimum value of the function, $|V_{inv} - V_{tan}|$, where V_{inv} is the effective inviscid velocity calculated from the local pressure to upstream total pressure ratio and the free-stream total temperature, and V_{tan} is the magnitude of the local velocity in the direction of the surface tangent. This search provides an initial means of determining the location of the boundary layer edge using the assumption that the boundary layer edge total pressure and total temperature are equal to the free-stream values. This assumption is valid for cases that do not include strong shocks or nonuniform total pressure or total temperature inflow profiles at the upstream boundary, which is the case for all of the solutions to be presented here. This first criterion usually overestimates the boundary layer thickness on the pressure side of the airfoil so that further criteria are required to determine the location of the boundary layer edge accurately. The second criterion consists of a search from the min ($|V_{inv} - V_{tan}|$) location to the wall for the position where the absolute value of the vorticity nondimensionalized by the upstream velocity exceeds a predetermined value, ω_{limit}, which has been given a value of 1.0. This search is used to make sure that the edge of the boundary layer coincides with the edge of the vorticity layer. Finally, a search is performed from the wall to the point where $|\omega| > \omega_{limit}$ to find the maximum velocity. The boundary layer edge is then defined to be located where the velocity reaches 99 percent of the maximum velocity. This series of searches has been found to determine the boundary layer edge reliably even for complex geometries as shown by Davis et al. (1987).

The Baldwin–Lomax (1978) two-layer algebraic turbulence model is used in the VISCAS Navier–Stokes procedure in conjunction with a body normal grid in order to be as consistent with boundary layer theory as possible. An example of the

body normal grid is shown in Fig. 3 for the transonic compressor cascade discussed in the Results section. The intersection points of the body normal grid and the computational grid are calculated and stored prior to initiation of the time marching scheme. The flow variables and the vorticity from the computational grid are interpolated onto the body normal grid where the eddy viscosity is calculated using the Baldwin–Lomax model. Once the eddy viscosity is determined, it is interpolated back onto the computational grid. With this implementation, the eddy viscosity distribution can be computed from the wall to the outer boundary of the computational mesh without having to make any a priori estimate of the viscous layer thickness outside of which the eddy viscosity is usually abruptly forced to zero. Thus, this technique allows the turbulence model to distinguish where and how the eddy viscosity should decrease in the outer part of the viscous layer. In addition, the body normal implementation increases the accuracy of the turbulence model in regions of the flow where the tangential computational grid lines rapidly depart from the surface normals such as for turbine and highly staggered compressor cascade geometries.

Minor modifications have been made to the Baldwin–Lomax turbulence model in the VISCAS Navier–Stokes procedure. In separated flow regions, the value of the normal shear stress τ, used in the calculation of the transformed normal distance from the wall y^+, where

$$y^+ = \frac{\sqrt{\rho\tau}y}{\mu} \tag{1}$$

for the inner layer of the Baldwin–Lomax turbulence model, is the magnitude of the maximum normal shear stress within the shear layer. This value is used in Equation (1) instead of the wall shear stress value, which was suggested by Baldwin and Lomax (1978) in order to maintain an inner layer eddy viscosity distribution in the vicinity of separation points where the wall shear stress goes to zero. The local values of the density and the coefficient of viscosity at the maximum shear stress location are also used in equation (1). This modification in the inner layer model was first used by Carter and Wornom (1975) for the calculation of turbulent separated flows. In the outer layer of the Baldin–Lomax model, a search is performed for the location of the maximum value of the function

$$F = y|\omega|\,[1-\exp(-y^+/A^+)] \tag{2}$$

where ω is the vorticity and A^+ is the Van Driest damping constant, as part of the procedure to define the mixing length for the outer layer region. The search for the maximum of this function is limited in the VISCAS procedure to be between the wall and the edge of the boundary layer. This eliminates spurious false values of F_{max}, which might be located in the inviscid portions of the flow field, resulting in erroneous large values in the eddy viscosity. In separated flow regions, two maximum values in the F function exist due to the absolute value imposed on the vorticity in equation (2). Special logic is not used in the current procedure to choose the location of the value of F_{max} a priori in separated flows. For the separated flows shown in this paper, the location of F_{max} was determined to be the farthest maximum from the wall within the displaced shear layer region. The various constants used in the Baldwin–Lomax turbulence model as implemented in the VISCAS Navier–Stokes procedure are identical to those described by Baldwin and Lomax (1978). A detailed investigation is required in order to modify and validate this turbulence model for separated flows. As will be shown in the Results section, the present implementation of the Baldwin–Lomax turbulence model has been found to be a possible source of error in the immediate vicinity of separated flow regions but does, however, give good results in terms of cascade total pressure loss, even for separated flows.

Results

A detailed numerical investigation has been conducted for several cascade geometries in which results calculated by the VISCAS Navier–Stokes procedure were compared with experimental data. The results to be shown in this paper are for a transonic compressor cascade reported by Stephens and Hobbs (1979) and a subsonic compressor cascade tested by Taylor and Pugnier (1979) and reported by Hobbs and Weingold (1984). For each of these compressor cascades, comparisons are shown between the Navier-Stokes solutions and the experimental data for the airfoil surface pressure distributions, exit gas angle, and exit total pressure loss.

The Navier–Stokes and Euler solutions shown in this paper were considered converged when the maximum change of the total mass flux, $\Delta\rho v_{max}$, within the computational domain was less than 3×10^{-4} which corresponded to three orders magnitude reduction in the residual from its initial value. Three levels of multiple-grid in addition to the base fine grid were used to accelerate convergence to steady state for all of the numerical solutions. All of the viscous solutions were computed assuming fully turbulent, adiabatic flow. As will be shown in the following results, transition modeling was not necessary for the flows within these compressor cascades to achieve good agreement with experimental data.

All of the Navier–Stokes and Euler calculations shown in this paper were computed using an Alliant FX-8 parallel/vector mini-supercomputer. This computer is currently configured to have seven central processing units, which work together concurrently on a given computation. Parallelization within the Alliant computer is performed using a shared memory system similar to the Cray supercomputer. Optimization of the VISCAS code has been performed exclusively by the Alliant compiler, which vectorizes inner DO-loops and parallelizes outer DO-loops. Typical Navier–Stokes calculations using a 193 streamwise by 33 tangential computational grid took roughly 1000 iterations corresponding to 40 min of CPU time on the Alliant computer. Recent benchmark results with this code indicate that the same calculation could be performed in approximately 2 min on a Class VI supercomputer. Thus, with the use of a supercomputer, an entire loss versus incidence prediction such as those to be shown below with typically eight points over the incidence range could be computed in 16 min of CPU time.

Transonic Compressor Cascade. Figure 2 shows the computational mesh used for a transonic compressor cascade reported by Stephens and Hobbs (1979). This compressor section was tested in a transonic cascade facility at DFVLR in Porz-Wahn, Federal Republic of Germany. The wind tunnel is a closed-loop, continuously running facility with variable nozzle and variable test section height. An important feature of this tunnel is its extensive endwall boundary layer control system, which is essential for controlling the secondary flows induced by the strong gapwise pressure gradients of supercritical cascades.

The inlet and exit static pressure was measured by static taps on the cascade wall. For this cascade, the upstream measurement plane was axially 25 mm (0.984 in.) from the leading edge plane. The exit measurement plane was 22 mm (0.866 in.) from the trailing edge plane. Ten cascade airfoils of 69.85 mm (2.75 in.) chord and 167.64 mm (6.6 in.) span were used in the experimental facility. A downstream traverse probe was used to measure total and static pressures as well as flow angles. The suction and pressure sides of two separate airfoils, which formed a common flow passage, were instrumented with pressure taps to provide detailed pressure distributions.

The computational mesh shown in Fig. 2 for the Navier–Stokes calculations consists of 193 points in the streamwise direction and 33 points in the tangential direction,

Table 1 Aerodynamic conditions for transonic compressor cascade

Inc.	M_1	β_1	M_2	β_2	H_2/H_1	P_{T_2}/P_{T_1}	Re_1
-10.0	.7312	57.0	.5920	89.28	.9584	.9766	373,860.
-4.8	.7257	51.8	.5821	91.21	.8900	.9926	379,637.
-2.8	.7313	49.8	.5861	90.20	.8635	.9932	375,852.
0.0	.7654	47.0	.5604	90.84	.8657	.9936	316,727.
3.2	.7346	43.8	.5574	89.87	.8094	.9929	384,572.
5.0	.7355	42.0	.5395	90.26	.8036	.9884	402,740.
7.0	.7376	40.0	.4902	89.14	.8542	.9563	327,352.

which provide a total of 65 points over one blade gap. Approximately 17 streamwise points were located in the immediate vicinity of the leading edge. A total of 30 points were distributed in the streamwise direction along the wake centerline and 21 points were used around the surface of the trailing edge.

The VISCAS Navier–Stokes procedure was used to compute several test conditions that had a common inlet Mach number of typically 0.73 over a wide range of inlet gas angles to investigate the ability of this procedure to predict the pressure distributions, profile total pressure loss, and exit flow angle. The aerodynamic conditions that were used in the computations for this compressor cascade are the corrected experimental conditions given in Table 1. The inlet Mach numbers given in Table 1 have been increased from the actual measured values by 0.03 as suggested by Stephens (1979) and the exit-to-inlet streamtube height ratio was adjusted accordingly to preserve continuity.

Figure 4 shows a comparison between the predicted and measured mass-averaged total pressure loss as a function of incidence. Very good agreement exists between the predicted loss and the experimental data. The Navier–Stokes technique accurately predicts both the absolute levels of loss as well as the positive and negative stalling incidence. The fact that the fully turbulent Navier–Stokes calculations are in good agreement with the experimental data for this cascade, suggests that transition of the boundary layer from laminar to turbulent flow probably occurred in the experiment very close to the leading edge, perhaps near the minimum pressure points on each side of the airfoil. The absolute level of loss predicted for the 7.0 deg incidence case is low compared to the experimental data but the Navier–Stokes scheme has successfully predicted the onset of the rapid rise in the loss relative to the design conditions. The loss level at this high positive incidence condition is extremely sensitive to small changes in the inlet flow angle and the error between the calculation and the experimental data could be due to measurement uncertainty.

The predicted total pressure loss profile at a location 22 mm (0.886 in.) downstream of the trailing edge (i.e., at the experimental exit measurement plane) for the 0.0 deg design point incidence is compared with the experimental traverse data in Fig. 5. This figure shows that reasonable agreement exists between the predicted solution and the experimental data. In addition, Fig. 5 shows that the predicted total pressure loss is confined to a viscous region within the wake downstream of the trailing edge and that the predicted total pressure loss in the inviscid regions of the flow is essentially zero. Similar agreement between the predicted Navier–Stokes total pressure loss profiles and the experimental data exists for all of the remaining incidence points shown in Fig. 4 with the exception of the -10.0 deg and 7.0 deg incidence cases where the flow was stalled. For these cases, the physical width of the total pressure loss profile was in good agreement with the experimental data but the magnitude of the total pressure loss within the profile was predicted to be too large. This discrepancy is probably due to the inadequacy of the turbulence model for these highly separated flow conditions, as will be further discussed below. Further research is needed to modify and validate the Baldwin–Lomax turbulence model for separated flows.

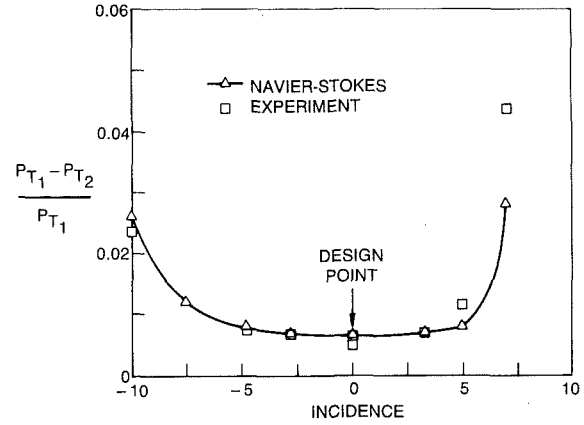

Fig. 4 Predicted loss versus incidence for transonic compressor cascade

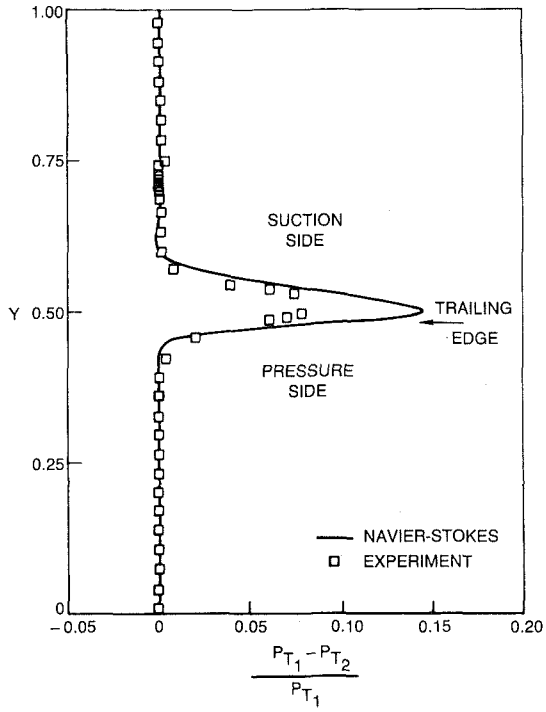

Fig. 5 Predicted loss profile for 0.0 deg design point incidence

A comparison between the predicted and measured exit flow angle as a function of incidence is shown in Fig. 6. The prediction and the experimental data differ by a constant 2 deg over the entire incidence range. This discrepancy is probably due to the different streamtube height distributions between the Navier–Stokes calculation and the actual flow in the experiment. Numerical investigations have shown that the predicted exit flow angle is sensitive to the streamtube height distribution within the cascade passage. In the Navier–Stokes procedure, the streamtube height distribution is assumed to be a linear variation between the leading and trailing edges of the cascade whereas in the actual flow, the streamtube height probably varies nonlinearly in both the axial and tangential directions within the entire flow passage. Unfortunately, details of the streamtube height distribution were not determined for the actual flow, but rather the ratio of the exit streamtube height to that at the inlet was calculated from continuity using the measured inlet and exit Mach numbers and flow angles and the exit total pressure loss. Further work is needed to pinpoint the reasons for the discrepancy between the experimental exit gas angles and those predicted with the Navier–Stokes procedure.

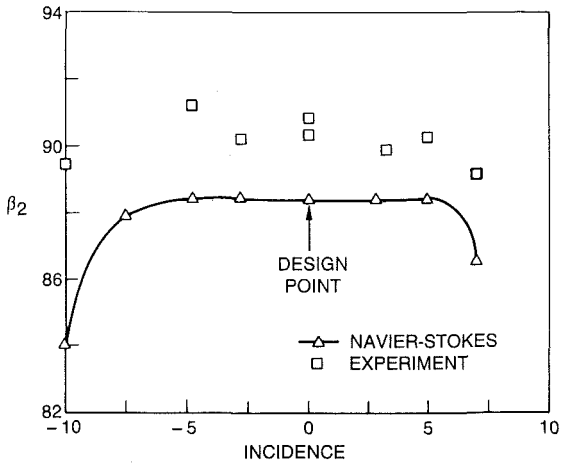

Fig. 6 Predicted exit angle versus incidence for transonic compressor cascade

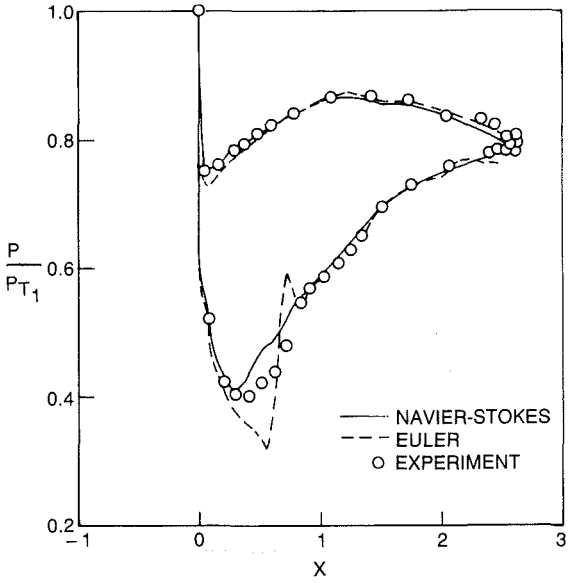

Fig. 7 Predicted pressure distribution, 0.0 deg incidence

A comparison of the predicted pressure distributions with the experimental data for the 0.0 deg incidence design point case is shown in Fig. 7. The inviscid (Euler) solution is also shown in this figure as an indication of the amount of inviscid/viscous interaction occurring in the flow. Good agreement exists between the Navier–Stokes solution and the experimental data except at the minimum pressure point on the suction side where the Navier–Stokes approach slightly overpredicts the pressure. Figure 7 shows a significant difference between the inviscid and viscous solutions in the transonic region of the flow for the suction side of the airfoil. The inviscid solution predicts a shock whereas the viscous solution does not. Convergence of the Navier–Stokes solution occurred in 915 iterations.

Similar agreement exists between the Navier–Stokes solutions and the experimental data for the pressure distributions at -2.8 deg and 3.2 deg incidence as that shown for the 0.0 deg incidence case. The Navier–Stokes solution converged for these calculations in 883 and 858 iterations, respectively.

As a demonstration of the VISCAS Navier–Stokes procedure at off-design conditions, Figs. 8 and 9 show the predicted pressure distributions compared to the experimental data for -4.8 deg and 5.0 deg incidence. As in the design point case, good agreeement exists between the viscous solutions and the experimental data. Likewise, significant in-

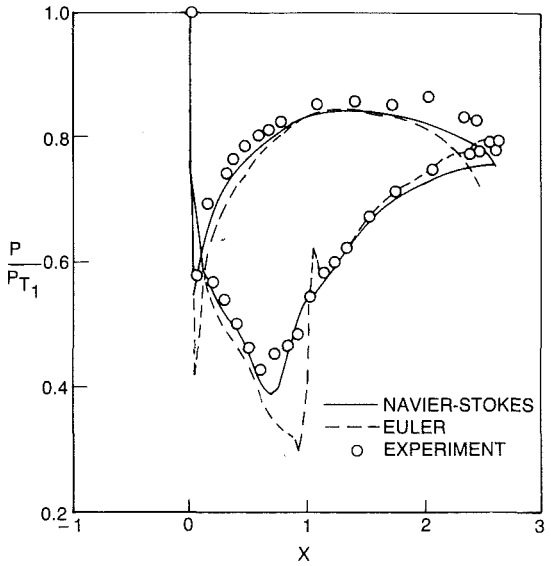

Fig. 8 Predicted pressure distribution, −4.8 deg incidence

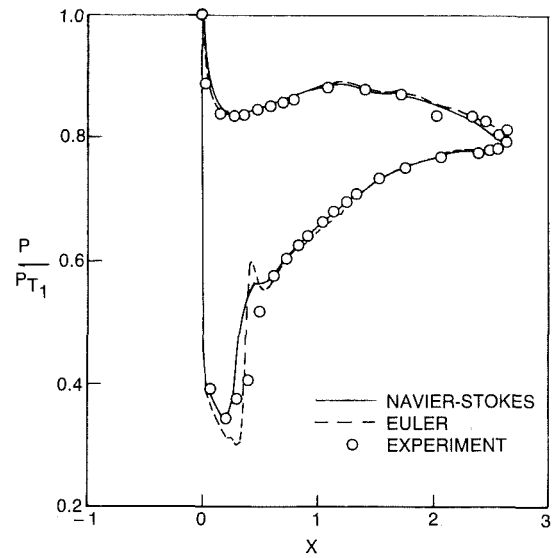

Fig. 9 Predicted pressure distribution, 5.0 deg incidence

viscid/viscous interaction is demonstrated in these cases as indicated by the large differences between the inviscid and viscous solutions in the transonic regions of the flow. Convergence was reached in the Navier–Stokes solutions for the -4.8 deg and 5.0 deg incidence cases in 917 and 970 iterations, respectively.

A very difficult case for Navier–Stokes techniques to compute is the flow over airfoils near the stall incidence where very large regions of separated flow exist. As separated flow regions grow in size, the flow field becomes increasingly unsteady in nature, which correspondingly makes it increasingly difficult for time marching Navier–Stokes algorithms to determine a steady-state solution. Figures 10 and 11 show the solution for the transonic compressor cascade at -10.0 deg incidence at negative stall. The pressure distribution given in Fig. 10 shows good agreement between the predicted Navier–Stokes solution and the experimental data except in the aft portion of the cascade. This discrepancy is probably due to the difference in the local streamtube height distribution between the Navier–Stokes calculation and the actual flow. The flow field in the experimental cascade facility was

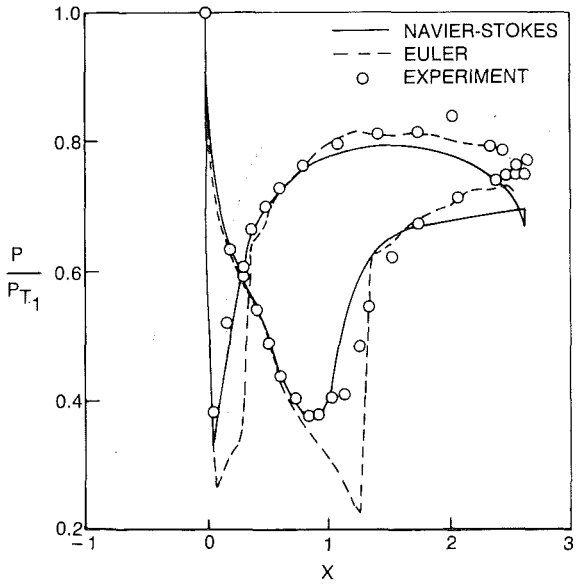

Fig. 10 Predicted pressure distribution, −10.0 deg incidence

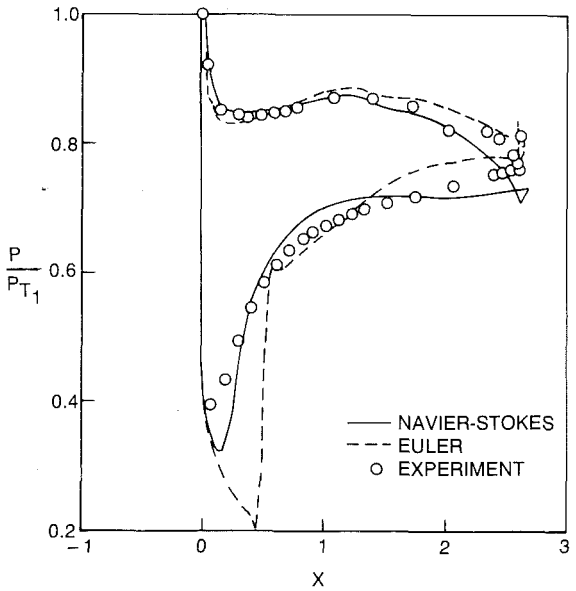

Fig. 12 Predicted pressure distribution, 7.0 deg incidence

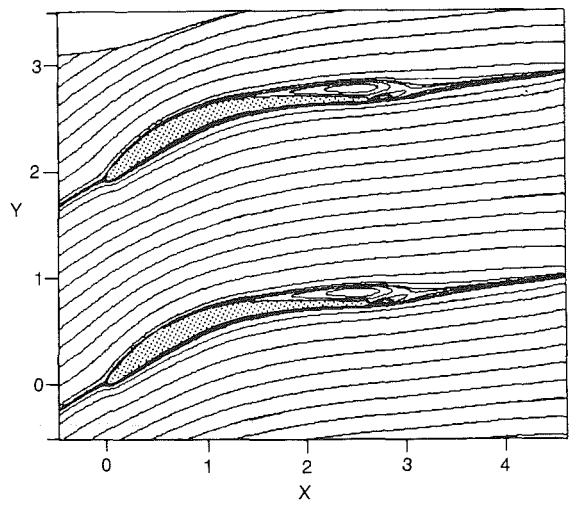

Fig. 11 Predicted streamlines, −10.0 deg incidence

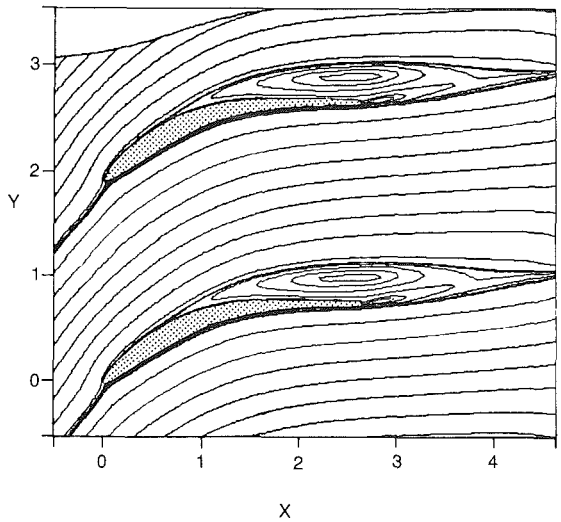

Fig. 13 Predicted streamlines, 7.0 deg incidence

most likely highly three-dimensional for this stalled flow case, making exact agreement between the quasi-three-dimensional viscous calculation and the experimental data difficult to obtain. In addition, the Baldwin–Lomax turbulence model in the Navier–Stokes calculation may likely be a source of error since this model has only been validated for attached flows. The predicted pressure distribution of the Euler calculation is in better agreement with the experimental data in this aft region of the cascade flow. However, in the transonic region, the inviscid pressure distribution exhibits a strong shock, which is not present in the experimental data.

The streamline pattern given in Fig. 11 shows that significant separation occurs on the suction side over the aft portion of the airfoil. A secondary vortex is predicted to exist immediately behind the trailing edge. The flow between 4 and 44 percent axial chord on the pressure side of the airfoil is also separated although the streamlines in Fig. 11 do not show this because the separated flow region is very thin (i.e., 0.1 percent of the cascade chord).

Similarly, Figs. 12 and 13 show the comparison between the Navier–Stokes solution and the experimental data at a positive incidence stall of 7.0 deg incidence. As in the −10.0 deg incidence case, fairly good agreement exists between the Navier–Stokes solution and the experimental data for the pressure distributions shown in Fig. 12. The discrepancies between the prediction and the experimental data again are probably due to inconsistencies in the streamtube height distribution through the cascade passage between the calculation and the experiment as well as possible errors introduced by the turbulence model for this highly separated flow case. The actual flow in the experiment at this incidence was also very likely to be highly three dimensional since most of the suction side of the airfoil was separated. The predicted inviscid pressure distribution has good agreement with the experimental data on the pressure side of the airfoil but poor agreement exists on the suction side. Comparison between the inviscid and viscous solutions show that a very strong inviscid/viscous interaction occurs in the flow due to the large separation on the suction side. Figure 13 shows that two vortices are predicted to exist in the flow field. A large primary vortex is predicted on the suction side of the airfoil due to the separation of the suction side boundary layer. A secondary vortex which is driven by the primary suction side vortex and the flow which leaves the pressure side of the airfoil is located behind the trailing edge base region.

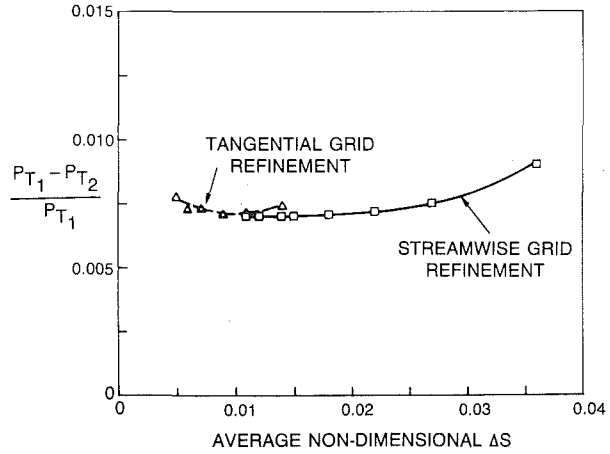

Fig. 14 Predicted loss versus average nondimensionalized grid spacing

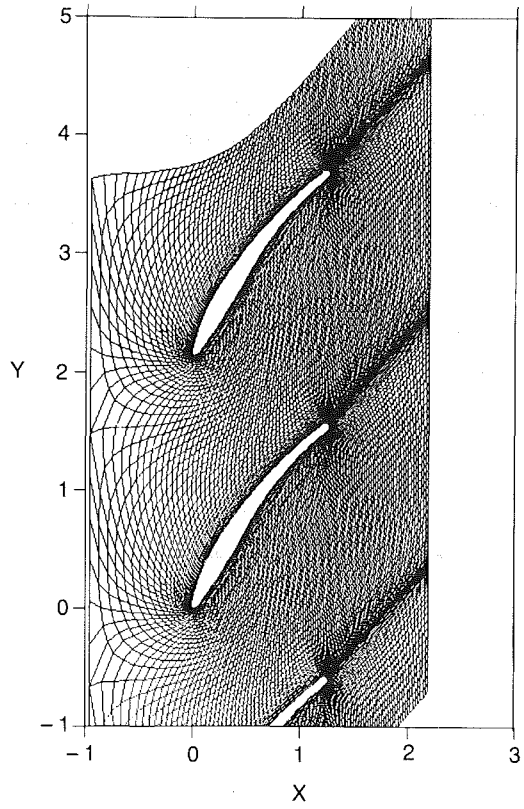

Fig. 15 Computational mesh for subsonic compressor cascade

Convergence was difficult to obtain for the −10.0 deg and 7.0 deg incidence cases due to the unsteady nature of the separated flow regions. Once the maximum residual in the total mass flux within the computational domain reached the usual converged level of 3×10^{-4} for these cases, the convergence history became somewhat cyclic. This cyclic convergence behavior was observed to correspond to a shifting of the separated flow regions. Further studies are currently underway to investigate these quasi-unsteady separated flow fields using the time accurate version of the VISCAS analysis.

Grid Refinement Investigation. An investigation was performed to determine the effect of grid spacing on the predicted loss levels and the pressure distributions for this cascade. Figure 14 shows the predicted loss as a function of average nondimensionalized grid spacing in both the streamwise and tangential directions for the 0.0 deg incidence case. The averaged nondimensionalized streamwise grid spacing is defined as the average grid spacing along the airfoil surface/wake boundary divided by the airfoil chord. For the tangential direction, the averaged nondimensionalized grid spacing is defined as the cascade gap-to-chord ratio divided by the number of tangential computational points over one gap.

Table 2 Summary of total pressure loss versus computational grid point density

No. of Streamwise Points	No. of Tangential Points	$(P_{T_1}-P_{T_2})/P_{T_1}$
321	33	.0070
289	"	.0070
257	"	.0070
225	"	.0070
193	"	.0071
161	"	.0072
129	"	.0075
97	"	.0090
193	65	.0077
"	57	.0073
"	49	.0073
"	41	.0071
"	33	.0071
"	25	.0074

For the streamwise grid refinement study, calculations were performed using 33 points in the tangential direction with the number of points varying in the streamwise direction between 97 and 321 in increments of 32 to determine the effect of streamwise grid spacing on the predicted loss and pressure distributions. In addition, a tangential grid refinement study was performed by varying the number of points in the tangential direction from 25 to 65 in increments of 8 using 193 points in the streamwise direction. Table 2 gives a summary of the cases computed in this grid refinement study. Figure 14 shows that the predicted loss became insensitive to the streamwise grid spacing below an average nondimensionalized grid spacing of 0.02 (which corresponded to 161 streamwise points with 33 tangential points). The predicted skin friction and displacement thickness distributions became insensitive to grid spacing below 0.02 average nondimensionalized streamwise grid spacing as well. The predicted pressure distributions and exit gas angle showed little sensitivity to grid spacing in either direction for this attached flow case. The curves presented in Fig. 14 indicate that the Navier–Stokes calculations shown in Figs. 7–9 where the flow remains attached are grid independent.

A similar streamwise and tangential grid spacing sensitivity study is required for the negative and positive stalling incidence flows to establish if the solutions for these flows are truly grid independent. Such a study may, however, be complicated by the fact that the unsteadiness of these flows may be amplified with refined grids, thereby making it difficult to obtain conclusive results.

Subsonic Compressor Cascade. A similar numerical investigation was conducted for the subsonic compressor cascade shown in Fig. 15, which was tested experimentally by Taylor and Pugnier (1979) and reported by Hobbs and Weingold (1984). This Controlled Diffusion cascade was tested at the United Technologies Research Center High Speed Cascade Tunnel, which has test capabilities similar to the DFVLR cascade tunnel. The facility is an open circuit tunnel, which uses pressurized air exhausting through the test section

Table 3: Aerodynamic conditions for subsonic compressor cascade

Inc.	M_1	β_1	M_2	β_2	H_2/H_1	P_{T_2}/P_{T_1}	Re_1
-10.4	.6071	37.43	.5351	42.30	1.0051	.9733	312,982.
-8.6	.6114	35.60	.4815	43.83	.9912	.9938	303,079.
-6.8	.6177	33.80	.4615	45.12	.9597	.9952	301,065.
-4.9	.6144	31.94	.4342	45.04	.9544	.9957	295,234.
-3.1	.6053	30.08	.4218	45.35	.9120	.9959	291,771.
-0.9	.5634	27.93	.3845	44.66	.8894	.9962	273,432.
1.1	.5965	25.87	.4115	44.78	.8112	.9952	273,432.
3.0	.5998	24.03	.3984	43.53	.8070	.9835	290,534.
4.1	.5651	22.89	.3726	43.96	.7835	.9780	278,208.
4.9	.5983	22.07	.3805	42.26	.8039	.9675	289,843.

to atmospheric pressure. Tunnel side wall boundary layers are removed by perforated plates upstream of the test section, and top and bottom wall boundary layers are removed by a scoop on the top wall and slots on the bottom wall. A completely independent suction system is used to remove corner boundary layers through slots at the intersection of the airfoil suction surface with the side walls, to prevent spanwise flow of the endwall boundary layer.

Cascade instrumentation included several rows of static pressure taps in the sidewalls upstream and downstream of the cascade and combination total pressure/angle probes located in a traverse station 39.1 mm (1.54 in.) axially upstream of the leading edge plane and roughly 18 mm (0.71 in.) axially downstream of the trailing edge plane. Eight cascade airfoils of 50.8 mm (2.0 in.) chord and 101.6 mm (4.0 in.) span were used in the experimental facility. As for the transonic cascade, the pressure and suction surfaces of two separate airfoils, which formed a common flow passage, were instrumented with pressure taps to provide airfoil surface pressure distributions.

The computational mesh shown in Fig. 15 for the Navier–Stokes calculations consists of 193 points in the streamwise direction and 33 points in the tangential direction. Approximately 17 streamwise computational points were located in the immediate vicinity of the leading edge. A total of 35 points were distributed along the wake centerline in the streamwise direction and 28 points were located around the trailing edge. The average nondimensionalized streamwise and tangential grid spacings for this case were both 0.018, which is smaller than the average nondimensionalized grid spacing for the transonic cascade previously shown.

As in the previous transonic numerical investigation, the VISCAS Navier–Stokes procedure was used to compute the flow through the subsonic compressor cascade shown in Fig. 15 corresponding to the experimental conditions given in Table 3 which had a common inlet Mach number of 0.60. Comparisons were made between the predicted and experimental pressure distributions, total pressure loss, and exit flow angles to establish the reliability and accuracy of the present Navier–Stokes scheme.

A comparison between the measured and predicted mass-averaged total pressure loss as a function of incidence for the subsonic cascade is shown in Fig. 16. Very good agreement exists between the experimental data and the predicted loss. The Navier–Stokes technique accurately predicted the negative stalling incidence but predicted the positive stalling incidence to be approximately 2 deg more positive than that which was measured experimentally. The absolute levels in loss predicted by the Navier–Stokes scheme for all of the incidences below the positive 3.0 deg stalling incidence were in good agreement with the experimental data. Numerical results have indicated that if transition of the boundary layer from laminar to turbulent is delayed slightly behind the leading edge of the cascade on the suction side of the airfoil for the cases above 3.0 deg positive incidence, laminar separation and subsequent stall of the flow occur immediately behind the leading edge.

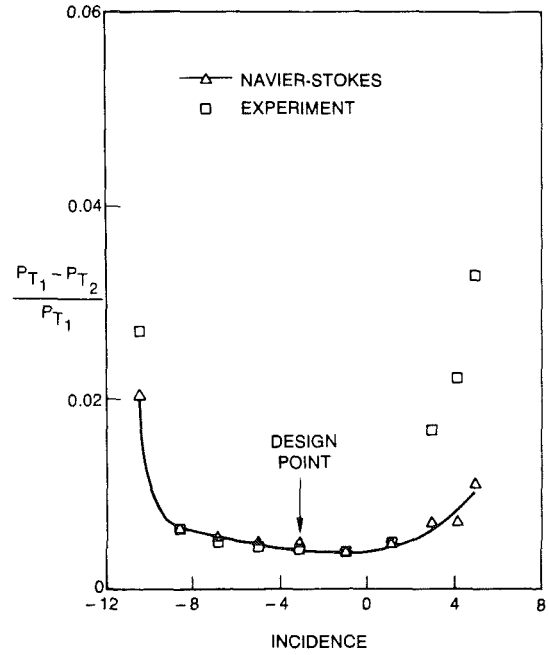

Fig. 16 Predicted loss versus incidence for subsonic compressor cascade

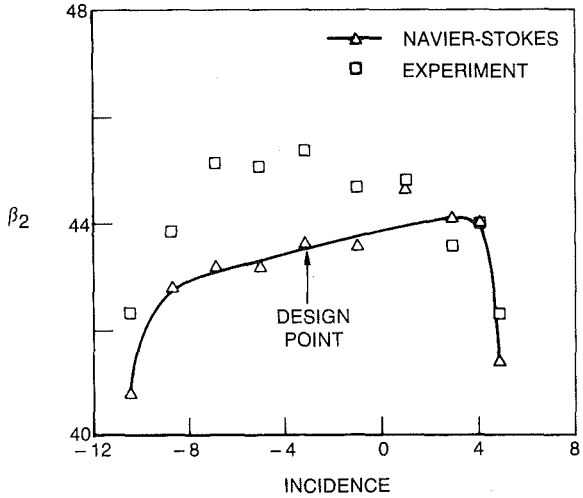

Fig. 17 Predicted exit angle versus incidence for subsonic compressor cascade

The predicted loss levels for these transitional cases increase to the levels of the experimental data and the flow fields become highly unsteady in nature and exhibit vortex shedding. The differences between the fully turbulent predictions and the experimental data for the total pressure loss for these high positive incidence cases will be further discussed below in terms of the cascade surface pressure distributions. The favorable agreement between the fully turbulent Navier–Stokes prediction and the experimental loss data for the incidences less than 3.0 deg, however, suggests that most of the flow on this compressor cascade for the lower incidence cases was turbulent and that transition probably occurred in the experiment close to the leading edge of the airfoil.

Figure 17 shows a comparison between the experimental and predicted Navier–Stokes exit gas angles for this subsonic compressor cascade. Similar to the transonic cascade, the Navier–Stokes procedure in general predicts the correct trend in the exit flow angle as a function of incidence but underpredicts the absolute level of the exit flow angle between 1 and 2 deg depending upon the incidence. This discrepancy is

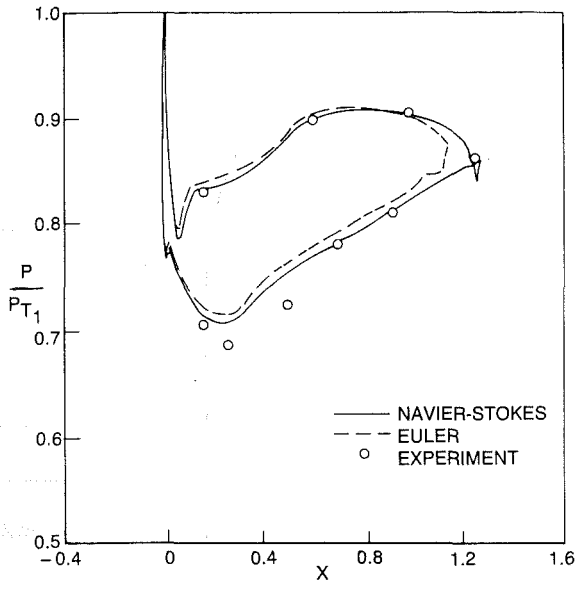

Fig. 18 Predicted pressure distribution, −3.1 deg incidence

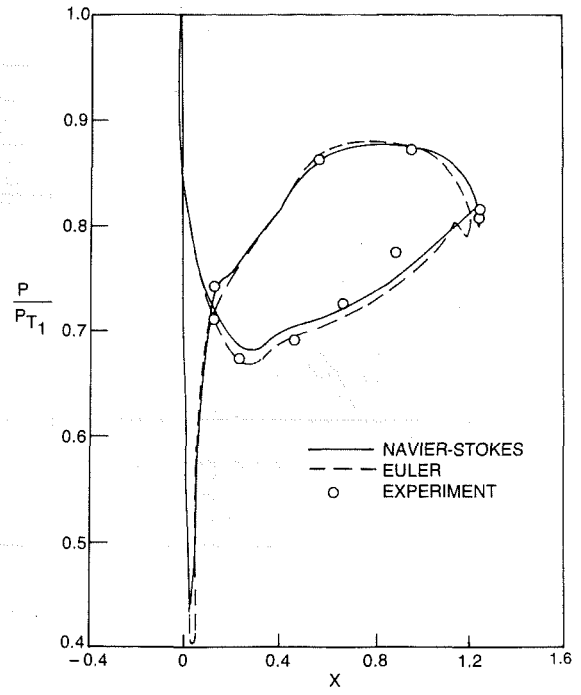

Fig. 19 Predicted pressure distribution, −8.6 deg incidence

probably due to the differences in the streamtube height distributions between the Navier–Stokes calculation and the actual flow. As previously explained, the predicted exit flow angle has been found to be sensitive to the streamtube height distribution. Further work is needed to determine the exact reason for this decrepancy.

The predicted pressure distribution for the subsonic cascade is compared with the experimental data at the design point incidence of −3.1 deg in Fig. 18. Good agreement exists between the viscous solution and the experimental data except near the minimum pressure point on the suction side, where the Navier–Stokes analysis overpredicts the pressure. As in the previous transonic case, the inviscid (Euler) solutions are also shown as an indication of the inviscid/viscous interaction effects on the flow. Very little interaction occurs in this flow

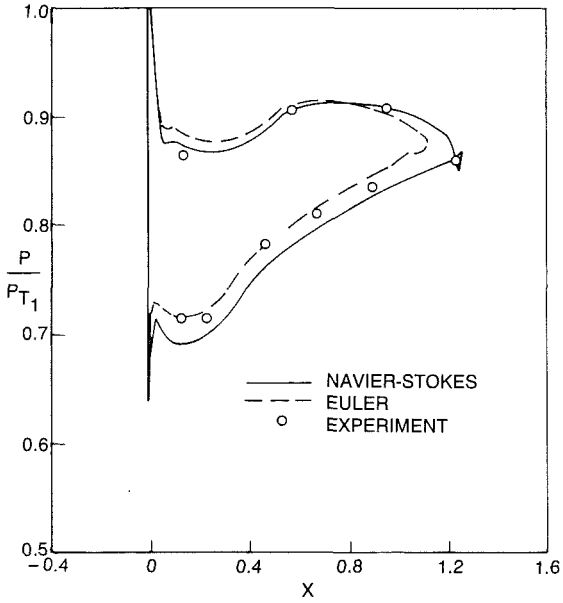

Fig. 20 Predicted pressure distribution, 1.1 deg incidence

field as indicated by the minor difference between the viscous and inviscid solutions.

Comparison between the Navier–Stokes solution and the experimental data for off-design flows at incidences of −8.6 deg and 1.1 deg are shown in Figs. 19 and 20. The viscous solutions are in good agreement with the experimental data at these incidences. As in the design point case, very little inviscid/viscous interaction occurs for the −8.6 deg incidence case. Differences between the inviscid and viscous solutions for the 1.1 deg incidence case show that the inviscid/viscous interaction in this flow is more significant, however, due to the increase in the suction side boundary layer thickness at this positive incidence.

The agreement between the predicted pressure distribution and experimental data for the −6.8, −4.9, and −0.9 deg incidence cases is similar to that for the cases previously shown in Figs. 18–20. The solutions for all of these cases indicated attached flow over the entire airfoil surface.

The predicted results of the Navier–Stokes scheme at −10.4 deg incidence, which is at or beyond the negative stalling incidence, is shown in Figs. 21 and 22. As shown in Fig. 21, both the inviscid and viscous predicted pressure distributions are in poor agreement with the experimental data. The predicted streamline pattern given in Fig. 22 shows two vortices: a very large pressure side separation vortex and a much smaller secondary vortex immediately behind the trailing edge. The poor agreement between the experimental data and the Navier–Stokes solution for the pressure distribution shown in Fig. 21 may be due to the inadequacy of the Baldwin–Lomax turbulence model for the very large separation zone. However, numerical results have shown that if the incidence used in the calculation is varied from −10.4 to −9.0 deg, excellent agreement can be obtained between the experimental data and the predicted viscous pressure distribution, suggesting that the measured inlet gas angle may be in error for this case. The streamwise extent of the pressure side separation for the −9.0 deg case is roughly the same as that shown in Fig. 22 but the height of the separated region is only half of that of the −10.4 deg case.

Fig. 23 shows the predicted pressure distributions with the experimental data at 4.9 deg positive incidence, which is greater than the positive stalling incidence. Reasonable agreement exists between the Navier–Stokes calculation and the experimental data for this case. Separation of the flow was

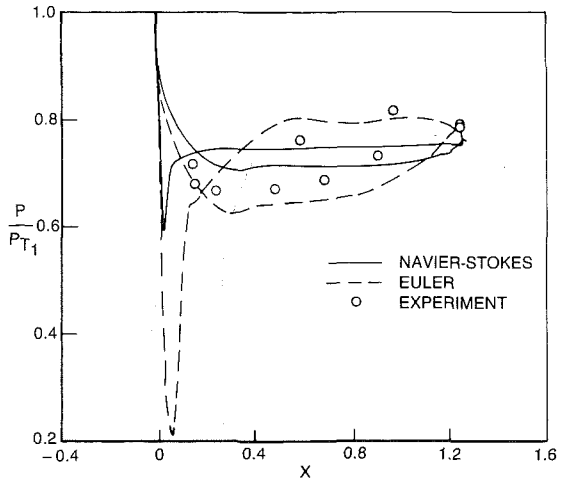

Fig. 21 Predicted pressure distribution, −10.4 deg incidence

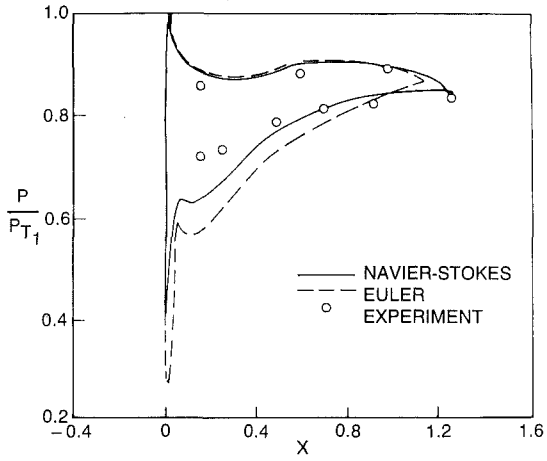

Fig. 23 Predicted pressure distribution, 4.9 deg incidence

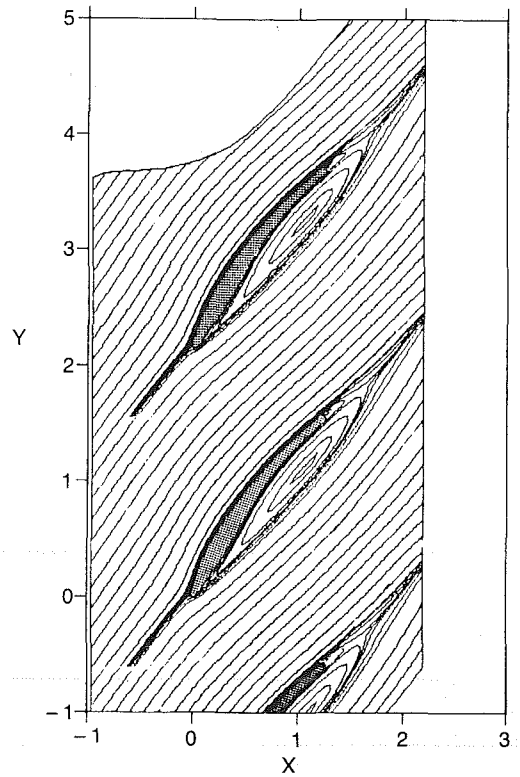

Fig. 22: Predicted streamlines, −10.4 deg incidence

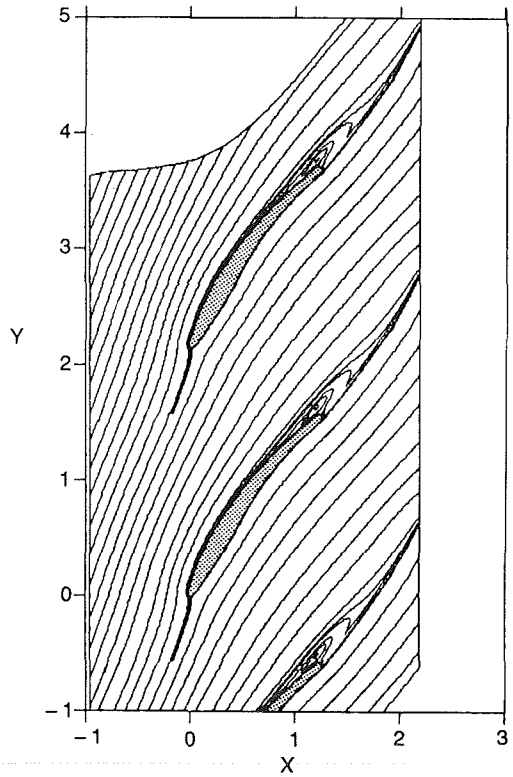

Fig. 24 Predicted streamlines, 4.9 deg incidence

predicted to occur on the aft 60 percent of the airfoil suction side surface at this incidence. As shown in Fig. 16, however, the Navier–Stokes calculation underpredicts the loss for this flow condition. Numerical results have indicated that if transition is delayed slightly behind the leading edge where, as shown in Fig. 23, a large undershoot in the pressure occurs followed by a severe adverse pressure gradient, laminar separation of the flow occurs immediately behind the leading edge. As a result, the flow remains separated over the entire suction side surface of the airfoil and the flow becomes highly unsteady. The predicted loss levels for this transitional case are in much better agreement with the experimental data. Further work is required using an unsteady analysis, however, to determine whether the time average of the unsteady pressure distribution for this transitional case is in better agreement with the experimental data than that shown in Fig. 23, which corresponded to fully turbulent flow.

The predicted streamline pattern for the fully turbulent 4.9 deg positive incidence case is shown in Fig. 24. The streamlines shown in this figure indicate that a single vortex is predicted on the suction side of the airfoil. This is in contrast to the stall incidence cases shown in Figs. 11, 13, and 22 for the transonic and subsonic compressor cascades where two vortices were predicted.

Concluding Remarks

Results from a numerical investigation using the VISCAS cascade Navier–Stokes procedure are shown as a demonstration of this technique for the prediction of compressor cascade performance over the entire incidence range. Viscous solutions are compared with experimental data for surface pressure distributions, total pressure loss, and exit flow angles for two compressor cascades to show the accuracy and reliability of this numerical procedure. In addition, results from a grid

refinement study in which the streamwise and tangential grid point densities were varied independently are presented to demonstrate that the Navier–Stokes solutions are grid independent.

This investigation represents an important step in the development of a numerical tool that can be used by turbomachinery designers to optimize cascade designs over a wide range of flow conditions. This paper demonstrates that Navier–Stokes procedures can be used to predict compressor cascade total pressure loss provided that careful numerical techniques are utilized in order to maintain low levels of truncation error and errors associated with numerical smoothing operators. Research is continuing in the areas of transition modeling, turbulence modeling for separated flows, and improved modeling of the quasi-three-dimensional streamtube height variation through the cascade passage in order to develop a reliable design tool that is applicable to a wide range of flow phenomena and cascade geometries.

Acknowledgements

This work was supported by Pratt and Whitney and the United Technologies Research Center under the Corporate Research Program. The authors appreciate the help of Mr. John Horan in providing information regarding the compressor cascade experiments.

References

Balwin, B. S., and Lomax, H., 1978, "Thin-Layer Approximation and Algebraic Model for Separated Turbulent Flows," AIAA Paper No. 78-257.

Carter, J. E., and Wornom, S. F., 1975, "Solutions for Incompressible Separated Boundary Layers Including Viscid-Inviscid Interaction," *Aerodynamic Analyses Requiring Advanced Computers*, Part I, NASA Langley Research Center, pp. 125–150.

Chima, R. V., 1987, "Analysis of Inviscid and Viscous Flows in Cascades With an Explicit Multiple-Grid Algorithm, *AIAA Journal of Propulsion*, Vol. 3, No. 5, pp. 397–405.

Davis, R. L., Ni, R. H., and Carter, J. E., 1987, "Cascade Viscous Flow Analysis Using the Navier–Stokes Equations," *AIAA Journal of Propulsion*, Vol. 3, No. 5, pp. 406–414.

Hah, C., 1986, "Navier–Stokes Calculation of Three-Dimensional Compressible Flow Across a Cascade of Airfoils With an Implicit Relaxation Method," AIAA Paper 86-0555.

Hobbs, D. E., and Weingold, H. D., 1984, "Development of Controlled Diffusion Airfoils for Multistage Compressor Application," ASME *Journal of Engineering for Gas Turbines and Power*, Vol. 106, pp. 271–278.

Nakahashi, K., Nozaki, O., Kikuchi, K., and Tamura, A., 1987, "Navier–Stokes Computations of Two- and Three-Dimensional Cascade Flow Fields," AIAA Paper No. 87-1315.

Ni, R. H., 1982, "A Multiple Grid Scheme for Solving the Euler Equations," *AIAA Journal*, Vol. 20, pp. 1565–1571.

Norton, R. J., Thompkins, W. T., Jr., and Haimes, R., 1984, "Impact Finite Difference Schemes with Non-Simply Connected Grids – A Novel Approach," AIAA Paper No. 84-0003.

Rai, M., 1987, "Unsteady Three-Dimensional Navier–Stokes Simulations of Turbine Rotor-Stator Interaction," AIAA Paper No. 87-2058.

Rhie, C., 1986, "A Pressure Based Navier–Stokes Solver Using the Multigrid Method," AIAA Paper No. 86-0207.

Schafer, O., Fruhauf, H. – H., Bauer, B., and Guggolz, M., 1986, "Application of a Navier–Stokes Analysis to Flows Through Plane Cascades," ASME *Journal of Engineering for Gas Turbines and Power*, Vol. 108, pp. 103–111.

Shamroth, S. J., McDonald, H., and Briley, W. R., 1984, "Prediction of Cascade Flowfields Using the Averaged Navier–Stokes Equations," ASME *Journal of Engineering for Gas Turbines and Power*, Vol. 106, pp. 383–390.

Sorenson, R. L., 1980, "A Computer Program to Generate Two-Dimensional Grids About Airfoils and Other Shaped by the Use of Poisson's Equation," NASA TM-81198.

Stephens, H. E., and Hobbs, D. E., 1979, "Design and Performance Evaluation of Supercritical Airfoils for Axial Flow Compressors," NAVAIR Report FR11455.

Subramanian, S. V., and Bozzola, R., 1987, "Numerical Simulation of Three-Dimensional Flow Fields in Turbomachinery Blade Rows Using the Compressible Navier–Stokes Equations," AIAA Paper No. 87-1314.

Taylor, W., and Pugnier, G., 1979, "Performance Characteristics for a Cascade of Controlled Diffusion Airfoils – Case D," UTRC Report R79-230807-2.

Thompson, J. F., Thames, F. C., and Mastin, C. W., 1974, "Automatic Numerical Generation of Body-Fitted Curvilinear Coordinate System for Field Containing Any Number of Arbitrary Two-Dimensional Bodies," *Journal of Computational Physics*, Vol. 15, No. 3, pp. 299–319.

Weinberg, B. C., Yang, R. J., McDonald, H., and Shamroth, S. J., 1986, "Calculation of Two and Three-Dimensional Transonic Cascade Flow Fields Using the Navier–Stokes Equation," ASME *Journal of Engineering for Gas Turbines and Power*, Vol. 108, pp. 93–102.

Numerical Analysis of Airfoil and Cascade Flows by the Viscous/Inviscid Interactive Technique

C. J. Hwang

F. L. Jiang

J. M. Hsieh

Institute of Aeronautics and Astronautics,
National Cheng Kung University,
Tainan, Taiwan

S. B. Chang

Chung-Shan Institute of Science
& Technology,
Taichung, Taiwan

A viscous-inviscid interaction calculation is performed to study the steady, two-dimensional, incompressible/subsonic compressible, attached and separated flows for isolated airfoils and airfoil cascades. A full-potential code was coupled with a laminar/transition/turbulent finite difference code using the semi-inverse method. For the potential flow, the finite element method is employed and the circulation is considered as an unknown parameter. In order to handle the problem efficiently, an automatic grid generation technique is necessary. For the incompressible flow, the solution can be achieved without iteration. However, for the compressible flow, a "pseudotime integral" is used to find a steady-state solution. To understand the viscous effect, the boundary layer equations are solved by the implicit, finite difference method. For the turbulent flow, the algebraic eddy-viscosity formulation of Cebeci and Smith is used. The location of transition from laminar to turbulent flow is predicted or specified by empirical data correlations. The transitional region is taken into account by an empirical intermittency factor. With regard to separated flows, the FLARE approximation and inverse method are introduced. In order to evaluate the present solution procedure, the numerical results are compared to the theoretical and experimental data given in other papers and reports.

Introduction

In order to design new aircraft and turbomachinery, an efficient and accurate numerical solution procedure is required. Cebeci et al. (1986) combined an inviscid-flow method based on conformal mapping and a boundary-layer procedure based on the numerical solution of differential equations to calculate flows around four different airfoils. A fast viscous-inviscid interaction procedure—integral boundary layer method and Jameson's multigrid alternating direction implicit schemes for potential flow—has been developed to compute viscous flows over airfoils by Melnik and Brook (1985). For the flows around airfoil cascades, several studies, which include potential flow calculations, boundary layer techniques, treatments of wake, and interaction procedure, have been presented (Olling and Dulikravich, 1987; Citavý, 1987; Hansen et al., 1980). Even though many viscous-inviscid interactive techniques have been used, it is worthwhile to study this problem by a different approach. In this work, the potential flows are calculated by the finite element method and the finite difference scheme is applied to the boundary layer equation.

For the potential flow, the analytical and numerical approaches, which include conformal transformation (Gostelow, 1965; Halsey, 1979), singularity method (Martensen, 1971), streamline curvature method (Bindon and Carmichael, 1971), finite difference (Dodge, 1976; Ives and Liutermoza, 1979; Caspar, 1983; Jameson, 1974) and finite element methods (Pelz and Jameson, 1985; Laskaris, 1978; Baskharone and Hamed, 1981; Ecer and Akay, 1981; Deconinck and Hirsch, 1981), have been used to investigate the physical flow phenomena of airfoils and cascades of blades. In this paper, the concepts of Baskharone and Hamed (1981) are combined with those of Ecer and Akay (1981). Even though Baskharone and Hamed (1981) mentioned that the unique solution without any externally imposed constraints can be obtained by simply including the circulation as a nodeless degree of freedom in the finite element formulation, the authors used a Kutta condition as an external constraint. The finite element equations, which contain velocity potential and circulation, are solved by Gaussian elimination. In order to reduce the bandwidth of matrix, an automatic mesh generation technique (Segerlind, 1976), renumbering idea (Collins, 1973), and special treatment of the periodic boundary condition are introduced.

The boundary layer can be calculated in the direct or inverse method (Cebeci and Bradshaw, 1984; Carter and Wornom, 1975). From the discussions (Cebeci et al., 1986), the box method (Keller and Cebeci, 1972) is introduced in the present study. For attached flow, the boundary layer equations are solved by the direct method and the velocity on the matching surface between the viscous and inviscid parts of flow field is specified. When the flow begins to separate, the inverse ap-

Contributed by the International Gas Turbine Institute and presented at the 33rd International Gas Turbine and Aeroengine Congress and Exhibition, Amsterdam, The Netherlands, June 5–9, 1988. Manuscript received by the International Gas Turbine Institute September 15, 1987. Paper No. 88-GT-160.

proach is required and the displacement thickness needs to be prescribed. For the viscous-inviscid interaction, several approaches have been proposed by Carter (1979), LeBalleur (1981), Veldman (1981), and Kwon and Pletcher (1979). To minimize the amount of changes to the inviscid code, the wall transpiration coupling concept, semi-inverse method, and the idea of Carter (1979) to update the displacement thickness are employed in this work.

Potential Flow

Finite Element Equations. For the potential theory, the governing equations are simplified and the dimensionless forms are expressed as follows:

For the two-dimensional, steady, incompressible flow

$$\frac{\partial^2\phi}{\partial x^2}+\frac{\partial^2\phi}{\partial y^2}=0 \tag{1}$$

For the two-dimensional, steady, compressible flow

$$\frac{\partial\left(\rho\dfrac{\partial\phi}{\partial x}\right)}{\partial x}+\frac{\partial\left(\rho\dfrac{\partial\phi}{\partial y}\right)}{\partial y}=0 \tag{2}$$

and

$$\frac{1}{2}V^2+\frac{1}{\gamma-1}a^2=k$$

or

$$\left(\frac{V}{V_\infty}\right)^2+\frac{2}{r-1}\frac{a^2}{V_\infty^2}=\frac{k}{\frac{1}{2}V_\infty^2}=1+\frac{2}{\gamma-1}\frac{1}{\mathrm{M}_\infty^2} \tag{3}$$

In the above equations, x, y, ρ are dimensionless parameters divided by c (chord length) or ρ_∞ (density at upstream location).

By using the linear triangular element, Galerkin method, and pseudotime formulation (Ecer and Akay, 1981), the following finite element equations are obtained:

$$\frac{\Delta t}{\omega_1}K\dot{\Phi}+K\Phi=f \tag{4}$$

where

$$K=\sum_e\int_{\mathrm{Re}^n}\rho_e\{\nabla N\}\cdot\{\nabla N^T\}dA$$

$$f=\sum_e\int_{\partial\mathrm{Re}\cap\partial R}\{N\}\rho_e\nabla\phi\cdot\mathbf{n}dl$$

$$\Phi=\sum_e\phi_e \tag{5}$$

$$\dot{\Phi}=\sum_e\frac{\partial}{\partial t}\phi_e$$

$$\rho_e=\left(\frac{k-\frac{1}{2}V^2}{k-\frac{1}{2}V_\infty^2}\right)^{\frac{1}{\gamma-1}}$$

Finally, the time derivative term $\dot{\Phi}$ in equation (4) is approximated by the center difference at time $t=(n+1/2)\Delta t$. Equation (4) is rewritten as

$$K^{n+\frac{1}{2}}\bar{\Phi}^{n+1}=f^{n+\frac{1}{2}} \tag{6}$$

$$\Phi^{n+1}=\omega_1\bar{\Phi}^{n+1}+(1-\omega_1)\Phi^n \tag{7}$$

To simplify the calculation, $K^{n+1/2}$ and $f^{n+1/2}$ are replaced by K^n and f^n. For the incompressible flow, the time derivative term $\dot{\Phi}$ and ρ_e in the K and f terms are canceled. Without iterative process, the solution is obtained by the Gaussian elimination. Assuming the results of incompressible flow to be the initial guess, the solutions for compressible flow can be obtained from equations (6) and (7).

Boundary Treatments. The solution domains (or computational domains) shown in Figs. 1 and 2 are used to treat the single airfoil and cascade flow. In the present problems, sides 1, 2, 3, 5 in Figs. 1 and 2 are considered to be the outer boundaries, and sides 4, 6 in Figs. 1 and 2 belong to inner boundaries. For the outer boundaries excluding the periodical boundaries (sides 1 and 5 in Fig. 2), the velocity potential and normal gradient of the velocity potential are specified at side 2 and sides 1, 3, 5, respectively. The values of specified variables are dependent on the upstream and downstream conditions, for example, the angle of attack and configuration of blades. Because the flow is inviscid and there is no flow injection, the normal component of velocity on the surfaces of airfoil or

Nomenclature

A = area
a = sonic velocity
c = chord length of airfoil
C_f = friction coefficient
C_p = pressure coefficient $= \dfrac{(p-p_\infty)}{(\frac{1}{2}\rho_\infty V_\infty^2)}$
f = column matrix in equation (4)
H = total enthalpy
l = distance along the edge of element
M = Mach number
N = shape function
$\mathbf{n}$ = unit normal direction out of element
p = static pressure
R^n = area of computational domain
Re = Reynolds number
∂R = boundary of computational domain
t = time
u = x or tangential component of velocity
V = magnitude of velocity for the potential flow
V_n = normal component of transpiration velocity along the airfoil or blade
x, y = physical space coordinates
α = angle of attack
β = inlet or exit angle
Γ = circulation
γ = ratio of specific heat
δ^* = displacement thickness
ρ = density
σ = solidity = chord of blade divided by tangential spacing
τ = turbulent intensity
ϕ = velocity potential
ω_1, ω_2 = relaxation factor

Subscripts

in = inlet location
e = element or edge of boundary layer
ex = exit location
∞ = upstream or free-stream location

Superscript

i = iterative times

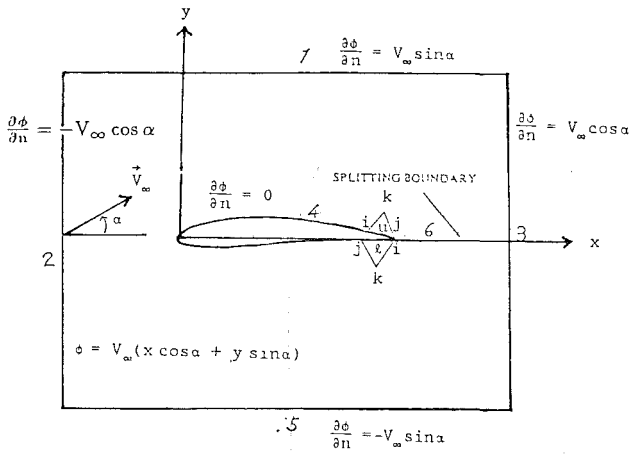

Fig. 1 Computational domain for airfoil flow

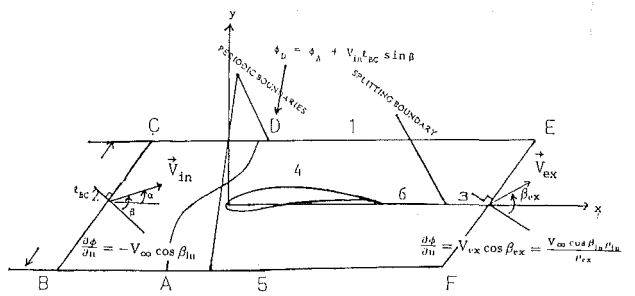

Fig. 2 Computational domain for cascade flow

blade is zero. For the splitting boundary (side 6 in Figs. 1 and 2), the treatment of Baskharone and Hamed (1981) is introduced and a nodeless variable Γ appears in the finite element formulation. In this work, the Kutta condition is required to be an external constraint. Near the trailing edge, the flow speeds on the upper and lower surfaces of the airfoil are equal at equal distances from the trailing edge. For the cascade flow, the periodic boundary is similar to the splitting boundary, if the node numbers on the side 1 and side 5 (Fig. 2) are consistent with each other.

Boundary Layer Flow

In the present study, the steady, incompressible/subsonic compressible, attached/separated boundary layer flow are investigated. The surface of airfoil or blade is adiabatic and no mass transfer is considered. The boundary layer is divided into laminar, transition, and fully turbulent regions in the streamwise direction. For the compressible flow, the governing equations are the continuity equation, the linear momentum equation in the streamwise direction, and the total enthalpy equation. For incompressible flow, the energy equation is not considered. In order to avoid the numerical instability, the FLARE approximation is applied in the separated flow and the streamwise convective terms ($u\partial u/\partial x$ and $u\partial H/\partial x$) are neglected in the recirculation region.

Laminar Boundary Layer. Near the leading edge of the airfoil or blade, a laminar boundary layer is assumed. The box method is used to compute the attached flow in the direct approach. The inviscid velocity on the airfoil surface is provided from the potential flow code. If laminar separation occurs, the inverse approach is required and the prescribed displacement thickness is necessary. For the viscosity coefficient, the Sutherland formulation is employed.

Transition Region. The calculation of transitional boundary layer is an important and difficult problem. For the isolated airfoil flow, the transition location and intermittency factor, which account for the transitional region that exists between a laminar and turbulent flow, are predicted and calculated by the formula given in Cebeci et al. (1986). When the cascade flow is studied, the phenomenon of natural transition that occurs in an attached flow is simulated by Abu-Ghannam and Shaw (1980). With regard to the transition due to the laminar separation bubble, the transition location is predicted by the expression given in Roberts (1975). Even though the size of a laminar separation bubble can be calculated by the empirical relation Roberts (1975), there is no formula to provide the end of transition point. Abrupt transition (no transition region) is employed in this kind of problem.

Turbulent Boundary Layer. As in the numerical treatment of laminar boundary layer, the box method in the direct and inverse mode is applied to calculate the turbulent boundary layer at the end of transition. In this paper, the algebraic eddy-viscosity formulation of Cebeci and Smith (Cebeci and Bradshaw, 1984) is employed. According to the expression for wall boundary-layer flows, eddy viscosity is defined by two separate formulas (inner and outer layers).

Numerical Analysis. After the Falkner–Skan transformation and dimensionless variables are introduced, the boundary layer equations are formulated into simultaneous first-order differential equations. By using the box central difference scheme and Newton linearization, the block tridiagonal matrix equations can be solved by the Keller block elimination method. Because the boundary layer equations are parabolic, the initial condition with the given boundary conditions on the surface of airfoil and edge of boundary layer is required. To obtain this initial condition, the one-dimensional box method is used to solve the boundary layer equation, in which the x-direction derivatives are set to be zero. Besides the above discussions, the convergent criterion, grid distribution, and adjustment due to growth of boundary layer were described in detail by Cebeci and Bradshaw (1984).

Viscous-Inviscid Interaction

The purpose of viscous-inviscid interaction is to find a matched viscous and inviscid solution. Veldman (1981) discussed direct, inverse, and semi-inverse methods to accomplish this. In the present work, a semi-inverse method is introduced. The coupling boundary condition in the inviscid code on the airfoil or blade is a transpiration velocity V_n normal to the airfoil. The values of $\nabla\phi\cdot\mathbf{n}$ shown in equation (5) are replaced by those of V_n. The mathematical form of V_n is expressed as follows:

$$V_n = \frac{1}{\rho_e}\frac{d(\rho_e u_e \delta^*)}{dx} \tag{8}$$

The displacement thickness, which is the new boundary condition of boundary layer calculation, is obtained by the relaxation formula given by Carter (1979)

$$\delta^{*i+1} = \delta^{*i}\left[1+\omega_2\left(\frac{u_e}{V}-1\right)\right] \tag{9}$$

where u_e and V are obtained from the boundary layer and potential flow calculations, respectively. V represents the magnitude of velocity of the element, at which the surface node is located.

The solution procedure can be summarized as follows:

1 The potential equation with $V_n = 0$ on the airfoil surface is solved by the finite element method.

2 The boundary layer code is run in the direct approach with edge velocity provided from step 1 until separation is reached. The displacement thickness is calculated directly

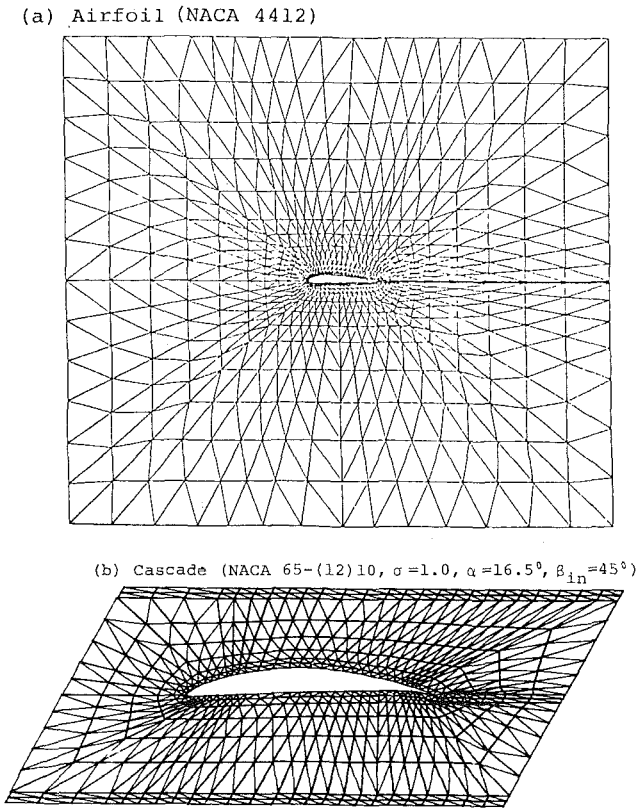

Fig. 3 Grid distribution for the airfoil and cascade flows

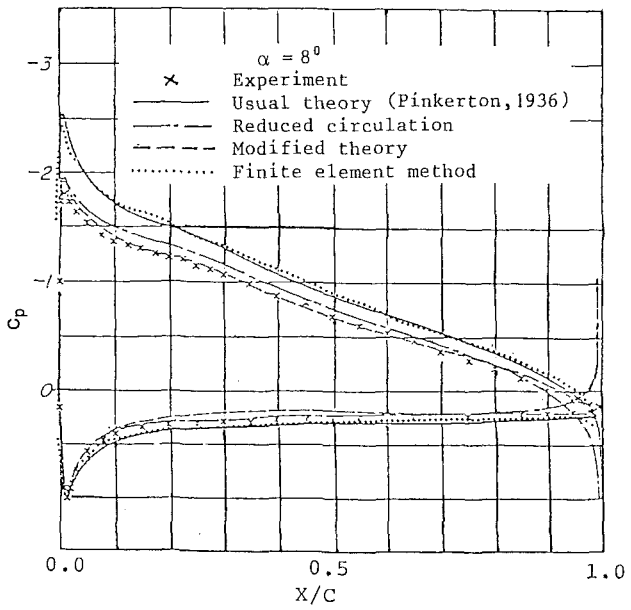

Fig. 4 Pressure distribution on the NACA 4412 airfoil

from the boundary layer code. After the separation point, the linear extrapolation is used to get the rest of initial guess of δ^*.

3 Step 1 is applied again and the boundary layer code is run in the direct mode before a specified point and in the inverse mode on the rest of the airfoil with δ^* determined from step 2. The specified point is described from step 2 and located before the separation point.

4 Carter's formula for updating the δ^* values is applied. The transpiration velocity V_n on the surface of the airfoil is computed.

5 According to the V_n values given by step 4, the potential code is run until the convergent solution is achieved.

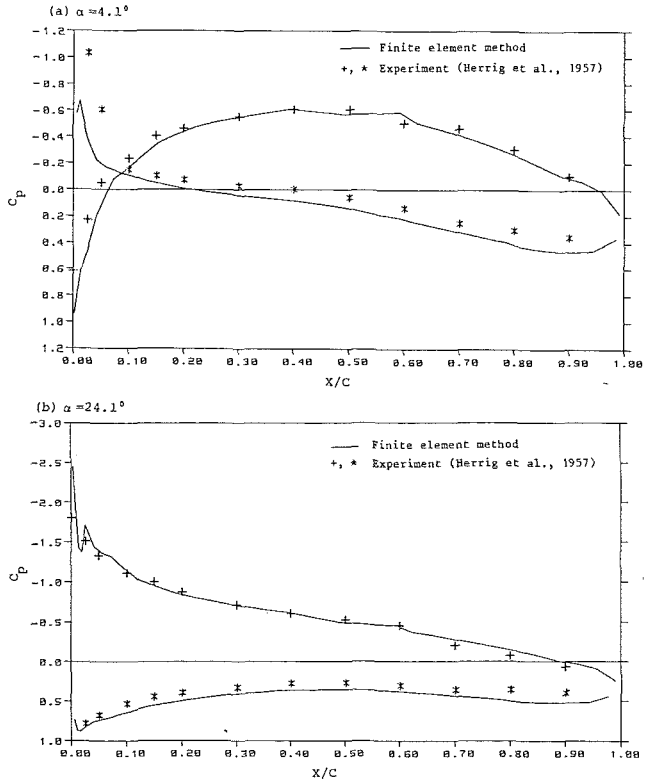

Fig. 5 Pressure distribution on the NACA 65-(12)10 blade cascade for different values of angle of attack ($\beta_{in} = 30$ deg, $\sigma = 1.0$)

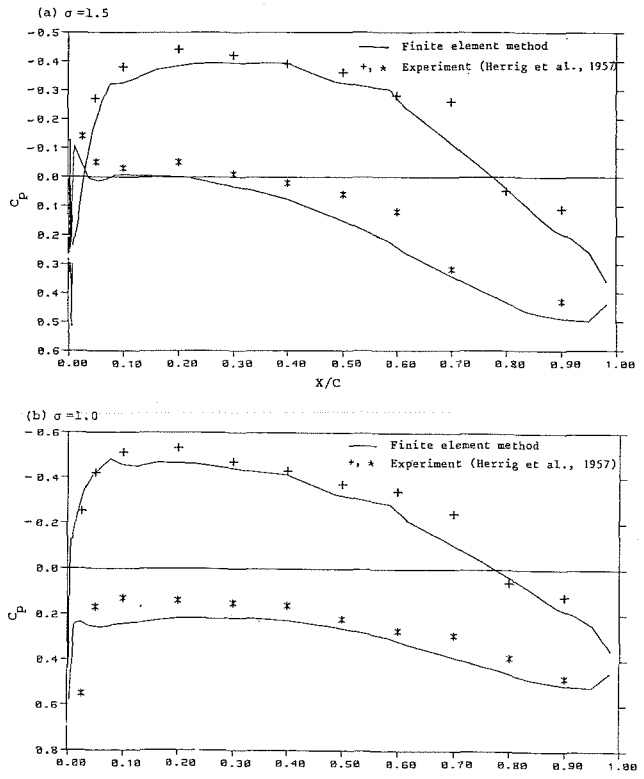

Fig. 6 Pressure distribution on the NACA 65-810 blade cascade for different values of solidity ($\beta_{in} = 45$ deg, $\alpha = 9.7$ deg)

6 The boundary layer code is run with the δ^* values determined from step 4.

7 Steps 4-6 are repeated until the convergence criterion ($|(\delta^{*i} = \delta^{*i-1})/\delta^{*i}| < \epsilon$, ϵ is a small value) achieved.

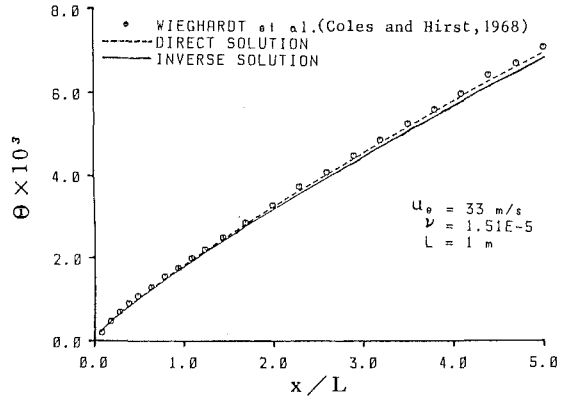

Fig. 7 Momentum thickness distributions on the flat plate ($Re = 2.19 \times 10^6$)

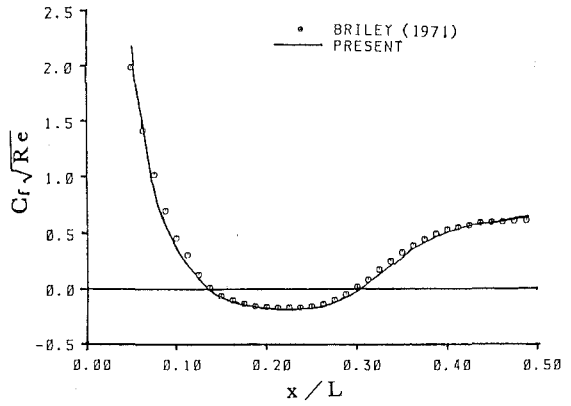

Fig. 8 Distribution of friction coefficient for the laminar flow with separation bubble ($Re = 2.08 \times 10^4$)

Results and Discussion

Under the procedure of mesh generation, two samples of grid distribution are shown in Fig. 3. The configuration of elements has been arranged carefully. The elements are small along the surface of the airfoil, and coincide with the corresponding relations on the splitting and periodic boundaries.

Solutions of Potential Flows Around Isolated Airfoil and Airfoil Cascades. In this section, flow around a NACA 4412 airfoil and NACA 65-(12)10, NACA 65-810 blade cascades are studied. For the incompressible flow, the finite element solutions are presented in Figs. 4–6. As shown in Fig. 4, the numerical result of the finite element method is almost the same as the theoretical solution. For the two values of angles of attack, the numerical results of flow passing through a NACA 65-(12)10 blade cascade are shown in Fig. 5. It is apparent that the finite element solutions agree well with the experimental data except for the regions near the leading edge. When the flows around the NACA 65-810 blade cascade with different solidities are considered, the resulting numerical solutions are shown in Fig. 6. Near the leading edge, the difference between finite element and experimental results is significant when the solidity is equal to 1.5. Even though the numerical solutions don't match very well with the experimental data, the trend of C_p is satisfied. From the above discussions, it is obvious that the finite element solutions have been proved to be valid for the incompressible potential flow. With regard to compressible flow, the numerical results are shown at the end of this section.

Solutions of Boundary Layer Flows. To evaluate the theory, solution procedure, and reliability of the boundary

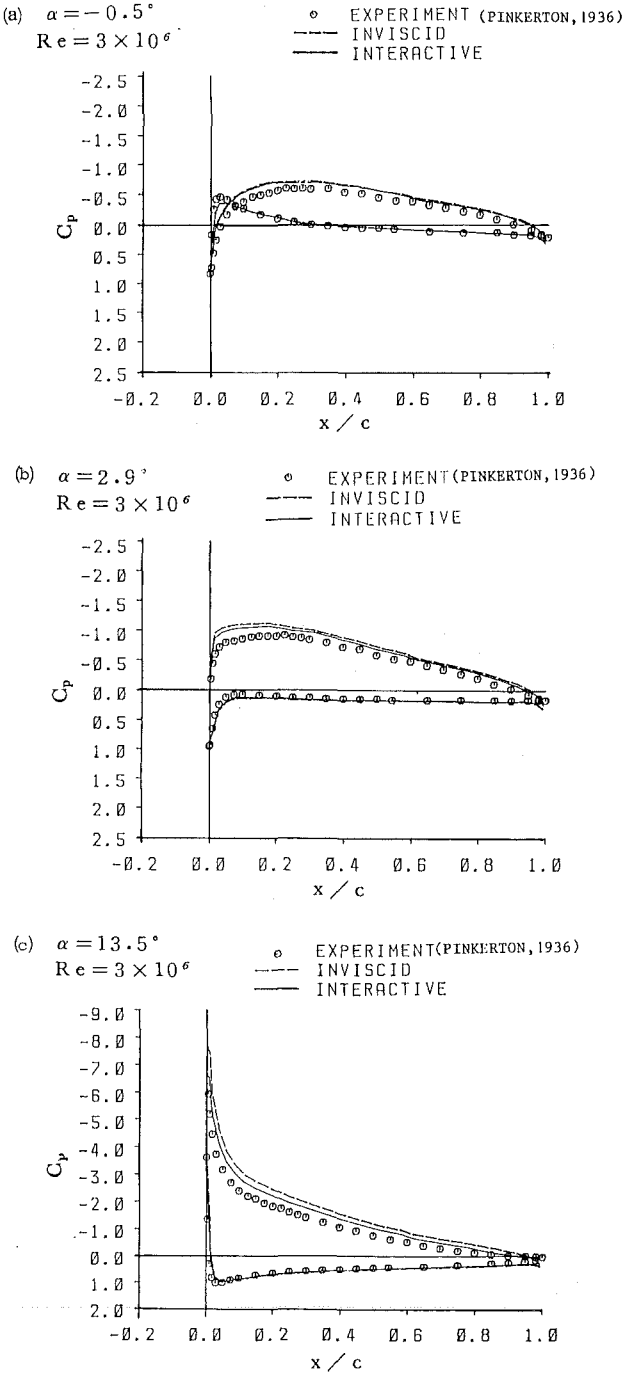

Fig. 9 Pressure distributions on the NACA 4412 airfoil

layer code, the turbulent flow over the flat plate is discussed first. This flow field problem, which is No. 1400 (Coles and Hirst, 1968), is solved by the direct and inverse methods. The calculation is advanced in direct mode from the leading edge, and the transition point is specified at $x = 0.001$ m. If the inverse method is applied, the same procedure is operated before $x = 0.087$ m. After that point, the inverse approach is introduced. The results given in Fig. 7 show that the numerical solutions are close to the experimental data. As mentioned by Carter and Wornom (1975), the deduced edge velocity deviated from unity by 5 percent when Δx was chosen to be 0.025 in the inverse calculation. Even though a different scheme is applied in the present work, the small difference in the direct and inverse solutions is expected due to the above reason. For the laminar flow with separation bubble, the Navier-Stokes equation has been solved by Briley (1971). In

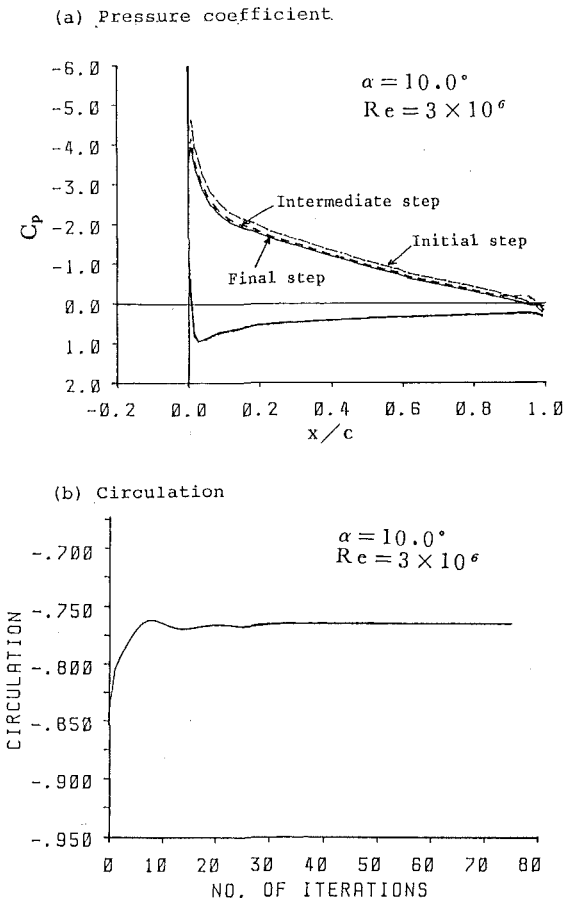

Fig. 10 Convergence histories of pressure coefficient and circulation for the NACA 4412 airfoil flow

this case, the displacement thickness (Briley, 1971) is chosen to be the boundary condition and the inverse method is applied after $x/L = 0.05$. The comparison with the Briley data, which are given in Fig. 8, is satisfactory. From the above results and discussions, it is confirmed that the box method with direct and inverse modes is suitable for the attached and separated incompressible flows. For each case, it takes about two minutes of CPU in VAX 8600. As for the compressible flow problems, the results are given in the following discussions.

Solutions of Airfoil and Cascade Flows by the Viscous-Inviscid Interaction. In this section, incompressible/compressible flows around a NACA 4412 airfoil and compressible flows passing through a NACA 65-(12)10 blade cascade are studied. For the incompressible flow, the pressure distributions on the airfoil for different angles of attack are presented in Fig. 9. Even though the improvement due to the viscous correction is small for the small angle of attack, the solution of viscous-inviscid interaction is significantly closer to experimental data when the angles of attack become large. The overshoot near the leading edge is suppressed also. As shown in Fig. 10, the convergence histories of pressure coefficient and circulation are investigated. Except near the trailing edge, where boundary layer separation is observed and inverse method with an initial guess of δ^* must be used, the convergence is fast. In order to understand the relation between circulation and angle of attack, the results of experiment, potential flow, and interaction are given in Fig. 11. It is apparent that the inclusion of the viscous effects has moved the prediction toward the experiment. To evaluate further the solution procedure, compressible flows around the NACA 4412 airfoil are studied. For the different values of Mach number, the pressure distributions with/without boundary

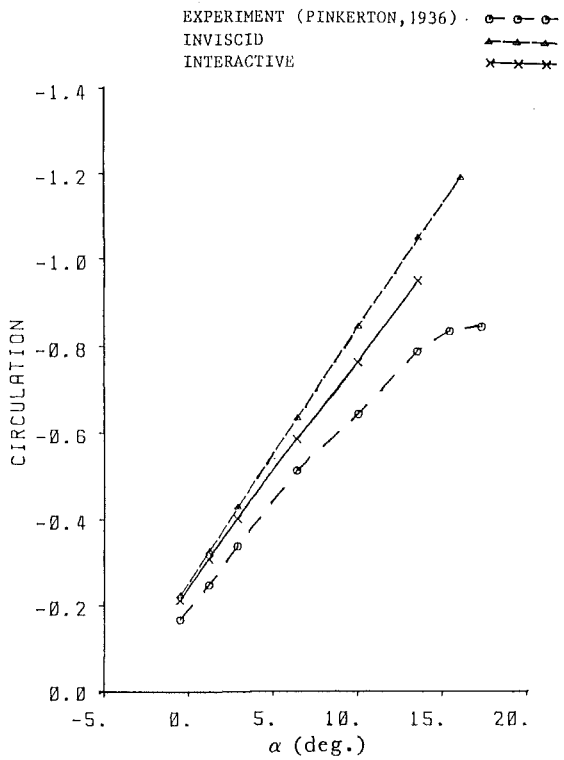

Fig. 11 Relation between circulation and angle of attack for the NACA 4412 airfoil flow

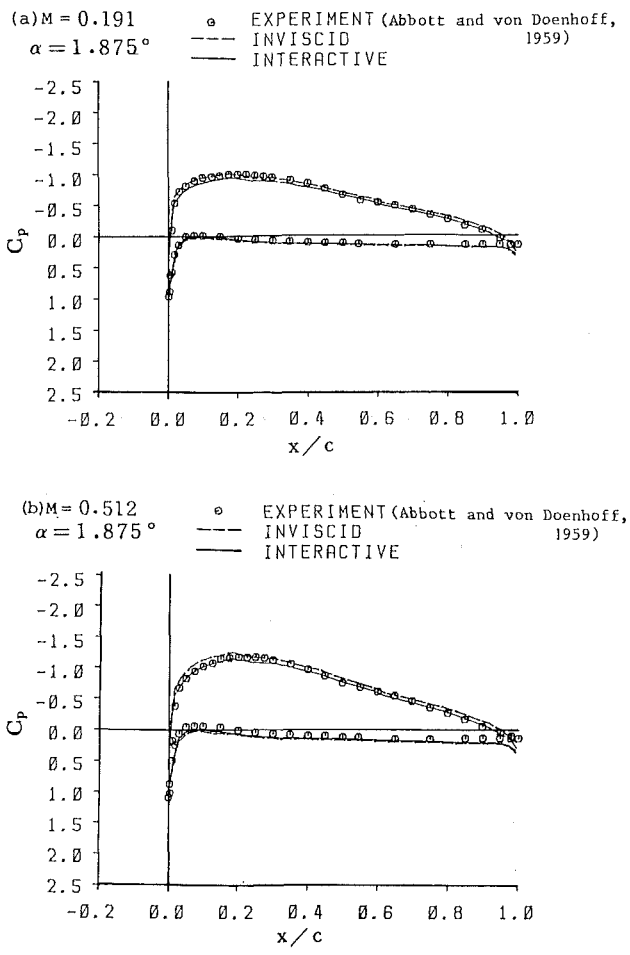

Fig. 12 Pressure distributions on the NACA 4412 airfoil

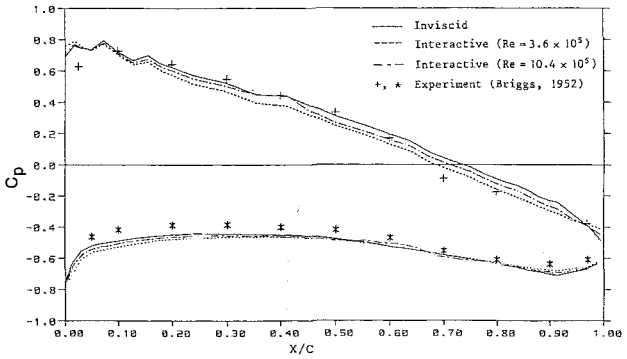

Fig. 13 Pressure distribution on the NACA 65-(12)10 blade cascade ($M = 0.42$, $\tau = 0.01$, $T_{in} = 288$ K)

layer effect are plotted in Fig. 12. The comparisons with the experimental data are satisfactory.

One important purpose of this work is to study the cascade flow by the viscous-inviscid interaction. The computational domain, which is shown in Fig. 3(*b*), contains 590 nodes (1084 triangular elements), and is used to calculate the flow passing through a NACA 65-(12)10 cascade of blades. The chord length is 0.076 mm, and the turbulent intensity is 1 percent. Because the experiment was conducted at a Reynolds number between 3.6×10^5 and 10.4×10^5 when the Mach number is equal to 0.42, the numerical results for two values of Re (3.6×10^5 and 10.4×10^5) are presented. Besides the above conditions, the inlet temperature T_{in} is chosen to be 288 K. Even though the numerical oscillations appear near the leading edge, the numerical values of C_p plotted in Fig. 13 show satisfactory comparisons with the experimental data. It should be pointed out that all computations were performed on a VAX 8600. When ϵ is chosen to be 0.01, about 41 and 94 minutes of CPU time are used for $\mathrm{Re}=10.4\times10^5$ and 3.6×10^5, respectively.

Conclusions and Recommendations

A viscous-inviscid interactive procedure has been developed to study the steady, two-dimensional, incompressible/subsonic compressible, attached and separated flows for isolated airfoils and airfoil cascades. The method is based on the finite element and finite difference approaches. For potential flow, the Galerkin method, pseudotime formulation, automatic mesh generation, and renumbering are introduced. The circulation is considered as the nodeless variable and the Kutta condition is introduced to be an external constraint. For the laminar/transition/turbulent boundary layer flow, the implicit finite difference method in the direct/inverse mode is employed. The algebraic eddy-viscosity formulaton of Cebeci and Smith is chosen to be the turbulent model. The location of transition and transitional region are decided by the empirical relations. To complete the computation, the semi-inverse method with wall transpiration model and relaxation formula proposed by Carter (1979) is used in this work.

On the basis of the results presented, it can be concluded that the present solution procedure is reliable. In this work, the numbers of iterations required for convergence of the interaction procedure are about 60 and 100 for the airfoil and cascade flows, respectively. As mentioned by Edwards and Carter (1985), the quasi-simultaneous method presented by Veldman (1981) could improve the convergence rate about three to four times over that of the present semi-inverse method. If the complete physical behavior of the airfoil and cascade flows are studied, the inclusion of the wake effect is required. The modeling of turbulent wake, interaction procedure, and dividing streamline will be emphasized in future work.

References

Abbott, I. H., and von Doenhoff, A. E., 1959, "Flow About Wing Sections at High Speed," in: *Theory of Wing Sections*, Dover, New York, pp. 261–268.

Abu-Ghannam, B. J., and Shaw, R., 1980, "Natural Transition of Boundary Layers—The Effects of Turbulence, Pressure Gradient, and Flow History," *Journal of Mechanical Engineering Science*, Vol. 22, No. 5, pp. 213–228.

Baskharone, E., and Hamed, A., 1981, "A New Approach in Cascade Flow Analysis Using the Finite Element Method," *AIAA Journal*, Vol. 19, No. 1, pp. 65–71.

Bindon, J. P., and Carmichael, A. D., 1971, "Streamline Curvature Analysis of Compressible and High Mach Number Cascade Flows," *Journal of Mechanical Engineering Science*, Vol. 13, No. 5, pp. 344–357.

Briggs, W. B., 1952, "Effect of Mach Number on the Flow and Application of Compressibility Corrections in a Two-Dimensional Subsonic-Transonic Compressor Cascade Having Varied Porous-Wall Suction at the Blade Tips," NACA TN 2649.

Briley, W. R., 1971, "A Numerical Study of Laminar Separation Bubbles Using the Navier-Stokes Equation," *Journal of Fluid Mechanics*, Vol. 47, pp. 713–736.

Carter, J. E., 1979, "A New Boundary-Layer Inviscid Interaction Technique for Separation Flow," AIAA paper 79-1450.

Carter, J. E., and Wornom, S. F., 1975, "Solutions for Incompressible Separated Boundary Layers Including Viscous-Inviscid Interaction," NASA SP-347, pp. 125–150.

Caspar, J. R., 1983, "Unconditionally Stable Calculation of Transonic Potential Flow Through Cascades Using an Adaptive Mesh for Shock Capture," ASME *Journal of Engineering for Power*, Vol. 105, pp. 504–513.

Cebeci, T., and Bradshaw, P., 1984, "Finite-Difference Solution of Boundary-Layer Equations," in: *Physical and Computation Aspects of Convective Heat Transfer*, Springer-Verlag, New York, pp. 385–428.

Cebeci, T., Clark, R. W., Chang, K. C., Halsey, N. D., and Lee, K. 1986, "Airfoils With Separation and the Resulting Wakes," *Journal of Fluid Mechanics*, Vol. 163, pp. 323–347.

Citavý, J., 1987, "Performance Prediction of Straight Compressor Cascades Having an Arbitrary Profile Shape," ASME JOURNAL OF TURBOMACHINERY, Vol. 109, pp. 114–122.

Coles, D. E., and Hirst, E. A., 1968, "Computation of Turbulent Boundary Layers," Vol. 2, AFOSR-IFP-Stanford Conference.

Collins, R. J., 1973, "Bandwidth Reduction by Automatic Renumbering," *International Journal for Numerical Methods in Engineering*, Vol. 6, pp. 345–356.

Deconinck, H., and Hirsch, Ch., 1981, "Finite Element Methods for Transonic Blade-to-Blade Calculation in Turbomachines," ASME *Journal of Engineering for Power*, Vol. 103, pp. 665–677.

Dodge, P. R., 1976, "A Non-orthogonal Numerical Method for Solving Transonic Cascade Flows," ASME Paper No. 76-GT-63.

Ecer, A., and Akay, H. U., 1981, "Investigation of Transonic Flow in a Cascade Using the Finite Element Method," *AIAA Journal*, Vol. 19, No. 9, pp. 1174–1182.

Edwards, D. E., and Carter, J. E., 1985, "A Quasi-Simultaneous Finite Difference Approach for Strongly Interacting Flow," *Third Symposium on Numerical and Physical Aspects of Aerodynamic Flows*, pp. 1.63–1.73.

Gostelow, J. P., 1965, "Potential Flow Through Cascades—A Comparison Between Exact and Approximate Solutions," Aeronautical Research Council, CP No. 807.

Halsey, N. D., 1979, "Potential Flow Analysis of Multielement Airfoils Using Conformal Mapping," *AIAA Journal*, Vol. 17, No. 12, pp. 1281–1288.

Hansen, E. C., Serovy, G. K., and Sockol, P. M., 1980, "Axial-Flow Compressor Turning Angle and Loss by Inviscid-Viscous Interaction Blade-to-Blade Computation," ASME *Journal of Engineering for Power*, Vol. 102, pp. 28–34.

Herrig, L. J., Emery, J. C., and Erwin, J. R., 1957, "Systematic Two-Dimensional Cascade Tests of NACA 65-Series Compressor Blades at Low Speeds," NACA TN 3916.

Ives, D. C., and Liutermoza, J. F., 1979, "Second-Order Accurate Calculation of Transonic Flow Over Turbomachinery Cascades," *AIAA Journal*, Vol. 17, No. 8, pp. 870–876.

Jameson, A., 1974, "Iterative Solution of Transonic Flows Over Airfoils and Wings, Including Flows at Mach I," *Commnunications on Pure and Applied Mathematics*, Vol. XXVII, pp. 283–309.

Keller, H. B., and Cebeci, T., 1972, "Accurate Numerical Methods for Boundary-Layer Flows. II: Two-Dimensional Turbulent Flow," *AIAA Journal*, Vol. 10, No. 9, pp. 1193–1199.

Kwon, O. K., and Pletcher, R. H., 1979, "Prediction of Incompressible Separated Boundary Layers Including Viscous-Inviscid Interaction," ASME *Journal of Fluids Engineering*, Vol. 101, pp. 466–472.

Laskaris, T. E., 1978, "Finite-Element Analysis of Three-Dimensional Potential Flow in Turbomachines," *AIAA Journal*, Vol. 16, No. 7, pp. 717–722.

LeBalleur, J. C., 1981, "Strong Matching Method for Computing Transonic Viscous Flows Including Wakes and Separations-Lifting Airfoils," *La Recherche Aerospatiale* (English edition), No. 1981-3, pp. 21–45.

Martensen, E., 1971, "The Calculation of Pressure Distribution on a Cascade

of Thick Airfoils by Means of Fredholm Integral Equations of the Second Kind," NASA TT F-702.

Melnik, R. E., and Brook, J. W., 1985, "The Computation of Viscid/Inviscid Interaction on Airfoils With Separated Flow," *Third Symposium on Numerical and Physical Aspects of Aerodynamic Flows*, pp. 1.21–1.37.

Olling, C. R., and Dulikravich, G. S., 1987, "Viscous-Inviscid Computations of Transonic Separated Flows Over Solid and Porous Cascades," ASME JOURNAL OF TURBOMACHINERY, Vol. 109, pp. 220–228.

Pelz, R. B., and Jameson, A., 1985, "Transonic Flow Calculations Using Triangular Finite Elements," *AIAA Journal*, Vol. 23, No. 4, pp. 569–576.

Pinkerton, R. M., 1936, "Calculated and Measured Pressure Distributions Over the Midspan Section of the NACA 4412 Airfoil," Report No. 563, NACA.

Roberts, W. B., 1975, "The Effect of Reynolds Number and Laminar Separation on Axial Cascade Performance," ASME *Journal of Engineering for Power*, Vol. 97, pp. 261–274.

Segerlind, L. J., 1976, "Computer Programs for Finite Element Instruction," in: *Applied Finite Element Analysis*, Wiley, New York, pp. 365–377.

Veldman, A. E. P., 1981, "New, Quasi-Simultaneous Method to Calculate Interacting Boundary Layers," *AIAA Journal*, Vol. 19, No. 1, pp. 79–85.

Automated Design of Controlled-Diffusion Blades

J. M. Sanz
NASA Lewis Research Center,
Cleveland, OH 44135

A numerical automation procedure has been developed to be used in conjunction with an inverse hodograph method for the design of controlled-diffusion blades. With this procedure a cascade of airfoils with a prescribed solidity, inlet Mach number, inlet air flow angle, and air flow turning can be produced automatically. The trailing edge thickness of the airfoil, an important quantity in inverse methods, is also prescribed. The automation procedure consists of a multidimensional Newton iteration in which the objective design conditions are achieved by acting on the hodograph input parameters of the underlying inverse code. The method, although more general in scope, is applied in this paper to the design of axial flow compressor blade sections, and a wide range of examples is presented.

Introduction

Three-dimensional flow analysis codes are increasingly playing a more important role in the design process of axial turbomachinery blading. These codes are generally used to analyze blade configurations that have been designed by two-dimensional methods. The fast computer generation of two-dimensional blade sections with prescribed aerodynamic characteristics still has a central role in the blade design process.

Inverse hodograph codes for the design of controlled-diffusion blades have proven to be an excellent source of innovative designs, both in the subsonic and the transonic regime (Bauer et al., 1977; Sanz, 1984). One advantage of these methods over direct design methods, aside from the generation of shock-free airfoils, is that the design philosophy can be incorporated into the design process from the start, by imposing a given surface speed distribution that reflects the desired aerodynamic behavior. Also, because the geometry is totally constructed by the method, it can produce body shapes that could hardly be predicted with direct methods (Sanz et al., 1985). In general, the use of inverse hodograph methods requires expertise on the part of the user; it hardly can be seen as a "black box" method.

Both direct and inverse methods require an iteration procedure to generate a blade section that meets the desired flow characteristics. In the direct design method a specified geometry is modified by interacting with a two-dimensional flow solver until the desired flow conditions are met. In the case of inverse hodograph methods, an airfoil with a prescribed speed distribution is obtained but an iteration process is still necessary to achieve the other geometric and flow requirements.

In this paper an automated procedure is presented that has been developed for use with the Inverse Hodograph Design Code (LINDES) described by Sanz (1978). In this code, three input hodograph design parameters and a prescribed surface pressure distribution control the flow characteristics at the design point. The solidity of the cascade, the inlet Mach number, and the inlet air flow angle are brought to their desired values by modifying the three hodograph design parameters in successive computer runs. The lift imposed by the input pressure distribution determines the air flow turning of the cascade.

The automation procedure described in this paper consists of a multidimensional Newton method in which the objective functions are the cascade solidity, the inlet Mach number, the inlet air flow angle, the air flow turning, and the trailing edge closure or gap conditions. An input speed distribution with three free parameters is used in the automation procedure. The Newton iteration will then use six independent variables to achieve six objective functions.

Base Inverse Hodograph Method

The base inverse design code used for the automation procedure has been described by Sanz (1983), and a users' manual was recently published (Sanz, 1987). The purpose of this section is to review only those aspects of the basic method and design process needed to introduce the input parameters that are to be controlled by the automation procedure. A complete description of the base method is given in the above references and references therein.

The inverse hodograph method constructs an analytical solution for the potential flow equations. The equations for the potential and stream functions φ, ψ have the hodograph, canonical, complex characteristic form

$$\varphi_\xi = \tau_+ \psi_\xi$$
$$\varphi_\eta = \tau_- \psi_\eta \tag{1}$$

where

$$\tau_\pm = \pm i \frac{\sqrt{1-M^2}}{\rho}$$

The computational complex variables ξ and η are defined in a fixed, hodographlike domain by means of a solution-

Contributed by the International Gas Turbine Institute and presented at the 33rd International Gas Turbine and Aeroengine Congress and Exhibition, Amsterdam, The Netherlands, June 5–9, 1988. Manuscript received by the International Gas Turbine Institute September 30, 1987. Paper No. 88-GT-139.

dependent conformal transformation. The details of the method have been described by Bauer et al. (1977) and Sanz (1983).

The solution to the system given by equation (1) is expressed in the form

$$\varphi(\xi,\eta)=\mathrm{Re}\{\varphi_1(\xi,\eta)\log(\eta-\eta_1)+\varphi_2(\xi,\eta)\log(\eta-\eta_2)+\varphi_3(\xi,\eta)\}$$
$$\psi(\xi,\eta)=\mathrm{Re}\{(\psi_1(\xi,\eta)\log(\eta-\eta_1)+\psi_2(\xi,\eta)\log(\eta-\eta_2)+\psi_3(\xi,\eta)\} \quad (2)$$

The points η_1 and η_2 correspond to the location of the upstream and downstream singularities, respectively. They are located at the foci (Sanz, 1983) of a fixed ellipse whose boundary corresponds to the subsonic part of the airfoil. The eccentricity of this ellipse determines the distance between these two points, and is prescribed in the code by means of a parameter R, the radius of a circular ring, $1 < |z| < R$, topologically equivalent to the ellipse. By increasing or decreasing the parameter R, the solidity of the cascade σ decreases or increases. The actual value of the solidity is part of the solution, hence the necessity of successive computer runs to adjust to the desired value.

After the single valuedness of the stream function is imposed in equation (2) and the circulation over the airfoil is determined from the input speed distribution, two other arbitrary constants must be specified; this is done by means of two input parameters. These two parameters, M_0 and Θ, control the inlet Mach number M_1 and inlet air angle β_1 and have to be modified appropriately until the desired values of M_1 and β_1 are achieved.

It was stated by Sanz (1983) that the elliptic transformation introduced there has the property that each of the input parameters R, M_0, and Θ has a dominant effect over each of the output parameters σ, M_1, and β_1, respectively. It is this property of the elliptic mapping that is exploited in the Newton iteration process.

As part of the solution, the body shape is found by using the integral

$$x+iy=\int\frac{e^{i\theta}}{q}\,(d\varphi+i\,d\psi/\rho) \quad (3)$$

The residue of this integral, given by the vector

$$dx+i\,dy \quad (4)$$

is another output quantity of the design code, corresponding to the trailing edge opening. The automation procedure adjusts the normal and streamwise components of this vector until the desired trailing edge thickness dn_{te} is obtained, while the streamwise trailing edge gap ds_{te} is forced to vanish. This produces a sharp trailing edge cut normal to the local flow direction and a prescribed trailing edge thickness.

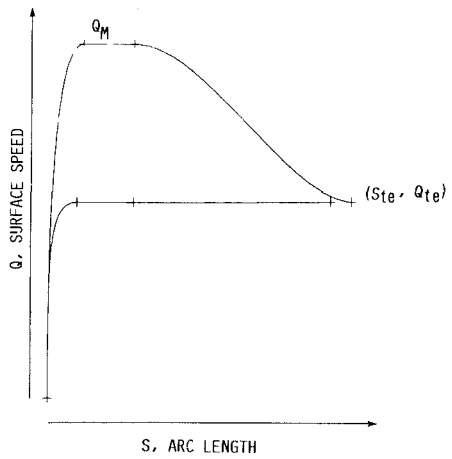

Fig. 1 Generic surface speed distribution

Input Speed Distribution

During manual operation of the design code the design goals σ, M_1, and β_1 are achieved by acting on the input parameters R, M_0, and Θ previously described. Next, the input pressure distribution is adjusted to obtain the necessary flow turning $\Delta\beta$ and the desired trailing edge gap condition (Sanz, 1983). The flow turning is adjusted by varying the lift and the trailing edge gap by modifying the trailing edge speed and the relative arc length of the blade suction and pressure sides.

In order to be effective, the automation procedure must be able to use a family of pressure distributions defined by as few parameters as possible, but with sufficient versatility to produce the desired geometry. In this work, the speed distribution is defined by piecewise polynomial curves with all its coefficients except three fixed beforehand. For each type of application, different polynomials can be chosen. In particular, Bezier polynomials have proven to be convenient for the present work.

Figure 1 represents a generic speed distribution appropriate for axial compressor blades. In this curve, the trailing edge speed Q_{te} and the arc length S_{te} of either the suction or pressure side are left as free parameters on which the automated procedure can act. A third free parameter Q_M is set as the difference between the peak speed on the suction and

Nomenclature

dn_{te} = trailing edge thickness
ds_{te} = streamwise trailing edge gap
M = local Mach number
M_0 = hodograph input parameter to control inlet Mach number
M_1 = inlet Mach number
Q_M = peak value of input speed distribution
Q_{te} = trailing edge speed
R = hodograph input parameter to control solidity
S_{te} = suction-to-pressure side arc length ratio
β_1 = inlet air angle
$\Delta\beta$ = air flow turning
Θ = hodograph input parameter to control inlet air angle
ξ, η = canonical complex characteristic hodograph variables
ρ = density
σ = cascade solidity
ϕ, ψ = potential and stream functions

Figure Nomenclature

BET1 = inlet air angle β_1
BET2 = exit air angle
DELB = air flow turning $\Delta\beta$
DNTE = inviscid trailing edge thickness dn_{te}
DSTE = inviscid streamwise trailing edge gap ds_{te}
LOSS = loss coefficient
M1 = inlet Mach number M_1
M2 = exit Mach number
SOL = solidity σ
TEV = trailing edge thickness after boundary layer subtraction
THCR = maximum thickness to chord ratio

pressure sides; by controlling the area under the curve, it has a direct effect on the lift imposed by the speed distribution.

It is worthwhile to note here that other parameters could also be left free, thus increasing the number of independent variables in the Newton iteration. For instance, the slope of the speed distribution at the leading edge has a direct effect on the maximum thickness of the airfoil, and could, conceivably, be added as a new free parameter. But, as stated earlier, the six free design parameters previously described have the important property that each has a dominant effect on one of the design objectives with only a secondary effect on the others.

The new form of definition of the speed distribution, which is essential to the automation procedure, has the additional advantage of making the design process less sensitive to spurious fluctuations in the speed distribution than when it was defined by a cubic spline, as it was previously done on the basic code. Besides, this new mode of defining the speed distribution does not seem to impose any limitation over the possibilities of the underlying code. In fact, because of the capability of making local changes in the areas needed, it promises to enhance these possibilities.

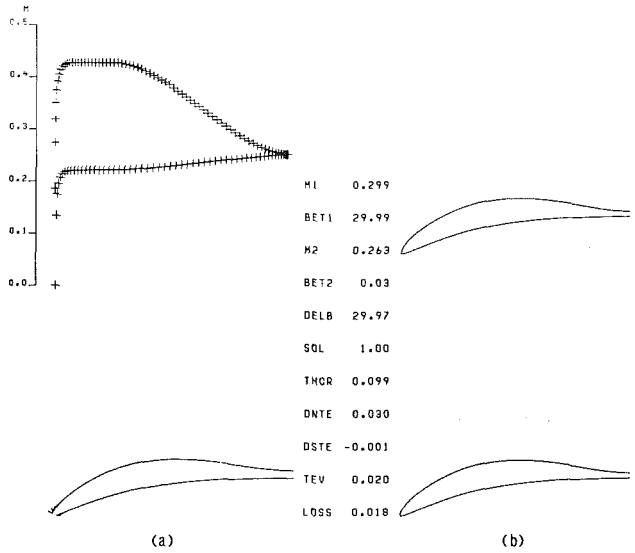

Fig. 2 Low-speed stator tip section

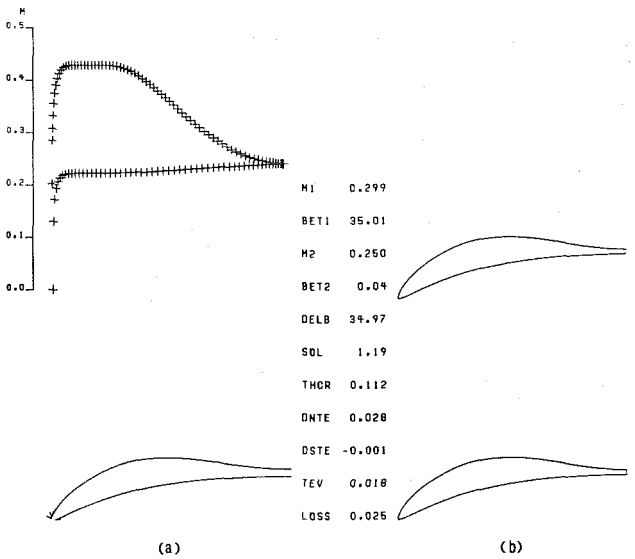

Fig. 3 Low-speed stator midtip section

Automation

Consider the solution to the flow equations, generated by each cycle of the inverse code, as a vector valued function

$$\bar{y} = \bar{F}(\bar{x}) \tag{5}$$

where

$$\bar{x} = (R, \mathrm{M}_0, \Theta, Q_{\mathrm{M}}, Q_{te}, S_{te}) \tag{6}$$

is the vector formed with $N = 6$ input parameters and

$$\bar{y}(\sigma, \mathrm{M}_1, \beta_1, \Delta\beta, dn_{te}, ds_{te}) \tag{7}$$

is the vector of output conditions. The objective function for the automation procedure is the vector

$$\bar{y}_0 = (\sigma, \mathrm{M}_1, \beta_1, \Delta\beta, dn_{te}, ds_{te})_0 \tag{8}$$

of specified output conditions.

A Newton iteration is established to solve the vector equation

$$\bar{F}(\bar{x}) - \bar{y}_0 = 0 \tag{9}$$

by means of the relation

$$\bar{x}_{n+1} = \bar{x}_n - \mathrm{J}^{-1}(\bar{x}_n)\,(\bar{y}_n - \bar{y}_0) \tag{10}$$

where J is the Jacobian matrix

$$\mathrm{J} = \left(\frac{\partial Fi}{\partial xj}\right) \tag{11}$$

The numerical evaluation of the Jacobian matrix J requires $N+1$ cycles, one to calculate the starting point and N more, in which all but one of the independent variables are frozen, to compute the partial derivatives in J. Once the Jacobian matrix has been evaluated, it can be inverted and the new input vector $\bar{x}_{n+1}$ is calculated. The process can then be repeated until a given tolerance

$$\mathrm{Tol} = \max |\,(\bar{y} - \bar{y}_0)_i\,|, \quad i = 1, N \tag{12}$$

is achieved.

Each iteration step consists of $N+1$ cycles and yields a second-order accurate method. We have found that faster convergence can be obtained by freezing the Jacobian J after the first $N+1$ cycles have been performed. Although, in this case, the method is then first-order accurate, only one cycle is required per iteration step. In either case, some relaxation is added for stability purposes.

The method converges well; about 40 cycles are enough to bring the tolerance, equation (12), below a value of 10^{-3}. In subsonic blade design the procedure is robust and, provided that a judicious choice is made, it will converge to the desired solution even from a relatively distant initial guess.

Examples

In this section, several examples are presented that have been developed to test the automation procedure. All the examples presented use the same input speed distribution shown in Fig. 1. As stated earlier, this speed distribution is defined with only three free parameters, Q_{te}, S_{te}, and Q_M, on which the automation can act. The automation will search within this three-parameter family until a speed distribution is found that achieves the objective function. In so doing, the speed distribution shape will change according to the changes imposed on the parameters Q_{te}, S_{te}, and Q_M by the automated procedure.

One important point that the examples show is that starting from the same initial guess of speed distribution a broad range of airfoils can be obtained. A flat top speed distribution has been chosen, which is representative of a design philosophy. Accelerated profiles, for instance, could equally have been chosen and would result in different blade shapes.

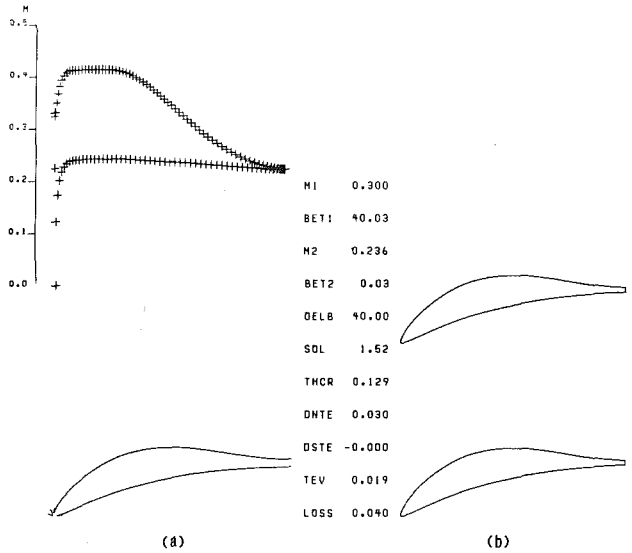

Fig. 4 Low-speed stator midhub section

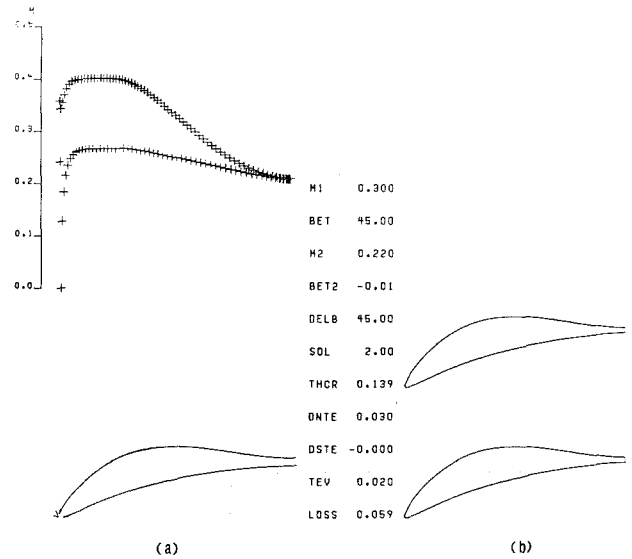

Fig. 5 Low-speed stator hub section

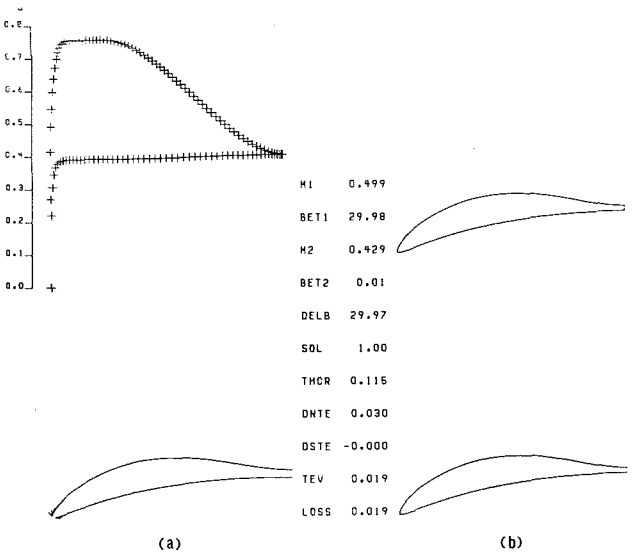

Fig. 6 Midspeed stator tip section

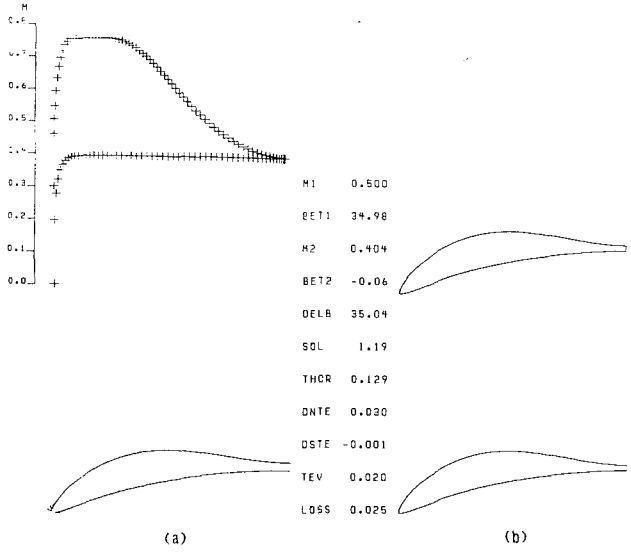

Fig. 7 Midspeed stator midtip section

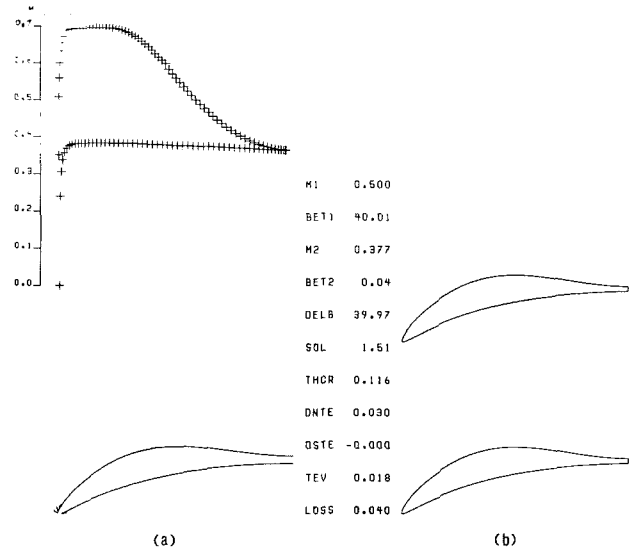

Fig. 8 Midspeed stator midhub section

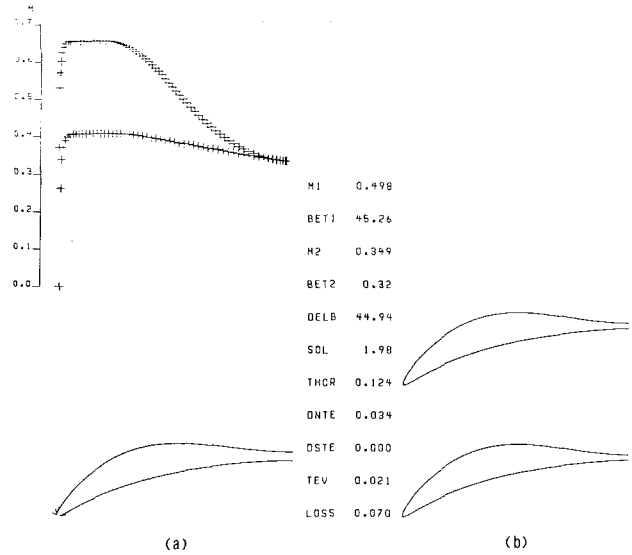

Fig. 9 Midspeed stator hub section

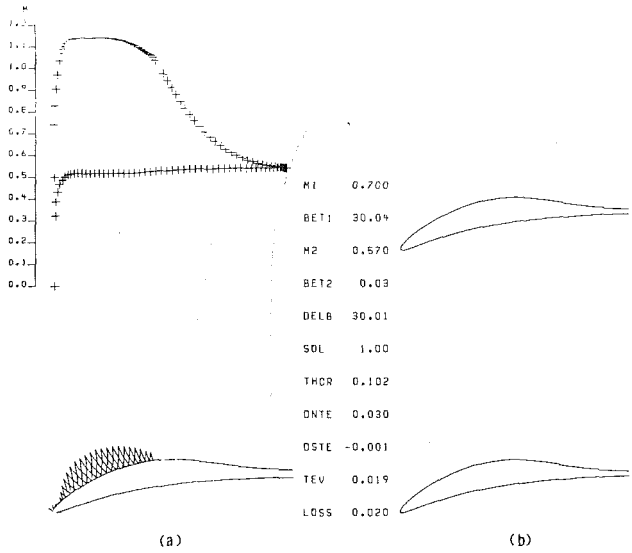

Fig. 10 Transonic stator section

As a first example, a stator blade for a low-speed fan is chosen. Four sections are designed, all with an inlet Mach number of 0.3 and inlet air angles of 45, 40, 35, and 30 deg from hub to tip. The four sections, radially equidistant, have solidities varying from 2 at the hub to 1 at the tip. In all sections, the flow is required to turn to the axial direction.

The same initial guess is used for all sections, and an inviscid trailing edge thickness of 3 percent is imposed in all of them. Figures 2(*a*) to 5(*a*) show the inviscid airfoil and output surface Mach number distribution at the design point. Figures 2(*b*) to 5(*b*) present the cascade plane with the body shape after the boundary layer has been subtracted.

The next example, Figs. 6 to 9, shows a higher speed blade, inlet Mach number of 0.5, and the same air inlet angles, flow turning, and solidities as the previous case. All the objectives were achieved, but the hub section presented an excessive amount of diffusion when a trailing edge thickness of 3 percent was specified. This section was then redesigned, imposing an inviscid trailing edge thickness of 3.5 percent.

Finally, a transonic, shock-free tip section is designed with the same flow conditions as the tip sections in the two previous cases, but with an inlet Mach number of 0.7 (see Fig. 10). Although the design is achieved, it required an initial guess closer to the design point. The parameter M_0 has to be chosen well under the value that produces the objective design, in order to obtain first a subsonic blade of approximately the same solidity inlet air angle, and flow turning. The shock-free design problem is intrinsically different from the subsonic design and special care has to be exercised to produce a relevant case. Although the method solves a mathematically well-posed problem, there is no guarantee that every given pressure distribution will produce a physically meaningful shock-free solution, hence the necessity of starting from a reasonable guess.

Conclusion

In this paper, the automated design of controlled diffusion blades is proven to be feasible. For this purpose, an automation procedure has been developed for the design of axial turbomachinery blading to be used in conjunction with an inverse hodograph design code. With this automated design method, the inlet Mach number, inlet air flow angle, air flow turning, solidity, and trailing edge thickness of a cascade of airfoils are prescribed.

Applications to axial compressor stator blade design are presented. Two subsonic blades, each composed of four sections, and one transonic blade section are presented. All cases are produced with a single input speed distribution, defined by three free parameters, on which the automation procedure acts to yield the different blade sections.

References

Bauer, F., Garabedian, P., and Korn, D., 19877, *Supercritical Wing Sections III*, Springer-Verlag, New York.

Sanz, J. M., 1983, "Design of Supercritical Cascades With High Solidity," *AIAA Journal*, Vol. 21, No. 9, pp. 1289–1293.

Sanz, J. M., 1984, "Improved Design of Subcritical and Supercritical Cascades Using Complex Characteristics and Boundary-Layer Correction," *AIAA Journal*, Vol. 22, No. 7, pp. 950–956.

Sanz, J. M., McFarland, E. R., Sanger, N. L., Gelder, T. F., and Cavicchi, R. H., 1985, "Design and Performance of a Fixed, Nonaccelerating Guide Vane Cascade That Operates Over an Inlet Flow Angle Range of 60 deg," ASME *Journal of Engineering for Gas Turbines and Power*, Vol. 107, No. 2, pp. 477–484.

Sanz, J. M., 1987, "Lewis Inverse Design Code (LINDES) – Users' Manual," NASA TP-2676.

A New Variational Finite Element Computation for the Aerodynamic Inverse Problem in Turbines With Long Blades

Qin Ren

Yi Fengming

Wang Hongguang

Harbin Institute of Technology,
Harbin, People's Republic of China

In this paper a new finite element computation for the aerodynamic inverse problem in turbines with long blades is proposed. The influences of blade thickness, blade force, and other factors on aerodynamic parameters may be taken into account. The computational results are compared with those of the finite difference method in noncurvilinear coordinates. They indicate that this method has an appropriate accuracy, good suitability to the complex boundaries, and good convergence. This new finite element computation is a good method for aerodynamic design in turbines with long blades. By use of this method the influence of the various design factors (curved and leaned blades, blade thickness, etc.) on the distributions of the aerodynamic parameters can be studied.

Introduction

It has been more than ten years since the finite element method was first applied to solve throughflow in turbomachines. Using the finite element method, the numerical computation of the meridional flow field in turbomachines was accomplished by Alder and Krimerman (1974). There, the variational principles, which are equivalent to the quasi-Poisson equations deduced from the momentum equations, were used. The exact variational principle for the compressible throughflow in turbomachines was obtained and the finite element computation was accomplished by Oates et al. (1976). Because the actuator disk theory was adopted, the aerodynamic parameters inside the blade channel could not be computed by this method. Hirsch and Warzee (1976) introduced the stream function into the momentum equations. The finite element equations were obtained by a weighted residuals method for every isoparametric element. By use of this method the single-stage and multistage compressors were computed. In the formulation, the assumption of axisymmetric flow was also made. In the present paper, the variational principle derived by Liu (1981) for the aerodynamic inverse problem on an S_2 surface in turbomachines was applied. When we take the first-order variation of the variational principle for the divided isoparametric elements and let it equal zero, the finite element equations will be obtained. The computations of the flow parameters inside the blade channel can be made by this method, and the influences of the blade thickness, blade force, and other factors on the distributions of flow parameters along the blade height may be also taken into account. The computational results of this method applied to an example were compared with those of the finite difference method. They show that this is a good method for aerodynamic design in turbines with long blades.

Basic Equations and Boundary Conditions

Introducing the stream function ψ into the radial component of the momentum equation, the following principal equation can be written:

$$\frac{\partial}{\partial r}\left(k\frac{\partial \psi}{\partial r}\right)+\frac{\partial}{\partial z}\left(k\frac{\partial \psi}{\partial z}\right)+f(r, z)=0 \tag{1}$$

where

$$k=\frac{1}{B\rho r}$$

$$f(r, z)=\frac{1}{W_z}\left(T\frac{\partial s}{\partial r}-\frac{\partial H}{\partial r}\right)+\frac{W_\phi \partial(V_u r)}{r\partial r W_z}+\frac{F_r+f_r}{W_z}$$

Subsequently, the tangential component of the momentum equation will be

$$W_r\frac{\partial}{\partial r}(V_u r)+W_z\frac{\partial}{\partial z}(V_u r)=(F_\phi+f_\phi)r \tag{2}$$

The energy equation will be:

For the rotor:

$$H=C_pT+\frac{W^2}{2}-\frac{\omega^2 r^2}{2}=C_pT_w^*-\frac{\omega^2 r^2}{2}=\text{const} \tag{3}$$

For the stator:

Contributed by the International Gas Turbine Institute and presented at the 33rd International Gas Turbine and Aeroengine Congress and Exhibition, Amsterdam, The Netherlands, June 5–9, 1988. Manuscript received by the International Gas Turbine Institute December 18, 1987. Paper No. 88-GT-275.

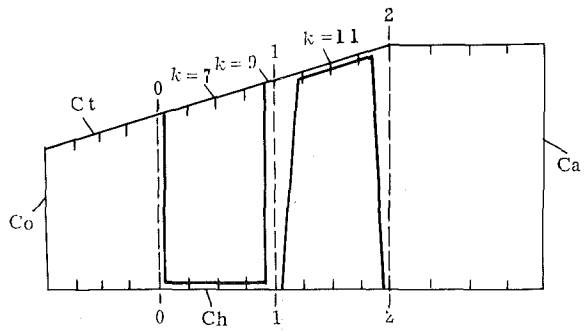

Fig. 1 The computational domain on the meridional plane

$$I = C_p T + \frac{v^2}{2} = C_p T^* \tag{3a}$$

The equation of state will be:

$$p = \rho R T \tag{4}$$

The condition of integrability of the streamsurface S_2 will be

$$\frac{\partial}{\partial r}\left(\frac{F_z}{F_\phi r}\right) = \frac{\partial}{\partial z}\left(\frac{F_r}{F_\phi r}\right) \tag{5}$$

From the streamsurface relation the equation can be written

$$F_r W_r + F_z W_z + F_\phi W_\phi = 0 \tag{6}$$

The distribution of $V_u r$ along the blade height will be

$$V_u r = \Gamma(r, z) \tag{7}$$

The relevant boundary conditions can be stated as (Fig.1):

1 Assuming that C_o, C_a at the inlet and outlet boundaries are orthogonal to the streamlines, the distribution of the stream function ψ can be given along the boundaries;

2 the distribution of the stream function ψ is given along the tip and hub boundaries;

3 all aerodynamic parameters are continuous at the boundaries between the rotor and the stator.

Variational Principle and Finite Element Equations

In accordance with Liu's VPS, the solution of the aerodynamic inverse problem on the S_2 streamsurface is equivalent to the extreme value of the variational principle

$$I_\psi = \iint_A \left\{\frac{k}{2}\left[\left(\frac{\partial \psi}{\partial r}\right)^2 + \left(\frac{\partial \psi}{\partial z}\right)^2\right] - f\psi\right\} dr dz \tag{8}$$

with the conditions

$$\psi_{ch,cz} = (\psi_{ch,cz})_{pr}$$

$$\psi_{co,ca} = (\psi_{co,ca})_{pr}$$

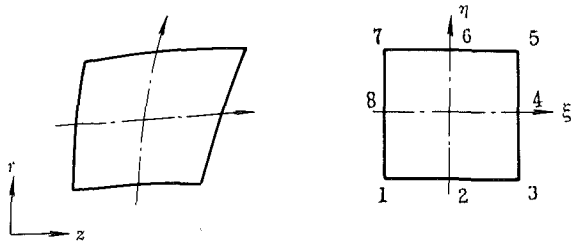

Fig. 2 Isoparametric element (eight nodes)

When we divide the computational domain into curvilinear quadrilaterals and use isoparametric elements with eight nodes (Fig. 2) for discrete functional analysis, the first-order variation of the variational principle can be obtained as

$$\delta I_\psi = \Sigma \iint_e \{k\psi^T (HH^T (HH^T + \overline{HH}^T) - f\bar{N}^T |J|\}\delta\psi d\xi d\eta \tag{9}$$

where

$\bar{N}$ = the shape function

$$|J| = \frac{\partial r}{\partial \xi}\frac{\partial z}{\partial \eta} - \frac{\partial z}{\partial \xi}\frac{\partial r}{\partial \eta}$$

$$H = \left(\frac{\partial z}{\partial \eta}\frac{\partial \bar{N}}{\partial \xi} - \frac{\partial z}{\partial \xi}\frac{\partial \bar{N}}{\partial \eta}\right)/|J|$$

$$\bar{H} = \left(\frac{\partial r}{\partial \xi}\frac{\partial \bar{N}}{\partial \eta} - \frac{\partial r}{\partial \eta}\frac{\partial \bar{N}}{\partial \xi}\right)/|J|$$

Let the transpose elementary coefficient matrix

$$M_e^T = \iint_e k(HH^T + \overline{HH}^T)/|J| d\xi d\eta \tag{10}$$

and the transpose right-hand vector

$$F_e^T = \iint_e f\bar{N}^T |J| d\xi d\eta$$

and

$$\delta I_\psi = 0$$

Then the global finite element equation

$$[M]\{\psi\} = \{F\}$$

is obtained, where

$$[M] = \Sigma M_e$$

$$\{F\} = \Sigma F_e$$

Thus the aerodynamic design of turbines with long blades belongs to the solution of equation (10).

Nomenclature

B = blockage factor of the blade
C_p = specific heat at constant pressure
f = viscous force
$\mathbf{F}$ = blade force
H = relative total enthalpy
I = total enthalpy
l = streamline
$\mathbf{n}$ = unit vector perpendicular to the streamsurface
r, ϕ, z = cylindrical coordinates fixed on rotor
$\bar{r}$ = $(r - r_h)/(r_t - r_h)$
R = gas constant
s = entropy
p = static pressure
T = static temperature
V = absolute velocity
w = relative velocity
α = flow angle in absolute flow
β = flow angle in relative flow
γ = ratio of specific heats
ξ, η = local coordinates of the elements
ρ = density
ψ = stream function
ω = angular speed of the rotor

Subscripts and Superscripts

e = pertaining to element
h = hub
pr = prescribed
r, ϕ, z = pertaining to r, ϕ, and z directions
t = tip
$*$ = total parameter

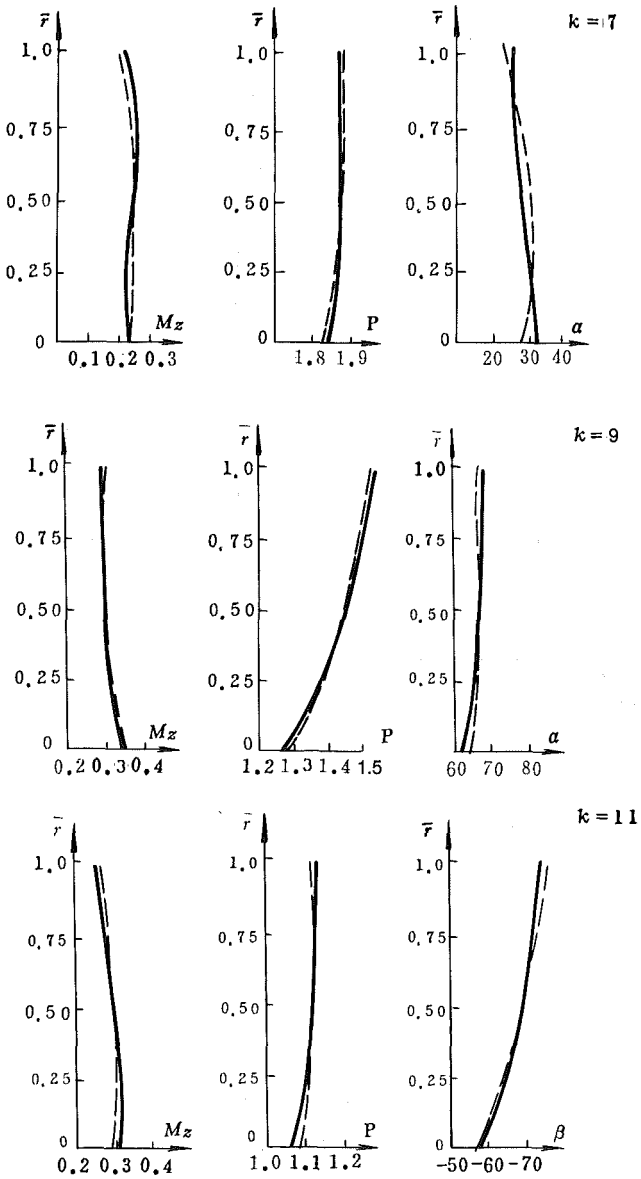

Fig. 3 Comparison of the results with those obtained by FDM: —FEM; - - -FDM

In general, the blade force can be calculated by using the condition of integrability. But, it is inconvenient. In this paper the following steps were adopted.

As **F** is parallel to **n**, from equation (6)

$$\frac{F_r}{F_\phi}=\frac{n_r}{n_\phi}=-r\frac{\partial\phi}{\partial r}$$

can be written.

Neglecting the viscous force term f_ϕ in equation (2) we have

$$F_\phi=\left[W_z\frac{\partial(V_u r)}{\partial z}+W_r\frac{\partial(V_u r)}{\partial r}\right]/r$$

Hence

$$F_r=-\left[W_z\frac{\partial(V_u r)}{\partial z}+W_r\frac{\partial(V_u r)}{\partial r}\right]\Big/\frac{\partial\phi}{\partial r} \tag{11}$$

Since

$$\frac{rd\phi}{dl}=\frac{W_\phi}{W_l}$$

we take the integral along l; the following equation

$$\phi_{i+1}=\phi_i+\frac{1}{2}\left(\frac{W_\phi}{rW_l}\Big|_{i=1}+\frac{W_\phi}{rW_l}\Big|_i\right)\Delta l \tag{12}$$

can be obtained. If the values ϕ on the generatrix of the streamsurface are given, then the distribution of ϕ will be computed by use of equation (12). By way of numerical differentiation the $\partial\phi/\partial r$ can be first found out and then the blade force F_r will be obtained.

Computation of Thermodynamic Parameters

When the distribution of ψ and the thermodynamic state at the inlet are known, some thermodynamic parameters can be found as follows:

1 The total temperatures and relative total temperatures can be computed by application of the energy equations.

2 The distribution of entropy can be computed in accordance with the Aeiley loss correlations.

3 The density distribution can be computed by successive iterations according to

$$\frac{\rho}{\rho^*}=\left\{1-\frac{\gamma-1}{2}\left(\frac{1}{B\rho r}\right)^2\left[\left(\frac{\partial\psi}{\partial r}\right)^2+\left(\frac{\partial\psi}{\partial z}\right)^2\right]-\frac{\gamma-1}{2}\frac{(V_u r)^2}{r^2}\right\}^{\frac{1}{\gamma-1}} \tag{13}$$

Example and Computation Results

Following the above method, a computer program was written. An aerodynamic design for a turbine stage was made. For that stage there have been some results computed by the finite difference method (Wang, 1983; Zhu, 1985). The meridional plane of the stage is shown in Fig. 1. The hub and tip radius at sections 0-0, 1-1, and 2-2 are given, respectively, as

$$r_{oh}=305\text{ mm},\quad r_{1h}=305\text{ mm},\quad r_{2h}=305\text{ mm}$$

$$r_{ot}=400\text{ mm},\quad r_{1t}=424\text{ mm},\quad r_{2t}=451\text{ mm}$$

In front of the stage, the inlet region was extended to C_o. Behind the stage, the outlet region was extended to C_a. The whole computational domain was divided into eight parts in the axial direction and five parts in the radial direction. There are 40 elements and 147 nodes in total. The relaxation factors of 0.3 ~ 1.0 were taken in the iterative process. The number of iterations is 13 and an accuracy of 10^{-4} for ψ was determined.

In order to evaluate this method, the results were compared with those obtained by the finite difference method in noncurvilinear coordinates (Wang, 1983) (Fig. 3). The latter has been a widespread applied method in recent years in China. In Fig. 3, the comparison of axial Mach number M_z, static pressure p, and flow angle α (or β) of the two methods was made for stations of $k=7$, 9, 11. The figure shows that the results of both methods are in good agreement along the majority of the blade height. There are only small differences at the hub and tip regions. Therefore, the method of this paper may be considered as an efficient method for solving the aerodynamic inverse problem on S_2 streamsurface in turbines. It has an appropriate accuracy, good adoptibility to the complex boundaries of the computational domain, and good convergence. Obviously, this method can be generalized to the aerodynamic design of axial compressors without difficulty. It can be used as a means for studying the influence of some design factors on the distribution of flow parameters along the blade height. For demonstration of the above statement, by use of this computer program the distribution of the flow parameters along the blade height for various leaned blades was computed. The computational results are shown in Fig. 4. This figure shows

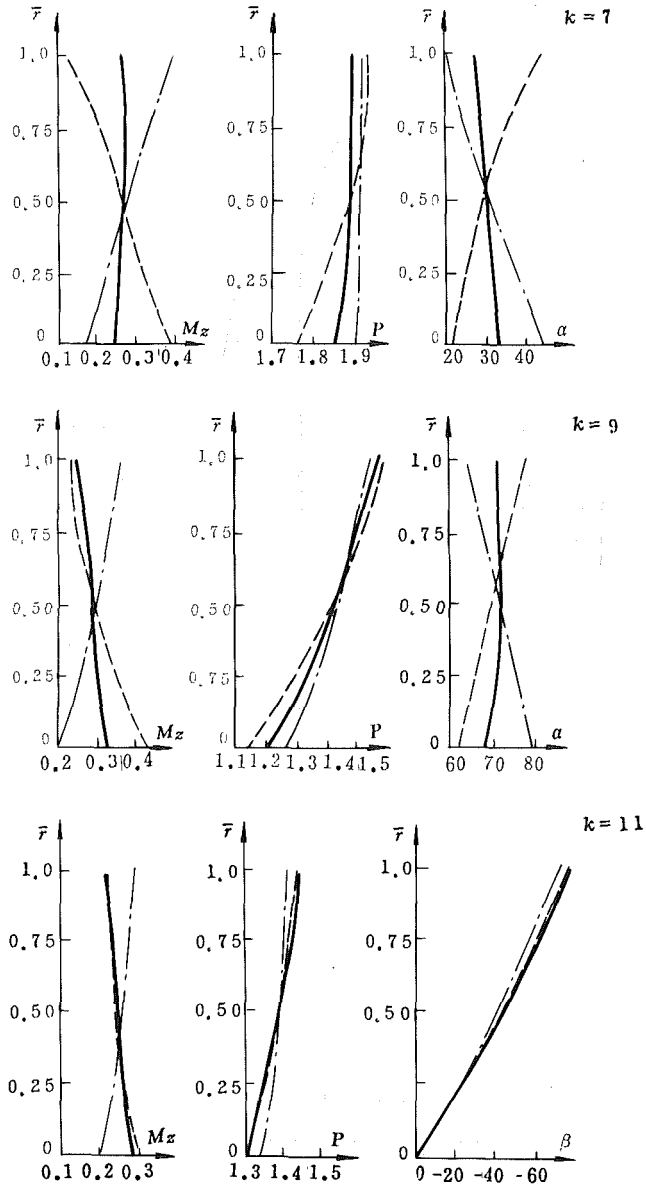

Fig. 4 Influence of the leaned blade on the flow parameters along the blade height: —$F_r = 0$; —•—forward-leaning blade; - - -backward leaning blade

that, if the blade differs from radial blade, the blade force F_r will not be zero. When the blade leans forward or backward the F_r and consequently the distribution of flow parameters will be different. It is obvious that by changing blade leaning, the blade force F_r and the static pressure p along the blade height can be altered. The better distribution of the static pressure p will minimize the radial hidden flow inside the boundary layer and consequently the secondary loss. It is conceivable that a similar computation can also be made for the curved blade. The computation of this paper verifies that the computer program is very effective for estimating the influence of various design factors on the distribution of the flow parameters along the blade height.

Conclusions

In the paper a new effective finite element method is presented for aerodynamic design in turbines with long blades. This method demonstrates appropriate accuracy, good adoptibility to the complex boundaries of the computational domain, and good convergence. The computer program referred to in the paper is comparatively compact and reasonable, and can be put into effect on a minicomputer. This method may be used to estimate the influence of some design factors, such as blade thickness and blade form, on the distribution of aerodynamic parameters along the blade height. It is equally effective and may be used with other numerical computational methods. The computer program can also be applied to the aerodynamic design of axial compressors with some modifications.

References

Adler, D., and Krimerman, Y., 1974, "The Numerical Calculation of the Meridional Flow Field in Turbomachines Using the Finite Element Method," *Israel J. of Technology*, Vol. 12.

Hirsch, Ch., and Warzee, G., 1976, "A Finite Element Method for Through Flow Calculations in Turbomachines," ASME *Journal of Fluids Engineering*, Vol. 98.

Lui, G. L., 1981, "Variational Principles (VPS) and Generalized VPS for the Inverse Problem on S_2 Relative Stream Surface in an Axial Turbomachine," *J. of Shanghai Institute of Mechanical Engineering*, No. 1.

Oates, G. C., Knight, C. J., and Carey, G. F., 1976, "A Variational Formulation of the Compressible Through Flow Problem," ASME *Journal of Engineering for Power*, Vol. 98, No. 1.

Wang, Z. Q., Li, G. L., and Xu, W. Y., 1983, "A Comparison of the Streamline Curvature Method With the Matrix Method Used for Turbomachinery Design in Non-orthogonal Curvilinear Coordinate System," International Gas Turbine Congress, Tokyo.

Zhu, X. J., 1985, "A Discussion About the Mean S_2 Stream Surfaces Applied to Calculation of Quasi-3-D Flow in Turbomachinery," Dissertation, Harbin Institute of Technology, Harbin, People's Republic of China.

Computation of Three-Dimensional Turbulent Turbomachinery Flows Using a Coupled Parabolic-Marching Method

K.R. Kirtley[1]

B. Lakshminarayana
Evan Pugh Professor of Aerospace Engineering. Fellow ASME

Applied Research Laboratory and Aerospace Engineering, The Pennsylvania State University, University Park, PA 16802

A new coupled parabolic-marching method was developed to compute the three-dimensional turbulent flow in a turbine endwall cascade, a compressor cascade wake, and an axial flow compressor rotor passage. The method solves the partially parabolized incompressible Navier–Stokes equation and continuity in a coupled fashion. The continuity equation was manipulated using pseudocompressibility theory to give a convergent algorithm for complex geometries. The computed endwall boundary layers and secondary flow compared well with the experimental data for the turbine cascade as did the wake profiles for the compressor cascade using a k–ϵ *turbulence model. Suction side boundary layers, pressure distributions, and exit stagnation pressure losses compared reasonably well with the data for the compressor rotor.*

Introduction

The viscous flow field in turbomachinery is highly complex. Endwall boundary layers give rise to a passage vortex, which overturns the flow near the endwalls. Blade boundary layers and wakes are characterized by their three dimensionality and highly complex turbulence structure. The flow field's complexity is further increased by the rotation and curvature of the geometry in question. The understanding of the viscous flow phenomena is important to the improvement of efficiency of the design, yet boundary layer and wake measurements on rotating blade rows, crucial to such understanding, are difficult to make. Thus, efficient numerical simulation of the flow field is required to augment the available experimental data base. Several techniques that are capable of computing such viscous flow phenomena were developed by Dawes (1987), Hah (1986), Moore and Moore (1981), Rhie (1983), Briley et al. (1985), and Kwak et al. (1986).

The need exists for the efficient solution of the incompressible Navier–Stokes equation for marine applications. Techniques such as Rhie's (1983) are capable of computing incompressible turbomachinery flows but require the use of correcting Poisson equations. Convergent solutions of such equations are subject to a compatability constraint when Neumann boundary conditions are used and this can be difficult to enforce numerically. In an effort to avoid these Poisson equations, Pouagare and Lakshminarayana (1986) developed a single-pass, space-marching method that solves the coupled form of the partially parabolized Navier–Stokes equation. Strong pressure interaction cannot be captured with this technique and multiple passes of the domain shows divergent behavior (see Kirtley, 1987). A new method developed by Kirtley (1987) solves the coupled form of the partially parabolized Navier–Stokes (PPNS) equation, is stable for multiple passes of the domain, and is capable of capturing pressure interaction effectively. For numerical stability during the global iteration procedure, the continuity equation is modified with the introduction of a pseudocompressibility term originally from Chorin (1967). This modified continuity equation is coupled to the momentum equations and solved using a spatial integration procedure. The major objective of this work is to apply this new method to complex turbomachinery flows.

Since most turbomachinery flows are turbulent, a turbulence closure scheme must be included in the formulation. Two models are used here, namely a modified form of the Baldwin and Lomax (1978) algebraic eddy viscosity model and the two-equation k–ϵ model outlined by Rodi (1982). The k–ϵ model is parabolized to match the partially parabolized mean flow equations. Although rotation and curvature of the geometry greatly influence the turbulence, no modifications to the standard models have been made to incorporate these effects.

Governing Equations and Numerical Technique

If a main flow direction (streamwise) can be identified, as is usually the case for turbomachinery flows, the streamwise viscous diffusion of momentum can be neglected from the full Navier–Stokes equation. This gives the partially parabolized Navier–Stokes equation or PPNS. Streamwise integration is a stable solution procedure if the streamwise pressure gradient is forward differenced. With such differencing, multiple passes

[1] Present address: Research Engineer, Sverdrup Technology, Middleburg Heights, OH 44130.

Contributed by the International Gas Turbine Institute and presented at the 33rd International Gas Turbine and Aeroengine Congress and Exhibition, Amsterdam, The Netherlands, June 5–9, 1988. Manuscript received by the International Gas Turbine Institute December 10, 1987. Paper No. 88-GT-80.

of the domain are required to propagate downstream pressure information upstream. This type of system is difficult to use for complex turbomachinery flows. The various methods that have proved to be successful in computing internal incompressible flows have relaxed some conditions in the equations during the iterative process. Rhie (1983) and Kwak et al. (1986) relax the continuity constraint by lagging the solution of continuity and introducing an extra term, respectively. Pouagare and Lakshminarayana (1986) relax the streamwise pressure gradient term and Moore and Moore (1981) relax the transverse pressure gradient terms. Relaxing the pressure gradients was found to give a system that is globally unstable for the PPNS, i.e., unstable for multiple passes of the domain (see Kirtley, 1987). Thus, the theory of pseudocompressibility was incorporated to relax the continuity constraint during the global iterative procedure. In time-marching methods, this is achieved by adding a fictitious time derivative of the pressure to the continuity equation.

Since a parabolic-marching algorithm is under consideration, the continuity equation is written as

$$a(p^n - p^{n-1}) + \nabla \cdot \mathbf{V} = 0 \tag{1}$$

where n is a global iteration index and a is a relaxation parameter analogous to $1/\beta\Delta t$ in Kwak et al.'s (1986) work. With this modification, the governing equation can be written in generalized coordinates as

$$L_\xi + L_\eta + L_\zeta - 1/(\mathrm{J\,Re})(L_{\eta\eta} + L_{\zeta\zeta}) = 1/(\mathrm{J\,Re})L_{\eta\zeta} + S/\mathrm{J} \tag{2}$$

where

$$L_\xi = (\xi_x\partial_\xi A' + \xi_y\partial_\xi B + \xi_z\partial_\xi C)/\mathrm{J}$$

$$L_\eta = (\eta_x\partial_\eta A + \eta_y\partial_\eta B + \eta_z\partial_\eta C)/\mathrm{J}$$

$$L_\zeta = (\zeta_x\partial_\zeta A + \zeta_y\partial_\zeta B + \zeta_z\partial_\zeta C)/\mathrm{J}$$

$$L_{\eta\eta} = \eta_x\partial_\eta\{(1+\nu_t)\eta_x\partial_\eta D\} + \eta_y\partial_\eta\{(1+\nu_t)\eta_y\partial_\eta D\} + \eta_z\partial_\eta\{(1+\nu_t)\eta_z\partial_\eta D\}$$

$$L_{\zeta\zeta} = \zeta_x\partial_\zeta\{(1+\nu_t)\zeta_x\partial_\zeta D\} + \zeta_y\partial_\zeta\{(1+\nu_t)\zeta_y\partial_\zeta D\} + \zeta_z\partial_\zeta\{(1+\nu_t)\zeta_z\partial_\zeta D\}$$

$$L_{\eta\zeta} = \eta_x\partial_\eta\{(1+\nu_t)\zeta_x\partial_\zeta D\} + \eta_y\partial_\eta\{(1+\nu_t)\zeta_y\partial_\zeta D\} + \eta_z\partial_\eta\{(1+\nu_t)\zeta_z\partial_\zeta D\} + \zeta_x\partial_\zeta\{(1+\nu_t)\eta_x\partial_\eta D\} + \zeta_y\partial_\zeta\{(1+\nu_t)\eta_y\partial_\eta D\} + \zeta_z\partial_\zeta\{(1+\nu_t)\eta_z\partial_\eta D\}$$

and J is the Jacobian of the transformation given by

$$\mathrm{J} = \xi_x(\eta_y\zeta_z - \eta_z\zeta_y) - \eta_x(\xi_y\zeta_z - \xi_z\zeta_y) + \zeta_x(\xi_y\eta_z - \xi_z\eta_y) \tag{3}$$

$$A' = \begin{pmatrix} ap+u \\ u^2+p \\ uv \\ uw \end{pmatrix} \quad A = \begin{pmatrix} u \\ u^2+p \\ uv \\ uw \end{pmatrix} \quad B = \begin{pmatrix} v \\ uv \\ v^2+p \\ vw \end{pmatrix}$$

$$C = \begin{pmatrix} w \\ uw \\ vw \\ w^2+p \end{pmatrix} \quad D = \begin{pmatrix} o \\ u \\ v \\ w \end{pmatrix}$$

$$S = \begin{pmatrix} \xi_x a(\partial_\xi p^n - p_i^n + p_i^{n-1}) \\ 0 \\ \Omega^2 y + 2\Omega w \\ \Omega^2 z - 2\Omega v \end{pmatrix}$$

ξ is the streamwise direction and the x axis is coincident with the machine axis. ν_t is the eddy viscosity determined from the algebraic model or the two-equation k–ϵ model. Terms on the left-hand side of equation (2) are treated implicitly while those on the right-hand side are explicit. The subscript i denotes the streamwise location at which the solution is desired and the superscript n indicates the global iteration level. Second-order accurate backward differencing is used for streamwise

Nomenclature

A, B, C, D, S = vectors in the governing equations
a = pressure relaxation coefficient
c = chord length
C_p = coefficient of pressure = $2(p-p_I)/\rho V_M^2$
h = blade half-span
J = Jacobian of the grid transformation
k = turbulence kinetic energy
n = normal direction
p = static pressure
p_o = stagnation pressure = $p + 1/2\rho V^2$
q = dependent vector = $(p, u, v, w)^T$
R = radius nondimensionalized by tip
Re = Reynolds number = cV_M/ν
S = streamwise distance nondimensionalized by c
s = cascade blading spacing
u, v, w = nondimensional velocity components
U_s = streamwise velocity component
U_n = transverse velocity component
U_t = blade tip speed
V = total velocity vector
x, y, z = Cartesian coordinates
γ = space-to-chord ratio = s/c
δ = boundary layer thickness
ϵ = turbulence dissipation
θ_{11} = streamwise momentum thickness = $\frac{1}{c}\int_0^\delta \frac{U_s}{U_e}\left(1-\frac{U_s}{U_e}\right)dn$
ν_t = nondimensional eddy viscosity
ξ, η, ζ = body-fitted coordinates
ϕ = flow coefficient = V_m/U_t
ψ_{loss} = pressure-loss coefficient = $2(p_{oI}-p_o)/(\rho U_t^2)$
Ω = nondimensional rotation rate = $\Omega c/V_m$

Subscripts

B = bulk
e = edge of shear layer
i, j, k = indices in ξ, η, ζ directions, respectively
m = mean inlet
ps = pressure side
ss = suction side
t = tip

Superscripts

m = iteration index at station i
n = global iteration level

derivatives, except for the streamwise pressure gradient, which is forward differenced. A three-point central difference scheme is used for all transverse derivatives. The equation is linearized by using truncated Taylor series. This discretization is essentially the Euler implicit scheme, which can be written as

$$(Q_\xi{}' + Q_\eta{}' + Q_\zeta{}')\Delta q = R \tag{4}$$

Q_ξ = convection tems in ξ

Q_η = convection plus diffusion terms in η

Q_ζ = convection plus diffusion terms in ζ

R = remaining terms at $i-1$ and $i-2$

$\Delta q = q_i - q_{i-1} = [\Delta p, \Delta u, \Delta v, \Delta w]^T$

If equation (4) is solved using the Linearized Block Implicit (LBI) splitting procedure outlined by Briley and McDonald (1980), the resulting splitting error significantly reduces the overall accuracy of the method. This error, unlike that for time-marching methods, is multiplied by the streamwise change in the dependent vector Δq, which does not tend to zero. This error then will infect the solution by accumulating with each marching step. The following iterative LBI scheme is used to reduce the effects of the splitting error in the computation. Rewritting equation (4) in iterative form gives

$$(Q_\xi{}' + Q_\eta{}' + Q_\zeta{}')\Delta s^m = R'$$

$$R' = R - (Q_\xi{}' + Q_\eta{}' + Q_\zeta{}')\Delta q^{m-1} \tag{5}$$

with

$$\Delta s^m = \Delta q^m - \Delta q^{m-1} \tag{6}$$

and R' being the solution to the PPNS within the formal accuracy of the discretization. m is the local iteration level. The operator on the left-hand side of equation (5) is split in the usual LBI fashion; thus equation (5) is solved as

$$(Q_\xi{}' + Q_\eta{}')\Delta s^* = R'$$

$$(Q_\xi{}' + Q_\zeta{}')\Delta s^m = Q_\xi \Delta s^*$$

This is repeated until R' reaches some very small value.

Convergence can be improved by including a relaxation parameter

$$\Delta q^m = \Delta q^{m-1} + \omega \Delta s^m \tag{6a}$$

Convergence to two orders of magnitude is generally achieved in five iterations with $\omega = 0.8$. Once convergence is achieved and the mean flow computed, the eddy viscosity is determined using one of the two models. With this, the procedure is advanced to the next streamwise station. Once the domain has been computed, the new pressure field is stored and used in the source vector S for a repeated pass of the domain. The global iterative procedure is terminated when the computed pressure no longer changes with iteration.

The global stability of this method is investigated in depth by Kirtley (1987). The coefficient a must be positive for stability as could be inferred from the analogy to the time-marching algorithm. The value of a is determined in an ad hoc fashion. Smaller values of a give stronger convergence; however, if a is too small, the method will not converge for complex flows. Thus a is increased until convergence is demonstrated. For laminar flows a can vary from 0 to 5. For turbulent flows a will range from 10 to 30. The method has been shown to converge to machine precision for the developing laminar flow in a duct. The method was also calibrated by computing the laminar flow in an S-shaped duct with excellent comparison with the experimental data. No artificial dissipation has been included except that introduced through the one-sided differencing of the streamwise convection terms. The method has been found to converse global mass at convergence within the accuracy of the quadrature used to find the mass flow.

Initial and Boundary Conditions

For all solid surfaces, either the no-slip condition or the turbulent-slip condition is applied to the velocities. The turbulent-slip condition is based on the log law of the wall. Following boundary layer theory, the pressure gradient normal to the surface is set to zero. A two-point difference scheme is used to improve the coupling of the odd and even points. In periodic regions, periodic boundary conditions are applied to all variables in an explicit manner. Periodic nodes are treated as interior points and averaging is used during the iterative LBI process in the cross plane. For annular geometries, periodicity of the Cartesian velocity components is only obtained through a rotation of the velocity vector by the pitch angle.

For the k–ϵ turbulence model, wall functions are used to give boundary conditions on ϵ and k on the first grid point from a solid surface. This condition is applied no closer than $y^+ = 20$. In periodic regions, periodic boundary conditions are applied to ϵ and k implicitly using a periodic matrix solver. For inlet conditions, the algebraic model is used to give the eddy viscosity. Then equilibrium is assumed and ϵ and k are determined from the simplified equations.

For initial conditions, the inviscid pressure as determined from the two-dimensional panel method code of Giesing (1964) is used. Due to the forward differencing of the streamwise pressure gradient, only the velocity field needs to be specified at the inlet. The inviscid flow corresponding to the pressure distribution is used at the inlet with endwall boundary layers imposed on it. At the exit, the measured pressure distribution is usually used as the downstream boundary condition. Since the inlet pressure is not specified, the total drop or rise in pressure across the blade row can be determined accurately.

The leading edge flow has proven to be difficult to compute using the PPNS system. Only first-order pressure effects can be captured since streamwise diffusion of momentum is neglected. Thus, the computation is started just downstream of the leading edge. Horseshoe vortex systems, therefore, cannot be computed. This is not a major drawback for blades with a small leading edge radius such as compressor blades. However, for blunt leading edge blades such as turbine blades, the PPNS system cannot be used for accurate flow computations. Still, the new method is useful in computing other secondary flows along with three-dimensional blade and endwall boundary layers and wakes. For all the computations in this paper, periodic H-grids, generated algebraically, are used.

Results and Discussion

Endwall Cascade Flow. The three-dimensional turbulent flow in a turbine endwall cascade was computed using the present method. The flow was measured using a hot-wire probe by Flot and Papailiou (1975). The cascade is made up of NACA 65-12-A_{10}-10 blades with a stagger angle of -15 deg. The span-to-chord ratio is 2.1, the pitch-to-chord ratio is 0.8, and the flow Reynolds number is 389,000. The geometry and measurement locations are given in Fig. 1. Only the blade region was computed and the computational grid consisted of 30 points in the streamwise direction and 23×23 grid in the cross plane. Both the algebraic eddy viscosity model and the k–ϵ turbulence model were used to compute this flow. There was very little difference in computational results between the two models, but the use of the k–ϵ model required more computation time. The following results were from the two-equation model. The no-slip boundary condition on the velocity was used on the blade surfaces as well as on the end wall boundary. A symmetry boundary condition was applied at the midspan. The inviscid velocity distribution with the measured endwall boundary layer was used as inlet condition at the blade leading edge to start the computation.

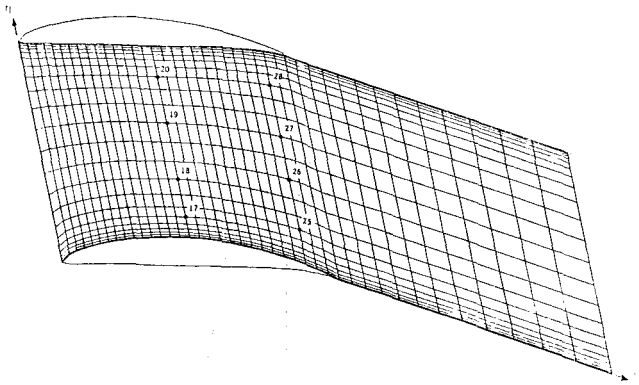

Fig. 1 Geometry, grid, and measurement locations for endwall cascade

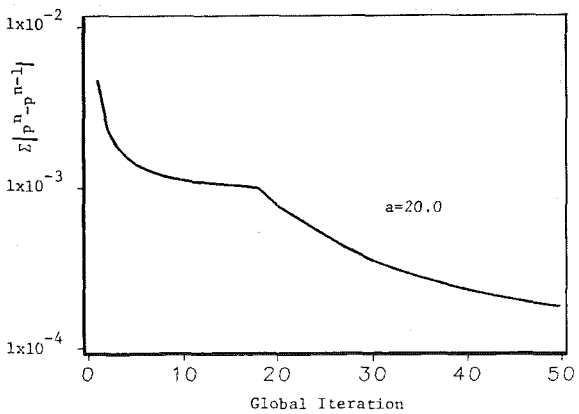

Fig. 2 Convergence history for the endwall cascade

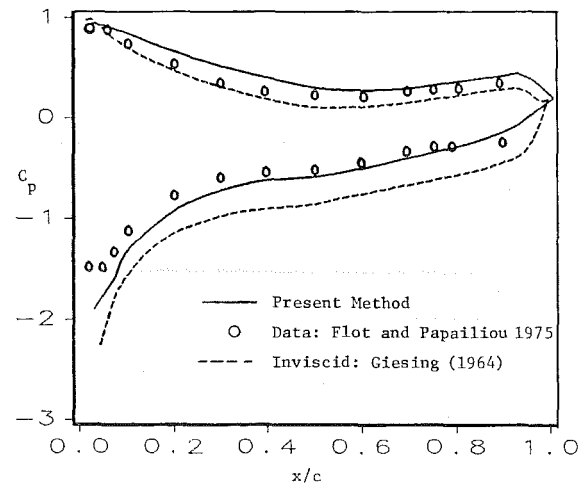

Fig. 3 Pressure distribution for the endwall cascade

The convergence history is presented in Fig. 2. For this case, a was set to 20 and the pressure residuals dropped one and one half orders of magnitude in 50 global iterations. After 80 iterations, the convergence flattened out and the computation was stopped in order to conserve CPU time. Recall that the method was shown to converge to machine precision for a simple flow. For engineering applications, demonstrating such convergence is costly and not generally necessary.

The computed pressure distribution at the midspan is compared to the experimental data in Fig. 3 with very good agreement. The inviscid pressure distribution computed from the panel code of Giesing (1964), used as the initial pressure distribution, is also presented in Fig. 3. The good agreement with the experimental data indicates that the present method is

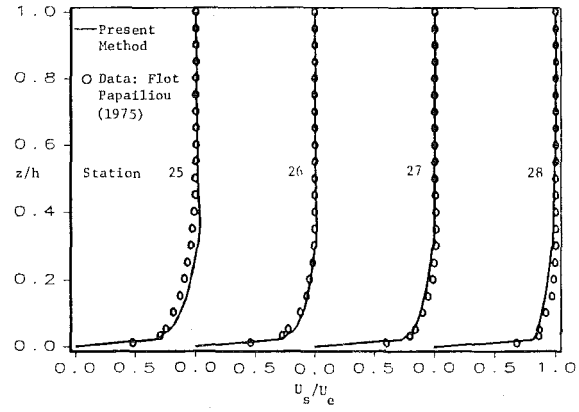

Fig. 4 Streamwise velocity profiles at 88 percent chord for the endwall cascade

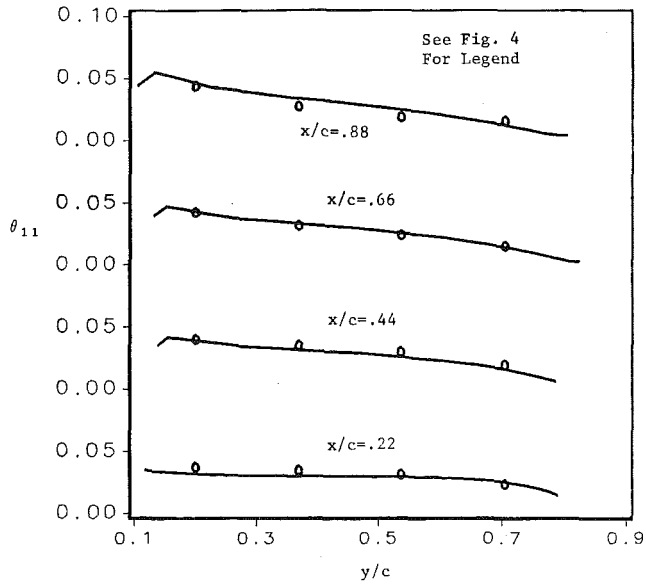

Fig. 5 Streamwise momentum thickness for the endwall cascade

capable of computing the viscous pressure field accurately, unlike the space-marching method used by Kirtley et al. (1986) for the same geometry.

The computed streamwise end wall velocity profiles at 88 percent chord are compared to the experimental data in Fig. 4. The agreement with the data is very good near the suction side and near midpitch. Near the pressure side, the results are not as good as near the suction side, and this may be due to a poor prediction of the pressure side blade boundary layers. Unfortunately, no blade boundary layers were measured to verify this. Figure 5 shows the computed streamwise momentum thickness compared to the experimental data. The blade-to-blade variation is well predicted, as is the magnitude of the momentum thickness. One can see that the secondary flow is convecting the low-momentum fluid to the suction side from the pressure side boundary layers thereby thinning them. The computed endwall secondary velocity profiles are compared to the experimental data at 88 percent chord in Fig. 6. At all locations, the overturning of the flow near the endwall is reasonably well predicted while the flow underturning in the outer reaches of the boundary layer is somewhat underpredicted. Since the streamwise profiles were well predicted, one can assert that the error is due to a poor prediction of the transverse pressure gradient near the endwall, which drives the secondary flow. Overall, however, the prediction of the secondary flow is good. This provides confidence in the

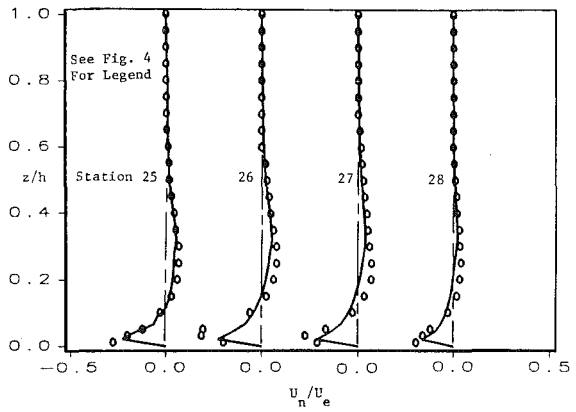

Fig. 6 Transverse velocity profiles at 88 percent chord for the endwall cascade

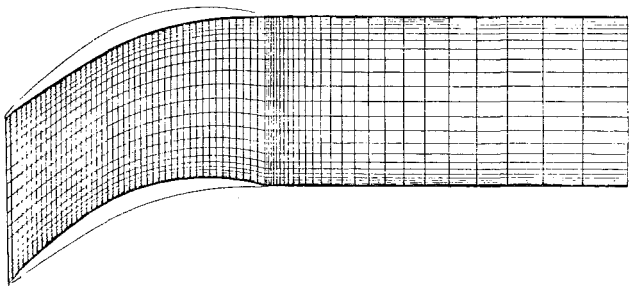

Fig. 7 Geometry and grid for Hobbs' cascade wake flow

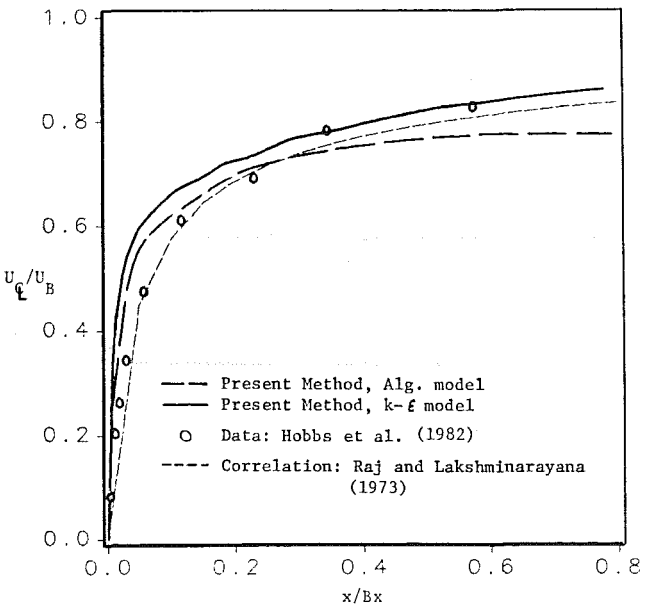

Fig. 8 Wake centerline velocity distribution for Hobbs' cascade

method's ability to compute pressure-driven secondary flow in cascades including the viscous effect near walls.

Compressor Cascade Wake Flow. The new parabolic-marching method was used to compute the turbulent wake of a compressor cascade. The flow field was measured by Hobbs et al. (1982) using a hot-film probe for the near wake and a five-hole probe for the far wake. The blades are double circular arc airfoils with a stagger angle of 20.77 deg. The space-to-chord ratio is 0.6 and the flow Reynolds number is 588,000. Although the experimental facility used endwall suction to ensure two dimensionality, the computation was carried out

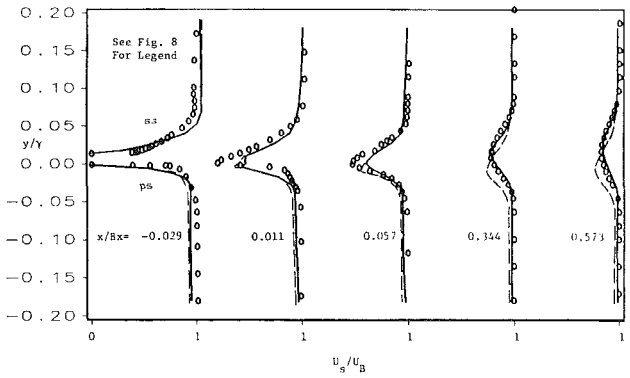

Fig. 9 Wake profiles for Hobbs' cascade

assuming an endwall was present and only results at the midspan were considered. The geometry and computational grid at the midspan are shown in Fig. 7. In order to save on CPU time and since the blade boundary layers are very thin, the inviscid inlet condition was applied near the midchord region where the boundary layers thickness of a typical turbulent boundary layer reached a height equal to the distance of the first grid point from the surface. The no-slip condition on the velocity was used on the blade surfaces.

The flow was computed with both the algebraic eddy viscosity model and the two-equation turbulence model. The wake centerline velocity computed with both turbulence models is compared to the experimental data in Fig. 8. X is the distance from the trailing edge and Bx is the axial chord length. Also displayed is the wake correlation of Raj and Lakshminarayana (1973). The agreement between the computation, experimental data, and correlation is good, however the computed wake defect is underpredicted in the near-wake region, while it is overpredicted in the far-wake region when the algebraic model is used. Using the k–ϵ model, the near wake behaves similarly but the far-wake decay is well predicted. The comparison of the computed wake profiles with the experimental data is given in Fig. 9. In the very near wake, the computed velocity profiles do not compare well with the experimental data near the wake centerline. In this region, the flow is very complex and difficult to compute. The nature of the turbulence is very complicated near the centerline of the wake and the algebraic turbulence model does not seem to have the necessary physics to resolve the strong interaction. Thus, the far wake is only adequately predicted. The wake centerline position is below the measured position and the wake spreading is less than measured. The wake spreading is a strong function of the turbulence and the empiricism based on bounded shear layers in the algebraic turbulence model may contribute to the poor prediction. The results using the two-equation k–ϵ model, which includes more physical considerations in its formulation, are much better.

The wake velocity profiles computed with the k–ϵ model show the same lack of agreement with the centerline data as with the computation with the algebraic model in the very near-wake region. In the far wake, the advantages of the k–ϵ model are clear with very good agreement between the computation and the measurements. The wake centerline position as well as the wake spreading is accurately predicted in the far-wake region. Overall, the prediction using the k–ϵ model is superior to the prediction using the algebraic model for all regions of the flow. The computed axial turbulence intensities are compared to the experimental data for the near wake region in Fig. 10. On the blade surface, the axial turbulence intensities compare very well with the data. This is not surprising since the established k–ϵ model has been "fine tuned" for wall bounded shear layers. In the near-wake region, the peak intensities are not well captured. This can be attributed to the over-

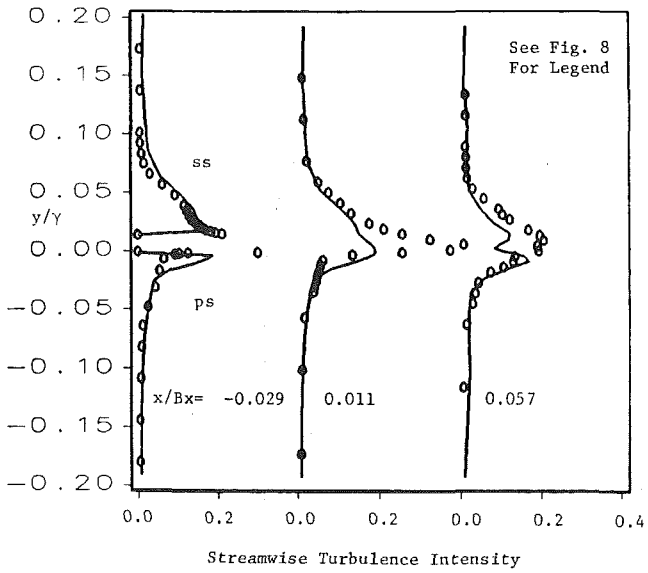

Fig. 10 Streamwise turbulence intensities in the wake of Hobbs' cascade

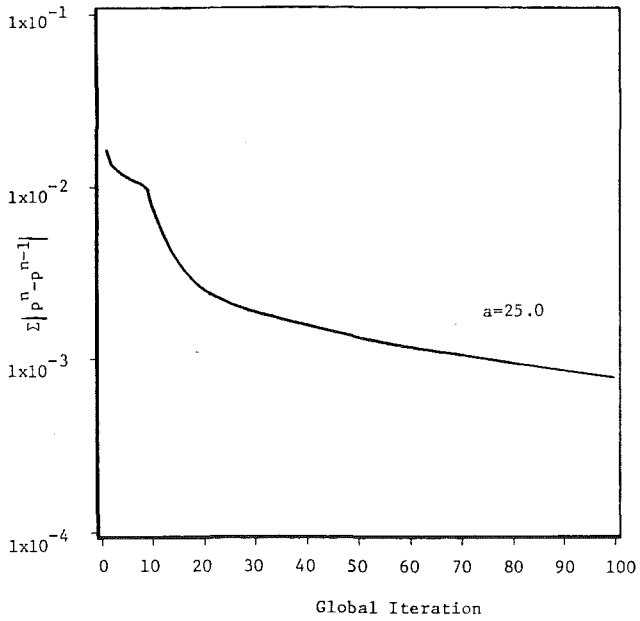

Fig. 12 Convergence history for the PSU rotor

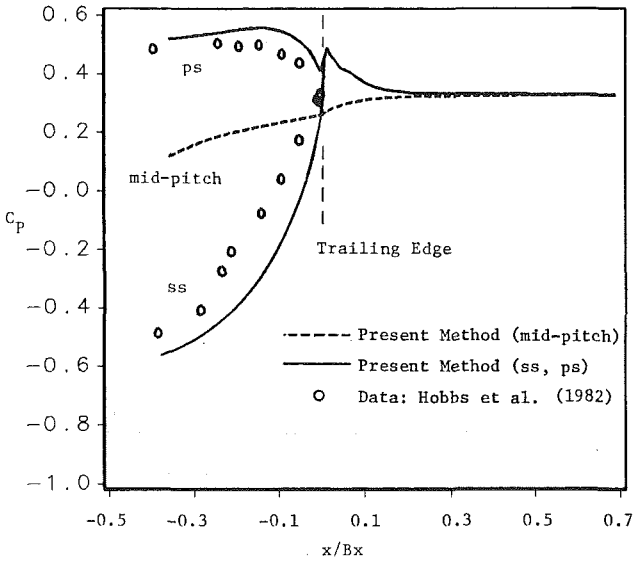

Fig. 11 Pressure distribution for Hobbs' cascade, algebraic model

prediction of the turbulence dissipation. For some coarse grid computations, this turbulence dissipation was so large that no turbulence could be sustained past the near wake region. Thus, there appears to be some grid dependence for this wake flow. Indeed, if the grid is refined in the axial direction near the trailing edge, divergent behavior appeared. This is due to the combination of large gradients of all variables, lack of streamwise diffusion of k and ϵ, and the use of wall functions on k and ϵ on the blade surface. It should be noted, though, that for a successful wake computation, special care had to be taken to ensure that the flow did not separate at the trailing edge during the global iteration procedure. Although the method is stable for laminar flow separation and turbulent flow separation with an algebraic model, use of the k–ϵ model generated incorrect turbulence kinetic energy and turbulence dissipation distributions in the strong interaction region, which generally led to divergent behavior. Such behavior can be damped out when the elliptic form of the k–ϵ equations is used, but not so with the present parabolized equations. In the far wake, a double peak in the streamwise turbulent intensity distribution is evident. While not measured for this case, the double peak is characteristic of many turbulent wake flows.

The computed pressure distribution in the wake region is shown in Fig. 11. The most important observation is that, in the wake region, while the streamwise pressure gradient in the outer flow is nearly constant, the pressure drops dramatically near the wake centerline close to the trailing edge. This localized effect is due to the acceleration of the wake centerline velocities. Thus, the transverse pressure gradient is not constant across the shear layer in the near wake region even for a noncurving wake. The lack of agreement with the data on the blade surfaces is due to the inviscid inlet conditions being applied at roughly 50 percent chord and not at the leading edge. This should not affect the accuracy of the wake predictions since the diffusion process is governed by the turbulence and not by the blade pressure distribution.

Flow in a Compressor Rotor. The final test of the present method was to compute the flow in the PSU axial flow compressor rotor. The facility is described in depth by Lakshminarayana (1980). The hub-to-tip ratio is 0.5 with the radius of the annulus wall being 0.466 m. The rotor is made up of 21 NACA 65-010 blades with the stagger angle varying from 22.5 deg at the hub ($R=0.5$) to 45 deg at the tip ($R=1.0$). The computations performed here were for the design flow coefficient of $\phi=0.56$. Although the tip clearance region is roughly 0.15 cm, the tip clearance effects were not included in the computation. Also, the measured relative inlet Mach number is 0.085 and the Mach number based on tip speed is 0.153; thus the assumption of incompressibility is valid.

The inviscid inlet conditions at the leading edge and the initial inviscid pressure field were generated by stacking several two-dimensional panel solutions using Giesing's (1964) program. Turbulent-slip boundary conditions were used on all blade surfaces. Major difficulties were encountered when the k–ϵ turbulence model was applied to this case, thus the computation was performed using the algebraic eddy viscosity model. The grid consisted of 30 points in the axial direction and 27 in both the transverse and radial directions.

The convergence history for the rotor computation using a equal to 25 can be seen in Fig. 12. Typically, the value of a should increase with increasing flow complexity much like decreasing the time step for time-marching methods. Con-

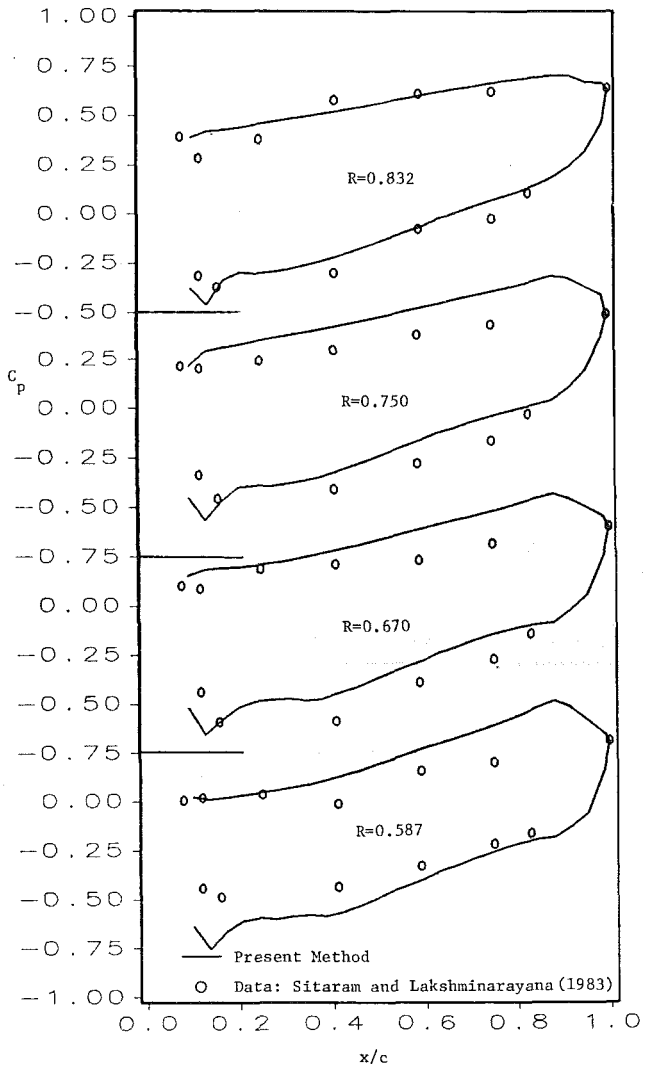

Fig. 13 Computed pressure distribution for the PSU rotor

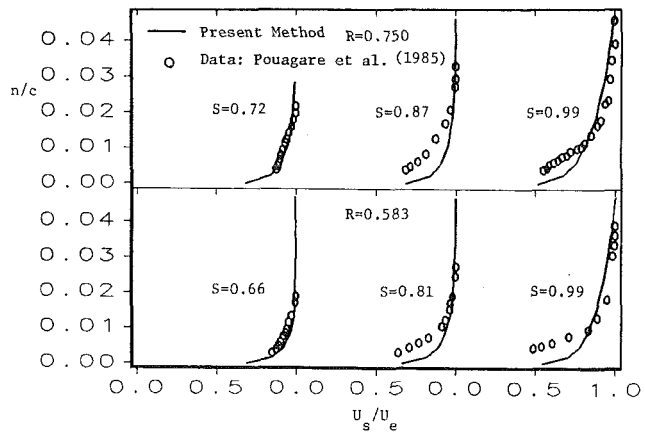

Fig. 14 Streamwise boundary layer profiles on the suction side for the PSU rotor

vergence of one and one half orders of magnitude was achieved in 100 global iterations. The computation was stopped to conserve the limited computer resources available. The computed pressure distribution at various radial locations is compared to the experimental data of Sitaram and Lakshminarayana (1983) in Fig. 13. The suction peak is well captured near the midspan; however, it is overpredicted in the

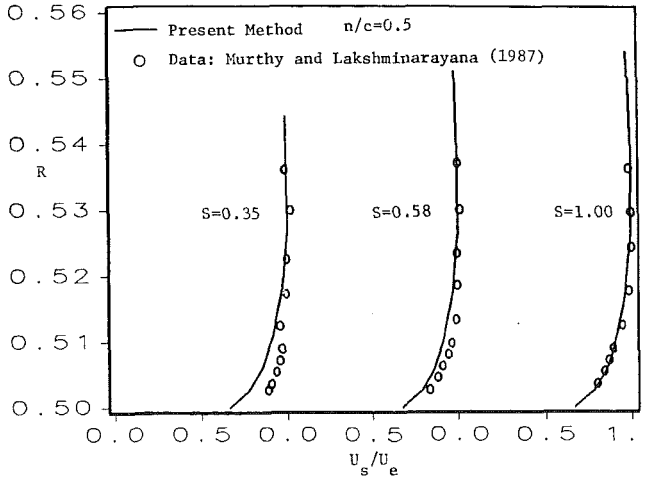

Fig. 15 Hub wall boundary layer profiles for the PSU rotor

hub wall region. The suction side pressure distribution agrees favorably with the experimental data. The pressure side C_P agrees well with the data at $R = 0.832$; however at lower values of R, a hump in the computed distribution is present near the trailing edge. The secondary flows near the hub wall were generally overpredicted. This extra flow turning leads to increased loading, which is evident from the C_P distribution.

The computed suction side boundary layer profiles are compared to the hot-wire data of Pouagare et al. (1985) in Fig. 14. The agreement with the data is good near the hub and midspan regions. Near the trailing edge, the boundary layer profiles are not well predicted, which may be due to the lack of wake interaction in the computation.

The computed pressure side boundary layers and radial flow profiles do not compare well with the data (not shown). The results are qualitatively correct; however, the magnitudes are somewhat underpredicted. This may be due to the use of the turbulent-slip boundary condition. The radial flow near the blade surface is driven by the normal gradient of the streamwise velocity. Thus, since the slip condition effectively reduces this gradient, the radial flows will not develop, as is the case. The computed hub wall boundary layer is compared to the experimental data of Murthy and Lakshminarayana (1987) in Fig. 15. The boundary layer growth on the hub wall is well captured as is the actual profile.

Finally, the computed stagnation pressure loss coefficient ψ_{loss}, based on the blade tip speed, is compared to the experimental data at the exit in Fig. 16. The agreement with the data is surprisingly good. The losses on the pressure side are somewhat underpredicted and the computed loss core, near $n/c = 0.3$, is closer to the suction side than the measured location of $n/c = 0.4$. Still, the stagnation pressure loss is one of the most difficult flow quantities to capture and the present method has done a reasonably good job of computing in at this location.

Conclusion

A new coupled parabolic-marching method was used to compute the flow in various forms of turbomachinery. A two-equation k-ϵ turbulence model was used to compute the flow in a rectilinear turbine endwall cascade. The computed pressure distribution and velocity profiles compared well with the experimental data. The development of the passage vortex was accurately captured. The wake of a similar cascade was computed using both the algebraic eddy viscosity model and the k-ϵ model. The computed near-wake flow showed only adequate comparison with the experimental data near the wake centerline. The far wake was not well predicted using the

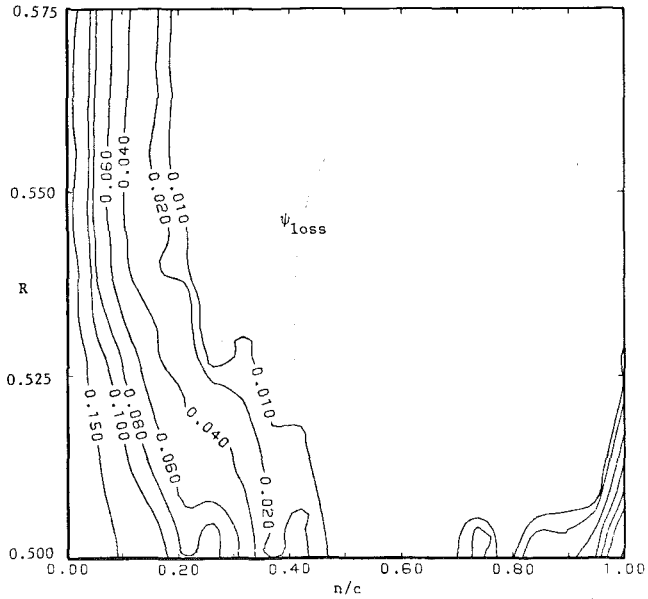

Fig. 16(*a*) Computed pressure loss contours at the PSU rotor exit

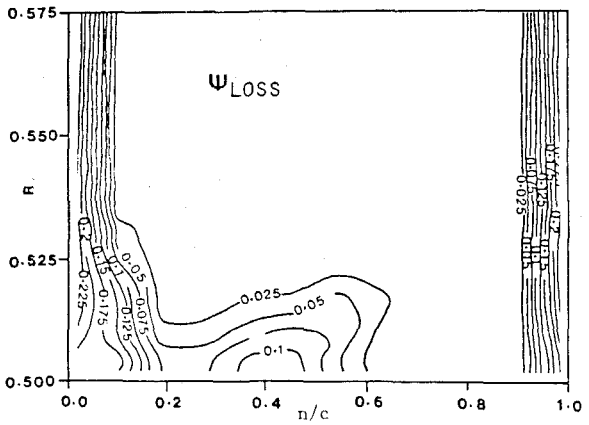

Fig. 16(*b*) Measured pressure loss contours at the PSU rotor exit

algebraic model. Both the wake decay and wake centerline did not match the data. When the k–ϵ model was used, the computed near-wake results were similar to those using the algebraic model; however, the far-wake results compared extremely well with the experimental data. Since the wake decay is a strong function of the turbulence, it is apparent that the use of a higher order turbulence model is necessary for accurate wake computations.

Finally, the new method was used to compute the flow in an axial flow compressor rotor. This flow was difficult to compute and perhaps signals the limit of complexity where the PPNS system can be applied. The computed suction side boundary layers compared reasonably well with the experimental data in the hub wall region. Suction side pressure distributions were close to the data at all radial locations; however, the pressure side C_p did not match the data very near the trailing edge. Computed exit stagnation pressure losses compared reasonably well with the data. Better predictions may be achieved using a finer grid and using the no-slip condition rather than turbulent slip. CPU time on the IBM 3090 at the Pennsylvania State University was 2.01×10^{-3} s/pt./it. for turbulent flow computations. It should be noted that the code as used here is in "research form," i.e., modular, unvectorized, and nonoptimized. When vectorized, the CPU time would be comparable to that of the NASA Ames INS3D full Navier–Stokes solver as reported by Warfield and Lakshminarayana (1987) for the same rotor geometry and grid. More importantly, only the pressure variable and grid node locations are stored in three-dimensional arrays. Thus for a $60 \times 31 \times 31$ grid, only 1.5 MB of memory is required. Overall, the new method showed its usefulness in computing pressure-driven secondary flows, wakes, blade boundary layers, and various other viscous effects in turbomachinery.

Acknowledgments

This work was performed at the Applied Research Laboratory under the sponsorship of the Naval Ship Research and Development Center. Use of the computed facilities at The Pennsylvania State University is greatly appreciated.

References

Baldwin, B. S., and Lomax, H., 1978, "Thin Layer Approximation and Algebraic Model for Separated Turbulent Flows," AIAA Paper No. 78-257.

Briley, W. R., Buggeln, R. C., and McDonald, H., 1985, "Solution of the Three-Dimensional Navier–Stokes Equations for a Steady Laminar Horseshoe Vortex Flow," AIAA Paper No. 85-1520.

Briley, W. R., and McDonald, H., 1980, "On the Structure and Use of Linearized Block Implicit Scheme," *J. Comp. Physics*, Vol. 34, pp. 54–73.

Chorin, A. J., 1967, "A Numerical Method for Solving Incompressible Viscous Flow Problems," *J. Comp. Physics*, Vol. 2, pp. 12–26.

Dawes, W. N., 1987, "A Numerical Analysis of the Three-Dimensional Viscous Flow in a Transonic Compressor Rotor and Comparison With Experiment," ASME JOURNAL OF TURBOMACHINERY, Vol. 109, pp. 83–70.

Flot, R., and Papailiou, K., 1975, "Couches Limits et Effets D'Extremities Dans les Turbomachines," METRAFLU, contract Dr. M. E. 73/373.

Giesing, J. P., 1964, "Extension of the Douglas-Neumann Program to Problems of Lifting, Infinite Cascades," Douglas Aircraft Company Report No. LB31653.

Hah, C., 1986, "Navier–Stokes Calculation of Three-Dimensional Compressible Flow Across a Cascade of Airfoils With an Implicit Relaxation Method," AIAA Paper No. 86-0555.

Hobbs, D. E., Wagner, J. H., Dannenhoffer, J. F., and Dring, R. P., 1982, "Experimental Investigation of Compressor Cascade Wakes," ASME Paper No. 82-GT-299.

Kirtley, K. R., 1987, "A Coupled, Parabolic-Marching Method for the Prediction of Three-Dimensional Viscous Incompressible Turbomachinery Flows," Ph.D. Thesis, Aerospace Engineering, The Pennsylvania State University, University Park, PA.

Kirtley, K. R., Warfield, M., and Lakshminarayana, B., 1986, "A Comparison of Computational Methods for Three-Dimensional Turbulent Turbomachinery Flows," AIAA Paper No. 86-1599.

Kwak, D., Chang, J. L. C., Shanks, S. P., and Chakravarthy, S. R., 1986, "A Three-Dimensional Incompressible Navier–Stokes Flow Solver in Primitive Variables," *AIAA Journal*, Vol. 24, No. 3, pp. 390–396.

Lakshminarayana, B., 1980, "An Axial Flow Research Compressor Facility Designed for Flow Measurement in Rotor Passages," ASME *J. Fluids Engr.*, Vol. 102, pp. 402–411.

Moore, J., and Moore, J. G., 1981, "Calculations of Three-Dimensional Viscous Flow and Wake Development in a Centrifugal Impeller," ASME *Journal of Engineering for Power*, Vol. 103, pp. 367–372.

Murthy, K. N. S., and Lakshminarayana, B., 1987, "Entwicklung der Nabengrenzschicht und Stromungsverluste in Rotor eines Axialkompressors," *Z. Flugwiss, Weltraumforsch*, Vol. 11, pp. 1–11.

Pouagare, M., Galmes, J. M., and Lakshminarayana, B., 1985, "An Experimental Study of the Compressor Rotor Blade Boundary Layer," ASME *Journal of Engineering for Power*, Vol. 107, pp. 364–373.

Pouagare, M., and Lakshminarayana, B., 1986, "A Space-Marching Method for Flows," *J. Comp. Physics*, Vol. 64, No. 2, pp. 289–415.

Raj, R., and Lakshminarayana, B., 1973, "Characeristics of the Wake Behind a Cascade of Airfoils," *J. Fluids Mech.*, Vol. 61, part 4, pp. 707–730.

Rhie, C. M., 1983, "Basic Calibration of a Partially-Parabolic Procedure Aimed at Centrifugal Impeller Analysis," AIAA Paper No. 83-0260.

Rodi, W., 1982, "Examples of Turbulence Models for Incompressible Flows," *AIAA Journal*, Vol. 20, No. 3, pp. 872–879.

Sitaram, N., and Lakshminarayana, B., 1983, "End Wall Flow Characteristics and Overall Performance of an Axial Flow Compressor Stage," NASA CR 3671.

Warfield, M. J., and Lakshminarayana, B., 1987, "Calculation of a Three-Dimensional Turbomachinery Rotor Flow With a Navier–Stokes Code," ASME Paper No. 87-GT-232.